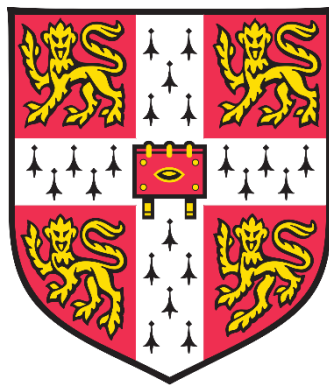


# **Improvement in the Growth and Superconducting Properties of Bulk Sm-Ba-Cu-O Superconductors Fabricated in Air**



**Wen Zhao**

Department of Engineering

University of Cambridge

This dissertation is submitted for the degree of

*Doctor of Philosophy*



# Declaration

I hereby declare that except where specific reference is made to the work of others, the contents of this dissertation are original and have not been submitted in whole or in part for consideration for any other degree or qualification in this, or any other University. This dissertation is the result of my own work and includes nothing that is the outcome of work done in collaboration, except where indicated specifically in the text. This dissertation contains less than 65,000 words including appendices, bibliography, footnotes, tables and equations and has fewer than 150 figures.

Wen Zhao  
2017



# Acknowledgements

My most heartfelt gratitude goes first and foremost to my supervisor, Prof. David A. Cardwell, for him being a tremendous mentor for me throughout four challenging yet enjoyable years. During this incredible journey, he has encouraged me and allowed me to grow as a research scientist. At the same time, his advice on both my research and career have been priceless. I am also greatly thankful for the excellent example he has provided as a successful and highly-respected professor so that I know what to pursue as the goal of my career.

I could not express my acknowledgements enough to my advisor, Dr Yunhua Shi, for her constant support and firm belief in me. She has been patiently guided me through challenging experiments and difficult data interpretation during my PhD. It is of great fortune for me to have such an experienced scientist as my advisor from whom I have learned so much.

I have always been grateful to Mr Anthony R. Dennis for his kind assistance with my experiments. He has offered his expertise and help consistently and warmly whenever I have encountered any problems in the laboratory. He has always gone out of his way to assist me with equipment and material characterisation to make sure that I could obtain results that I needed in time.

This thesis would have been impossible without the support of my amazing colleagues and friends in the Bulk Superconductivity Group: Prof. Archie Campbell, Dr John H. Durrell, Dr Mark D. Ainslie, Dr Namburi Devendra Kumar, Dr Difan Zhou, Dr Zhiwei Zhang, Dr Wei Zhai, Dr Jin Zou, Dr Di Hu, Dr Zhihan Xu, Mr Danny Huang, Miss Jasmin V. J. Congreve, Mr Kysen G. B. Palmer, Mr Jordan P. Rush, Miss Roberta Trupiano and Ms Meredith Packham. I could never thank them enough for their precious support and generous help throughout my PhD.

Words cannot express how grateful I am to Prof. Pavel Diko to have me in his lab in Slovakia to further my understanding of my material with their state of the art of microscopic techniques, to Dr Iris Buisman for patiently discussing with me on the EPMA characterisation of my material and kindly guiding me through the time-consuming measurement, and to Mr Jon J. Rickard for his warm-heartedly assistance with my SEM observations and image-taking.

I am greatly indebted to the China Scholarship Council for their generous funding, which removed financial concerns from my decision to embark on this amazing journey. I should also like to express my appreciation for financial support from the Department of Engineering, Fitzwilliam College, the Cambridge Philosophical Society, Edmission UK and the Institute of Physics for assistance towards the cost of attending several international conferences which have had a huge impact on my research.

I am sincerely grateful for all my dearest friends who have accompanied me through my PhD: I would love to thank Wei Zhai and Ailin Zhang for familiarizing me with Cambridge from the day I arrived and for their fun company ever since; I owe a huge debt of gratitude to Qian Wang, Long Zhang, Xiaorui Wei and Wei Bu for cheering me up whenever the going became tough; I would also like to acknowledge Qian Cheng, Difan Zhou and Danny Huang for keeping a would-be-boring laboratory life a fun one, especially for their joyful optimism throughout my studies. Without them, Cambridge would not have shone so brightly.

Last, but not the least, I would like to express my extensive appreciation to my parents who I love so much for always standing by my side regardless of my life-changing decisions, for constantly comforting me whenever I met difficulties in research or in life, for loving me ceaselessly and unconditionally so that I could be myself and for continually being excited as I have reached my dreams.



# List of publications

- [1]. **Zhao, W**; Shi, Y; Radušovská, M; Dennis, AR; Durrell, JH; Diko, P; Cardwell, DA; "Comparison of the Effects of Platinum and CeO<sub>2</sub> on the Properties of Single Grain, Sm-Ba-Cu-O Bulk Superconductors". *Supercond. Sci. Technol.*, 2016, 29, 125002 (11 pp)
- [2]. **Zhao, W**; Shi, Y; Dennis, AR; Cardwell, DA; "Use of Sm-123 + Sm-211 Mixed-Powder Buffers to Assist the Growth of SmBCO and ZrO<sub>2</sub>-doped SmBCO Single Grain Bulk Superconductors". *IEEE Transactions on Applied Superconductivity*, 2015, 25. ISSN 1051-8223
- [3]. Zhou, D; Shi, Y; **Zhao, W**; Dennis, AR; Beck, M; Ainslie, MD; Palmer, KGB; Cardwell, DA; Durrell, JH; "Full Magnetization of Bulk (RE)Ba<sub>2</sub>Cu<sub>3</sub>O<sub>7- $\delta$</sub>  Magnets With Various Rare-Earth Elements Using Pulsed Fields at 77 K". *IEEE Transactions on Applied Superconductivity*, 2017, 27 (4), 6800704 (4 pp)
- [4]. Shi, Y; Namburi, DK; **Zhao, W**; Durrell, JH; Dennis, AR; Cardwell, DA; "The use of buffer pellets to pseudo hot seed (RE)-Ba-Cu-O-(Ag) single grain bulk superconductors". *Supercond. Sci. Technol.*, 2016, 29, 015010 (8 pp)



# Abstract

Sm-Ba-Cu-O (SmBCO), which is a member of rare-earth barium cuprate [(RE)BCO] high-temperature superconductors, has significant potential for practical applications due to its higher critical transition temperature ( $T_c$ ), higher critical current density ( $J_c$ ), the so-called ‘peak effect’ characteristic at relatively high applied magnetic field and higher irreversibility field than that of the more established YBCO. The aim of this study is to investigate and overcome the obstacles in fabricating SmBCO bulk superconductors in air, to further improve their superconducting properties and, finally, to scale-up the fabrication of SmBCO single grains, therefore realising the engineering applications of this technologically important material.

A modified seeding technique using an MgO-NdBCO generic seed accompanied by a buffer layer has been developed to process the SmBCO system to increase the success rate of growing single domain, bulk SmBCO superconductors in air via a top-seeded melt growth process using a conventional chamber furnace. Subsequently, the effects of doping in SmBCO bulk superconductors on the performance of SmBCO superconductors containing different dopants are discussed based on an analysis of their superconducting properties, including  $T_c$  and  $J_c$ , and on the microstructures of the samples. Furthermore, the scale-up of SmBCO bulk superconductors has been achieved by the addition of silver to the precursor powders and the introduction of a Y-123 layer beneath the SmBCO bulk pre-forms. Finally, trapped field measurements on successfully grown SmBCO bulk superconductors up to 41 mm in diameter have been performed and used to demonstrate significantly improved field trapping ability due to the optimization of the processing and composition of the SmBCO system. An Ag-SmBCO single grain of diameter 31 mm has achieved 1.033 T at 77 K, which is the highest value of trapped field reported worldwide for SmBCO samples of a similar size grown in air.





3.2.1.	Solidification: Solute Diffusion Model and Pushing/trapping Theory .....	39
3.2.1.1.	Solute Diffusion Model.....	39
3.2.1.2.	Pushing / trapping Theory .....	40
3.2.2.	Oxygenation .....	43
3.2.3.	Growth Morphology and Microstructure .....	43
3.2.4.	Critical Current Density $J_c$ -related Properties of TSMG- processed SmBCO Bulk Single Grains .....	45
3.2.4.1.	Secondary Peak Effect .....	45
3.2.4.2.	Effects of Sm-211 Inclusions .....	45
3.2.4.3.	Effects of Dopants .....	46
3.2.4.4.	Improvement of Mechanical Properties of TSMG-processed SmBCO Bulk Single Grains.....	46
3.3.	Characterisation Techniques .....	47
3.3.1.	Microstructural Observation Techniques .....	48
3.3.1.1.	Optical Microscopy.....	48
3.3.1.2.	Scanning Electron Microscopy (SEM) .....	48
3.3.2.	Superconducting Characterisation Techniques .....	48
3.3.2.1.	Measurement of $T_c$ and $J_c$ .....	48
3.3.2.2.	Trapped Field Measurement.....	49
3.3.3.	Thermoanalytic Characterisation Technique : Differential Thermal Analysis (DTA) .....	50
3.3.4.	Chemical-analytic Characterisation Techniques .....	51
3.3.4.1.	Energy Dispersive X-ray Spectrometry (EDX).....	51
3.3.4.2.	X-ray Diffraction (XRD).....	51
3.3.4.3.	Electron Probe Micro-analyser (EPMA).....	52
3.4.	Summary .....	52
<b>4.</b>	<b>Chapter 4 Modified Seeding Technique Using a MgO-NdBCO Generic Seed by Employing a Buffer Layer .....</b>	<b>53</b>

4.1.	Introduction and Motivation .....	53
4.2.	Experimental .....	57
4.2.1.	Production of SmBCO Single Grains in Air by Cold Seeding.....	57
4.2.2.	Sample Characterisation.....	60
4.2.2.1.	Differential Thermal Analysis (DTA) and Microstructures of SmBCO Bulk Single Grains Fabricated with and without Buffer Layers .....	60
4.2.2.2.	Measurements of $T_c$ and $J_c$ of SmBCO Specimens with and without Buffer Layers .....	60
4.2.2.3.	Trapped Field Measurement of SmBCO with and without Buffer Layers	61
4.2.3.	Results and Discussion.....	61
4.3.	Summary .....	69
<b>5.</b>	<b>Chapter 5 Effects of Doping in Superconducting SmBCO Bulk Single Grains .....</b>	<b>71</b>
5.1.	Introduction and Motivation .....	71
5.2.	Comparison of the Effects of Platinum and CeO <sub>2</sub> on the Properties of Single-grain, SmBCO Bulk Superconductors .....	75
5.2.1.	Experimental Details.....	75
5.2.2.	Results and Discussion.....	78
5.2.3.	Summary .....	87
5.3.	Growth and Superconducting Properties of SmBCO Single Grains fabricated with Different Dopants.....	87
5.3.1.	Experimental Details.....	87
5.3.2.	Results and Discussion.....	92
5.3.2.1.	The Formation of Sm-2411 (Zr).....	92
5.3.2.2.	The Effects of Doping on the Growth of SmBCO Single Grains .....	95
5.3.2.3.	Doping Effects to Superconducting Properties and Microstructure of SmBCO Single Grains.....	103
5.3.3.	Summary .....	116
5.4.	Summary and Conclusions .....	117

<b>6. Chapter 6 SmBCO Bulk Single Grain Scale-up through Silver Addition.....</b>	<b>118</b>
6.1. Introduction and Motivation .....	118
6.2. Experimental .....	121
6.2.1. Production of SmBCO Single Grains with Silver Additions in Air by Cold Seeding with and without a Y-123 Layer.....	121
6.2.2. Characterisation .....	125
6.2.2.1. Differential Thermal Analysis (DTA) .....	125
6.2.2.2. Microstructure and Superconducting Properties, $T_c$ and $J_c$ , of the Ag-SmBCO Single Grains.....	125
6.2.2.3. Chemical Composition Analysis of the Ag-SmBCO Bulk Single Grains with and without a Y-123 Layer .....	126
6.2.2.4. Trapped Field Measurements of the Ag-SmBCO Bulk Single Grains ....	127
6.3. Results and Discussion .....	127
6.3.1. Reliable Growth of the Ag-SmBCO System (Scale-up from 10 mm to 41 mm in Diameter).....	127
6.3.2. Trapped Field Analysis of the Optimised Ag-SmBCO Bulk Single Grains ...	143
6.3.2.1. 2D-contour Maps of the Trapped Magnetic Fields of 1 mol. % ZrO <sub>2</sub> -doped Ag-SmBCO.....	144
6.3.2.2. 2D-contour Maps of the Magnetic Trapped Fields of the Ag-SmBCO Single Grains with Y-123 Layers.....	146
6.3.3. Discussion of the Effects of a Y-123 Layer on Ag-SmBCO System .....	159
6.3.3.1. Reliable Growth of Ag-SmBCO Single Grains.....	159
6.3.3.2. Superconducting Properties: $T_c$ and $J_c$ .....	161
6.3.3.3. Microstructural Analysis of the Distribution of Sm-211 Particles .....	167
6.3.3.4. Chemical Composition of the Sm <sub>1+x</sub> Ba <sub>2-x</sub> Cu <sub>y</sub> O <sub>z</sub> Matrix in Ag-SmBCO Processed with and without a Y-123 Layer .....	168
6.3.3.5. Trapped Field Profiles.....	173
6.4. Summary .....	175

<b>7. Chapter 7 Conclusions and Future Work .....</b>	<b>177</b>
7.1. Conclusions.....	177
7.2. Future Work.....	181
<b>8. References.....</b>	<b>184</b>



# List of figures

**Figure 1** Evolution of  $T_c$  of known superconducting materials: (1) Natural elements and simple compounds [7] [8] [13] [15] [17] [18] [19] [20] [21] [22]; (2) Organic superconductors (Buckminster fullerenes) [23] [24] [25]; (3) Organic superconductors [26] [27] [28] [29] [30]; (4) Heavy fermion superconductors [31] [32] [33] [34] [35] [36] [37]; (5) Cuprate superconductors [1] [2] [10] [11] [12] [38] [39]; (6) Iron based superconductors [14] [40] [41] [42] and (7) Unconventional superconductors [16].

**Figure 2** Illustration of the superconducting materials listed in Table 1.

**Figure 3** (a) Typical superconducting transition at  $T_c$  [7]; (b) representative  $T_c$  plot for a superconductor.

**Figure 4** Magnetic behaviour of (a) a hypothetical superconductor without the Meissner-Ochsenfeld effect (i. e. an ‘ideal’ conductor with zero resistance) and (b) a superconductor [49].

**Figure 5** Schematic illustration of the difference between type I and type II superconductors in terms of the penetration depth ( $\lambda$ ) and the coherence length ( $\xi$ ) [51].

**Figure 6** Temperature dependence of free energies for a superconducting and a normal state [53].

**Figure 7** (a) Mixed state with fluxoids inside a superconductor, (b) spatial distribution of superelectron density and (c) spatial distribution of magnetic flux density [53].

**Figure 8** Variation of applied magnetic flux density ( $B$ ) with temperature (T) for (a) a type I superconductor and (b) a type II superconductor [55].

**Figure 9** (1a) Schematic illustration of reversible and irreversible magnetization of a type II bulk superconductor [54]; (1b) An example of  $J_c$  curve of  $\text{YBa}_2\text{Cu}_3\text{O}_{7-\delta}$  specimen that gives M-H loop as shown in Figure 9 (1a); (2a) Schematic illustration of reversible and irreversible magnetization of a type II bulk superconductor with a secondary peak effect; (2b) An example of  $J_c$  curve of 1 mol. %  $\text{ZrO}_2$   $\text{SmBa}_2\text{Cu}_3\text{O}_{7-\delta}$  specimen that gives M-H loop as shown in Figure 9 (2a).

**Figure 10** Schematic illustration of the magnetisation process of an infinite slab of a type II superconductor with a thickness of  $2a$  in a field parallel to its surface. (a) An infinite slab in a magnetic field; (b) the distribution of the induced field  $B$  over the cross section of the infinite slab.

**Figure 11** Schematic trapped field profile of a superconducting bulk single grain [54].

**Figure 12** Oxygen-deficient perovskite structure of the superconducting SmBCO phase [53].

**Figure 13** A pseudo binary phase diagram for SmBCO system between the BaCuO<sub>2</sub> and ‘Sm202’ phases. The positions of all lines are approximate [54].

**Figure 14** Dominant phenomena affecting the microstructure of the SmBCO system in TSMG [53].

**Figure 15** Illustrative diagram of the principle of the solidification model for the growth of SmBCO: Sm concentration of the Sm-123 and Sm-211 solid ( $C_S^{123}$  and  $C_S^{211}$ ), Sm concentration of the Sm-123 and Sm-211 liquid ( $C_L^{123}$  and  $C_L^{211}$ ), Sm composition difference at Sm-123 and Sm-211 solid-liquid interface ( $\Delta C_{SL}^{123}$  and  $\Delta C_{SL}^{211}$ ) and flux liquid concentration difference ( $\Delta C_L$ ) [85].

**Figure 16** Schematic illustration showing a particle in front of the solid-liquid interface and the condition necessary for particle pushing: (a) for  $\Delta\sigma_0 > 0$ , the force ( $F_I$ ) due to the interfacial energy ( $\Delta\sigma_0$ ) is conducive to pushing; (b) for  $\Delta\sigma_0 < 0$ , the force ( $F_I$ ) is conducive to trapping. The drag force ( $F_D$ ) is always conducive to trapping [53].

**Figure 17** (a) Photograph of the top surface of a fully-grown SmBCO single grain; (b) an SEM image of a cross section view of a fully-grown SmBCO single grain; (c) schematic diagram of the growth sectors from the top view; (d) schematic diagram of the growth sectors on the cross-section of the SmBCO sample; (e) optical micrograph with the magnification of 1000 times of a polished surface of SmBCO superconductor marked with Sm-123 matrix and Sm-211 inclusions and (f) an SEM image of a cross section view of a fully-grown SmBCO single grain marked with the positions of cracks and pores.

**Figure 18** Schematic illustration of the section geometry for the preparation of the specimens for SQUID magnetometry.

**Figure 19** A typical cold-seeding heating profile used to fabricate SmBCO single grains showing all the growth-related temperatures.  $T_{max}$  is the highest temperature used in the whole heating profile. The integrity of the seed will be maintained as long as the melting temperature of the seeding material is higher than  $T_{max}$ .

**Figure 20** Schematic illustration of the TSMG process for the fabrication of single grain SmBCO using assorted buffers.

**Figure 21** (a) Schematic illustration of the bulk pre-form with an MgO-NdBCO generic seed on a buffer layer and how each single grain was cut for characterisation. (b) Illustration of the positions of the specimens within the parent bulk used for measuring  $T_c$  and  $J_c$ .

**Figure 22** Differential thermal analysis (DTA) traces of SmBCO pseudo pre-forms and MgO-NdBCO generic seeds.

**Figure 23** (a) SmBCO 16 mm in diameter fabricated without buffers; SmBCO 16 mm in diameter fabricated with 5 mm different buffers: (b) a Sm-211 buffer, (c) a SmBCO buffer and (d) a Sm-123 + Sm-211 mixed-powder buffer; (e) SmBCO 16 mm in diameter with a 3 mm Sm-123 + Sm-211 mixed-powder buffer; (f) SmBCO 20 mm in diameter with a 3 mm Sm-123 + Sm-211 mixed-powder buffer; SmBCO 20 mm in diameter with three different sizes of Sm-123 + Sm-211 mixed-powder buffers: (g)  $d=3$  mm,  $t=1.5$  mm, (h)  $d=3$  mm,  $t=3$  mm and (i)  $d=3$  mm,  $t=4.5$  mm; (j) Sm-123 + Sm-211 16 mm in diameter with a 3 mm Sm-123 + Sm-211 mixed-powder buffer.

**Figure 24** Micrographs at positions illustrated in Figure 21 (b) showing the Sm-211 distribution and particle size in the SmBCO matrix with and without Sm-123 + Sm-211 mixed-powder buffer layers: with the magnification of 1000 times: SmBCO with a Sm-123 + Sm-211 mix-powder buffer layer at positions at: (1) 1a, (2) 1b and (3) 2a and SmBCO without a Sm-123 + Sm-211 mix-powder buffer layer at positions at: (4) 1a, (5) 1b and (6) 2a.

**Figure 25** Comparison of  $T_c$  between SmBCO fabricated with and without Sm-123 + Sm-211 mixed-powder buffers at positions: (1) 1a, (2) 1b and (3) 2a; Comparison of  $J_c$  at 77 K between SmBCO with and without Sm-123 + Sm-211 mixed-powder buffers at positions: (4) 1a, (5) 1b and (6) 2a.

**Figure 26** Trapped field distributions (2D contour images) of the top-surfaces of the SmBCO single grains grown (1) with and (2) without a Sm-123 + Sm-211 mixed-powder buffer layer.

**Figure 27** Periodic Table of Elements marked with the constituent elements in SmBCO and the elements doped into the SmBCO precursor powder.

**Figure 28** Schematic illustration of the bulk pre-form with a thin film seed.

**Figure 29** Heating profile used to produce SmBCO + CeO<sub>2</sub> and SmBCO + Pt single grains.

**Figure 30** Schematic illustration of the positions of the bulk specimens within the single grain.

**Figure 31** Differential thermal analysis traces of SmBCO + CeO<sub>2</sub> and SmBCO + Pt precursor powders.

**Figure 32** Photographs of the top surfaces of SmBCO + CeO<sub>2</sub> and SmBCO + Pt single grains.

**Figure 33** Comparison of  $T_c$  for the sub-specimens along the  $a/b$ -axis and  $c$ -axis of the SmBCO + CeO<sub>2</sub> and SmBCO + Pt single grains.

**Figure 34** Comparison of  $T_c$  for specimens at the same position in the parent single grain for SmBCO + CeO<sub>2</sub> and SmBCO + Pt compositions.

**Figure 35** Comparison of  $J_c$  for specimens at the same position in the parent single grain for SmBCO + CeO<sub>2</sub> and SmBCO + Pt compositions.

**Figure 36** Comparison of  $J_c$  for sub-specimens at the same position in sample-compositions of SmBCO + CeO<sub>2</sub> and SmBCO + Pt.

**Figure 37** Micrographs at a magnification of 500× for the SmBCO + CeO<sub>2</sub> [(1a) and (1b)] and SmBCO + Pt samples [(2a) and (2b)] observed at equivalent positions in the parent single grain (position 1b in Figure 30). Micrograph (3) is for the undoped single grain SmBCO sample (pure SmBCO).

**Figure 38** EDX analysis of the Ce-containing second phase located on macro-cracks formed orthogonally to the *c*-axis in the single grain sample of composition SmBCO + CeO<sub>2</sub>.

**Figure 39** EDX analysis of the Ce-containing second phase formed in pores in the single grain sample of composition SmBCO + CeO<sub>2</sub>.

**Figure 40** Schematic illustration of the bulk pre-form with: (a) a thin film seed; and (b) a MgO-NdBCO generic seed on a buffer.

**Figure 41** Schematic illustration of the TSMG process for the growth of bulk SmBCO.

**Figure 42** How each single grain was cut following melt processing and illustration of the position of the sub-specimens within the parent bulk used for measuring  $T_c$  and  $J_c$ .

**Figure 43** X-ray diffraction patterns for solid-state reacted powders with starting compositions of Sm<sub>2</sub>O<sub>3</sub>, BaCO<sub>3</sub>, CuO and ZrO<sub>2</sub> after each calcination with the standard oxides as references for the temperatures and times shown. All peaks are indexed with different symbols to attribute the peaks to different standard oxides.

**Figure 44** (a) Analysis using International Centre for Diffraction Data Database; X-ray diffraction patterns for (b) powders after final calcination at 1040 °C for 50 h and (c) standard Sm-211.

**Figure 45** DTA traces of doped and undoped SmBCO with MgO-NdBCO generic seeds indicating the decomposition (melting) temperatures.

**Figure 46** Schematic illustration of the TSMG process for standard SmBCO growth.

**Figure 47** SmBCO single grains grown successfully with 1 mol. % different dopants (16 mm in diameter).

**Figure 48** Failed SmBCO single grain samples in the first batch and grown subsequently into single grains after minor adjustments in a following batch.

**Figure 49** Failed SmBCO with different dopants in different amounts.

**Figure 50** Successfully grown (1) SmBCO and SmBCO doped with 1 mol. %: (2) ZrO<sub>2</sub>; (3) BaZrO<sub>3</sub>; (4) Fine Sm-211; and (5) TiO<sub>2</sub> (three quarter of a single grain).

**Figure 51** Comparison of  $T_c$  for the specimens measured along the *a/b*-axis and the *c*-axis of (a) SmBCO; (b) SmBCO + 1 mol. % ZrO<sub>2</sub>; (c) SmBCO + 1 mol. % TiO<sub>2</sub>; (d) SmBCO +

1 mol. % BaZrO<sub>3</sub>; (e) SmBCO + 1 mol. % fine Sm-211; (f) the specimens yielding the highest  $T_c$  in each sample and (g) the average  $T_c$  in each sample and (h) schematic illustration of the positions of the specimens within the parent bulk used for measuring  $T_c$ .

**Figure 52** (a) Comparison of  $J_c$  for specimens along the  $a/b$ -axis and the  $c$ -axis of (a) SmBCO; (b) SmBCO + 1 mol. % ZrO<sub>2</sub>; (c) SmBCO + 1 mol. % TiO<sub>2</sub>; (d) SmBCO + 1 mol. % BaZrO<sub>3</sub>; (e) SmBCO + 1 mol. % fine Sm-211; (f) the specimens giving the highest  $J_c$  in each sample; (g) the average  $J_c$  in each sample and (h) illustration of the position of the specimens within the parent bulk used for measuring  $J_c$ .

**Figure 53** Successfully grown SmBCO samples containing (1) 1 mol. % ZrO<sub>2</sub> + 0.5 mol. % BaZrO<sub>3</sub>; (2) 1 mol. % ZrO<sub>2</sub>; (3) 0.75 mol. % ZrO<sub>2</sub> + 0.25 mol. % BaZrO<sub>3</sub>; (4) 0.5 mol. % ZrO<sub>2</sub> + 0.5 mol. % BaZrO<sub>3</sub>; (5) 0.25 mol. % ZrO<sub>2</sub> + 0.75 mol. % BaZrO<sub>3</sub> and (6) 1 mol. % BaZrO<sub>3</sub>.

**Figure 54** Comparison of  $T_c$  (a) and  $J_c$  (b) for the specimens at 1a, 1b and 1c positions in Figure 42 of standard SmBCO, 1 mol. % ZrO<sub>2</sub>-SmBCO, 1 mol. % ZrO<sub>2</sub> + 0.5 mol. % BaZrO<sub>3</sub>-SmBCO and 0.5 mol. % ZrO<sub>2</sub> + 0.5 mol. % BaZrO<sub>3</sub>-SmBCO.

**Figure 55** Micrographs showing the Sm-211 distribution and particle size in SmBCO, 1 mol. % ZrO<sub>2</sub>-doped SmBCO and 1 mol. % BaZrO<sub>3</sub>-doped SmBCO: with a magnification of 500 times: (a) SmBCO; (b) 1 mol. % ZrO<sub>2</sub>-doped SmBCO; (c) 1 mol. % BaZrO<sub>3</sub>-doped SmBCO; with a magnification of 1000 times: (d) SmBCO; (e) 1 mol. % ZrO<sub>2</sub>-doped SmBCO; (f) 1 mol. % BaZrO<sub>3</sub>-doped SmBCO and (g) an illustration of the positions where the micrographs were taken (the shaded area).

**Figure 56** Illustration of the positions of the regions where the microstructures were taken and compared in Figures 57 to 60.

**Figure 57** Micrographs showing the Sm-211 distribution and particle size in SmBCO, 1 mol. % ZrO<sub>2</sub>-doped SmBCO and 1 mol. % BaZrO<sub>3</sub>-doped SmBCO at section A in Figure 56 with a magnification of 500 times: (1) SmBCO; (2) 1 mol. % ZrO<sub>2</sub>-doped SmBCO; (3) 1 mol. % BaZrO<sub>3</sub>-doped SmBCO with a magnification of 1000 times: (4) SmBCO; (5) 1 mol. % ZrO<sub>2</sub>-doped SmBCO and (6) 1 mol. % BaZrO<sub>3</sub>-doped SmBCO.

**Figure 58** Micrographs showing the Sm-211 distribution and particle size in SmBCO, 1 mol. % ZrO<sub>2</sub>-doped SmBCO and 1 mol. % BaZrO<sub>3</sub>-doped SmBCO at section B in Figure 56 with a magnification of 500 times: (1) SmBCO; (2) 1 mol. % ZrO<sub>2</sub>-doped SmBCO; (3) 1 mol. % BaZrO<sub>3</sub>-doped SmBCO with a magnification of 1000 times: (4) SmBCO; (5) 1 mol. % ZrO<sub>2</sub>-doped SmBCO and (6) 1 mol. % BaZrO<sub>3</sub>-doped SmBCO.

**Figure 59** Micrographs showing the Sm-211 distribution and particle size in SmBCO, 1 mol. % ZrO<sub>2</sub>-doped SmBCO and 1 mol. % BaZrO<sub>3</sub>-doped SmBCO at section C in Figure 56 with a magnification of 500 times: (1) SmBCO; (2) 1 mol. % ZrO<sub>2</sub>-doped SmBCO; (3) 1 mol. % BaZrO<sub>3</sub>-doped SmBCO with a magnification of 1000 times: (4) SmBCO; (5) 1 mol. % ZrO<sub>2</sub>-doped SmBCO and (6) 1 mol. % BaZrO<sub>3</sub>-doped SmBCO.

**Figure 60** Micrographs showing the Sm-211 distribution and particle size in SmBCO, 1 mol. % ZrO<sub>2</sub>-doped SmBCO and 1 mol. % BaZrO<sub>3</sub>-doped SmBCO at section D in Figure 56 with a magnification of 500 times: (1) SmBCO; (2) 1 mol. % ZrO<sub>2</sub>-doped SmBCO; (3) 1 mol. % BaZrO<sub>3</sub>-doped SmBCO with a magnification of 1000 times: (4) SmBCO; (5) 1 mol. % ZrO<sub>2</sub>-doped SmBCO and (6) 1 mol. % BaZrO<sub>3</sub>-doped SmBCO.

**Figure 61** Schematic diagram of an Ag-SmBCO bulk pre-form with a Y-123 layer prior to TSMG.

**Figure 62** Schematic illustration of the heating profile used in the TSMG process for the assorted Ag-SmBCO single grains.

**Figure 63** Schematic illustration of the cutting scheme for the preparation of the SQUID specimens.

**Figure 64** Differential thermal analysis traces of SmBCO and Ag-SmBCO.

**Figure 65** Ag-SmBCO samples grown successfully: (a) 13 mm in diameter; (b) 16 mm in diameter; (c) 20 mm in diameter and (e) 25 mm in diameter; the samples of diameter 25 mm (d) and 31 mm (f) failed to grow in the form of a single grain.

**Figure 66** Ag-SmBCO samples with adjusted growth parameters in the heating profile: (a) 16 mm in diameter (as a benchmark); (b) 16 mm in diameter; (c) 20 mm in diameter were grown successfully; (d) and (e) 25 mm in diameter samples failed to grown in the form of a single grain.

**Figure 67** Schematic illustration of the heating profile used in the TSMG process for the Ag-SmBCO single grains with calcined precursor powders.

**Figure 68** Ag-SmBCO samples fabricated from calcined precursor powders: (a) without any treatment (as a benchmark); (b)-(g) precursor powders calcined at 550 °C for 6 h with MgO-NdBCO generic seeds; (h) precursor powders calcined at 550 °C for 6 h with a film seed and (i) precursor powders calcined at 550 °C for 6 h and bulk pre-form at 900 °C for 6 h and then melt-processed with an MgO-NdBCO generic seed.

**Figure 69** Schematic illustration of the heating profile used in the TSMG process for Ag-SmBCO with a Y-123 layer.

**Figure 70** Schematic illustration of the TSMG process heating profile for fabricating Ag-SmBCO bulk single grains of diameter 31 mm and 41 mm.

**Figure 71** Photographs of the polished top surfaces of (a) Ag-SmBCO and (d) 1 mol. % ZrO<sub>2</sub>-doped Ag-SmBCO and their trapped field profiles at both the top: (b) Ag-SmBCO and (e) 1 mol. % ZrO<sub>2</sub>-doped Ag-SmBCO and bottom: (c) Ag-SmBCO and (f) 1 mol. % ZrO<sub>2</sub>-doped Ag-SmBCO surfaces measured at a distance of 0.5 mm above the sample surface. The maximum trapped field values at the top and bottom surfaces are indicated in the figure.

**Figure 72** Photographs of the polished top surfaces of: (a) Ag-SmBCO without a Y-123 layer; (d), (g) and (j) Ag-SmBCO with Y-123 layers (repeated experiments) and their trapped field profiles at both the top: (b) Ag-SmBCO without a Y-123 layer; (e), (h) and (k) Ag-SmBCO with Y-123 layers and bottom: (c) Ag-SmBCO without a Y-123 layer; (f), (i) and (l) Ag-SmBCO with Y-123 layers surfaces measured at a distance of 0.5 mm above the sample surface. The maximum trapped field values at the top surfaces and bottom surfaces are indicated in the figure.

**Figure 73** Photographs of the polished top surfaces of: (a) Ag-SmBCO with a 12 g Y-123 layer and (d) Ag-SmBCO with a 6 g Y-123 layer and their trapped field profiles at both the top: (b) Ag-SmBCO with a 12 g Y-123 layer and (e) Ag-SmBCO with a 6 g Y-123 layer and bottom: (c) Ag-SmBCO with a 12 g Y-123 layer and (f) Ag-SmBCO with a 6 g Y-123 layer surfaces measured at a distance of 0.5 mm above the sample surface. The maximum trapped field values at the top surfaces and bottom surfaces are indicated in the figure.

**Figure 74** Photographs of the polished top surfaces of: (a) Ag-SmBCO with a 6 g Y-123 layer; (d), (g) and (j) 1 mol. % ZrO<sub>2</sub>-doped Ag-SmBCO with a 6 g Y-123 layer (repeated experiments) and their trapped field profiles at both the top: (b) Ag-SmBCO with a 6 g Y-123 layer; (e), (h) and (k) 1 mol. % ZrO<sub>2</sub>-doped Ag-SmBCO with a 6 g Y-123 layer; (c) Ag-SmBCO with a 6 g Y-123 layer; (f), (i) and (l) 1 mol. % ZrO<sub>2</sub>-doped Ag-SmBCO with a 6 g Y-123 layer surfaces measured at a distance of 0.5 mm above the sample surface. The maximum trapped field values at the top surfaces and bottom surfaces are indicated in the figure.

**Figure 75** Photographs of the polished top surfaces of: (a) Ag-SmBCO with a 6 g Y-123 layer; (d) Ag-SmBCO with a 4 g Y-123 layer and (g) Ag-SmBCO with four 1 g Y-123 pellets (arrangement shown in (h)) and their trapped field profiles at both the top: (b) Ag-SmBCO with a 6 g Y-123 layer; (e) Ag-SmBCO with a 4 g Y-123 layer and (i) Ag-SmBCO with four 1 g Y-123 pellets and bottom: (c) Ag-SmBCO with a 6 g Y-123 layer; (f) Ag-SmBCO with a 4 g Y-123 layer and (j) Ag-SmBCO with four 1 g Y-123 pellets surfaces measured at a

distance of 0.5 mm above the sample surface. The maximum trapped field values at the top surfaces and bottom surfaces are indicated in the figure.

**Figure 76** Photographs of the polished top surfaces of: (a) Ag-SmBCO without CIP and (d) Ag-SmBCO with CIP and their trapped field profiles at both the top: (b) Ag-SmBCO without CIP and (e) Ag-SmBCO with CIP and bottom: (c) Ag-SmBCO without CIP and (f) Ag-SmBCO with CIP surfaces measured at a distance of 0.5 mm above the sample surface. The maximum trapped field values at the top surfaces and bottom surfaces are indicated in the figure.

**Figure 77** Optical photographs of the cross sections of (a) Ag-SmBCO without CIP; (b) Ag-SmBCO with CIP.

**Figure 78** Photographs of the polished top surfaces of: (a) Ag-SmBCO a film seed and (d) Ag-SmBCO with an MgO-NdBCO generic seed and their trapped field profiles at both the top: (b) Ag-SmBCO a film seed and (e) Ag-SmBCO with an MgO-NdBCO generic seed and bottom: (c) Ag-SmBCO a film seed and (f) Ag-SmBCO with an MgO-NdBCO generic seed surfaces measured at a distance of 0.5 mm above the sample surface. The maximum trapped field values at the top surfaces and bottom surfaces are indicated in the figure.

**Figure 79** Photographs of the polished top surfaces of: (1) Ag-SmBCO 31 mm in diameter and (4) Ag-SmBCO 41 mm in diameter and their trapped field profiles at both the top: (2) Ag-SmBCO 31 mm in diameter and (5) Ag-SmBCO 41 mm in diameter and bottom: (3) Ag-SmBCO 31 mm in diameter and (6) Ag-SmBCO 41 mm in diameter surfaces measured at a distance of 0.5 mm above the sample surface. The maximum trapped field values at the top surfaces and bottom surfaces are indicated in the figure.

**Figure 80** Photographs of the Ag-SmBCO single grain samples without a Y-123 layer: (a) top view, (c) side view and (e) bottom view and Ag-SmBCO with a Y-123 layer: (b) top view, (d) side view and (f) bottom view. Illustrations of the cross-sectional view (g) and side view (h) of the growth along the  $c$ -axis.

**Figure 81** Normalised magnetic moment as a function of temperature for Ag-SmBCO with and without a Y-123 layer with specimens corresponding to positions shown in Figure 63.

**Figure 82** Critical current density,  $J_c$ , as a function of magnetic field for Ag-SmBCO with and without a Y-123 layer with specimens corresponding to positions shown in Figure 63.

**Figure 83** Calculated values of  $x$  and  $y$  in Ag-SmBCO with and without a Y-123 layer from the seed along  $c$ -axis.

**Figure 84** Micrographs at a magnification of  $500\times$  for Ag-SmBCO fabricated without a Y-123 layer: (a) under the seed, (b) near the bottom of the sample; and Ag-SmBCO with a Y-123 layer: (c) under the seed, (d) near the bottom of the sample.

**Figure 85** Molar ratios of the elements in the matrix of Ag-SmBCO fabricated with and without a Y-123 layer with increasing distance from the seed along  $c$ -axis.

**Figure 86** The concentration distribution of Sm and Ba in Ag-SmBCO fabricated with and without a Y-123 layer.

**Figure 87** 3D and 2D contour maps of the trapped field distribution at the top surfaces: (a), (c), (e) and (g) and at the bottom surfaces: (b), (d), (f) and (h) of Ag-SmBCO single grains fabricated with and without a Y-123 layer.



# List of tables

**Table 1** Commercially available and most commonly applied superconducting materials

**Table 2** Different compositions of mixed-powder buffers employed in this study.

**Table 3** Different geometric configurations of the buffers employed in this study.

**Table 4** Summary of the elements and corresponding compounds doped into the SmBCO precursor powder.

**Table 5** Summary of the EDX analysis for the Ce-containing second phase located on macro-cracks formed orthogonally to the *c*-axis in the single grain sample of composition SmBCO + CeO<sub>2</sub>.

**Table 6** Summary of the EDX analysis for the Ce-containing second phase formed in pores in the single grain sample of composition SmBCO + CeO<sub>2</sub>.

**Table 7** A list of commercial source and purity information on dopants added into SmBCO in this research.

**Table 8** A list of dopants added into SmBCO and the corresponding amount used in this research.

**Table 9** The dimension of each Ag-SmBCO pellet as a bulk pre-form and as a processed bulk single grain.

**Table 10** The weight of Y-123 and Yb<sub>2</sub>O<sub>3</sub> pressed as a combined supporting pellet under the Ag-SmBCO bulk pre-form.

**Table 11** The size and weight of each Ag-SmBCO sample displayed in Figure 65.

**Table 12** The growth-related parameters of the corresponding heating profile for the Ag-SmBCO samples listed in Figure 65 (the changes are highlighted in red).

**Table 13** The size and weight of each Ag-SmBCO sample displayed in Figure 66.

**Table 14** The growth-related parameters of the corresponding heating profile for the Ag-SmBCO samples listed in Figure 66 (the changes are highlighted in red).

**Table 15** Ag-SmBCO samples 25 mm in diameter with different amounts of Y-123 layers and pre-treatment with fabrication details summarised in Table 16.

**Table 16** Details of Ag-SmBCO samples shown in Table 15 with different amounts of the Y-123 layers and pre-treatments.

**Table 17** CIP-ed 1 mol. % ZrO<sub>2</sub>-doped Ag-SmBCO samples 25 mm in diameter with different starting compositions of the precursor powders with BaO<sub>2</sub> or BaO and different amounts and arrangements of Y-123 layers with fabrication details summarised in Table 18.

**Table 18** Details of CIP-ed 1 mol. % ZrO<sub>2</sub>-doped Ag-SmBCO samples shown in Table 17 with different starting compositions of the precursor powders with BaO<sub>2</sub> or BaO and different amounts and arrangements of the Y-123 layers (the changes are highlighted in red).

**Table 19** Ag-SmBCO in the sizes of 31 mm and 41 mm with fabrication details summarised in Table 20.

**Table 20** Details of the Ag-SmBCO single grains grown into 31 mm and 41 mm in Table 19.

**Table 21** The maximum trapped field values measured at a distance of 0.5 mm above the sample surface at the top and bottom surfaces of Ag-SmBCO with thin film and MgO-NdBCO generic seeds (samples 25 mm in diameter).

**Table 22** The maximum trapped field values measured at a distance of 0.5 mm above the sample surface at the top surfaces and bottom surfaces of Ag-SmBCO with BaO<sub>2</sub> and BaO in the precursor powders (samples 25 mm in diameter).

# Abbreviations

AC	Alternating current
$B$	Magnetic flux density or magnetic induction
$B_t$	Trapped magnetic field
$B_{t, max}$	Maximum trapped magnetic trapped field on the surface of bulk superconductor
CIP	Cold isostatic pressing
DC	Direct current
XRD	X-ray Diffraction
DTA	Differential Thermal Analysis
SEM	Scanning Electron Microscopy
SQUID	Superconducting Quantum Interface Device
EDX	Energy Dispersive X-ray Spectrometry
EPMA	Electron Probe Micro-analyser
ZFCM	Zero field cooling magnetization
PFM	Pulsed field magnetization
$F$	Force
FCM	Field cooling magnetization
$F_D$	Drag force
$F_I$	Force due to interfacial energy
$F_L$	Lorentz force

$F_p$	Pinning force
$f_p$	Pinning force
SmBCO	$\text{SmBa}_2\text{Cu}_3\text{O}_{7-\delta}$
$b_i$	Local internal induced field
Sm-123ss	Solid solution of $\text{SmBa}_2\text{Cu}_3\text{O}_{7-\delta}$
$H$	Magnetic field strength
$H_a$	Applied magnetic field
$H_c$	Critical magnetic field
$H_{c1}$	Lower critical magnetic field
$H_{c2}$	Higher critical magnetic field
$H_p$	Penetration field
HTS	High temperature superconductors
$H_m$	Maximum applied field
$H_{irr}$	Irreversibility field
$m_i$	Local Magnetisation
$M$	Magnetisation
MRI	Magnetic resonance imaging
NMR	Nuclear magnetic resonance
FCL	Fault current limiters
SMES	Superconducting magnetic energy storage
$J$	Current density

$J_c$	Critical current densities
YBCO	$\text{YBa}_2\text{Cu}_3\text{O}_{7-\delta}$
NdBCO	$\text{NdBa}_2\text{Cu}_3\text{O}_{7-\delta}$
Mg-NdBCO	MgO-doped $\text{NdBa}_2\text{Cu}_3\text{O}_{7-\delta}$
LaBCO	$\text{La}_{5-x}\text{Ba}_x\text{Cu}_5\text{O}_{5(3-\delta)}$
$R$	Growth rate
$R^*$	Critical growth rate
$r$	Mean radius of Sm-211 particles
$r_a^*$	Critical radius of Sm-211 particles for $a$ -direction growth
$r_c^*$	Critical radius of Sm-211 particles for $c$ -direction growth
RE	Rare earth
(RE)BCO	$(\text{RE})\text{Ba}_2\text{Cu}_3\text{O}_{7-\delta}$
$T_c$	Critical transition temperature
$\Delta T_c$	Transition width
$T_g$	Temperature for single grain growth under isothermal conditions
$c$ -GS	$c$ -growth sector
$a/b$ -GS	$a/b$ -growth sector
$T_m$	Maximum melting temperature
$T_p$	Peritectic temperature
$T_s$	Seeding temperature

TSMG	Top-seeded melt growth
Sm-123	$\text{SmBa}_2\text{Cu}_3\text{O}_{7-\delta}$
Sm-211	$\text{Sm}_2\text{BaCuO}_5$
Sm-242	$\text{Sm}_2\text{Ba}_4\text{Cu}_2\text{O}_9$
OCMG	Oxygen-controlled melt growth
TSIG	Top-seeded infiltration and growth
$V$	Volume of the interaction region
$d$	Diameter of a non-superconducting particle
$N$	Number of pinning centres
$U_p$	Pinning energy
$\Delta T$	Undercooling
$\Delta E$	Condensation energy per unit volume
$\Delta M$	Difference in the magnetisation
$\Delta\sigma_0$	Interfacial energy
$\Delta\sigma_{lp}$	Liquid/particle interfacial energy
$\Delta\sigma_{sl}$	Solid/liquid interfacial energy
$\Delta\sigma_{sp}$	Solid/particle interfacial energy
$\delta$	Oxygen content
$\lambda$	London penetration depth
$\kappa$	Ginzburg-Landau constant
$v$	Velocity of a fluxoid

$\mu_0$	Permeability of free space
$\eta$	Melt viscosity
$\xi$	Coherence length
$n_s$	Concentration of superelectrons
$\Delta C_{SL}^{123}$	Sm composition difference at Sm-123 solid-liquid interface
$\Delta C_{SL}^{211}$	Sm composition difference at Sm-211 solid-liquid interface
$\Delta C_L$	Flux liquid concentration difference
$C_S^{123}$	Sm concentration of the Sm-123 solid
$C_S^{211}$	Sm concentration of the Sm-211 solid
$C_L^{123}$	Sm concentration of the Sm-123 liquid
$C_L^{211}$	Sm concentration of the Sm-211 liquid



# CHAPTER 1

## INTRODUCTION

### 1.1. Research Background

The synthesis of  $\text{La}_{5-x}\text{Ba}_x\text{Cu}_5\text{O}_{5(3-\delta)}$  (LaBCO) cuprates by Bednorz and Müller in 1986 [1] represented the start of a new era in the evolution of superconducting materials given the relatively high critical transition temperature,  $T_c$ , of this material of 35 K. Later, in 1987, Maw-Kuen Wu and Ching-wu Chu replaced lanthanum with yttrium to fabricate  $\text{YBa}_2\text{Cu}_3\text{O}_{7-\delta}$  (YBCO), raising the  $T_c$  to 93 K [2]. It was discovered subsequently that other rare-earth elements, such as gadolinium (Gd), samarium (Sm) and neodymium (Nd), can be employed to replace yttrium in YBCO to form other rare-earth superconducting cuprates, denoted as  $(\text{RE})\text{Ba}_2\text{Cu}_3\text{O}_{7-\delta}$  [(RE)BCO] (RE=Gd, Sm, Nd and etc.) and that these materials have been found to be promising candidates for practical applications for a variety of high field quasi permanent magnets when processed in bulk form. Compared with conventional superconductors transitioning into the superconducting state at temperatures near absolute zero, the (RE)BCO superconductors are also referred to as high-temperature superconductors (HTS) due to their comparatively higher  $T_c$ . In general, the field generating capacity of HTS exceeds significantly the maximum practical field produced by a permanent magnet (1.5 T) and is determined by the magnitude and homogeneity of the critical current density,  $J_c$ , of the material. (RE)BCO superconductors also exhibit the highest irreversibility field over a wide temperature range and are therefore the most promising materials for applications at high current and high magnetic field. Unfortunately, the ability of (RE)BCO bulk superconductors to carry current and, hence, to generate magnetic field, is limited severely by the presence of grain boundaries in the sample microstructure, which results in a large decrease in  $J_c$ . It is necessary, therefore, to process (RE)BCO in the form of large, single grains to avoid the presence of grain boundaries.

## 1.2. Subject and Aims of This Thesis

$\text{SmBa}_2\text{Cu}_3\text{O}_{7-\delta}$  (SmBCO), a member of the  $(\text{RE})\text{Ba}_2\text{Cu}_3\text{O}_{7-\delta}$  [(RE)BCO] family of high-temperature superconductors, has significant potential for practical applications due to its high  $T_c$ , high  $J_c$ , the so-called ‘peak effect’ characteristic in its  $M-H$  behaviour in high applied magnetic field, and high irreversibility field. Being capable of supporting macroscopic currents at the temperature above the boiling point of liquid nitrogen (77 K), SmBCO bulk superconductors can be used potentially for a variety of high field quasi permanent magnet applications such as magnetic bearings [3] and flywheel energy storage systems [4]. It is necessary to process SmBCO materials in the form of large, single grains to avoid the presence of grain boundaries, which is essential for a SmBCO bulk superconductor to carry current, and hence to generate magnetic field [5]. In general, the processing conditions of SmBCO bulk superconductors are more complicated than YBCO, due primarily to the high melting temperature of the precursor powders, rapid growth rate, which is difficult to control, and the need to process the material under reduced oxygen partial pressure to inhibit the substitution of Sm on the Ba site in the superconducting SmBCO matrix [6]. Additionally, the mechanical properties of a top-seed-melt-growth (TSMG)-processed SmBCO bulk superconductor are poor due to its ceramic nature. One of the most severe problems originating from the growth mechanism of TSMG is the formation of pores and cracks in the superconducting matrix, which is detrimental to its mechanical properties. In terms of growth, poor mechanical properties result in the formation of cracks during fabrication, leading invariably to failure in obtaining a bulk single grain. Therefore, this thesis focuses on addressing these challenges to enable reliable growth and improvement of the superconducting properties of SmBCO bulk single grains via three main adjustments in the SmBCO system, including the use of a modified seeding technique, employing a buffer layer between the seed and the bulk pre-form and doping and the addition of silver into the bulk-preform to scale-up the system.

### 1.3. Outline of This Thesis

This thesis comprises seven chapters in total.

A basic introduction of superconductivity is presented in Chapter 2, which covers a brief history of superconductivity and an overview of the development of the most currently adopted superconducting materials and their applications. The basic physical phenomena and concepts related to superconductivity introduced or explained in this chapter are: zero resistance, the Meissner-Ochsenfeld effect, definition of type I and type II superconductors and superconducting properties of bulk single grains such as critical transition temperature ( $T_c$ ), critical current density ( $J_c$ ), field trapping ability, mixed state, flux pinning, the Bean critical state model and magnetization of type II superconductors. Applications of (RE)BCO superconducting bulk single grains are then summarised, followed by a literature review of up-to-date research on the processing and properties of superconducting SmBCO bulk single grains.

Chapter 3 focuses mainly on the fundamentals related to the fabrication of superconducting SmBCO bulk single grains. In order to understand the SmBCO system more thoroughly, this chapter describes the crystallographic structure of SmBCO superconductors, the top-seeded melt growth (TSMG) process used commonly to fabricate the material, theories concerning solidification during the TSMG process, the oxygenation process, the growth morphology, the secondary peak effect, effects of Sm-211 inclusions and dopants, and the mechanical properties of bulk SmBCO single grains. The characterisation techniques employed in this thesis are also summarised in this chapter.

Chapters 4, 5 and 6 present the key experimental components of this thesis and describe the experimental work carried out on bulk SmBCO over the past three years.

The current research on SmBCO system starts with the development of a modified seeding technique using an MgO-NdBCO generic seed by employing a buffer layer as described in Chapter 4. A small pellet, i.e. a buffer layer, inserted between the seed and the bulk pre-form, proved to be effective in inhibiting the diffusion of elements from the seed into the bulk microstructure, and vice versa, and to accommodate lattice mismatch between the seed and the precursor pellet. In order to improve the reliability of seeding, buffers of different compositions have been investigated for a variety of geometric configurations. By

incorporating such a buffer layer in the growth process, single domain, bulk SmBCO samples have been fabricated reliably in air by TSMG using a conventional chamber furnace. Furthermore, the measured superconducting properties,  $T_c$  and  $J_c$ , of the samples, and especially directly under the buffer layer, have been investigated in detail. The trapped fields of the SmBCO single grains synthesized with and without a buffer layer have been measured and compared in order to establish the advantages of the buffer layer technique.

Chapter 5 discusses mainly the effects of doping on superconducting SmBCO bulk single grains. This chapter is divided into two sections: in the first section, a comparison of the effects of the addition of platinum and CeO<sub>2</sub> on SmBCO bulk single grains is performed. The fabrication of large, single grain bulk SmBCO containing 1 wt. % CeO<sub>2</sub> and 0.1 wt. % Pt using a TSMG process is reported. The performance of the bulk superconductors containing these two different dopants is evaluated based on an analysis of their superconducting properties, including  $T_c$  and  $J_c$ , and on the microstructure of the samples. The discussion focuses primarily on their ability to refine the size of Sm-211 particles trapped in the superconducting Sm-123 matrix, which act as effective flux pinning centres, on the cost of the dopants to assess their potential economic benefit for use in medium to large scale production processes of SmBCO bulk superconductors, and on the generation of macro-cracks and Sm-211 free regions in the sample microstructure. In the second section, for an optimized SmBCO precursor composition containing CeO<sub>2</sub>, compounds with different elements were added into SmBCO bulk single grains as dopants to observe how they affect the SmBCO system. With the assistance of commercial thin film seeds, single domain, bulk SmBCO samples of different dimensions with a large number of different dopants have been fabricated systematically in air by the TSMG process using a conventional chamber furnace. Detailed studies have been performed on  $T_c$  and  $J_c$  along the  $a/b$ - and  $c$ - axes of the single grains containing 1 mol. % ZrO<sub>2</sub>, BaZrO<sub>3</sub>, TiO<sub>2</sub> and 'Sm-2411', respectively, to further reveal the effects of the dopants on sample properties.

Chapter 6 includes the details of the scale-up of the processing of SmBCO bulk single grains containing silver. In order to scale-up the SmBCO system for the purpose of quasi-magnet industrial applications, silver was added to the SmBCO system and a Y-123 layer was employed under the SmBCO bulk pre-form. The growth of SmBCO single grains with silver addition was studied initially through various approaches, including precursor-powder sintering, doping with 1 mol. % ZrO<sub>2</sub>, CIP treatment of the bulk pre-form and the addition of a Y-123 layer under the pressed bulk pellet prior to melt processing. Secondly, to compare

the impact of all the treatments on SmBCO with silver addition, trapped fields of successfully grown single grains were measured and the results analysed. The roles of the Y-123 layer and its impact on the appearance, superconducting properties ( $T_c$  and  $J_c$ ), microstructure, chemical composition, and field-trapping ability of the SmBCO bulk single grains, are discussed in detail.

Finally the major results of this research are summarized in Chapter 7 and suggestions for future research are outlined.

# CHAPTER 2

## BACKGROUND

In this chapter, an introduction to the background of the concepts related to superconductivity from the viewpoint of the development of superconducting materials, basic physics and practical applications are presented. Current research on bulk SmBCO superconductors, on which this thesis is based, is also reviewed.

### 2.1. Development of Superconducting Materials and Their Applications

#### 2.1.1. Development of Superconducting Materials

The critical transition temperature of a superconductor, denoted as  $T_c$ , is the temperature at which the material transitions from a normal state to a superconducting state. In Figure 1, the historical evolution of the  $T_c$  of superconducting materials is illustrated following the discovery of superconductivity by Kamerlingh-Onnes in 1911 [7].

Various natural elements and simple compounds exhibit superconductivity at extremely low temperatures, including lead at 7.2 K [8], niobium at 9.2 K [8] and Nb<sub>3</sub>Sn at 18.3 K [9]. Heavy fermion superconductors and organic superconductors have been discovered more recently.

Bednorz and Müller successfully synthesized a La-Ba-Cu-O (LaBCO) ceramic in 1986, which exhibited a zero resistance state at 35 K [1]. Later, in 1987, Maw-Kuen Wu and Ching-wu Chu replaced the lanthanum in LaBCO with yttrium, i.e., synthesising a Y-Ba-Cu-O (YBCO) superconductor, which raised  $T_c$  to 93 K [2]. Significantly, this temperature is above the boiling point of liquid nitrogen (77 K). The significance of this discovery is that, with a  $T_c$  higher than 77 K, liquid nitrogen could be used as a coolant for superconducting YBCO for

the first time. Liquid nitrogen is much cheaper, safer and easier to use than liquid helium, which had been used exclusively prior to 1986 in the field of superconductivity. The discovery of YBCO superconductors accelerated the development in superconducting materials significantly. During the late 1980s and the early 1990s, superconducting materials with even higher  $T_c$  than YBCO were discovered, such as Bi-Sr-Ca-Cu-O at 108 K [10], Tl-Ba-Ca-Cu-O at 127 K [11] and Hg-Ba-Ca-Cu-O at 153 K under 30 GPa [12]. In addition, (RE)-Ba-Cu-O [(RE)BCO] superconductors, which are of the same family as YBCO with yttrium replaced by a rare earth element, such as Gd, Sm and Nd, were found to be particularly promising candidates for practical applications.

The more recent discovery of  $MgB_2$  and the iron-based superconductors has broadened further the family of superconducting materials. Unlike YBCO,  $MgB_2$  has a lower anisotropy, larger coherence length and clean grain boundaries to current flow and therefore is a good candidate for practical applications [13]. The discovery of superconductivity in the iron-based compounds attracted remarkable attention, given that superconductivity and ferro-magnetism had previously been thought to be exclusive. Strikingly, more than 3000 papers have already been published on Fe-based superconductors and, in 2014, single-layer films of FeSe was reported to have a  $T_c$  of 109 K [14].

There are also some non-conventional superconductors that exhibit fascinating properties, such as higher  $T_c$  or layered two-dimensional superconductivity. Examples for these materials include  $H_3S$ , superconducting at 203 K under 155 GPa [15] and  $Na_xCoO_2 yH_2O$  ( $x \approx 0.35$ ,  $y \approx 1.3$ ) with the observation of superconductivity in two-dimensional  $CoO_2$  layers [16].

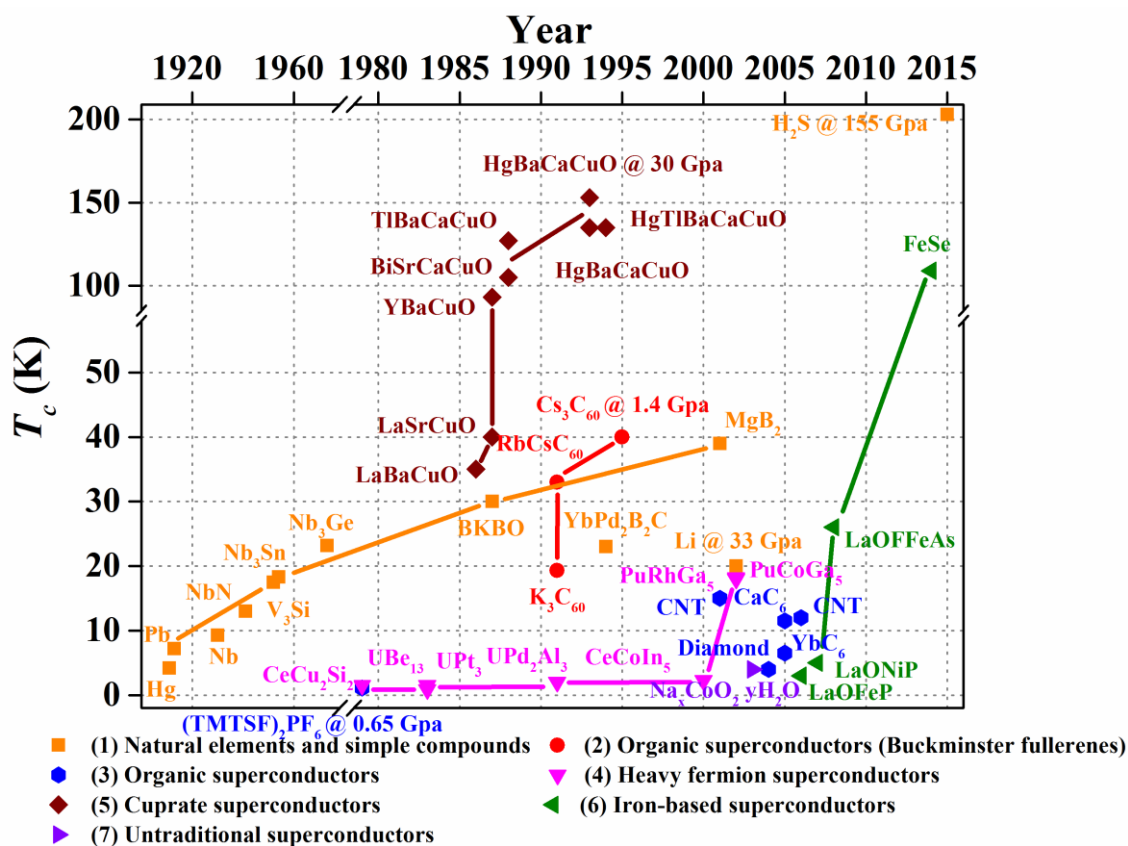


**Figure 1** Evolution of  $T_c$  of known superconducting materials: (1) Natural elements and simple compounds [7] [8] [13] [15] [17] [18] [19] [20] [21] [22]; (2) Organic superconductors (Buckminster fullerenes) [23] [24] [25]; (3) Organic superconductors [26] [27] [28] [29] [30]; (4) Heavy fermion superconductors [31] [32] [33] [34] [35] [36] [37]; (5) Cuprate superconductors [1] [2] [10] [11] [12] [38] [39]; (6) Iron based superconductors [14] [40] [41] [42] and (7) Unconventional superconductors [16].

## 2.1.2. Applications of Superconducting Materials

Since the discovery of superconductivity in 1911, ongoing attempts to apply superconductors with their unique properties to practical applications have focused on various material forms, including wires and tapes, thin films and bulk single grains. In general, wires and tapes are employed in the transportation of large electric currents without power loss and for the generation of high magnetic fields; thin films are employed in superconducting devices utilizing quantum phenomena and bulk materials with strong magnetic flux pinning are used in levitation and shielding applications.

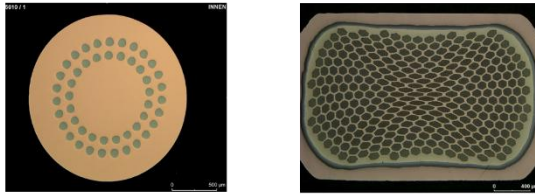
Table 1 lists the forms of superconducting materials that are employed most commonly and are available commercially. These materials are illustrated in Figure 2. NbTi and Nb<sub>3</sub>Sn are used widely in the form of wire in magnetic resonance imaging (MRI), nuclear magnetic resonance (NMR) and fusion accelerators, while Bi<sub>2</sub>Sr<sub>2</sub>CaCu<sub>2</sub>O<sub>8</sub>, Bi<sub>2</sub>Sr<sub>2</sub>Ca<sub>2</sub>Cu<sub>3</sub>O<sub>10</sub> and YBa<sub>2</sub>Cu<sub>3</sub>O<sub>7-δ</sub> in the form of wires are employed in windings for cables, fault current limiters (FCL) and superconducting magnetic energy storage (SMES). GdBa<sub>2</sub>Cu<sub>3</sub>O<sub>7-δ</sub> superconductors can be applied in magnetic levitation (maglev) in bulk form. The newly discovered MgB<sub>2</sub> superconductors have significant potential for application in either wire or bulk form, since they perform as wires in applications similar to Bi<sub>2</sub>Sr<sub>2</sub>CaCu<sub>2</sub>O<sub>8</sub> and are also applicable in bulk forms for MRI and NMR.

**Table 1** Commercially available and most commonly applied superconducting materials

Materials	Forms	Images	Applications
NbTi	Wires	Figure 2 (a) [43]	MRI
Nb <sub>3</sub> Sn	Wires	Figure 2 (b) [43]	NMR and fusion accelerators
Bi <sub>2</sub> Sr <sub>2</sub> CaCu <sub>2</sub> O <sub>8</sub>	Wires		
Bi <sub>2</sub> Sr <sub>2</sub> Ca <sub>2</sub> Cu <sub>3</sub> O <sub>10</sub>	Wires	Figure 2 (c) [44]	Windings for cables, FCL and SMES, <i>etc.</i>
YBa <sub>2</sub> Cu <sub>3</sub> O <sub>7-δ</sub>	Wires	Figure 2 (d) [45]	
GdBa <sub>2</sub> Cu <sub>3</sub> O <sub>7-δ</sub>	Bulks	Figure 2 (e) [46]	Maglev, <i>etc.</i>
MgB <sub>2</sub>	Wires, Bulks	Figure 2 (f) [47]	Applications similar to Bi <sub>2</sub> Sr <sub>2</sub> CaCu <sub>2</sub> O <sub>8</sub> wires MRI and NMR, <i>etc.</i> in bulk forms

**Bruker EST / Bruker Corporation**

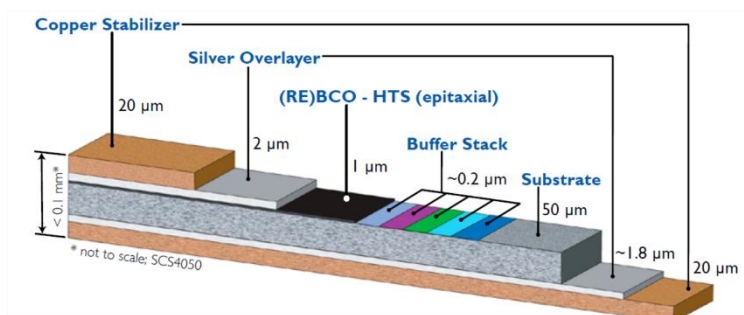
**(a) NbTi wires (b) Nb<sub>3</sub>Sn wires**



**Sumitomo Electric Ltd. (c) Bi-2223 wires**

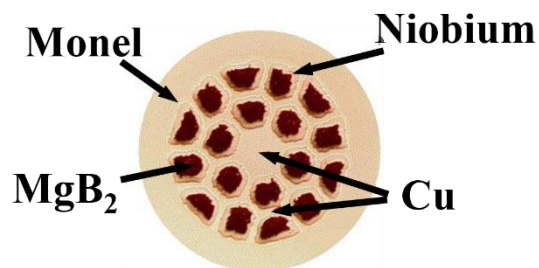


**Superpower Inc. (d) (RE)BCO coated wires**



**Nippon Steel & Sumitomo Metal**

**(e) 150 mm GdBCO bulk**



**Hyper Tech Research, Inc.**

**(f) MgB<sub>2</sub> wires by PIT**

**Figure 2** Illustration of the superconducting materials listed in Table 1.

## 2.2. Basic Physics of Superconductors

### 2.2.1. Zero Resistance

It is known commonly that the electrical resistivity of a non-superconducting, metallic material in its normal state decreases linearly when it is cooled, since the thermal vibration of the atoms decreases and the conduction electrons are scattered less frequently. The decrease of resistance is linear down to a relatively low temperature, and below this point, it decreases progressively less quickly. In contrast, a superconductor shows a remarkably different behaviour: when it is cooled, its electrical resistance decreases in a similar way to that of a metal, but, on reaching a critical temperature, it suddenly loses all electrical resistance to the flow of DC current, transitioning into a zero resistance state. This is the first hallmark of superconductivity, as shown in Figure 3 (a).

A representative  $T_c$  plot for a superconductor is shown in Figure 3 (b). The onset  $T_c$  for a superconductor occurs at the temperature when the magnetic moment asymptotically reaches zero and the offset  $T_c$  is defined as the temperature at which the magnetic moment is 90 % of its value when the sample is completely superconducting. Additionally, the transition width  $\Delta T_c$  describes the difference between the onset and offset  $T_c$ , with a difference,  $\Delta T_c$ , of less than 1 K generally indicating a good superconductor. Moreover, although  $T_c$  is an intrinsic property of the material, it does vary typically with compositional variations at different positions within a bulk superconductor.

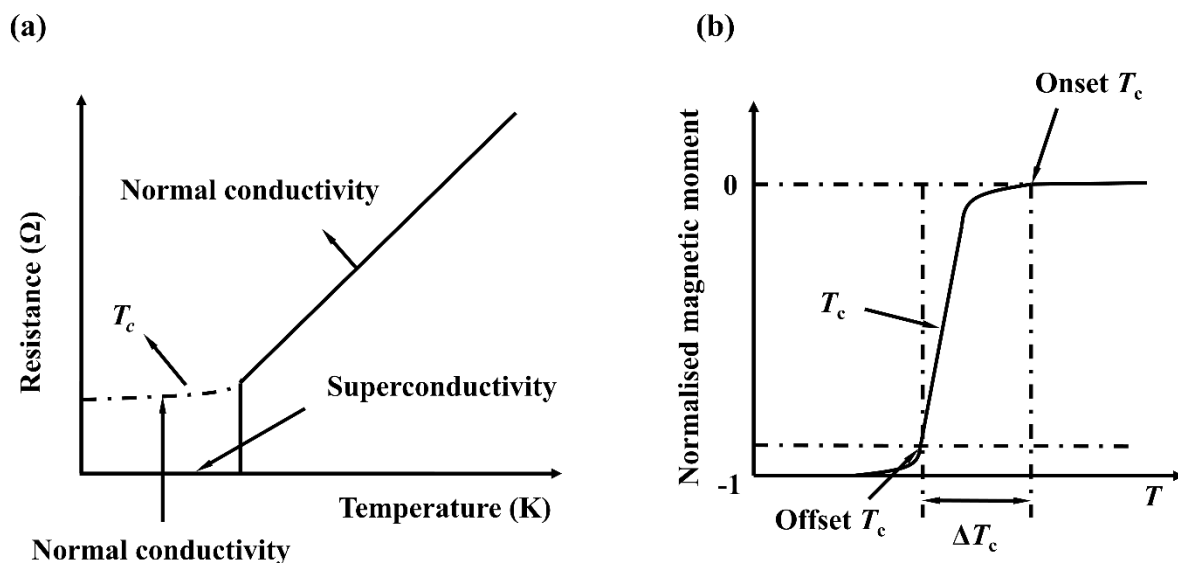


**Figure 3** (a) Typical superconducting transition at  $T_c$  [7]; (b) representative  $T_c$  plot for a superconductor.

## 2.2.2. The Meissner-Ochsenfeld Effect

A second hallmark of superconductivity is the Meissner-Ochsenfeld effect, which was discovered in 1933 by Meissner and Ochsenfeld. This phenomenon is the expulsion of magnetic flux from the interior of a superconductor in its superconducting state in the presence of a weak magnetic field [48].

A superconductor exhibits only zero resistance below  $T_c$ . If this were to act as an ‘ideal’ conductor with no resistance, the amount of magnetic flux enclosed would not be able to change and, consequently, the flux distribution in the superconductor would remain as it was when the material became resistanceless, as shown in Figure 4 (a). However, a real superconductor behaves differently, as illustrated in Figure 4 (b); not only is a magnetic field excluded from entering the superconductor, but also the field in an originally normal sample is expelled as it is cooled through  $T_c$ , demonstrating the existence of the Meissner-Ochsenfeld effect.

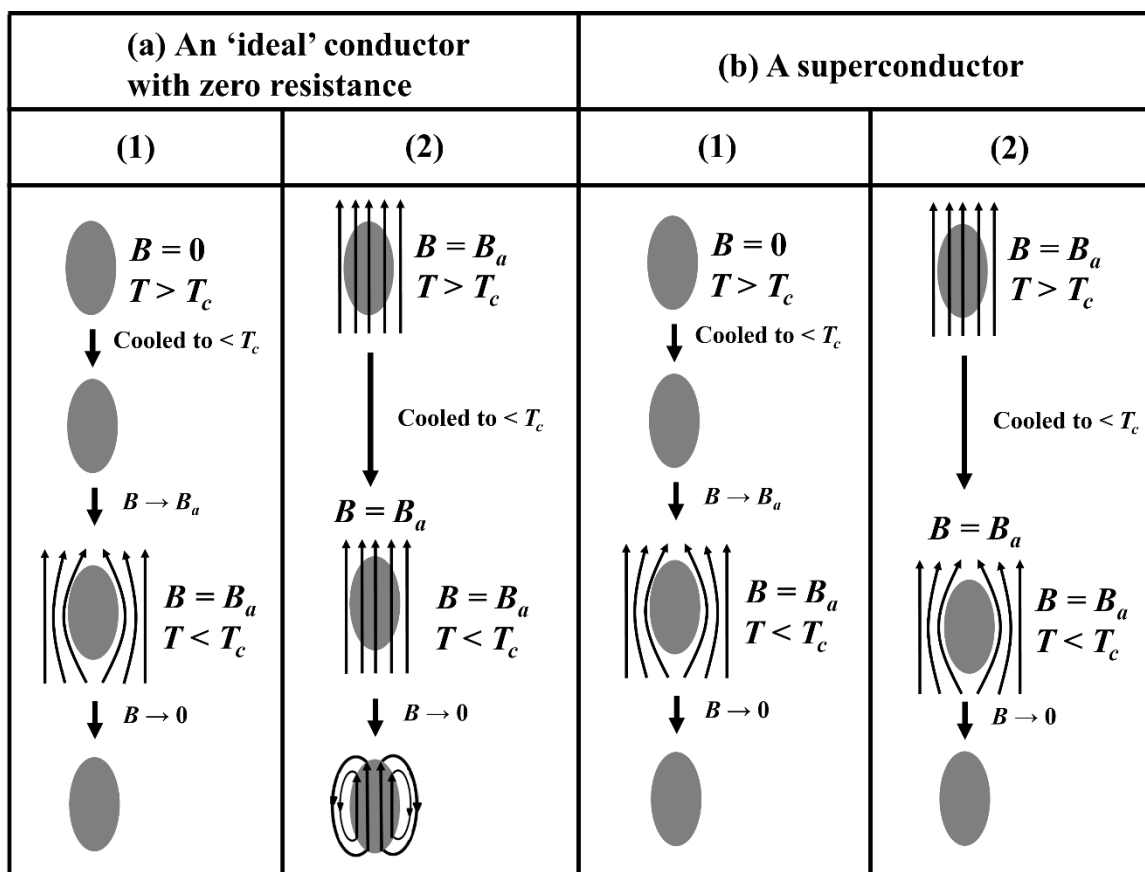


**Figure 4** Magnetic behaviour of (a) a hypothetical superconductor without the Meissner-Ochsenfeld effect (i. e. an 'ideal' conductor with zero resistance) and (b) a superconductor [49].

### 2.2.3. Type I and Type II Superconductors

There are many criteria used to classify superconductors, including whether the superconductivity of the material can be explained by a particular theory (low-temperature and high-temperature superconductors), by material type (natural elements, alloys and ceramics) and by the value of surface energy at the boundary between a normal state and a superconducting state (superconductivity is type I if the surface energy is positive; otherwise it is type II). Research in this thesis is related closely to type II superconductors and therefore it is necessary to describe in more detail the classification of type I and type II materials.

With the exception of Niobium (Nb), Vanadium (V) and Technetium (Tc), all type I elemental superconductors with a negligible demagnetizing factor exhibit full Meissner-

Ochsenfeld flux expulsion in the superconducting state. In 1957, however, Abrikosov published a theoretical paper pointing out that there might be another class of superconductor exhibiting an incomplete Meissner-Ochsenfeld effect. This led to the realisation of another class of superconductors, now known as type II superconductors [50].

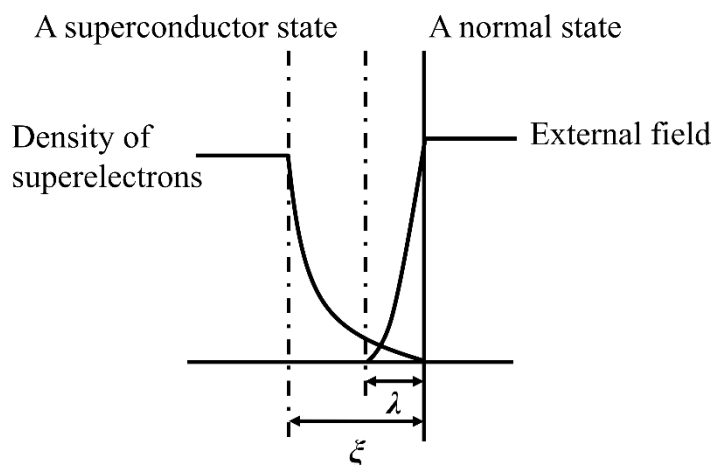
The difference between type I and type II superconductors can be explained by considering the surface energy between a normal state and a superconducting state. If a superconductor exhibits a positive surface energy, then the free energy between the two states is minimized by having as small an area of interstate boundary as possible and this superconducting material is classified as type I; On the other hand, if a superconductor exhibits a negative surface energy, i.e. if energy is released on forming the interstate boundary, it is energetically favourable for the superconductor to divide into a large number of thin domains in order to make the area of the interstate boundary as large as possible. Therefore, if the surface energy is negative, a superconductor in a magnetic field would tend to divide into normal and superconducting states and, as a result, the superconductor is classified as type II.

When transitioning into a superconducting state, there is not an abrupt change from fully normal to fully superconducting behaviour. The superconducting state involves the pairing of electrons of opposite spin in energy levels close to the Fermi surface, which then form bosons. These so-called Cooper pairs condense into a low energy ground state, which drives the transition to zero resistance. As a result, a normal state is transformed to a superconducting state over the physical distance of the so-called coherence length ( $\xi$ ). In addition, the magnetic flux penetrates a finite distance into the surface of a superconductor, which is known as the penetration depth ( $\lambda$ ) [51].

The relation between the penetration depth ( $\lambda$ ) and the coherence length ( $\xi$ ) can also be used to determine if a surface energy is positive or negative and, in turn, if the material is a type I or a type II superconductor. If the coherence length is longer than the penetration depth, the total free energy is increased in the vicinity of the boundary, that is to say there exists a positive surface energy; whereas if the coherence length is shorter than the penetration depth, then the surface energy is negative. The relative values of the coherence length and the penetration depth vary for different superconducting materials. In most pure metals, the coherence length has a value of about  $10^{-6}$  m, which is considerably greater than the penetration depth, which is typically about  $5 \times 10^{-8}$  m. The surface energy is positive in such materials and they are classified as type I superconductors. However, a reduction in the electron mean free path, caused, for example, by impurities in a metal reduces the coherence

length and increases the penetration depth and, as a result, the coherence length can easily be shorter than the penetration depth. Alloys or sufficiently impure metals, therefore, are usually type II superconductors. Figure 5 shows a schematic illustration of the difference between type I and type II superconductors in terms of the penetration depth ( $\lambda$ ) and the coherence length ( $\xi$ ).

### Type I superconductors



### Type II superconductors

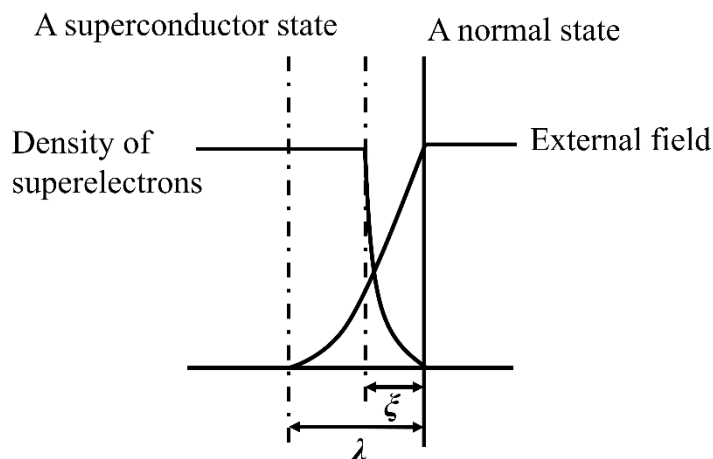


**Figure 5** Schematic illustration of the difference between type I and type II superconductors in terms of the penetration depth ( $\lambda$ ) and the coherence length ( $\xi$ ) [51].

In addition, the ratio of the penetration depth ( $\lambda$ ) to the coherence length ( $\xi$ ) can be written as the Ginzburg-Landau constant  $\kappa$  ( $\kappa = \lambda / \xi$ ). Considering the close relation between  $\kappa$ ,  $\lambda$ ,  $\xi$  and the surface energy,  $\kappa$  varies for different superconductors and can be used to determine whether a superconductor is type I or type II depending on whether the value of  $\kappa$  is smaller

or greater than  $1/\sqrt{2}$  (if  $\kappa < 1/\sqrt{2}$ , corresponding to positive surface energy, type I superconductor; if  $\kappa > 1/\sqrt{2}$ , corresponding to negative surface energy, type II superconductor) [52].

## 2.2.4. Type II Superconductors

Type II superconductors have unique features compared to type I, such as the mixed state, a lower critical field,  $H_{c1}$  and upper critical field,  $H_{c2}$ . The inherent features of type II superconductors are described in this section.

### 2.2.4.1. The Mixed State

The transition between the normal state and the superconducting state is an ordinary phase transition, as is the solid-liquid phase transition. The temperature dependence of free energies for a normal state and a superconducting state is shown in Figure 6. Additional energy is required to exclude the applied magnetic field,  $(1/2) \mu_0 H_a^2$ , where  $\mu_0$  is the permeability of free space and  $H_a$  is the applied magnetic field, when a magnetic field is applied to a superconductor, which reduces the stability of the superconducting state. A superconductor is driven into a normal state when this energy exceeds the energy lost by the superconducting transition. Therefore, the energy difference between a superconducting state and a normal state, is given by  $(1/2) \mu_0 H_c^2$ , where  $H_c$  is the critical magnetic field [53].

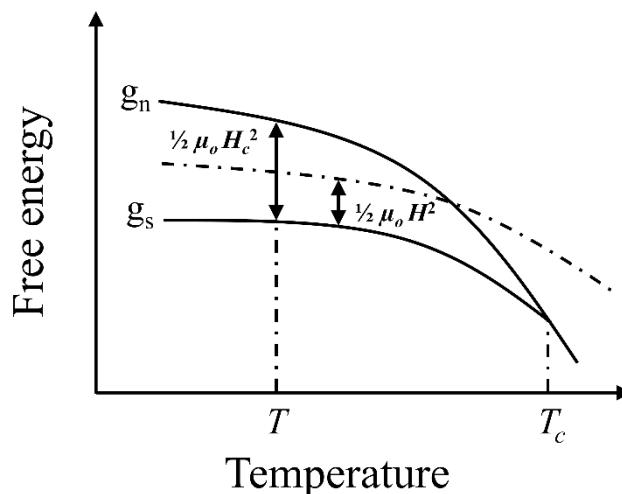


**Figure 6** Temperature dependence of free energies for a superconducting and a normal state [53].

If a normal state appears within a superconductor with boundaries lying parallel to the direction of the applied magnetic field [49], the appearance of such a normal state will change the free energy of the superconductor in the presence of an applied magnetic field of strength less than  $H_c$ . In this situation, there are two contributions to this free energy change: one arising from the bulk of the normal state and one due to its surface. In an applied magnetic field  $H_a$ , the free energy per unit volume of the normal state is greater than that of the superconducting state by an amount equal to  $1/2\mu_0 (H_c^2 - H_a^2)$ . For a type I superconductor with a positive surface energy, in order to form a normal state, there will be an increase in free energy due both to the bulk and to the surface of the normal state. As a result, the appearance of a normal state is energetically unfavourable, and a type I superconductor remains superconducting when a magnetic field of less than  $H_c$  is applied.

However, the surface energy between the normal and superconducting state in a type II superconductor is negative. In order to produce the minimum free energy, therefore, a large number of regions of normal state form in the superconducting material when a magnetic field is applied. The material divides into a fine-scale mixture of superconducting and normal states whose boundaries lie parallel to the applied field, the arrangement being such as to give the maximum boundary area. This is called ‘the mixed state’ because of the co-existence of the superconducting and normal states. The penetrating magnetic field is quantized into so-called fluxoids in the mixed state, as shown in Figure 7 (a).

To achieve the lowest free energy state for a type II superconductor in the mixed state, a favourable configuration of the magnetic field in a superconductor is one in which the material is threaded by fluxoids lying parallel to the applied field. A fluxoid has a very small radius because the smaller the radius of a cylinder the larger the ratio of its surface area to its volume. Since the superconducting bulk is diamagnetic, the magnetic flux due to the applied field is opposed by a diamagnetic surface current that circulates around the perimeter of the specimen. This diamagnetic material is threaded by flux parallel to the applied magnetic field with individual fluxoids screened by circulating current vortices with a sense of rotation opposite to that of the diamagnetic surface current, as illustrated in Figure 7 (a). The current encircling one fluxoid interacts with the magnetic field produced by the current encircling any other fluxoid and, as a result, any two fluxoids repel each other, which is somewhat similar to the repulsion between similar poles in two parallel solenoids or bar magnets. Because of this mutual interaction, the fluxoids threading a superconductor in the mixed state are not random, but arrange themselves into a regular periodic hexagonal array. Towards the centre of each fluxoid the concentration  $n_s$  of superelectrons falls to zero, so the centre of each fluxoid is defined by a very thin core (strictly a line), as shown in Figure 7 (b). Furthermore, the minima in the superelectron concentration are about two coherence-length wide. Also, the flux density is zero in the vortex cores and falls to a small value over a distance equal to about the penetration depth ( $\lambda$ ) away from the cores, as shown in Figure 7 (c) [53].

The appearance of the fluxoids results in a lowering of the free energy when a magnetic field is applied to a type II superconductor. The number  $n_s$  of superelectrons at each fluxoid core decreases and energy must be provided to split-up the Cooper pairs. As an approximation, each fluxoid is as equivalent to a cylinder of radius  $\xi$ . The appearance of a core will, therefore, result in a local increase in free energy of  $\pi\xi^2 \cdot (1/2) \mu_0 \mathbf{H}_c^2$  per unit fluxoid length due to the decrease in electron order. However, the material is not diamagnetic over a radius of about  $\lambda$ , so there is a local decrease in magnetic energy approximately equal to  $\pi\lambda^2 \cdot (1/2) \mu_0 \mathbf{H}_a^2$  per unit fluxoid length. If there is to be a net reduction in free energy by the formation of fluxoids, then:  $\pi\xi^2 \cdot (1/2) \mu_0 \mathbf{H}_c^2 < \pi\lambda^2 \cdot (1/2) \mu_0 \mathbf{H}_a^2$ . According to this relation, if the mixed state is to appear in an applied magnetic field of less than  $\mathbf{H}_c$  (a necessary condition, otherwise an applied field would drive the whole superconductor into the normal state before the mixed state could establish itself), the condition  $\xi < \lambda$  must hold. This is the same condition as that

derived for negative surface energy, supporting the notion that the mixed state is produced by the application of a magnetic field to a type II superconductor [54].

To conclude, a type I superconductor can exist in one of two states, a superconducting state or a normal state [(Figure 8 (a)], whereas a type II superconductor can be in one of the three states, a superconducting state (or a Meissner-Ochsenfeld state under a small applied magnetic field), the mixed state and a normal state [Figure 8 (b)] [49].

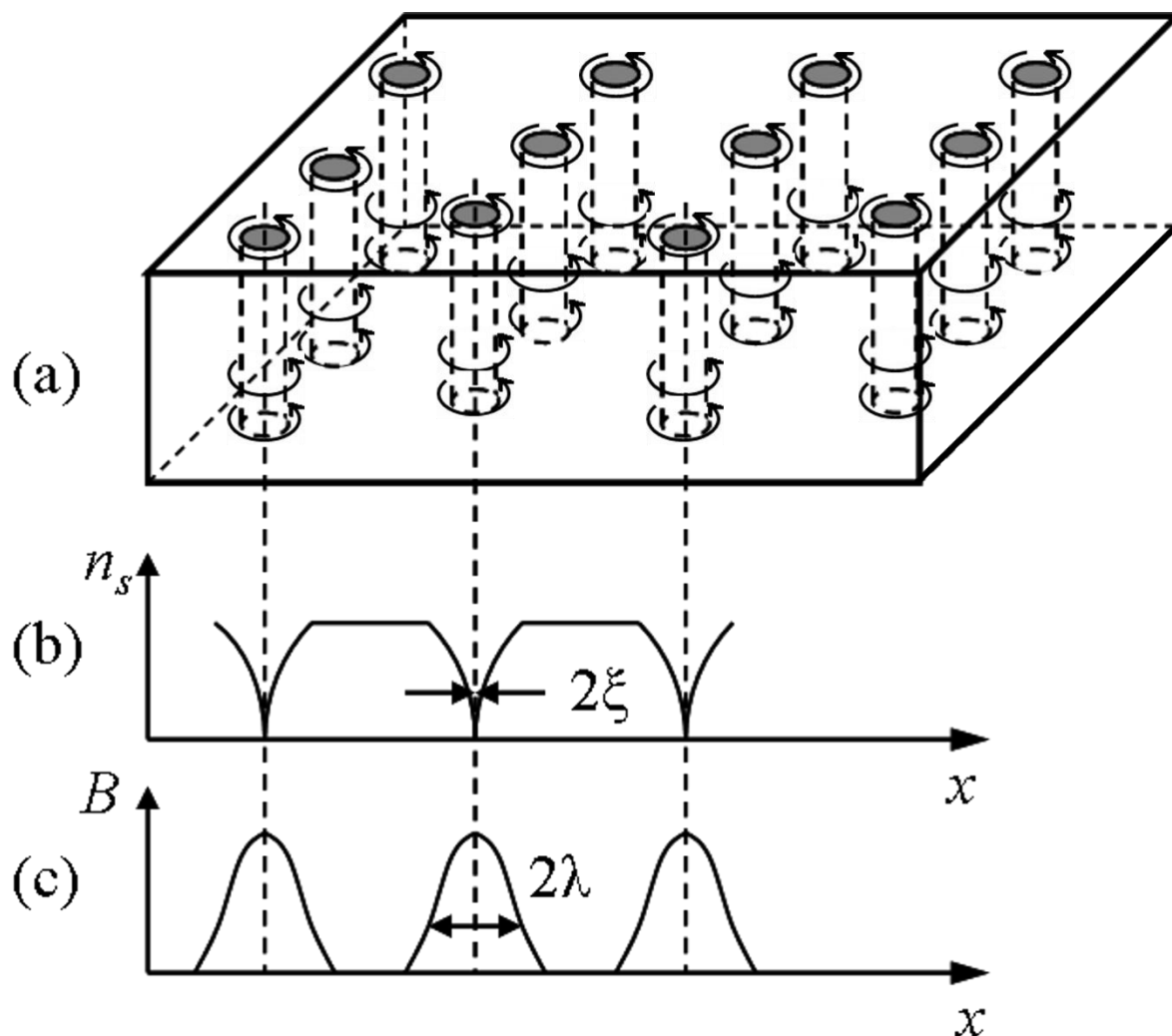


**Figure 7** (a) Mixed state with fluxoids inside a superconductor, (b) spatial distribution of superelectron density and (c) spatial distribution of magnetic flux density [53].

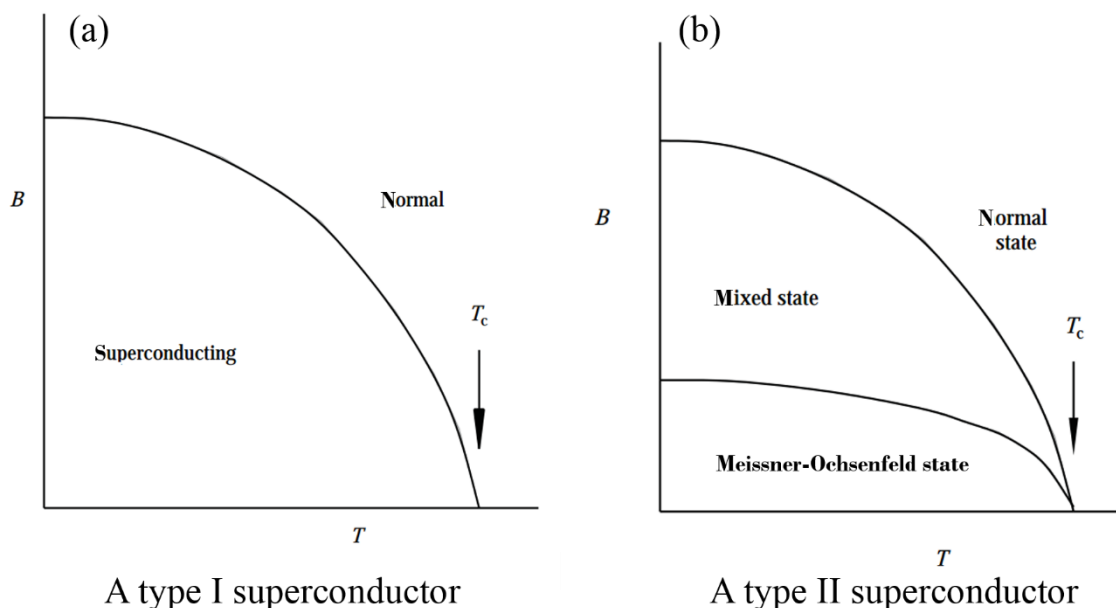


**Figure 8** Variation of applied magnetic flux density ( $B$ ) with temperature ( $T$ ) for (a) a type I superconductor and (b) a type II superconductor [55].

#### 2.2.4.2. Lower Critical Field, $H_{c1}$ and Upper Critical Field, $H_{c2}$

When a magnetic field is applied to a type II superconductor, it is energetically favourable for it to enter the mixed state. To drive a type II superconductor into the mixed state, a certain minimum strength of applied field is required, which is defined as the lower critical field,  $H_{c1}$ . If the applied field is further increased, a type II superconductor is driven, eventually, into a normal state at the upper critical field,  $H_{c2}$ .

A type II superconductor transitions from the Meissner-Ochsenfeld state into the mixed state and parallel fluxoids are formed at the lower critical field  $H_{c1}$ . The average flux density increases simultaneously as the strength of the applied magnetic field is increased above  $H_{c1}$ . With a further increase of the applied magnetic field until the upper critical field,  $H_{c2}$ , is reached, the flux density becomes equal to  $\mu_0 H_a$  and the material enters the normal state.

### 2.2.4.3. Magnetization of Type II Superconductors

The illustration of reversible and irreversible magnetization of a type II bulk superconductor is shown in Figure 9 (1a) [An example of  $J_c$  curve of an  $\text{YBa}_2\text{Cu}_3\text{O}_{7-\delta}$  specimen that gives M-H loop as illustrated in Figure 9 (1a) is shown in Figure 9 (1b); For a type II bulk superconductor with a secondary peak effect (definition of a secondary peak effect will be covered in Section 3.2.4.1), a schematic illustration of reversible and irreversible magnetization is shown in Figure 9 (2a) with a corresponding example of  $J_c$  curve of a 1 mol. %  $\text{ZrO}_2$   $\text{SmBa}_2\text{Cu}_3\text{O}_{7-\delta}$  specimen in Figure 9 (2b)]. In the Meissner-Ochsenfeld state ( $H < H_{c1}$ ), a superconducting surface current screens the external magnetic field so that the magnetic induction  $B$  in the bulk superconductor disappears. In the mixed state between  $H_{c1}$  and  $H_{c2}$ , magnetic flux penetrates the superconductor in the form of flux lines. As the external field increases towards  $H_{c2}$ , the size of the superconducting region between the normal conducting cores of the flux lines decreases to zero, and the sample transitions to the normal state. The  $M$ - $H$  dependence of a defect-free type II superconductor is reversible, and after removal of the external field, no magnetic flux is trapped within the superconductor.

The  $M$ - $H$  dependence becomes highly irreversible if a type II superconductor contains defects that interact with the penetrating flux lines. It appears that almost any kind of imperfection with dimensions as large as, or larger than, the coherence length can pin magnetic flux, therefore leading to magnetic irreversibility. Flux density is large at the surface and decreases with increasing distance from the surface of a type II superconductor because of pinning. For an applied field  $H_a > H_{c1}$ , the magnetic field starts to penetrate into the body of a superconductor, and, in particular, at the penetration field  $H_p$ , the internal magnetic field reaches the centre of the superconductor. It is seen clearly in Figure 9 (1a) that, for  $H_{c1} < H < H_p$ , the irreversible magnetization curve deviates only gradually from the straight line of perfect diamagnetism, demonstrating a strong shielding effect. For a field  $H > H_p$ , the magnetization starts to decrease, which reflects the reduction of the critical current density with increasing magnetic field. The irreversible magnetization for a type II superconductor becomes zero at  $H = H_{irr}$ , where  $H_{irr}$  is the irreversibility field, in contrast to the reversible magnetization which disappears at  $H = H_{c2}$ .

A direct consequence of this field distribution is that the maximum trapped field of a superconducting magnet depends on its size. The gradient of the field profile is determined

by the critical current density of a superconductor. Therefore, large current loops are required in large bulk superconductors, coupled with high critical current densities in order to generate large trapped fields in superconducting magnets.

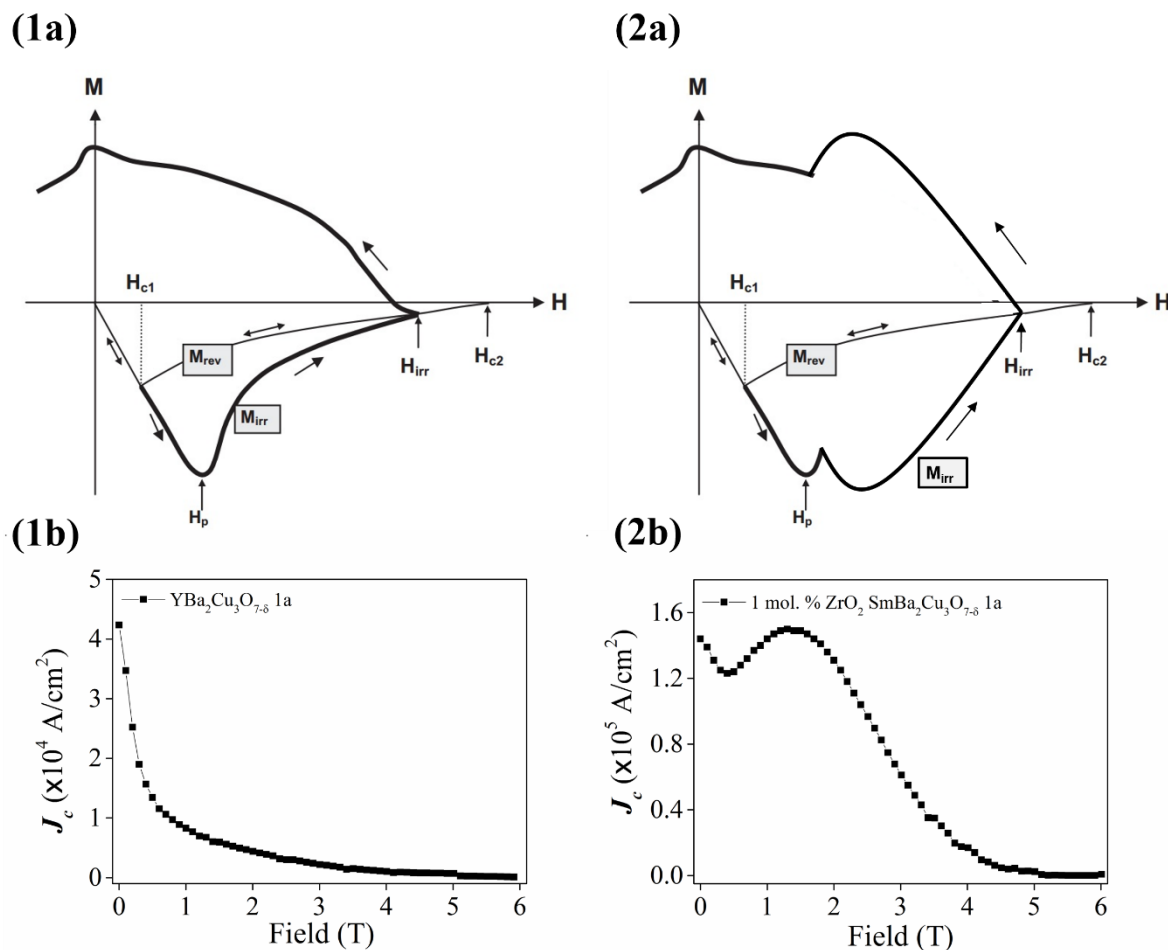


**Figure 9** (1a) Schematic illustration of reversible and irreversible magnetization of a type II bulk superconductor [54]; (1b) An example of  $J_c$  curve of  $\text{YBa}_2\text{Cu}_3\text{O}_{7-\delta}$  specimen that gives M-H loop as shown in Figure 9 (1a); (2a) Schematic illustration of reversible and irreversible magnetization of a type II bulk superconductor with a secondary peak effect; (2b) An example of  $J_c$  curve of 1 mol. %  $\text{ZrO}_2$   $\text{SmBa}_2\text{Cu}_3\text{O}_{7-\delta}$  specimen that gives M-H loop as shown in Figure 9 (2a).

#### 2.2.4.4. Critical Current Density, $J_c$ and Flux Pinning

The maximum DC current density that passes through a superconductor with zero resistance is called the critical current density, and is denoted as  $J_c$  [51].  $J_c$  is one of the most important

properties for the applications of superconductors.  $J_c$  in type I and reversible type II superconductors is too low for feasible applications [49] [56]. Therefore, only  $J_c$  within the context of an irreversible type II superconductor will be reviewed here.

The interplay between currents and fluxoids in a superconducting material results in a driving force on the flux lines that put them into motion, which leads to the dissipation of energy, manifested as an electric potential within the material (i.e. Faraday's Law). Under these conditions, therefore, the material can no longer be considered to be superconducting. Prevention of fluxoid motion, or flux pinning, up to a high critical current density  $J_c$ , is therefore essential for practical applications of superconducting materials. Fortunately, flux pinning is a quite general phenomenon related to the presence of lattice defects in commonly produced materials, including dislocations, point defects, voids, grain boundaries and precipitates.

In the absence of pinning centres, the fluxoid distribution inside a superconductor in a magnetic field  $H > H_{cI}$  is uniform; on the other hand, when pinning centres are present, the fluxoids are trapped upon entering or leaving the superconductor, leading to a flux density gradient and then to an irreversible magnetization loop [55]. If the diameter of a non-superconducting particle is  $d$ , the energy saved (i.e. the pinning energy) is evaluated by multiplying the condensation energy per unit volume [ $\Delta E = (1/2) \mu_0 H_c^2$ ] by the volume of the interaction region ( $V = \pi \xi^2 d$ ), i.e.

$$U_p = \Delta E \times V = (1/2) \mu_0 H_c^2 \pi \xi^2 d \quad (2-1)$$

once trapped by this region, the same amount of energy is required in order to remove the fluxoid over the distance of  $\xi$  from the particle, which causes flux pinning and an associated pinning force ( $f_p$ ) given by the distance ( $\xi$ ) is:

$$f_p = (1/2) \mu_0 H_c^2 \pi \xi d \quad (2-2)$$

A practical superconductor in the mixed state contains many pinning centres and a number of fluxoids. If a unit volume contains  $N$  pinning centres with an average particle diameter of  $d$  and all of the centres contribute to pinning, the pinning force ( $F_p$ ) per unit volume is given by:

$$F_p = N \times f_p \quad (2-3)$$

When a current with current density ( $\mathbf{J}$ ) flows through a superconductor in the presence of a magnetic field ( $\mathbf{B}$ ), the magnetic flux quanta is subjected to a Lorentz force ( $\mathbf{F}_L = \mathbf{J} \times \mathbf{B}$ ) and will move in a direction perpendicular to that of both the current and the applied field. If the velocity of a fluxoid is represented by  $v$ , a voltage  $E = v \times \mathbf{B}$  will be generated in the direction of the electric current to produce resistance and hence dissipate energy. However, if a pinning force that can suppress the movement of the magnetic flux exists in the superconductor, the current will flow without resistance. Therefore, assuming  $\mathbf{J}_c$  is obtained when  $\mathbf{F}_p$  becomes equal to the Lorentz force ( $\mathbf{F}_L$ ),  $\mathbf{J}_c$  is represented as:

$$\mathbf{J}_c = N (1/2) \mu_0 \mathbf{H}_c^2 \pi \xi d / \mathbf{B} \quad [57] \quad (2-4)$$

This definition indicates that the value of  $\mathbf{J}_c$  depends on the distribution of pinning centres and their sizes within the superconducting material. There is no energy difference for fluxoid motion within the interior of the superconductor in the case of a particle larger than the coherence length, resulting in reduced effective flux pinning.

The rare-earth cuprates [(RE)BCO] are typical type II superconductors and include YBCO and SmBCO, on which this thesis is based. Although there are similarities between (RE)BCO and YBCO, an extra issue for (RE)BCO in flux pinning compared to YBCO is the appearance of the so-called peak effect [56] [57] [58]. For YBCO,  $\mathbf{J}_c$  usually decreases monotonically when the applied field increases. On the other hand,  $\mathbf{J}_c$  for (RE)BCO superconductors becomes higher at higher fields (1 T to 2 T) after an initial decrease in  $\mathbf{J}_c$  in increasing applied field. This effect is called the ‘peak effect’, which makes it possible for (RE)BCO bulk single grains to generate a particularly large trapped field at intermediate field values. The pinning mechanism of the peak effect can be explained by the presence of several micro-defects in the material, of which solid solution phases is one type of pinning centre at higher field. When the applied field is higher, the solid solution phases become non-superconducting and are converted effectively into (field-induced) pinning centres [59].

### 2.2.4.5. Measurement and Calculation of $J_c$ Using the Bean's Critical State Model

The most straightforward method used to measure  $J_c$  of bulk superconductors is based on transport current and drop in voltage, as is done when measuring the resistance of conventional metals. The superconducting state in a transport measurement, however, is often unstable due to the heat generated by the contact resistance, which can be severe in HTS bulk superconductors [60].

Due to the difficulty of measuring transport critical current, a method used more frequently to estimate  $J_c$  is based on volume magnetisation, which requires an assumed current distribution within the sample, and is based primarily on experience and understanding. In a DC field, either the Bean or Kim model is then used to estimate  $J_c$  [61][62]. Single grains should be used for the measurement of  $J_c$  and the magnetic field should be applied parallel to the sample  $c$ -axis (definitions related to the crystallographic structure of a (RE)BCO bulk single grain will be given in Chapter 3). The response of a superconductor to AC magnetic field in the presence of a DC field can also be used to measure  $J_c$  via the Campbell method [63].

One of the most common models used to estimate  $J_c$  is the Bean's critical state model, which describes the magnetisation of a type II superconductor in a critical state [61]. The basic concept of the Bean critical state model is that an irreversible superconductor can carry a limiting, macroscopic superconducting current density. The applied field can penetrate into the superconductor at a field greater than the lower critical field ( $H_{c1}$ ), and persistent superconducting current can flow when the flux lines are pinned against the Lorentz force by defects in the superconductor. Figure 10 shows a schematic illustration of the magnetisation process of an infinite slab of a type II superconductor with a thickness of  $2a$  in a field parallel to its surface based on the Bean critical state model. The model assumes that supercurrents flow with a density equal to the critical current density ( $\pm J_c$ ). If this magnitude of current flows everywhere in the specimen, it is said to be in the critical state ( $H = H^*$ ). The key point of the Bean critical state model is that  $J_c$  is independent of the applied magnetic field and is constant within the sample. The relation is given by the Maxwell equation:

$$\nabla \times \mathbf{B} = \mu_0 \mathbf{J}_c = \text{Constant} \quad (2-5)$$

where  $\mathbf{B}$  is the magnetic induction in T,  $J_c$  is given in  $\text{A m}^{-2}$  and  $\mu_0$  is the permeability of free space.

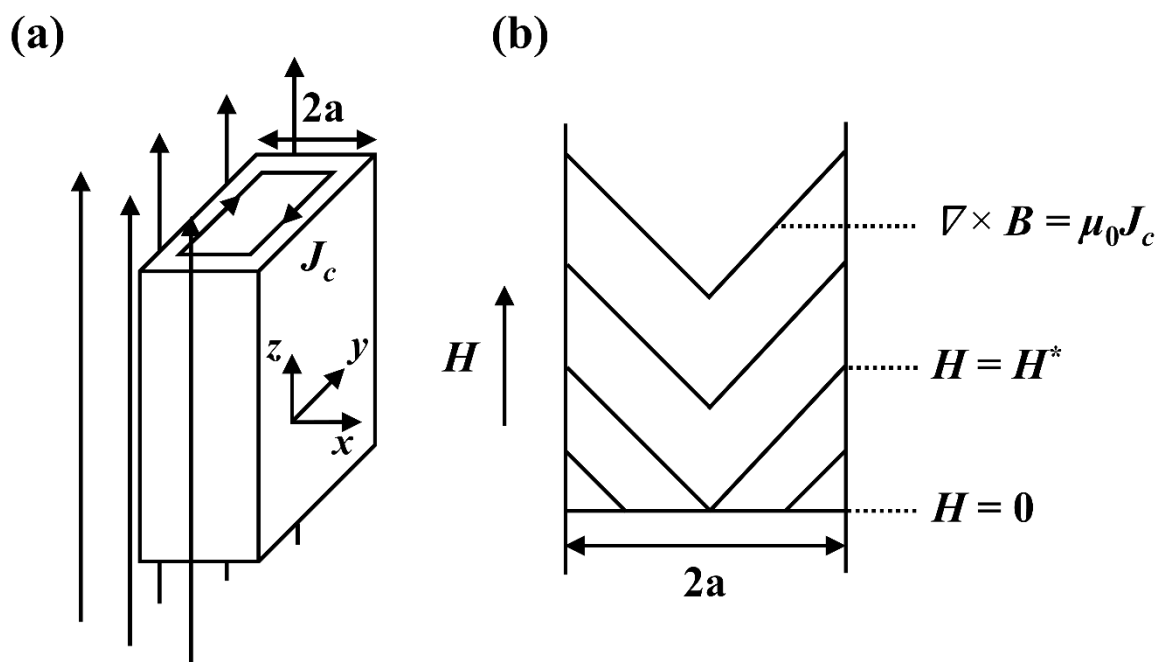


**Figure 10** Schematic illustration of the magnetisation process of an infinite slab of a type II superconductor with a thickness of  $2a$  in a field parallel to its surface. (a) An infinite slab in a magnetic field; (b) the distribution of the induced field  $\mathbf{B}$  over the cross section of the infinite slab.

Bean treated the problem of current flow in a superconducting bulk macroscopically, i.e. by treating  $\mathbf{M}$  and  $\mathbf{B}$  in the definition  $\mathbf{B} = \mu_0 (\mathbf{M} + \mathbf{H})$  as average values within the sample volume. The local internal induced field is defined as

$$\mathbf{b}_i = \mathbf{B}/\mu_0 \quad (2-6)$$

and local magnetisation  $\mathbf{m}_i$  is defined as

$$\mathbf{m}_i = \mathbf{b}_i - \mathbf{H} \quad (2-7)$$

where  $\mathbf{H}$  is the applied field. Then the average  $\mathbf{M}$  is obtained by integration over the volume:

$$\mathbf{M} = \int (\mathbf{m}_i) dv \quad (2-8)$$

where  $v$  is the volume of the sample being magnetised. The relation between  $M$ ,  $H$  and  $J_c$  can be obtained from (2-5), (2-6), (2-7) and (2-8). In the case of an infinite thin slab with a thickness of  $a$ , the results of the integration for increasing and decreasing applied field are:

$$M(H)^- = -J_c \cdot a/2; \text{ when } H \geq H^* \quad (2-9)$$

$$M(H)^+ = J_c \cdot a/2; \text{ when } 0 \leq H \leq H_m - 2H^* \quad (2-10)$$

where  $H_m$  is the maximum field applied to the superconductor. The difference in the magnetisation  $\Delta M$  is then given by;

$$\Delta M = M(H)^+ - M(H)^- = J_c \cdot a, H^* \leq H \leq H_m - 2H^* \quad (2-11)$$

It can be seen that  $J_c$  depends only on  $\Delta M$  in the range of  $H^* \leq H \leq H_m - 2H^*$ , and, therefore,  $J_c$  can be calculated directly by measuring  $\Delta M$ .

It was assumed in the Bean critical state model that,  $J_c$  is a constant. In general,  $J_c$  of a type II superconductor decreases as the applied field increases. Therefore, it is necessary to consider the dependence of  $J_c$  on the magnetic field when applying this model.

More recently, Chen *et al.*[62] calculated the relation between  $J_c$  and its magnetisation of an infinite rectangular sample based on the Bean critical state model. The resulting  $M(H)$  is described as:

$$\Delta M = M(H)^+ - M(H)^- = J_c \cdot a \cdot (1-a/3b) \quad (2-12)$$

where  $H$  is larger than  $2H^*$ ,  $a$  and  $b$  are dimensions of the cross section of the sample, and  $b \geq a$ . This formula is referred as the extended Bean critical state model and is used widely in the estimation of  $J_c$  of (RE)BCO single grains. It is used throughout this thesis.

#### 2.2.4.6. Field Trapping of the Superconducting Bulk Single Grains

The field trapping profile of a bulk superconductor is shown schematically in Figure 11, assuming a field-independent  $J_c$  according to the Bean critical state model. The maximum trapped field  $B_{max}$  depends not only on the gradient of this field profile but also on the radius,

$R$ , of the current loop. The field gradient is determined by  $J_c$  of the supercurrents or the pinning force exerted by the pinning centres on the flux lines.

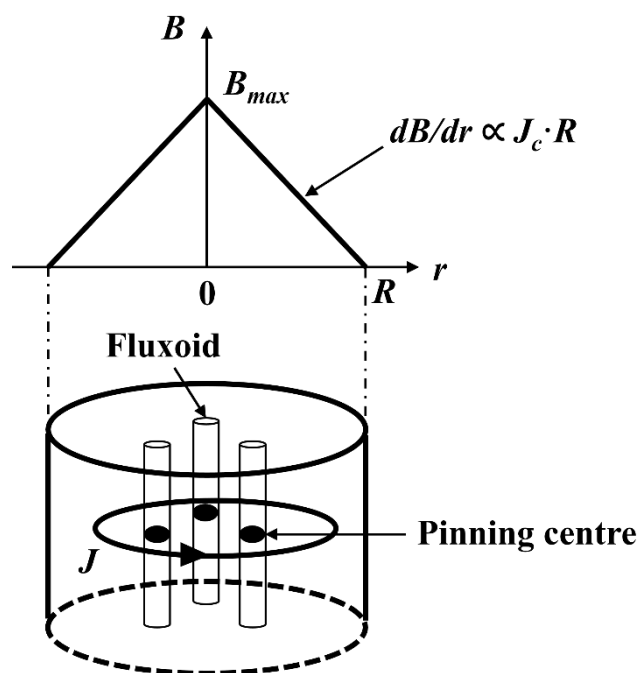


**Figure 11** Schematic trapped field profile of a superconducting bulk single grain [54].

Bulk superconductors as a source of magnetic field need to be magnetized before application. There are three main methods to energize bulk superconductors, including field cooling magnetization (FCM), zero field cooling magnetization (ZFCM) and pulsed field magnetization (PFM).

In FCM, a superconducting bulk material is first placed in the bore of a high field external magnet and is then exposed to a field generated by the external magnet in its normal state. After the external magnetic field has stabilised, the bulk material is cooled to a superconducting state below  $T_c$ . The external magnetic field is then removed, causing the supercurrents in the bulk to redistribute and generate a magnetic field. Field cooling magnetization can only be used for ex-situ magnetization, in which the bulk magnet is energized before installation. On the other hand, in ZFCM, the material is first cooled to a superconducting state below  $T_c$  and then an external magnetic field is applied to magnetize the material. The FCM is used as the main magnetizing method in this thesis, because the FCM technique has the advantage of a lower applied magnetizing field, which needs only to correspond approximately to the expected maximum trapped field in the superconductor,

while in ZFCM, the applied field needs to be at least twice as large as the maximum trapped field, assuming that  $J_c$  does not vary with applied field.

The third way to magnetize a bulk single grain is PFM, in which a bulk superconductor is first cooled to below  $T_c$ . An external electromagnet then generates a pulsed field to magnetize the bulk material [64]. In this fast rising and falling pulse field, regions of the bulk are heated to a normal state to enable the flux to penetrate into the interior of the superconductor. If the bulk is cooled appropriately, it can return to a superconducting state to effectively trap the pulsed field. PFM is an energy-efficient way of magnetization compared to FCM. It can also be used in an in-situ magnetization process, which involves energizing the bulk sample after installation and pre-cooling to the required temperature. However, the disadvantages of this technique are: first, it is difficult to control accurately the level of the resulting field, because it depends critically on heating/cooling conditions; and second, PFM requires an external field that is much larger, albeit transient, than the final field trapped in the bulk magnet.

### **2.3. Applications of (RE)BCO Superconducting Bulk Single Grains**

(RE)BCO superconducting bulk single grains have significant potential for engineering applications due to their potential to trap large magnetic fields. A combination of repulsive and attractive forces, for example, can suspend or levitate a magnetic object in mid-air. Additionally, in quasi permanent magnet applications, bulk superconductors can act as the main source for large magnetic fields [65].

A substantial mass of up to 200 kg can be lifted using the repulsive force between a Fe-Nd-B magnet and an YBCO bulk superconductor cooled in liquid nitrogen. A magnetically-levitated train (or a maglev train) can be suspended in the air above a single track, and propelled using repulsive and attractive forces between magnetic tracks on the rail and in the train. The only friction exerted in a maglev system is that between the carriage and the air due to the absence of physical contact between the track and the vehicle. Consequently, maglev trains can potentially travel at very high speeds with reasonable energy consumption and low noise levels. Systems have been proposed that can operate at up to  $650 \text{ km h}^{-1}$ , which is far

faster than conventional rail transport. Trapped field magnets may replace conventional NbTi racetrack coils, which are currently used in Japanese maglev trains [66]. Numerical simulation has shown that field trapping magnets can be used for maglev trains if  $J_c$  of the sample is larger than  $10^5 \text{ A}\cdot\text{cm}^{-2}$  at the operating field with a diameter exceeding 10 cm and of mechanical strength greater than 100 MPa. These requirements demand further materials development relative to the current state of the art, but are clearly achievable with (RE)BCO bulk superconductors.

A superconducting bearing is a simple motor-like device, with bulk (RE)BCO used as a stator with a permanent magnet rotor. The attractive and repulsive forces between the motor and stator cause the stator to suspend, whereby it is able to spin freely. It is found that SmBCO is superior to YBCO in superconducting bearings because of its higher  $J_c$  and lower creep rate [67]. One application is a bearing for an energy-storage flywheel system. Since the superconducting bearing has no friction under ideal conditions, it is possible to store rotational kinetic energy for long periods. A second advantage of an energy-storage flywheel system is that it can deliver energy quickly. The Boeing Company in the USA, the Institute of Electrical Machines in Germany and ISTEK in Japan all have designed and built prototype flywheels with 10 kWh total stored energy [68].

Large single grains of (RE)BCO can trap magnetic fields of several Tesla below  $T_c$ , and thus have the potential for applications as quasi permanent magnets. A record trapped field of 17.6 T has been observed recently in an arrangement of two GdBCO/Ag single grain bulk superconductors at 26 K, which underlines the potential field-generating performance of these technologically important materials [69]. As a result, various power devices, for which permanent magnets have been employed, may potentially be replaced by superconducting quasi permanent magnets.

## 2.4. Development of SmBCO Bulk Superconductors

Several attempts to grow SmBCO bulk superconductors have been reported in literature. Babu *et al.* reported a practical processing method for fabricating SmBCO single crystals in air [70], which was economical and offered considerable freedom in terms of processing and

reproducibility. The process was based primarily on the development of a new type of generic seed crystal that effectively promoted the epitaxial nucleation of any (RE)BCO system, and, secondly, suppressed the formation of Sm-Ba solid solution in a controlled manner within large grains processed in air.

Recently, Shi *et al.* developed a novel, simple and low-temperature post-annealing approach to overcome the sensitivity of  $T_c$  to Sm/Ba substitution, in order to simplify the fabrication of SmBCO and to increase its reliability with a view to practical processing [71].

At the same time, attempts to improve the superconducting properties of SmBCO have been reported, including the addition of  $\text{Sm}_2\text{Ba}_4\text{Cu}_1\text{M}_1\text{O}$  [Sm-2411(M)], where M = tungsten (W), niobium (Nb) and bismuth (Bi), as a new kind of pinning centre [72] and  $\text{SmBa}_2\text{Cu}_{2.67}\text{Al}_{0.33}\text{O}_{6+\delta}$  as a novel dopant [73]. In addition, Sun *et al.* successfully grew high performance SmBCO bulk superconductors in air through melt-textured growth by adding a novel Ba-rich  $\text{Sm}_2\text{Ba}_4\text{Cu}_2\text{O}_9$  (Sm-242) compound to the precursor powders. It was found that, with the addition of 10 mol. % Sm-242, a high  $T_c$  of over 94 K with a sharp transition width,  $\Delta T_c$  (i.e. less than 1 K), in SmBCO was achieved [74].

Peng *et al.* found that the crystal growth slowed down and terminated prematurely due to a reduced effective supersaturation under a conventional slow-cooling mode. In their new process, an accelerated cooling was applied so that a trapping mode, controlled continuous growth was realized [75].

Even more recently, Congreve *et al.* investigated the recycling process of SmBCO. In this, additional liquid-rich phase powder (powders that can provide the  $\text{Ba}_3\text{Cu}_5\text{O}_{6.72}$  liquid phase for the peritectic reaction introduced in Section 3.2) was provided beneath a failed sample, and infiltrated upwards to contribute a sufficient concentration of additional Sm species at the growth front to enable samples to grow relatively easily in the form of single grains by producing a more uniform composition at the growth front. This led directly to an increased tolerance to the presence of Ag and Ce-rich agglomerates. Importantly, they observed that the recycled samples had a much more uniform composition, and therefore exhibited more uniform superconducting properties, than single grain samples fabricated by a primary growth process [76].

Li *et al.* have successfully produced high-quality single domain SmBCO bulk superconductors in air by a top seeded infiltration and growth (TSIG) method with a new

solid phase of  $(\text{Sm}_2\text{O}_3 + x \text{BaCuO}_2)$  and liquid phase [77], which reduced significantly the cost of the synthesis procedure.

However, these aforementioned approaches only improve the superconducting properties of SmBCO to a limited extent and do not generally enable scale-up of the system, which is critical for practical applications. Therefore, other approaches such as the addition of silver (Ag) to improve the mechanical properties of SmBCO have been developed. Sakai *et al.* reported that Ag addition led to a reduction in sample porosity and is effective in increasing the mechanical strength of a SmBCO bulk [78]. Ikuta *et al.* found that adding Ag to the starting precursor powders worked very effectively to circumvent the problems they encountered in the melt-processing of large samples [79]. Finally, Wu *et al.* successfully grew SmBCO/Ag bulk superconductors by a cold-seeding melt-growth process and well-textured SmBCO bulk single grains with 5 wt. %  $\text{Ag}_2\text{O}$  addition were fabricated reproducibly under ambient atmosphere [80].

The next chapter will review the fundamentals related to the fabrication of superconducting SmBCO bulk single grains for a more thorough understanding of the system.

# CHAPTER 3

## FABRICATION OF SUPERCONDUCTING SMBCO BULK SINGLE GRAINS

SmBCO, one of the (RE)BCO cuprate superconductors, has significant potential for practical applications due to its superior superconducting properties. Therefore, in this chapter, three main points most-related to the fabrication of practical SmBCO single grain bulk superconductors are discussed: firstly, the nature of the SmBCO material from a microstructural viewpoint explaining its crystallographic structure; secondly the required characteristics of the material, such as avoiding grain boundaries and the generation of sufficient flux pinning centres, and, finally, how to achieve a SmBCO superconducting bulk single grain with all the qualities for application from precursor preparation to the fabrication process.

### 3.1. Crystallographic Structure of SmBCO

High- $T_c$  superconductivity in cuprate materials appears in structures that contain anionic  $(\text{CuO}_2)^-$  layers stacked alternately between compensating cationic metal or metal-oxide layers. These structures can be represented by a general formula:  $\text{B}^{\text{b}+}[(\text{CuO}_2)^-]_n\text{C}^{\text{c}+}_{n-1}$ , which distinguishes the building units according to their functionality: the building units  $[(\text{CuO}_2)^-]$  represent layers consisting of  $\text{CuO}_4$  polyhedra, which share corners in an almost planar arrangement and these layers are essential for the superconducting behaviour in these cuprate materials, forming the conducting block; the cationic metal oxide spacing layer B is stacked between consecutive conducting blocks and the spacing layer B is the second fundamental structural component of HTS cuprates. The intra-block layer C, only appears for extended conducting elements, with two or more layers in the conducting block.

The electronic structure in the normal state in the cuprates is metallic in nature, and is strongly correlated with their crystal structure, chemical bonding and composition.

Furthermore, secondary structural features (such as defects on the atomic, nanoscopic, or microscopic scale) also have a strong influence on the material properties.

From the crystallographic point of view, SmBCO superconductors have a distorted oxygen-deficient perovskite structure, as shown in Figure 12. Because of different electronic, magnetic and structural interactions, the stoichiometry, fine structure and properties of the resulting superconducting compounds will be influenced strongly by preparation and annealing conditions. Note that the stacking axis appearing on the longest unit cell parameter is denoted as the  $c$ -axis, with the plane perpendicular to the  $c$ -axis being labelled as the  $a/b$ -plane [54].

The chemical formula of the SmBCO superconducting phase is  $\text{SmBa}_2\text{Cu}_3\text{O}_{7-\delta}$  ( $\delta = 0-1$ ), which is typically abbreviated as SmBCO or Sm-123. The oxygen atoms at the top and bottom faces in the SmBCO crystallographic structure are the least stable energetically and may be lost most readily from the unit cell. Therefore, with this loss of oxygen atoms, the  $\delta$  value in  $\text{SmBa}_2\text{Cu}_3\text{O}_{7-\delta}$  changes between 0 and 1. Meanwhile, a change of orthorhombic ( $a \neq b$ ) to tetragonal ( $a = b$ ) structure occurs when the number of oxygen atom decreases from 7 to 6. The compound has the highest  $T_c$  when  $\delta$  equals 0, and loses its superconductivity when  $\delta$  decreases to 0.6 [53].

Instead of forming a stoichiometric  $\text{SmBa}_2\text{Cu}_3\text{O}_{7-\delta}$  phase compound, however, a solid solution of  $\text{Sm}_{1+x}\text{Ba}_{2-x}\text{Cu}_3\text{O}_{7-\delta}$  (Sm-123ss) is formed in SmBCO, corresponding to an atomic substitution on the Ba site by Sm. This leads to a depression in  $T_c$ , which can be explained partly in terms of the decrease of the carrier density associated with the trivalent Sm ion, replacing the divalent Ba ion. As a result, the structural change is associated with disorder in the CuO chain site, which is accompanied by the introduction of extra oxygen ions at anti-chain sites to maintain the charge balance [81].

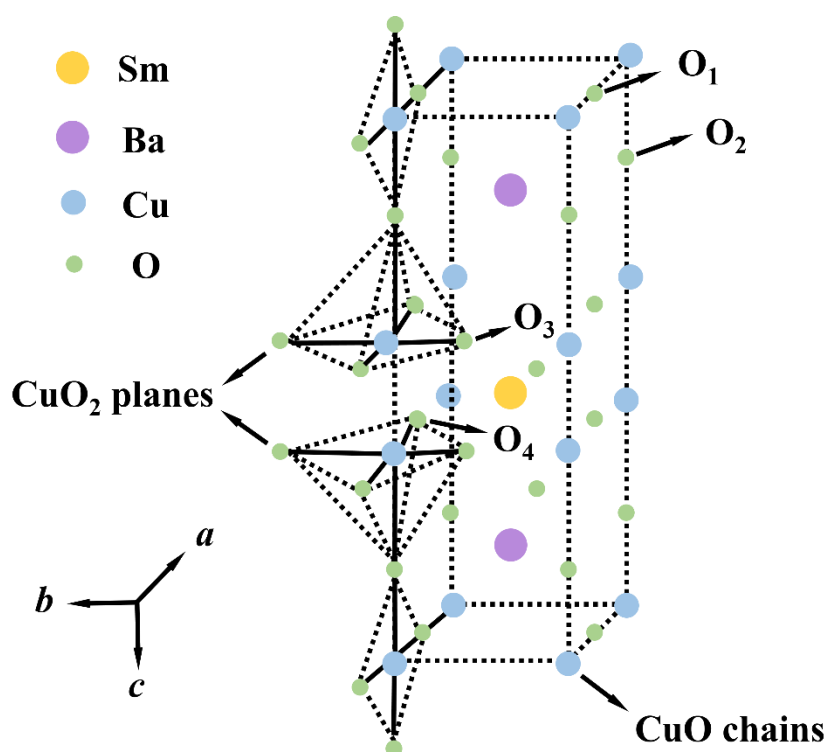


**Figure 12** Oxygen-deficient perovskite structure of the superconducting SmBCO phase [53].

### 3.2. Fabrication of SmBCO Single Grains by Top Seeded Melt Growth (TSMG)

It has been established for some time that the presence of grain boundaries in polycrystalline, bulk SmBCO superconductors causes a large reduction in  $J_c$ . Due primarily to the existence of the  $(\text{CuO}_2)^-$  layers along the  $a/b$ -plane, SmBCO exhibits two-dimensional anisotropy in its superconducting properties. On a microscale, if the coupling of the  $(\text{CuO}_2)^-$  layers is weak, supercurrents cannot flow across grain boundaries. On a macroscale, the existence of secondary phases at grain boundaries or the presence of large grain misorientation angles can act as barriers to the supercurrent charge carriers due to the large energy loss associated with the flow of current across these non-superconducting regions. Although sintering is widely accepted as an effective method to fabricate oxide materials, sintered SmBCO superconductors suffer from various weak-link problems, including large grain misorientation angles, the presence of second phases at grain boundaries, randomly oriented multigrains, and

so on [53]. At an early stage of research, enhancement of  $J_c$  was not realized immediately due to the limitations of existing fabrication techniques. Theoretically, in order to obtain superconducting materials with high  $J_c$ , the following factors should be achieved: (a) optimization of oxygen content; (b) elimination of weak links; (c) a highly orientated structure; (d) low porosity and (e) the introduction of effective pinning centres to the sample microstructure. Appropriate annealing after growth can address factor (a). Melt processing techniques, including directional solidification processes, help achieve factors (b), (c) and (d). The addition of several secondary elements, such as Pt or Ce, have been identified to be effective in generating a fine dispersion of non-superconducting  $\text{Sm}_2\text{Ba}_1\text{Cu}_1\text{O}_5$  (Sm-211) particles, which form pinning centres in the superconducting Sm-123 matrix (through the peritectic reaction) to achieve (e) [55].

Melt processing is recognised as the most effective and important technique for the development of high-quality, high  $J_c$  bulk superconducting cuprates. As a result, a basic understanding of the fundamentals of crystal growth and processing is essential to control the melt process. During melt processing, SmBCO superconductors solidify in the presence of a seed from a partially molten state in a temperature gradient, resulting in the formation of a highly aligned structure with strongly coupled boundaries.

As discussed in Section 3.1, if SmBCO is melt-processed in air, Sm-123ss will form and exhibit a low onset  $T_c$  with a broad transition width,  $\Delta T_c$ , due to the substitution of Sm on the Ba site. Therefore, an oxygen-controlled melt growth (OCMG) process has been developed to grow SmBCO with greatly improved  $T_c$  and  $J_c$ . This is because the peritectic temperature of Sm-123ss decreases with the concentration of Sm on the Ba site under an atmosphere of reduced oxygen partial pressure [82], which allows the preferential formation of near stoichiometric SmBCO. OCMG is based on a peritectic solidification reaction with  $p_{\text{O}_2}$  controlled at the melt-growth stage where the solidification of the Sm-123 phase takes place. The peritectic solidification reaction employed in this study for the SmBCO system occurs at the peritectic temperature,  $T_p$  (1070 °C for SmBCO system), where  $\text{SmBa}_2\text{Cu}_3\text{O}_{7-\delta}$  (Sm-123) is formed from solid  $\text{Sm}_2\text{Ba}_1\text{Cu}_1\text{O}_5$  (Sm-211), a Ba-Cu-O based liquid phase (L) and oxygen gas (G);



Although OCMG-processed SmBCO has great potential for applications with superior superconducting properties, the control of oxygen partial pressure requires a specially

designed furnace and therefore raises the cost of the product, which has motivated the development of an air-based melt process for this material. This, in turn, has led to an effective top seeded melt growth (TSMG) technique for growing SmBCO single grains. TSMG is largely identical to OCMG, except for the ambient growth atmosphere instead of the controlled  $p_{O_2}$  atmosphere. TSMG consists generally of the following steps: (a) the preparation of precursor powders and the pre-form pressing; (b) the selection of a suitable seed; (c) control of the seeding process; (d) single grain nucleation and growth via a controlled peritectic solidification reaction and (e) post oxygenation of the non-superconducting tetragonal phase to generate the superconducting orthorhombic phase. To form a nearly stoichiometric SmBCO phase via TSMG, it is necessary to engineer the precursor composition towards the Ba-rich direction to avoid the severe Sm/Ba substitution, which is achieved in this research by adding an extra 2 wt. %  $BaO_2$  into the precursor powders. Commercially available precursor powders were used throughout, followed by mixing thoroughly by a motorised pestle and mortar (details will be discussed in the experimental section in each chapter). A small single crystal was used to provide a nucleation centre, in which the crystal orientation of the growth matches that of the nucleation source. The seed crystal must necessarily have a higher melting temperature than the seeded material [55] (seeding in this thesis will be explored in depth in Chapter 4), and, with the help of the seeds, elimination of weak links and highly orientated structure in a bulk single grain can be obtained. During TSMG, a seed with its  $c$ -axis aligned perpendicular to the surface of the pellet enables SmBCO to grow into a single grain, which exhibits significantly enhanced magnetic flux trapping ability.

A pseudo-binary phase diagram of the SmBCO system is shown in Figure 13, which illustrates the various phase changes at different temperatures [54]. The dotted lines in Figure 13 indicate a possible route to grow stoichiometric  $SmBa_2Cu_3O_{7-\delta}$ . The composition of the precursor powders for the SmBCO system used in this thesis contains mainly of a mixture of 75 wt. % Sm-123 and 25 wt. % Sm-211 powders, which can be converted to 56.8 mol. % of  $BaCuO_2$  as indicated by the vertical dotted line. Therefore, when the mixture is heated to temperatures above 1070 °C, the system will consist of Sm-211 and the liquid phase, resulting in complete decomposition of Sm-123 at these temperatures. Sm-123, Sm-211 and the liquid phase co-exist when the temperature range is lowered to between 1070 °C and 1040 °C. Subsequently, if the temperature is decreased further from 1040 °C to as low as 780 °C, with the starting composition of 75 wt. % Sm-123 and 25 wt. % Sm-211, the Sm-123

matrix will form with embedded Sm-211 particles. Under such circumstances, the substitution of Sm onto the Ba site in the superconducting matrix will be severe, and  $x$  in  $\text{Sm}_{1+x}\text{Ba}_{2-x}\text{Cu}_3\text{O}_{7-\delta}$  could vary roughly from 0 to 0.5, as illustrated in Figure 13. A Ba-rich precursor is necessary to avoid this problem, resulting in the addition of an extra 2 wt. %  $\text{BaO}_2$  to the precursor powders in this research, with the corresponding changes in the growth-related temperatures incorporated in the melt process.

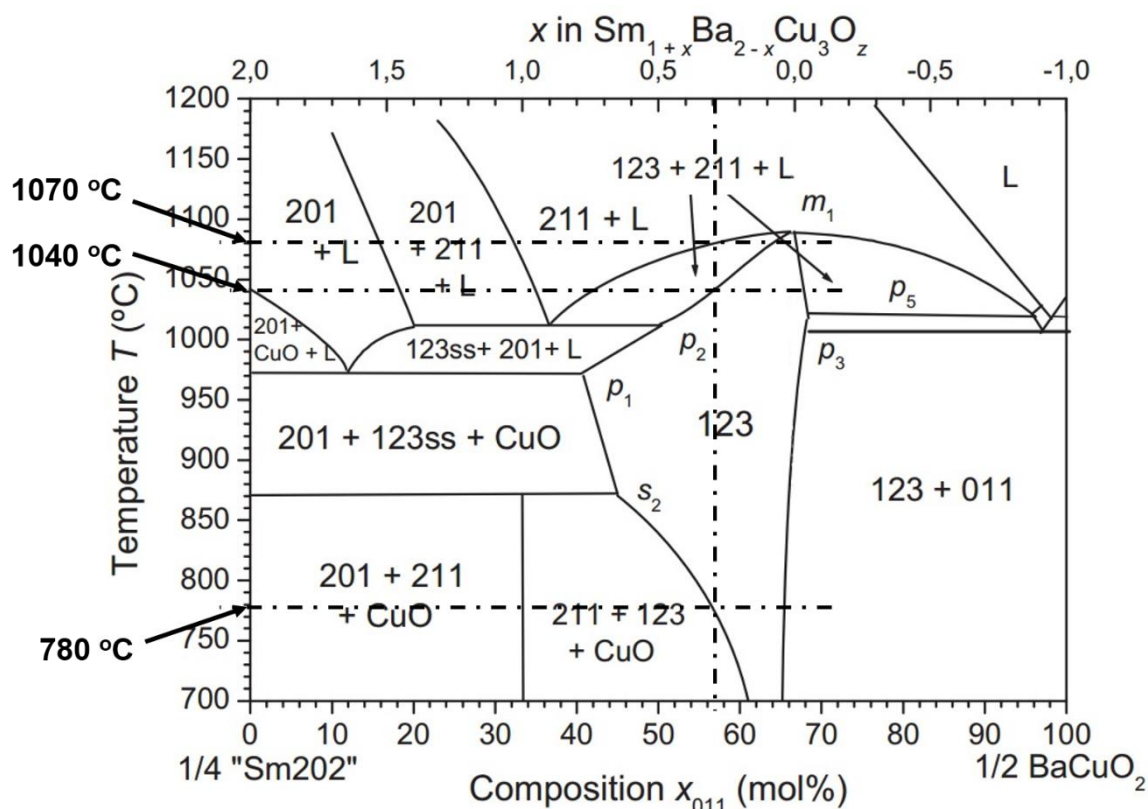


**Figure 13** A pseudo binary phase diagram for SmBCO system between the  $\text{BaCuO}_2$  and ‘Sm202’ phases. The positions of all lines are approximate [54].

Summarising from the phase diagram, in the TSMG process used in this study, the mixture of Sm-123 and Sm-211 powders is heated up typically to around 1087 °C and held for a short period of time, during which Sm-123 decomposes to Sm-211, the liquid phase and oxygen gas. The partially molten precursor pellet is then cooled quickly to the peritectic temperature ( $T_p$ ), which is around 1070 °C for the SmBCO system, and then cooled slowly through  $T_p$ . The SmBCO single grain nucleates epitaxially from a seed during the slow cooling process by the peritectic solidification reaction explained above.

### 3.2.1. Solidification: Solute Diffusion Model and Pushing/trapping Theory

#### 3.2.1.1. Solute Diffusion Model

As discussed earlier in Section 3.2, a SmBCO single grain is formed by TSMG through a peritectic solidification reaction between Sm-211 and a Ba-rich liquid phase. Solidification from the melt, in general, is associated with the interface kinetics and/or mass transport. SmBCO, when grown as a single grain, has the characteristic morphology of faceted growth along a specific growth direction. Such morphology indicates that, in the peritectic solidification reaction, the necessary solutes are provided through liquid in the SmBCO melt process instead of by solid diffusion, as shown in Figure 14. A model based on limited diffusion in the liquid has been proposed by Izumi *et al.* [84], which is based on the following assumptions: (a) the limiting factor for the growth rate of the crystal is the rate of Sm diffusion in the liquid; (b) the interface of the growth front is planar and particles are spherical; (c) the peritectic reaction takes place isothermally; (d) the thermo-physical properties are constant and (e) no interaction exists between particles (even between particles of different sizes).

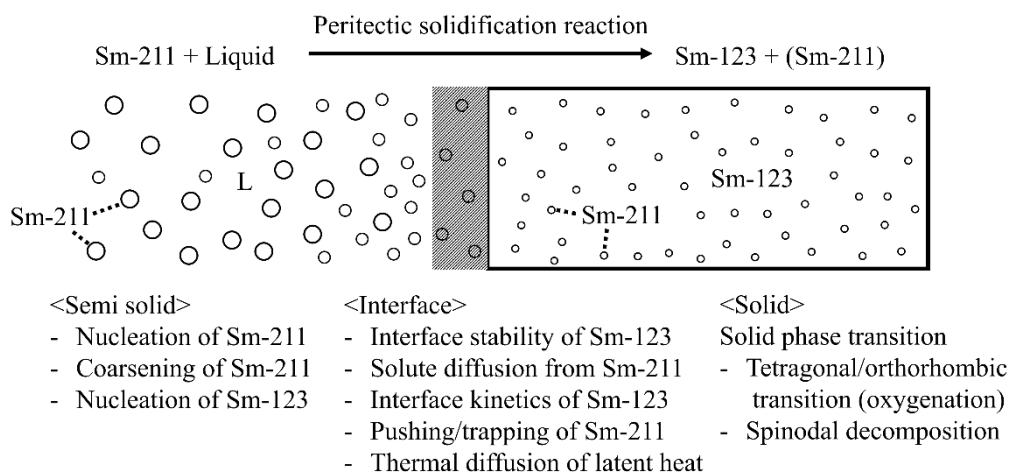


**Figure 14** Dominant phenomena affecting the microstructure of the SmBCO system in TSMG [53].

The driving force in the solute diffusion model is the difference in composition concentration at the interface between the liquid-Sm-211 and liquid-Sm-123 phases. In order to achieve steady growth of the interface, the total samarium flux from Sm-211 should be in equilibrium with the flux necessary for the growth of Sm-123. The principle of the proposed solidification model is illustrated schematically in Figure 15.

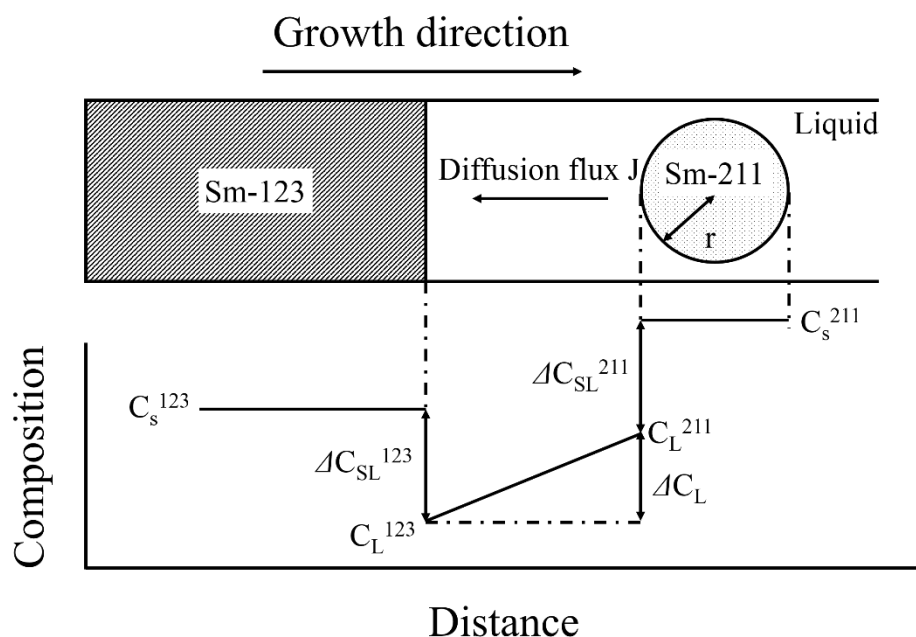


**Figure 15** Illustrative diagram of the principle of the solidification model for the growth of SmBCO: Sm concentration of the Sm-123 and Sm-211 solid ( $C_s^{123}$  and  $C_s^{211}$ ), Sm concentration of the Sm-123 and Sm-211 liquid ( $C_L^{123}$  and  $C_L^{211}$ ), Sm composition difference at Sm-123 and Sm-211 solid-liquid interface ( $\Delta C_{SL}^{123}$  and  $\Delta C_{SL}^{211}$ ) and flux liquid concentration difference ( $\Delta C_L$ ) [85].

Research shows that this model predicts that a higher balanced velocity for the continuous steady growth of crystals can be obtained under conditions of large undercooling and/or a smaller average particle size in the initial size distribution [55].

### 3.2.1.2. Pushing / trapping Theory

The macrosegregation and the size distribution of Sm-211 particles in the Sm-123 superconducting phase matrix are found to depend critically on the growth rate and growth

direction. Endo *et al.* [53] observed that these phenomena are similar to the pushing/trapping behaviour of foreign particles at an advancing solid/liquid interface during solidification. The interaction results in the application of a force to the particle, which, in turn, results in the particle being pushed along the solidification front or becoming trapped in the solid. Figure 16 is a schematic illustration showing a particle in front of the solid/liquid interface and the forces acting on the particle.

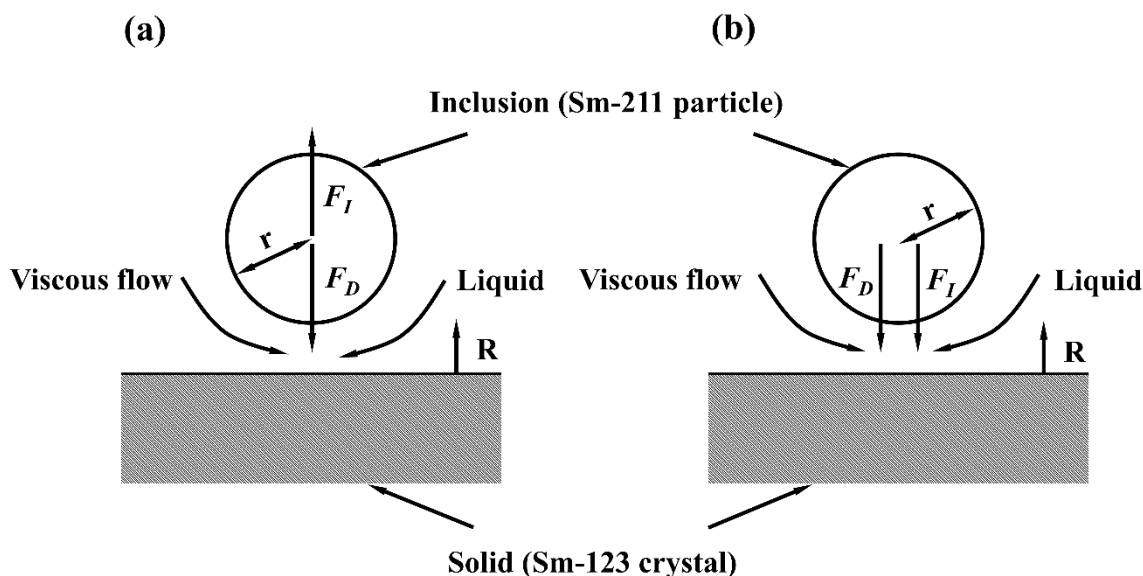


**Figure 16** Schematic illustration showing a particle in front of the solid-liquid interface and the condition necessary for particle pushing: (a) for  $\Delta\sigma_0 > 0$ , the force ( $F_I$ ) due to the interfacial energy ( $\Delta\sigma_0$ ) is conducive to pushing; (b) for  $\Delta\sigma_0 < 0$ , the force ( $F_I$ ) is conducive to trapping. The drag force ( $F_D$ ) is always conducive to trapping [53].

Here, we considered two dominant forces: (a) drag force ( $F_D$ ), due to viscous flow around the particle, which moves along with the interface at  $R$  relative to the melt; and (b) the force ( $F_I$ ) due to interfacial energy ( $\Delta\sigma_0$ ), which occurs as the interface approaches sufficiently close to the particle.

First, the interface energy ( $\Delta\sigma_0$ ) is discussed in the Sm-123/Sm-211 system and is defined as follows:

$$\Delta\sigma_0 = \Delta\sigma_{SP} - \Delta\sigma_{LP} - \Delta\sigma_{SL} \quad (3-1)$$

where  $\Delta\sigma_{SP}$ ,  $\Delta\sigma_{LP}$ , and  $\Delta\sigma_{SL}$  are the solid/particle, liquid/particle and solid/liquid surface energies, respectively.  $F_I$  is conducive to pushing if  $\Delta\sigma_0 > 0$ , while  $F_D$  is always conducive to

trapping. Therefore, the relation,  $\Delta\sigma_0 > 0$ , should be satisfied if Sm-211 particles are pushed ahead of the solid Sm-123 growth front. From the results of observing the microstructure in the melt-growth process, such as unidirectional solidification and undercooling solidification with top seeding, it is clear that the Sm-123 heterogeneous nucleation rarely takes place on the surface of Sm-211 particles in the supersaturated liquid, which suggests the relation  $\Delta\sigma_0 > 0$  holds in the Sm-123/Sm-211 system [53].

According to the pushing/trapping theory, the critical size ( $r^*$ ) of a particle, which is trapped by a solid, is determined roughly by a critical growth rate ( $R^*$ ) and interfacial energy ( $\Delta\sigma_0$ ), such that:

$$R^* \propto \Delta\sigma_0 \cdot [\eta \cdot (r^*)^n]^{-1} \quad (3-2)$$

where  $\eta$  is melt viscosity and  $n$  is an exponent ranging from 1 to 2.

To explain qualitatively the macrosegregation of Sm-211 as a function of growth rate ( $R$ ) and growth direction, the relationship between  $R$  and undercooling ( $\Delta T$ ) will be discussed further. In the case of smaller  $\Delta T$ , the critical radius ( $r_a^*$ ) of a Sm-211 particle for  $a$ -direction growth is smaller than  $r_c^*$  because of the anisotropy of growth rate and the assumption of positive  $\Delta\sigma_0$ . Therefore, the number of Sm-211 particles trapped by a Sm-123 crystal grown along the  $a$ -direction is larger than that along the  $c$ -direction due to the difference between  $r_a^*$  and  $r_c^*$ . The critical radii,  $r_a^*$  and  $r_c^*$ , at smaller  $\Delta T$  are considered to be relatively large in the size distribution of Sm-211 particles dispersed in front of the interface because the total volume fraction of Sm-211 particles is much less than the theoretical values for both growth directions.

In the case of larger  $\Delta T$ , the growth rates for both directions are increased, leading to a decrease in both  $r_a^*$  and  $r_c^*$ . Accordingly, even smaller Sm-211 particles, which were pushed at smaller  $\Delta T$ , are trapped by the Sm-123 matrix. There is an anomalous excess of Sm-211 volume fraction in both directions at larger  $\Delta T$ . From the relationship between the experimental total volume fractions,  $r_a^*$  and  $r_c^*$  for larger  $\Delta T$  could be speculated to be smaller than the smallest radius of Sm-211 particles in front of the interface [49].

However, one should be careful when applying the pushing/trapping theory to the Sm-123/Sm-211 system because this theory was proposed for inactive inclusions in solid and nonfaceted materials. In SmBCO growth, Sm-211 particles form active inclusions because they supply Sm-solute to Sm-123 by self-decomposition and, furthermore, SmBCO materials

grow with a facet. For example, it is possible that a quite different process takes place; i.e., the Sm-211 particles pushed out by the Sm-123 matrix are expected to become smaller due to self-decomposition in the process of supplying Sm-solute to SmBCO and/or become larger due to coarsening. In other words, the Sm-123/Sm-211 system should be treated more carefully by taking all the processes into account instead of just applying the pushing/trapping theory, and especially in combination with the diffusion model described in Section 3.2.1.1.

### 3.2.2. Oxygenation

As-grown SmBCO single grains are not superconducting after TSMG since the residual oxygen content of the lattice is too low. A post annealing oxygenation process at a temperature between 360 °C and 380 °C in pure oxygen atmosphere is therefore required to complete the transformation to the superconducting orthorhombic phase. Oxygenation is a diffusion-based reaction and therefore is difficult to achieve completely, particularly in large, dense and highly textured bulk samples. As a result, typical oxygenation times vary from several hours to several weeks, depending on the size and microstructure of the sample [53].

### 3.2.3. Growth Morphology and Microstructure

The different growth sectors describing the growth morphology of a SmBCO single grain are summarised in Figure 17. Figure 17 (a) shows the top surface of a fully-grown SmBCO single grain in which the  $a/b$ -plane of the seed at the centre of the top surface of the sample. The as-grown SmBCO single grain has grown epitaxially from the seed and exhibits characteristic, well defined four-fold growth symmetry. Figure 17 (c) shows a corresponding schematic diagram of the four  $a/b$ -growth sectors (referred as  $a/b$ -GS) at the top surface of the grain. The four facet lines (where the four  $a/b$ -growth sectors meet) appearing at the top surface of the SmBCO single grain indicate homogeneous and faceted growth. Additionally, Figure 17 (b) shows an SEM image of the cross-section of a fully-grown SmBCO single grain. As indicated in Figure 17 (d),  $c$ -growth sector (known as  $c$ -GS) and two  $a/b$ -GS grow

from the seed that are clearly evident from the sample cross-section. The  $a/c$ -growth sector boundary is where the  $a/b$ -GS and  $c$ -GS meet.

Figure 17 (e) shows an optical micrograph with the magnification of 1000 times of a polished surface of a SmBCO bulk superconductor, which illustrates the Sm-123 single grain embedded with discrete Sm-211 inclusions. In Figure 17 (e), the light green background is the Sm-123 superconducting matrix and the darker green spots of different sizes are the Sm-211 particle inclusions. Although the distribution of Sm-211 particles in the precursor powders is uniform before the TSMG process, the phenomenon of macro-segregation of Sm-211 inclusions in bulk SmBCO superconductors has been observed, which results directly in an inhomogeneous distribution of  $J_c$  throughout the bulk sample, similar to that observed in the YBCO system [86] [87] [88]. In addition, the randomly-occurring defects, such as cracks and pores, are marked in Figure 17 (f), which are seen commonly in the microstructures of TSMG-processed SmBCO single grains.

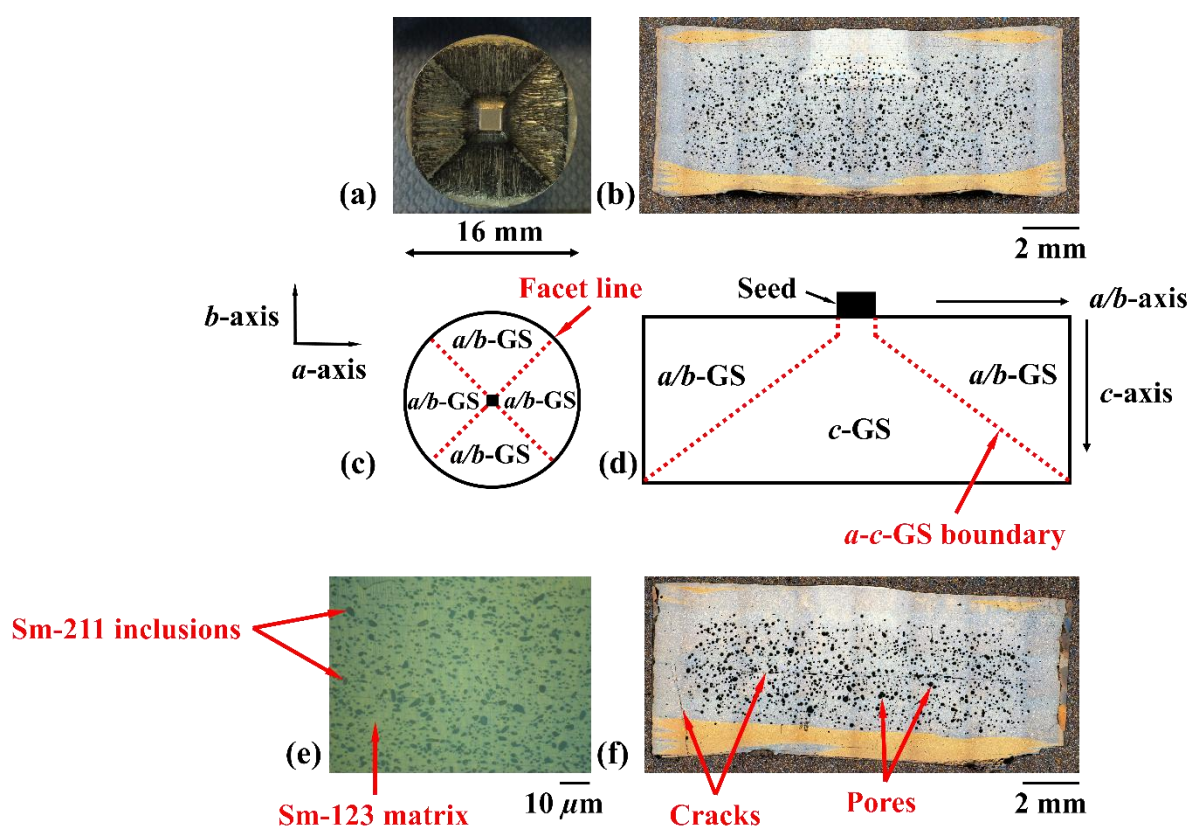


**Figure 17** (a) Photograph of the top surface of a fully-grown SmBCO single grain; (b) an SEM image of a cross section view of a fully-grown SmBCO single grain; (c) schematic diagram of the growth sectors from the top view; (d) schematic diagram of the growth sectors on the cross-section of the SmBCO sample; (e) optical micrograph with the magnification of 1000 times of a polished surface of SmBCO superconductor marked with Sm-123 matrix and

Sm-211 inclusions and (f) an SEM image of a cross section view of a fully-grown SmBCO single grain marked with the positions of cracks and pores.

### **3.2.4. Critical Current Density $J_c$ -related Properties of TSMG-processed SmBCO Bulk Single Grains**

#### **3.2.4.1. Secondary Peak Effect**

SmBCO, discussed in Chapter 2, exhibits a secondary peak effect in a fishtail shape as illustrated in Figures 9 (2a) and (2b), which results from enhanced  $J_c$  at intermediate fields compared to melt-processed YBCO. The peak effect is believed to originate from local oxygen-deficient regions in the SmBCO microstructure, and is also attributed to field-induced pinning. During TSMG, SmBCO tends to form a  $\text{Sm}_{1+x}\text{Ba}_{2-x}\text{Cu}_3\text{O}_{7-\delta}$  solid solution (Sm-123ss), in which  $T_c$  is depressed with the increasing Sm content, represented by the value of  $x$  in the chemical formula. The Sm/Ba substitution is believed to be responsible for the observed field-induced flux pinning and thus the secondary (fishtail) peak effect in SmBCO. In addition, even if SmBCO is fully oxygenated, the oxygen site disorder on the Cu-O chain in the Sm/Ba-substituted regions is still unavoidable since the trivalent  $\text{Sm}^{3+}$  ion in the bivalent  $\text{Ba}^{2+}$  site requires extra oxygen at the anti-chain site to satisfy conditions of charge neutrality. Therefore, as long as this type of local inhomogeneity is present, the secondary peak effect in SmBCO will be observed, even after full oxygenation of the sample [89].

#### **3.2.4.2. Effects of Sm-211 Inclusions**

One of the most commonly discussed pinning effects in the SmBCO system is associated with Sm-211 particles, which disperse in the Sm-123 matrix and contribute significantly to the enhancement of  $J_c$ . Controlling the content, distribution and size of the Sm-211 particles in the microstructure of TSMG-processed SmBCO is one of the most effective approaches to enhance  $J_c$  in the SmBCO system. Interfacial pinning between the superconducting Sm-123

phase matrix and the Sm-211 inclusions is undoubtedly the origin of the enhancement of the superconducting properties; other indirect effects have also been suggested, such as the increase of the dislocation density in the vicinity of the Sm-211 particles or the modification of the twin structure and density [90] [91] [92] .

### **3.2.4.3. Effects of Dopants**

The effects of a dopant such as Pt or Ce on the TSMG growth process is related mainly to the SmBCO growth conditions by the modification of the composition of the molten state (Sm-211 morphology and dissolution, interfacial energies and kinetics and viscosity of the melt, *etc.*). This, in turn, leads to a modification of the growth rate in both the *a/b*-planes and the *c*-direction, which results in an improved microstructure of the SmBCO single grain. With the introduction of such dopants to the nominal precursor compositions, some phases may be formed or the superconducting Sm-123 phase matrix might incorporate these doping elements. As a consequence,  $T_c$  of the fully processed grain will be affected. The second point to be noted is that the doping level should be adjusted for each dopant and process in order to optimize its effectiveness and to achieve a compromise between  $T_c$  and  $J_c$  [55]. More details relating to dopants in the SmBCO system will be discussed further in Chapter 5.

### **3.2.4.4. Improvement of Mechanical Properties of TSMG-processed SmBCO Bulk Single Grains**

In general, the mechanical properties of TSMG processed SmBCO bulk single grains are poor. In particular, cracks across the *a/b*-planes are observed frequently in the Sm-123 superconducting phase matrix [93] in addition to cracks parallel to *a/b*-planes, which is similar to the YBCO system. One of the most effective ways of improving the mechanical properties of bulk single grains is the resin impregnation technique. When a SmBCO bulk single grain is immersed in molten resin under a partial vacuum, resin can penetrate, or back-fill, into the bulk interior through the surface cracks, and fill any open, connected porosity [94]. In addition to the resin impregnation, a more commonly employed approach improving

the mechanical properties is by the addition of silver. Ag particles dispersed in the Sm-123 matrix can improve the mechanical properties significantly without deteriorating the superconducting properties of SmBCO bulk single grains, which can be achieved by adding  $\text{Ag}_2\text{O}$  to the nominal precursor powders.

In summary, SmBCO superconducting bulk single grains with high  $T_c$  and  $J_c$  are potential candidates for practical applications, given their characteristic peak effect properties in relatively high applied magnetic field and their high irreversibility field. Therefore, the fabrication of SmBCO bulk single grains without grain boundaries and with superior superconducting properties is the primary goal of this research.

### **3.3. Characterisation Techniques**

The experimental analysis of bulk SmBCO superconductors in this thesis has been achieved through various characterisation techniques. Microstructural observation techniques include optical microscopy and scanning electron microscopy (SEM). The superconducting characterisation techniques include the measurement of  $T_c$  and  $J_c$  by a Superconducting Quantum Interference Device (SQUID) magnetometer and trapped field scanning by a rotary Hall probe device. In addition, thermoanalytic characterisation was performed mainly by differential thermal analysis (DTA) and chemical composition analysis was achieved by a combination of energy dispersive x-ray spectrometry (EDX), X-ray powder diffraction (XRD) and electron probe micro-analysis (EPMA). These techniques are described briefly in this section.

### **3.3.1. Microstructural Observation Techniques**

#### **3.3.1.1. Optical Microscopy**

Optical microscopy was used to examine the size and distribution of the secondary particles in the as-grown SmBCO single grains, along both the  $a/b$ - and  $c$ - axes. The as-prepared superconducting pellets were cut into two halves along the  $c$ -axis through the seed and the exposed cross-section was polished sequentially using 120, 220, 320, 800, 1000, 1200 and 2400 grit SiC papers. Further polishing was achieved by using 3  $\mu\text{m}$  and 1  $\mu\text{m}$  diamond spray. A Nikon Eclipse ME600 optical microscope was used to observe the microstructures of the exposed cross-sections.

#### **3.3.1.2. Scanning Electron Microscopy (SEM)**

A scanning electron microscope (SEM) produces images of a sample by scanning it with a focused beam of electrons. The electrons interact with atoms in the sample, producing various signals that contain information about the sample's surface topography and composition. Therefore, in this thesis, SEM was used to investigate the microstructure of each SmBCO specimen by scanning the prepared cross-sections of the single grain samples.

### **3.3.2. Superconducting Characterisation Techniques**

#### **3.3.2.1. Measurement of $T_c$ and $J_c$**

The spatial changes in  $T_c$  and  $J_c$  of the specimens were measured using a Superconducting Quantum Interference Device (SQUID) MPMS XL magnetometer. The MPMS XL SQUID system is capable of measuring very small magnetic moments with a nominal sensitivity of

$1 \times 10^{-11} \text{ A m}^2$ . The range of the measurement temperature is from 1.9 K to room temperature and the magnetic field induction is  $\pm 7 \text{ T}$ .

The samples to be measured were cut into slices across their centre, with each slice being cut into smaller specimens, as shown schematically in Figure 18. A field of 0.002 T was applied to the samples after zero-field-cooling prior to the measurement of  $T_c$ . The extended Bean critical state model [62] was used to calculate  $J_c$  at 77 K from the measured magnetic hysteresis loops ( $M-H$  loops).

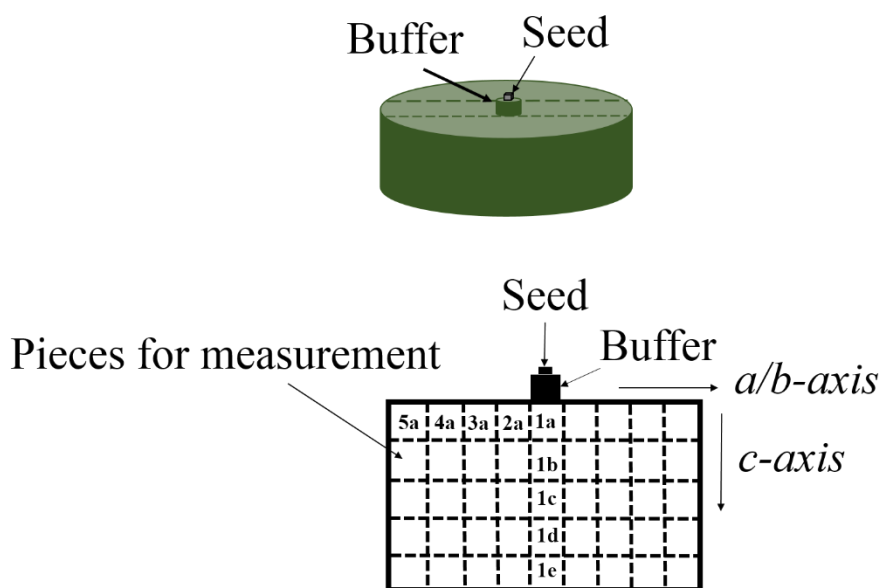


**Figure 18** Schematic illustration of the section geometry for the preparation of the specimens for SQUID magnetometry.

### 3.3.2.2. Trapped Field Measurement

The measurement of the field trapping ability of bulk SmBCO superconductors at 77 K is particularly important in determining the potential of these materials for high field, permanent magnet applications. Both the magnitude and the distribution of the trapped field are important for this purpose. The maximum trapped field of the sample indicates how well the superconductor will perform in an application. The mapping of the trapped field distribution on the surface of the sample is also a simple way of detecting if large cracks, grain boundaries or parasitic grain nucleation are present within the sample.

The measurements of trapped magnetic field were carried out by magnetizing the bulk samples with an electromagnet. Firstly, the bulk samples were cooled to 77 K by liquid nitrogen in a magnetic field of 1.3 T applied parallel to the *c*-axis and held there for 15 min. After switching off the external magnetic field, the trapped field profile was measured by a Hall probe in liquid nitrogen bath with a total gap between the top surface of the sample and the active area of the Hall sensor of 0.5 mm. Two-dimensional (2D) contour maps of the trapped field distribution were then generated by a rotating array of 18 Hall probes and plotted using Origin software.

### **3.3.3. Thermoanalytic Characterisation Technique: Differential Thermal Analysis (DTA)**

Differential thermal analysis (DTA) was performed in order to determine the growth-related temperatures in the heating profile used in the top-seeded melt growth (TSMG) process in this thesis. DTA, as a thermoanalytic technique, can detect exothermic or endothermic changes in the sample relative to an inert reference sample. Thus, DTA generates data on the transformations that have occurred, such as melting and crystallization, as the sample is heated and cooled over a wide temperature range. The area under a DTA peak represents the enthalpy change and is not affected by the heat capacity of the sample.

Pellets of diameter equal to their thickness (3 mm) were prepared for the DTA measurements in this thesis. A small, generic seed was placed at the centre of the top surface of the small pellet sample during this measurement to simulate the TSMG process at elevated temperatures.

### **3.3.4. Chemical-analytic Characterisation Techniques**

#### **3.3.4.1. Energy Dispersive X-ray Spectrometry (EDX)**

Energy dispersive X-ray spectrometry (EDX), which is based on an interaction between source of X-ray excitation and the measured sample, was performed simultaneously with SEM for elemental analysis and chemical characterization of a SmBCO sample through a cross-sectional scan. In general, EDX is capable of generating both qualitative and quantitative analysis, elemental mapping and line profile analysis as long as the sample is compatible with a moderate vacuum atmosphere and can be accommodated on the sample stage. As a result, it is applied widely to detect and analyse the presence of foreign components, corrosion evaluation, coating composition, rapid material alloy identification, small component material and phase identification and distribution [55]. In this thesis, alien chemical phases in the matrix of SmBCO were identified through qualitative analysis by scanning the cross-section of a SmBCO sample.

#### **3.3.4.2. X-ray Diffraction (XRD)**

X-ray powder diffraction (XRD) is used to determine the atomic and molecular structure of a crystalline structure, and, in this study, was performed by a SIEMENS Diffractometer D500 to confirm the formation of a crystal single phase. The International Centre for Diffraction Data Database was employed in this thesis to identify specific phases. Although XRD has its limitations, such as increased sensitivity to a homogeneous and single phase of an unknown material with the requirement to access to a standard reference file, knowledge of the sample weight and a difficulty to detect low amount of components in a mixed material [55], the technique was, nevertheless, used effectively to determine a newly synthesized phase through measurements on repeatedly ground sample powders in this study.

### 3.3.4.3. Electron Probe Micro-analyser (EPMA)

An electron probe micro-analyser (EPMA) is an analytical tool used commonly to determine non-destructively the chemical composition of micron-sized volumes at the surface of a solid material with a sensitivity at the level of ppm. It is the most precise and accurate micro-analysis technique available and all elements from boron to uranium and above can be analyzed. Major applications of this technique are found in the fields of geochemistry, mineralogy, geochronology and materials science including glass, ceramics and superconductors. The nature of wavelength dispersive spectroscopy, its general sensitivity, the ability to analyse light elements and reduced risks of erroneous interpretation of qualitative spectra are the main advantages of EPMA. Spectral resolution and detector dead time are much better than EDX [55]. In this research, detailed analysis of the chemical composition of the Sm-123 matrix, from the seed along the *c*-axis was carried out using EPMA (CAMECA SX 100).

## 3.4. Summary

Chapters 2 and 3 have summarised the theoretical fundamentals pertinent to superconductivity and the SmBCO system. Chapters 4, 5 and 6 will present the experiments and the corresponding results to address the problems in SmBCO bulk superconductors, such as low seeding reliability, severe substitution of Sm on Ba site and poor mechanical strength. The next chapter will present an overview of the modified seed technique termed as buffer-aided top seeded melt growth technique which improved the success rate of the single grain growth of SmBCO significantly.

# **CHAPTER 4**

## **MODIFIED SEEDING TECHNIQUE USING A MGO-NDBCO GENERIC SEED BY EMPLOYING A BUFFER LAYER**

### **4.1. Introduction and Motivation**

In general, the processing conditions of the SmBCO system are more complex than those for the YBCO system, due primarily to the high melting temperature of the precursor powders, rapid growth rate, which is difficult to control, and the need to process the material under reduced oxygen partial pressure to inhibit the substitution of Sm on the Ba site in the superconducting SmBCO phase matrix [6]. Therefore, initially, an oxygen controlled melt growth (OCMG) process was developed for the growth of SmBCO, based on a peritectic solidification reaction in which oxygen partial pressure is controlled accurately down to  $10^3$  Pa [95]. However, practically speaking, the OCMG process requires a specially-designed and expensive furnace to maintain the reduced oxygen atmosphere, which limits the feasibility of the process. As a result, the most challenging issue for the SmBCO system is to grow a single grain bulk sample in air using a conventional box furnace with appropriate superconducting properties for high field engineering applications.

The process used most commonly to realise ambient- $O_2$ -pressure growth is the top seeded melt growth (TSMG) technique, which consists generally of the preparation of precursor powders, pre-form pressing, the selection of a suitable seed, control of the seeding process, single grain nucleation and growth via a controlled peritectic solidification reaction during slow cooling and, finally, post oxygenation to drive the non-superconducting tetragonal phase into the superconducting orthorhombic phase.

Every step in the TSMG process is essential to grow a single grain sample successfully. Seeding contributes most critically to the growth success, meaning that, at the same time, it is also the most common mechanism of failure of the entire TSMG process. Hence, it is far from an exaggeration to say that choosing an appropriate seed is the very first step in developing an effective TSMG process. A single crystal that can provide a nucleation centre where the crystal orientation of the growth matches that of the nucleation source is usually referred to as a seed [96]. Since the formation of a granular microstructure can limit the induced current circulation, it is necessary to grow SmBCO bulk single grains that do not contain grain boundaries using a seed crystal with a similar lattice constant to Sm-123, but with a higher melting point [83].

Generally speaking, the seeding process takes place over a range of temperatures between the melting temperature  $T_{\max}$ , which is the highest temperature used in TSMG heating profile and  $T_{g1}$ , which is the temperature at which slow cooling commences and at which single grain growth begins. The seeding process in TSMG is generally achieved in two ways; via hot-seeding and cold-seeding techniques. In a hot-seeding technique, a seed is placed on the sample after the melting stage of the process to self-seed grain growth (between  $T_{\max}$  and  $T_{g1}$ ) in a specially designed furnace, while, in a cold-seeding technique, a seed crystal is placed on the top surface of the green sample pre-form prior to the heating process in a conventional box furnace.

The seed-choosing principle in a hot-seeding technique is that the structure of the seed crystal is identical to that of the target solidified phase (e.g. an NdBCO seed crystal is used to grow an NdBCO single grain [6]), thereby achieving a perfect crystallographic match, which is also the main advantage of this technique. However, there are various practical difficulties in the hot-seeding technique, such as special requirements for a furnace and careful control of the processing atmosphere at elevated temperatures of over 1000 °C during the peritectic solidification reaction.

A typical heating process for a cold-seeding process is shown in Figure 19. A reliable cold-seeding process would require the seed itself to retain its integrity (both structurally and chemically) for a duration of several hours at elevated temperatures and throughout the TSMG process. As a result, the melting temperature of the seed crystal required is necessarily higher than  $T_{\max}$  of the thermal process. In practice, this requires the seed to have a melting temperature that is up to 40 °C higher than the melting/peritectic temperature of the target RE-123 material (i.e. 1070 °C in the SmBCO system).

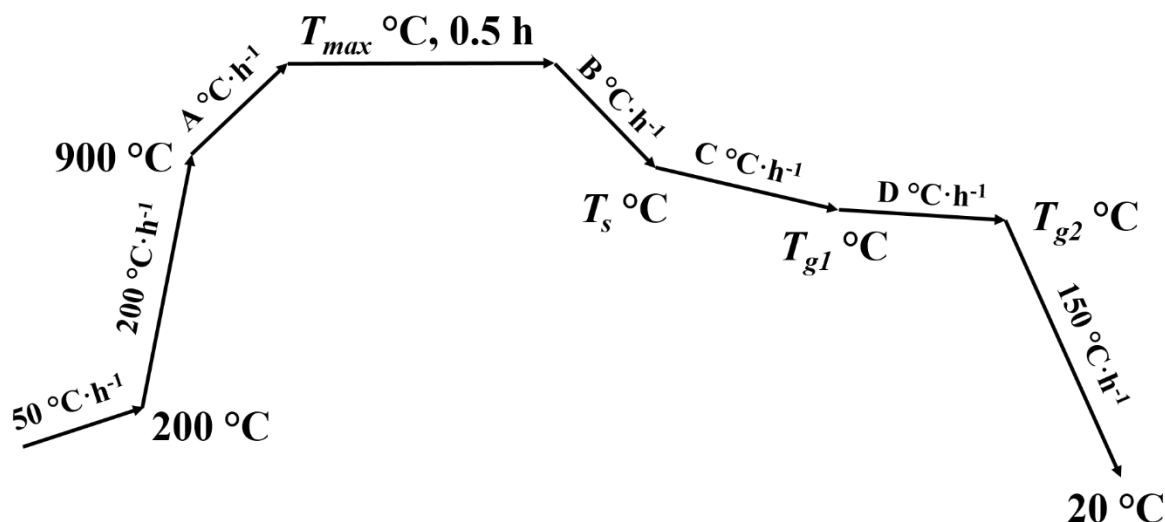


**Figure 19** A typical cold-seeding heating profile used to fabricate SmBCO single grains showing all the growth-related temperatures.  $T_{max}$  is the highest temperature used in the whole heating profile. The integrity of the seed will be maintained as long as the melting temperature of the seeding material is higher than  $T_{max}$ .

Of these two techniques, the cold-seeding method is used most widely to process single grains with the required orientation due to its flexibility, simplicity and low technical requirement for the furnace, and, therefore, is often adopted for batch processing of bulk single grain superconductors. However, the cold-seeding method also limits flexibility of the parameters in the melt process.  $T_{max}$  is required to be lower than the melting temperature of the selected seed crystal to avoid the decomposition of the seed during TSMG, and higher than  $T_p$  of the starting composition to enable thorough decomposition of the precursor powders. At the same time, this technique requires a careful adjustment of the heating profile, since there is the possibility that the seed may be partially dissolved at temperatures below its melting point [97]. At high temperatures, the seed melts partially at its interface with the SmBCO precursor pellet, so contact with the bulk pre-form may lead to contamination of the seeding material and consequently lower the melting temperature of the seed, which results in dissolving and/or the deterioration of the seed. A minimum thickness of 100  $\mu\text{m}$  is required, therefore, for the seed crystal to retain its integrity [98] to avoid such a problem.

There are three main different seeding materials for single-grain growth for the SmBCO system, which are MgO single crystals, MgO-NdBCO generic seeds and Nd(Sm)BCO thin film seeds. Due to the high melting temperature of the SmBCO precursor powders, MgO single crystals, in view of their relatively high peritectic temperatures, were used initially to

grow large SmBCO single grains in the absence of a more suitable seed [99]. However, reliable orientation control of the seeded grain cannot be achieved by employing MgO single crystals as a seeding material due to the relatively large lattice mismatch between the MgO single crystal and SmBCO matrix (typically > 20%).

Shi *et al.* reported that Mg-doping enhances the decomposition temperature of NdBCO single crystals, which were used subsequently as generic seeds for cold seeding of SmBCO [100]. The composition of a so-called generic seed is MgO-doped NdBa<sub>2</sub>Cu<sub>3</sub>O<sub>7- $\delta$</sub>  (abbreviated as MgO-NdBCO), which can simplify the fabrication of SmBCO superconducting bulk single grains since it allows SmBCO to grow under a more practical air atmosphere. Normally, during the sample growth, the *a/b*-plane of the seed crystal should be aligned parallel to the top surface of the pellet pre-form to obtain the desired grain orientation. To summarise the merits of generic seeds, they have higher melting points, good lattice matching parameters, good chemical stabilities and can be produced in relatively large numbers at low cost [100].

Therefore, in principle MgO-NdBCO generic seeds can be used as seeding materials to grow bulk SmBCO in air to overcome the high melting temperature of the bulk precursor powders. However, although MgO-NdBCO generic seeds can achieve improved growth orientation, it is difficult to choose an appropriate seed for the synthesis of a bulk single grain. Essentially, seeds are cleaved from a multi-grain MgO-NdBCO bulk sample fabricated by an unseeded melt growth process. In addition, the seed should not be too thin or too small. However, even though the seed may appear to be flawless optically, it may still fail to nucleate a single grain due, for example, to contamination by the target bulk composition. As a result, the seed-choosing process requires skill and is consequently time-consuming. Furthermore, the cause of growth failure due to poor seed quality is not usually obvious, and leads inevitably to precursor-powder waste. Hence, improving the reliability of the seeding process is an urgent requirement of the TSMG process.

It has been reported that NdBCO and SmBCO thin films grown on MgO substrates are suitable for use as cold seeds due to their superheating properties [99] and that YBCO/NdBCO/MgO thin film seeds can survive a  $T_{\max}$  in excess of 1120 °C [101]. These thin film seeds can assist the growth of SmBCO to produce single grains with well controlled orientation and provide superior  $T_p$ , minimal lattice misfit and high crystallinity, although they are generally more expensive when compared to MgO-NdBCO generic seeds [99].

Consequently, to overcome the seeding problems in the cold-seeding technique described above, several authors, including Kim *et al.* [102], Yao *et al.* [101] and Zhou *et al.* [103], have reported a method in which a small pellet is inserted between the seed and the bulk pre-form in other (RE)BCO systems. This method has proved to be effective in inhibiting the diffusion of elements from the seed into the bulk sample, and vice versa, and is able to accommodate lattice mismatch between a seed and the precursor pellet [103]. Even so, relatively few attempts have been reported to apply such a technique to the SmBCO system. To date, no research on the large scale production processes of SmBCO has succeeded and the reliability of the buffers has yet to be established.

The buffer technique is employed in this study for the growth of SmBCO samples and, as a result, the success rate of the growth process has been improved significantly. Single domain, bulk SmBCO samples have been fabricated successfully in air by a TSMG process using a conventional chamber furnace. In order to improve the reliability of seeding, buffers of different compositions have been used to increase the success rate of the SmBCO single grain growth. The geometric configurations of the buffers are discussed, and SmBCO single grains of various dimensions fabricated successfully using the optimised buffer layer technique. Furthermore, the superconducting properties,  $T_c$  and  $J_c$ , of the specimens, and directly under the buffer layer, in particular, have been investigated to establish the advantages of this technique. Finally, the trapped fields of SmBCO single grains synthesized with and without buffer layers have been measured and compared.

## 4.2. Experimental

### 4.2.1. Production of SmBCO Single Grains in Air by Cold Seeding

Precursor powders were prepared using commercially available Sm-123 (TOSHIMA, average particle size: 2-3  $\mu\text{m}$ ), Sm-211 (TOSHIMA, average particle size: 1-2  $\mu\text{m}$ ), BaO<sub>2</sub> (ALDRICH, purity 95 %; to suppress Sm/Ba substitution [70]) and CeO<sub>2</sub> (Alfa Aesar, purity 99.9 %; to refine Sm-211 particles [104]) powders. A motorized pestle and mortar was used to mix

thoroughly powders of composition (75 wt. % Sm-123 + 25 wt. % Sm-211) + 2 wt. % BaO<sub>2</sub> + 1 wt. % CeO<sub>2</sub>, prior to being pressed uniaxially under a load of 1.5 tons into a green pre-form (pellet-like) with diameters of 20 mm and 25 mm and thicknesses of 9 mm and 12.5 mm (each pellet shrinks to about 80 % of its original size after TSMG, corresponding to as-processed dimensions of 16 mm and 20 mm diameter and 7 mm and 10 mm thickness).

Buffers with three different compositions, as summarized in Table 2, were prepared in this research using commercially available Sm-123 (TOSHIMA, average particle size: 2-3 μm), Sm-211(TOSHIMA, average particle size: 1-2 μm), BaO<sub>2</sub> (ALDRICH, purity 95 %) and CeO<sub>2</sub> (Alfa Aesar, purity 99.9 %) powders with different combinations to obtain the target compositions. Sm-211 buffers contain only commercially available Sm-211 powders, whereas SmBCO buffers are small pellets of identical composition to the bulk pre-form. Sm-123 + Sm-211 mixed-powder buffers consist of only 75 wt. % Sm-123 and 25 wt. % Sm-211 powders (i.e. without BaO<sub>2</sub> and CeO<sub>2</sub> compared to the SmBCO buffers). A motorized pestle and mortar was again used to mix the powders of different compositions thoroughly, prior to being pressed uniaxially under a load of 0.5 tons into small green pre-forms with the dimensions listed in Table 3.

**Table 2** Different compositions of mixed-powder buffers employed in this study.

Buffers	Buffer constituent powders			
	Sm-123	Sm-211	BaO <sub>2</sub>	CeO <sub>2</sub>
Sm-211 buffers	×	√	×	×
SmBCO buffers	√	√	√	√
Sm-123 + Sm-211 mixed-powder buffers	√	√	×	×

**Table 3** Different geometric configurations of the buffers employed in this study.

No.	Diameter / mm	Thickness / mm	Ratio of diameter to thickness
1	5.0	5.0	1
2	3.0	1.5	2
3	3.0	3.0	1
4	3.0	4.5	2/3

The TSMG process was used to fabricate large, single grain SmBCO superconductors. An MgO-NdBCO generic seed was placed with its *a/b*-plane in direct contact with the top of the as-prepared buffer and the arrangement placed at the centre of the upper surface of the sample pre-form, as shown in Figure 21 (a), to yield the required grain orientation.

The heating profile used in this research is shown in Figure 20. The appropriate values of the melting point, grain nucleation, crystallization and the optimum final growth temperatures,  $T_m$ ,  $T_s$ ,  $T_{g1}$  and  $T_{g2}$ , were determined via differential thermal analysis (DTA). The pellet was initially heated slowly at  $50\text{ }^\circ\text{C h}^{-1}$  to  $200\text{ }^\circ\text{C}$  to stabilize the furnace temperature, then more rapidly at a rate of  $200\text{ }^\circ\text{C h}^{-1}$  to  $900\text{ }^\circ\text{C}$ . The temperature was then raised slowly to  $1087\text{ }^\circ\text{C}$  and held for 0.5 hour to ensure sufficient decomposition of the precursor pellet. The partially molten sample was then cooled at  $75\text{ }^\circ\text{C h}^{-1}$  to its seeding temperature, followed by further cooling to its crystallization temperature at  $1075\text{ }^\circ\text{C}$ , then cooled slowly to  $1067\text{ }^\circ\text{C}$  at a rate of  $1\text{ }^\circ\text{C h}^{-1}$ , followed by another slower cooling stage to  $1041\text{ }^\circ\text{C}$  at the rate of  $0.8\text{ }^\circ\text{C h}^{-1}$ . Finally, the sample was furnace cooled to room temperature at a ramping rate of  $150\text{ }^\circ\text{C h}^{-1}$ .

Subsequently, the as-grown SmBCO samples were oxygenated at  $360\text{ }^\circ\text{C}$  for fourteen days to drive the non-superconducting, tetragonal phase to the desired orthorhombic superconducting phase.

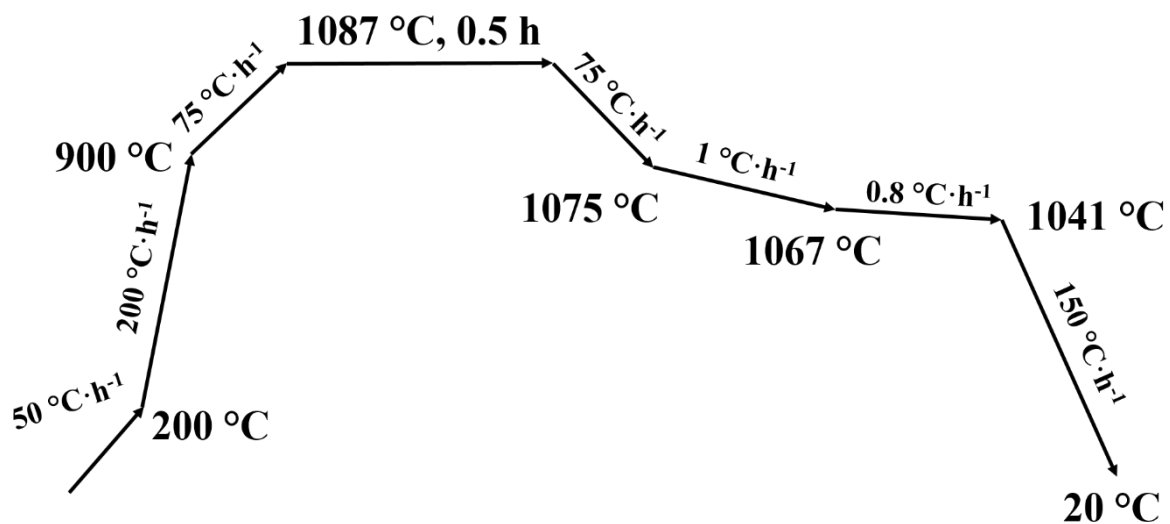


**Figure 20** Schematic illustration of the TSMG process for the fabrication of single grain SmBCO using assorted buffers.

## **4.2.2. Sample Characterisation**

### **4.2.2.1. Differential Thermal Analysis (DTA) and Microstructures of SmBCO Bulk Single Grains Fabricated with and without Buffer Layers**

Differential thermal analysis (DTA) was performed in order to determine the peritectic ( $T_p$ ), seeding ( $T_s$ ), crystallization ( $T_{g1}$ ) and final growth ( $T_{g2}$ ) temperatures in the heating profile used in the TSMG process. A pellet of a same diameter as its thickness of 3 mm (i.e. an aspect ratio of 1) with the same composition as a SmBCO bulk single grain and several small MgO-NdBCO generic seeds were prepared for the DTA measurements. A small, generic seed was placed at the centre of the top surface of the small pellet sample during the measurement to simulate the TSMG process at elevated temperatures.

Optical microscopy was carried out as described in Section 3.3.1.1 to examine the size and distribution of Sm-211 particles in the as-grown SmBCO single grains processed with and without buffer layers, along both the  $a/b$ - and  $c$ - axes.

### **4.2.2.2. Measurements of $T_c$ and $J_c$ of SmBCO Specimens with and without Buffer Layers**

The samples were cut into slices across their centre, with each slice being cut into smaller specimens, as shown schematically in Figure 21 (b). The spatial changes in  $T_c$  and  $J_c$  of the specimens with and without buffer layers with proximity to the seed were measured as described in Section 3.3.2.1.

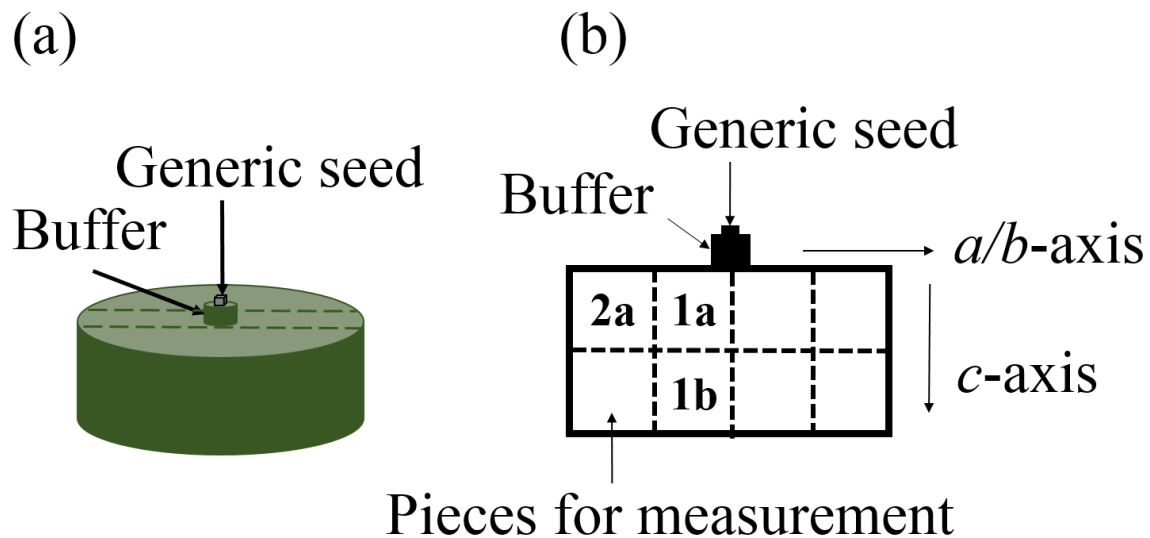


**Figure 21** (a) Schematic illustration of the bulk pre-form with an MgO-NdBCO generic seed on a buffer layer and how each single grain was cut for characterisation. (b) Illustration of the positions of the specimens within the parent bulk used for measuring  $T_c$  and  $J_c$ .

#### 4.2.2.3. Trapped Field Measurement of SmBCO with and without Buffer Layers

Measurements of the trapped magnetic fields of SmBCO with and without buffer layers were carried out by magnetizing the bulk samples with an electromagnet as described in Section 3.3.2.2.

### 4.2.3. Results and Discussion

Figure 22 shows DTA signals of SmBCO pseudo pre-form and MgO-NdBCO generic seeds. For a more accurate comparison,  $T_m$  is interpreted using a peak-temperature obtained from DTA as a benchmark. It can be seen from Figure 22 that the melting temperature of the MgO-NdBCO generic seeds is around 1102.7 °C, which is roughly 31 °C higher than that of the SmBCO pseudo pre-form, which melts at approximately 1071.8 °C. In order to determine the

heating profile,  $T_{max}$  should be set higher than the melting temperature of the SmBCO pre-form to ensure thorough powder melting, but, at the same time, lower than the melting temperature of the generic seed to guarantee the integrity of the seed during melt processing. This principle can be applied to all the TSMG-processed (RE)BCO bulk superconductors.  $T_{max}$  has even been set at around 50 °C higher than the melting temperature of YBCO precursor powders in previous studies, which essentially guarantees complete melting of the precursor powders to achieve successful synthesis of YBCO single grains [105]. However, due to the higher melting temperature of the SmBCO precursor powders,  $T_{max}$  is only 10-20 °C higher than the  $T_p$  of this system, which is another reason why SmBCO is more difficult to grow than YBCO. Therefore, in this chapter,  $T_{max}$  is set at 1087 °C as shown in Figure 20, which is only 15 °C higher than the melting temperature of the SmBCO precursor powders (measured as 1071.8 °C in this research).

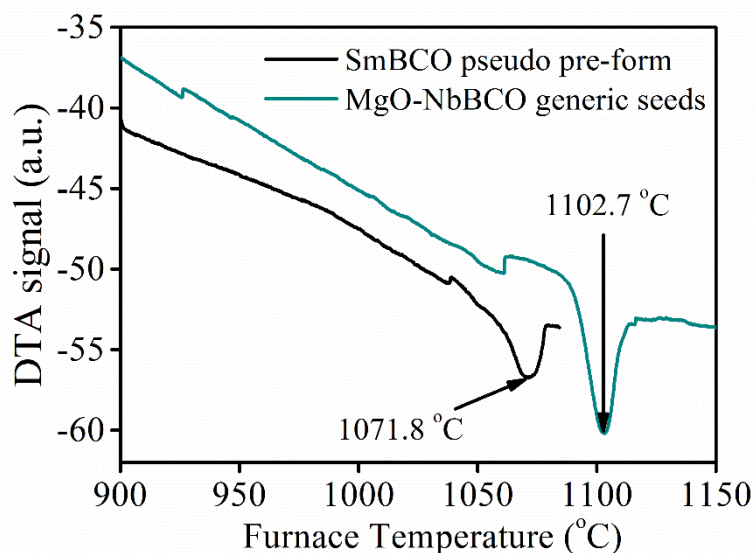


**Figure 22** Differential thermal analysis (DTA) traces of SmBCO pseudo pre-forms and MgO-NdBCO generic seeds.

Figure 23 (a) shows a photograph of the top surface of a SmBCO sample (10 g, 16 mm in diameter) grown successfully using the conventional TSMG process without the assistance of a buffer layer, which is evident from the presence of the four orthogonal growth sector boundaries. Unfortunately, further attempts to melt process samples of 20 g and 20 mm in diameter without buffer layers failed due to the poor performance of the generic seeds, which were cut artificially from the parent multi-grained MgO-NdBCO bulk samples. Buffers of 5 mm in both diameter and thickness with compositions of Sm-211 and SmBCO were used

subsequently to grow SmBCO samples of 16 mm in diameter. Photographs of the top surfaces of these samples are shown in Figures 23 (b) and (c). It can be seen clearly that neither Sm-211 nor SmBCO buffers can be employed to fabricate SmBCO single grains. In Figure 23 (c), four facet lines extended from the generic seed to the edge of the SmBCO buffer, but no further extension from the SmBCO buffer was observed on the surface of the bulk, indicating that a successful nucleation in the buffer does not ensure successful SmBCO single grain growth.

Further trials were made using Sm-123 + Sm-211 mixed powders as buffers to fabricate SmBCO single grains of mass 10 g and diameter 16 mm using buffers of 5 mm and 3 mm in both diameter and thickness, respectively. Photographs of successfully-grown samples in each case are shown in Figures 23 (d) and (e). Photographs in Figures 23 (d) and (e) show improved growth when Sm-123 + Sm-211 mixed-powder buffers are used compared to Sm-211 or SmBCO. Regardless of the buffer dimensions, SmBCO single grains can be formed, although a larger single grain is obtained when a buffer with dimensions of 3 mm in both diameter and thickness is used, rather than a buffer with dimensions of 5 mm in both diameter and thickness.

Samples of mass 20 g and diameter 20 mm were synthesized successfully following the success of fabricating a 10 g, 16 mm SmBCO by using a 3 mm Sm-123 + Sm-211 mixed-powder buffer, as shown in Figure 23 (f). Until this point, it appeared that buffers with dimensions of 3 mm in both diameter and thickness have advantages over buffers with equivalent dimensions of 5 mm when considering SmBCO single grain growth. The optimum geometric configuration of the buffer layer was determined by preparing three different sizes of buffers, as listed in Table 3 as buffers No. 2, 3 and 4. Correspondingly, samples grown using these buffers are shown in Figures 23 (g), (h) and (i). Only in Figure 23 (h) is the sample grown in the form of a SmBCO single grain, with samples in Figures 23 (g) and (i) containing either satellite grains or double facet lines. It can be concluded that buffers with an aspect ratio of 1, *i.e.* where the buffer diameter equals the buffer thickness, is the most beneficial ratio for growing larger, single grain SmBCO bulk superconductors. Buffer layers can, themselves, even grow into small single grains during the TSMG process that can be seen clearly by the naked eye during the fast cooling process at a temperature between  $T_{max}$  and  $T_{gl}$  and prior to the slow cooling process [106]. Importantly, this small, intermediate single grain serves later as an effective seed during the subsequent slow cooling process. In essence, it is significantly easier to form a smaller single grain of 3 mm diameter than a larger

one (5 mm diameter), which explains why a 3 mm buffer has higher success rate for the growth of SmBCO single grains.

It may be concluded from the successful and failed attempts to grow SmBCO samples with or without buffer layers that to achieve a growth of a single grain, the melting temperature of a buffer layer used should be higher than the melting temperature of the SmBCO precursor powders, while at the same time, with a composition as similar as possible to that of the target bulk single grains. The SmBCO buffer fails because of its identical melting temperature to that of the target grain. To support this assumption, bulk single grains with the same composition of Sm-123 + Sm-211 in the mixed-powder buffer were also grown successfully using the optimized buffer layer, as shown in Figure 23 (j). However, using the same melting temperature between the buffer and the bulk pre-form, the bulk did not grow as well as SmBCO since the melting temperature between the two components is the same. Furthermore, the failure to grow SmBCO using Sm-211 buffers may be attributed to a comparatively larger lattice mismatch. The cumulative effect of the mismatch could extend to several hundred micrometres in the area directly beneath the seed, which might result in the mis-arrangement of the atoms during the process of forming the single grain, causing the seeding process to fail [107].

In conclusion, the observed successful growth of SmBCO single grains with the assistance of buffers suggests that buffer layers effectively form a new 'seed' that overcomes the lattice mismatch between MgO-NdBCO generic seeds and the SmBCO bulk single grain. This also indicates that buffer layers can be used to fabricate SmBCO containing CeO<sub>2</sub> and other dopants, demonstrating that the buffers are relatively insensitive to the presence of impurities within the precursor pellets compared to MgO-NdBCO generic seeds. Therefore, these results demonstrate clearly that the use of optimized buffer layers has the potential to overcome the seeding-based difficulties for the growth of larger SmBCO single grain superconductors and the stabilisation of use of buffer layers enhances significantly the reliability of the MgO-NdBCO generic seeds and is an effective filter of impurities.

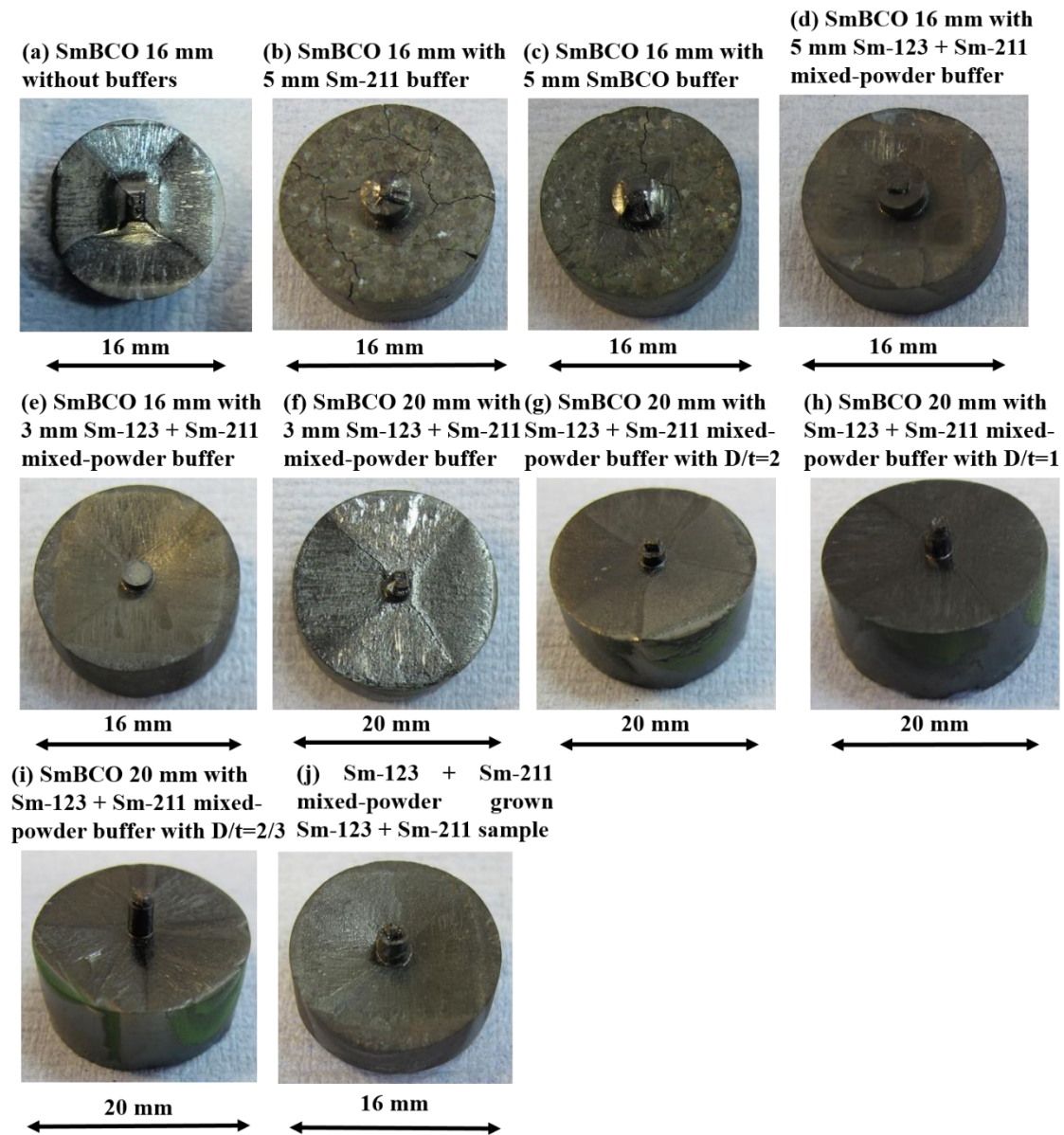


**Figure 23** (a) SmBCO 16 mm in diameter fabricated without buffers; SmBCO 16 mm in diameter fabricated with 5 mm different buffers: (b) a Sm-211 buffer, (c) a SmBCO buffer and (d) a Sm-123 + Sm-211 mixed-powder buffer; (e) SmBCO 16 mm in diameter with a 3 mm Sm-123 + Sm-211 mixed-powder buffer; (f) SmBCO 20 mm in diameter with a 3 mm Sm-123 + Sm-211 mixed-powder buffer; SmBCO 20 mm in diameter with three different sizes of Sm-123 + Sm-211 mixed-powder buffers: (g)  $d=3$  mm,  $t=1.5$  mm, (h)  $d=3$  mm,  $t=3$  mm and (i)  $d=3$  mm,  $t=4.5$  mm; (j) Sm-123 + Sm-211 16 mm in diameter with a 3 mm Sm-123 + Sm-211 mixed-powder buffer.

In order to further investigate the effects of employing buffer layers, SmBCO samples 16 mm in diameter fabricated with and without Sm-123 + Sm-211 mixed-powder buffer layers were

prepared and examined using optical microscopy. Previous research indicates that Y-211 particles tend to distribute from the seed throughout an as-grown single grain bulk sample [105]. Similar distributions of Sm-211 were also observed in SmBCO fabricated with and without buffer layers. Fewer Sm-211 particles are in the vicinity of the seed or the buffer/seed area, since the Sm-211 particles react with the liquid phase to form the Sm-123 phase more extensively in the neighbourhood of the seed or the buffer/seed area [108], whereas more and larger Sm-211 particles appear towards the bottom and circumference of the bulk along both the *a/b*- and the *c*-axes. However, although the size and distribution of Sm-211 particles near the bottom of the bulk single grains are similar, the situation in the vicinity of the seed or the buffer/seed area is moderately different. As illustrated in Figure 24, with the addition of a Sm-123 + Sm-211 mixed-powder buffer layer, more Sm-211 particles are observed under the seed compared to the sample fabricated without the assistance of a buffer. A possible explanation is that with the extra buffer layer thickness, position 1a in buffered SmBCO is equivalent to a slightly lower position in SmBCO fabricated without a buffer, such as position 1b. Consequently, it is reasonable to observe more Sm-211 particles at position 1a in buffered SmBCO, which, in turn, creates a more homogeneous distribution of Sm-211 particles throughout the sample.

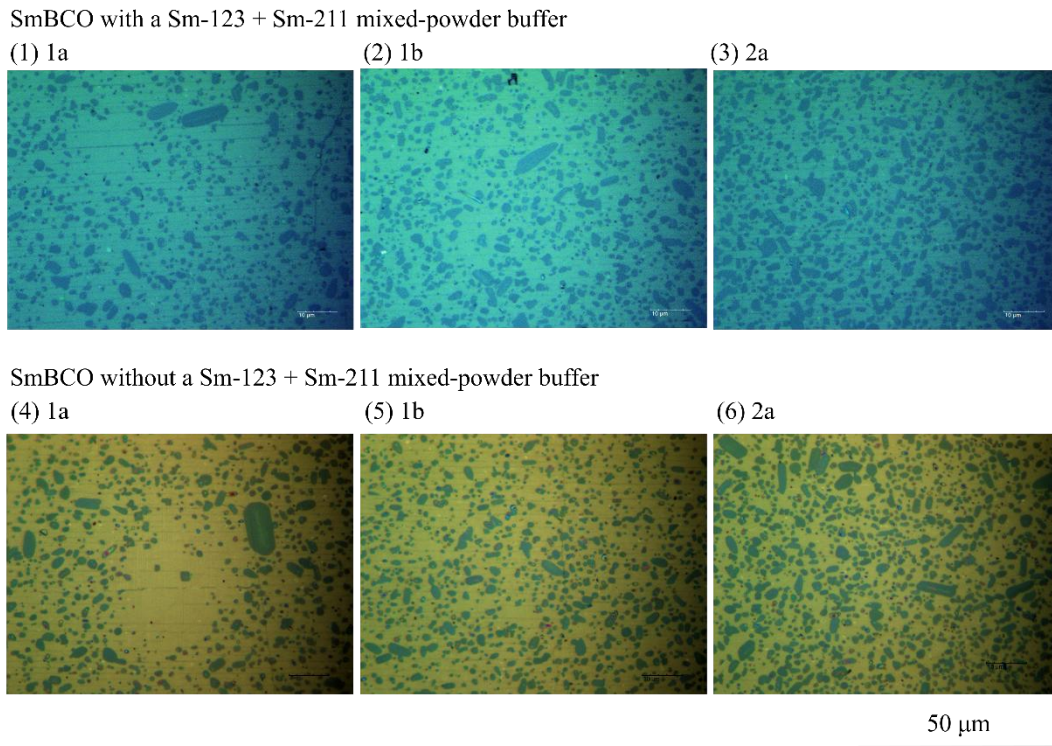


**Figure 24** Micrographs at positions illustrated in Figure 21 (b) showing the Sm-211 distribution and particle size in the SmBCO matrix with and without Sm-123 + Sm-211 mixed-powder buffer layers: with the magnification of 1000 times: SmBCO with a Sm-123 + Sm-211 mixed-powder buffer layer at positions at: (1) 1a, (2) 1b and (3) 2a and SmBCO without a Sm-123 + Sm-211 mixed-powder buffer layer at positions at: (4) 1a, (5) 1b and (6) 2a.

The superconducting properties ( $T_c$  and  $J_c$ ) measured at positions 1a, 1b and 2a corresponding to the microstructures in Figure 24 were observed and are summarized in Figure 25. The data shown are for bulk SmBCO single grains fabricated without a buffer and with a 3 mm Sm-123 + Sm-211 mixed-powder buffer. Generally speaking, the onset  $T_c$  in Figure 25 for all specimens is about 92.5 K, with a relatively sharp transition width,  $\Delta T_c$ , of less than 1 K, which indicates successful fabrication of the SmBCO single grains with good superconducting properties with or without a buffer layer ( $T_c$  is normalised by dividing by the temperature value of onset  $T_c$ ). Although both samples exhibit good superconducting properties, SmBCO fabricated with a Sm-123 + Sm-211 mixed-powder buffer has a sharper  $\Delta T_c$  at all the three positions. Two primary aspects are compared regarding  $J_c$ : the peak effect and the irreversibility field. The results show that buffered SmBCO has a higher  $J_c$ , especially in terms of the peak effect, while the irreversibility field values are largely similar in all specimens regardless of the use of a buffer layer.

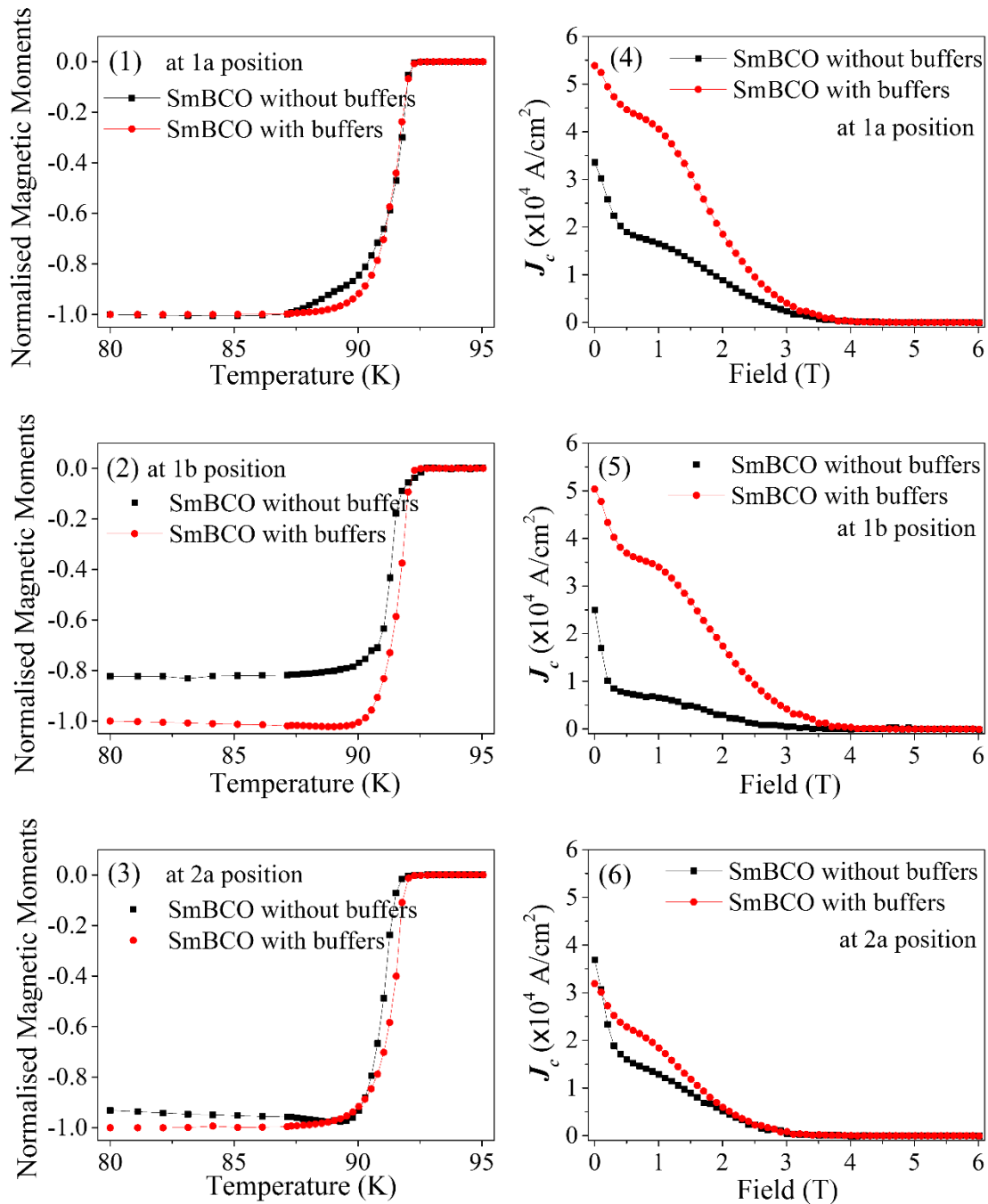


**Figure 25** Comparison of  $T_c$  between SmBCO fabricated with and without Sm-123 + Sm-211 mixed-powder buffers at positions: (1) 1a, (2) 1b and (3) 2a; Comparison of  $J_c$  at 77 K between SmBCO with and without Sm-123 + Sm-211 mixed-powder buffers at positions: (4) 1a, (5) 1b and (6) 2a.

Figure 26 shows the measured trapped fields of the top-surfaces of the SmBCO bulk single grains fabricated without a buffer and with a 3 mm Sm-123 + Sm-211 mixed-powder buffer. It can be seen that there is no noticeable difference in trapped field between the two samples.

The trapped field was anticipated theoretically to increase slightly for the buffered sample due to the increase in the pinning centre density in the buffer/seed area, assuming a uniform single grain microstructure [109]. However, the value of trapped field can also be influenced by the presence of other defects, such as cracks and pores, which occur randomly throughout the single grain microstructure [107]. Therefore, it can be concluded that the trapped fields observed for the single grains fabricated using a buffer layer improve slightly or remain unchanged for the modified process.

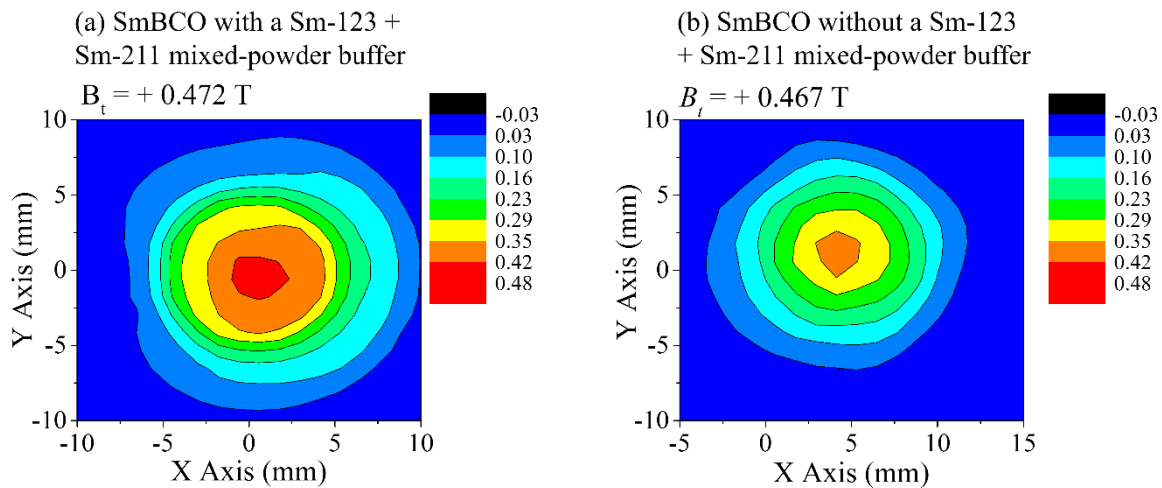


**Figure 26** Trapped field distributions (2D contour images) of the top-surfaces of the SmBCO single grains grown (1) with and (2) without a Sm-123 + Sm-211 mixed-powder buffer layer.

### 4.3. Summary

SmBCO single grains up to 20 mm in diameter and 10 mm in thickness with starting compositions of (75 wt. % Sm-123 + 25 wt. % Sm-211) + 2 wt. % BaO<sub>2</sub> + 1 wt. % CeO<sub>2</sub> have been fabricated successfully by TSMG in air using a MgO-NdBCO generic seed with a Sm-123 + Sm-211 mixed-powder buffer in a conventional chamber furnace. The use of a buffer layer aids the choice of seed crystals, which, as a consequence, are less critical to the success of the TSMG process, lead to a more uniform distribution of Sm-211 particles throughout the single grain sample, overcomes the lattice mismatch between a MgO-NdBCO generic seed and the SmBCO bulk single grain and is relatively more tolerant to the presence of impurities in the precursor pellets compared to the use of a MgO-NdBCO generic seed. As

a result, the superconducting properties,  $T_c$  and  $J_c$ , in the buffered SmBCO are improved significantly.  $T_c$  of the samples fabricated with or without buffer layers is similar, while  $\Delta T_c$  in the buffered SmBCO is sharper. The irreversibility fields and  $J_c$  are similar in both samples, although the buffered SmBCO exhibits a stronger peak effect. On the other hand, the peak values of the trapped fields remain largely unchanged. Finally, a Sm-123 + Sm-211 mix-powder buffer layer is used in subsequent research with an aspect ratio of 1, where the buffer diameter is equal to its thickness, which represents an optimum geometry for SmBCO single grain growth.

# CHAPTER 5

## EFFECTS OF DOPING IN SUPERCONDUCTING SMBCO BULK SINGLE GRAINS

### 5.1. Introduction and Motivation

Improving  $J_c$  can be achieved by introducing artificial flux pinning centres into the bulk superconducting matrix. Taking YBCO as an example, on which extensive research has been performed on melt-processed bulks,  $J_c$  at different positions along the cross-section of a single grain at 77 K differs significantly from location to location due, partially, to the uneven presence of a relatively large volume fraction of large (1-2  $\mu\text{m}$  in diameter) Y-211 inclusions in the bulk Y-123 phase matrix. As a result, it is necessary to develop new inclusions that can be introduced controllably into the YBCO bulk microstructure by doping and, in consequence, reduce the size of the Y-211 particles. YBCO has proved to be highly adaptable chemically since it can accommodate a wide variety of cationic and anionic substitutions. Skakle has reported a range of chemicals that can substitute to some extent into the YBCO structure and their effects on the properties of YBCO [110]. Elements may be doped into YBCO that do not occupy any site of the Y-Ba-Cu-O compositional elements, such as Ce, Pt, Zr, Ta and Ti, while there are other elements that incorporate directly into the lattice of YBCO, with different elements substituting at different sites depending on the processing conditions, variable oxygen content and the nature of the dopants. In general, elements such as Fe, Nb, Ga, Zn and Sn tend to substitute on the Cu site, elements such as Cl on the O site, elements such as Sc, Sr, Ca (for low levels of doping), Na and Gd on the Y site and elements such as Sm and La on the Ba site [110]. Other studies of YBCO indicate that Pt and  $\text{CeO}_2$  refine the size of Y-211 particles within the YBCO matrix, which correlates with an increase in trapped magnetic flux density and  $J_c$  [104]. Izumi *et al.* demonstrated that the addition of Pt, introduced as a contaminant from the crucible during the first partial melting step in the so-

called melt powder melt growth method, is effective in refining Y-211 particles in the fully processed single grain [111]. Kim *et al.* reported subsequently that needle-like and highly anisotropic Y-211 particles form in single grain YBCO samples containing Pt, whereas samples processed with CeO<sub>2</sub> contain finer Y-211 particles with reduced anisotropy [104][112]. More recently, Diko *et al.* have investigated and compared further the effect of these additions on the properties of single grains. The effect of Pt and CeO<sub>2</sub> on the aggregation of Y-211 particles in single grain YBCO samples and the microstructures of samples containing the two different dopants, in particular, have been studied and compared fully in detail [113][114]. Furthermore, Muralidhar *et al.* extended the study into the (Nd, Eu, Gd)-Ba-Cu-O [(NEG)BCO] system, which is more analogous to the SmBCO system and succeeded in enhancing  $J_c$  of the (NEG)BCO system through the refinement of 211 particles by the combined addition of Pt and CeO<sub>2</sub> [115][116].

Similar attempts for improving the superconducting properties of SmBCO bulk superconductors through pinning enhancement have also been reported, including the addition of traditional phases such as Sm-211 [82], a new type of pinning centre such as Sm-2411 [72] and a novel dopant such as SmBa<sub>2</sub>Cu<sub>2.67</sub>Al<sub>0.33</sub>O<sub>6+δ</sub> [73]. In this chapter, the elements highlighted in the Periodic Table of Elements in Figure 27 have been added to SmBCO as dopants in the form of different compounds as summarised in Table 4 in an attempt to investigate doping effects on the growth and superconducting properties of SmBCO single grains.

This chapter is divided into two sections:

In the first section, a comparison of the effects of addition of platinum and CeO<sub>2</sub> in SmBCO is discussed, given that comparable research has been performed on YBCO, although not yet on SmBCO. The fabrication of large, single grain bulk SmBCO containing 1 wt. % CeO<sub>2</sub> and 0.1 wt. % Pt using a TSMG process is reported. The performance of bulk superconductors containing different dopants is evaluated based on an analysis of their superconducting properties, including  $T_c$  and  $J_c$ , and on sample microstructure. Both CeO<sub>2</sub> and Pt dopants refine the size of Sm-211 particles trapped in the superconducting matrix, which act as effective flux pinning centres, although the addition of CeO<sub>2</sub> results broadly in improved superconducting performance of the fully grown bulk single grain. Furthermore, 1 wt. % CeO<sub>2</sub> is significantly cheaper than 0.1 wt. % Pt, which has clear economic benefits for use in medium to large scale production processes for these technologically important materials.

Finally, the use of CeO<sub>2</sub> results generally in the formation of finer Sm-211 particles and to the generation of fewer macro-cracks and Sm-211 free regions in the sample microstructure.

In the second section, precursor powders of SmBCO containing optimum CeO<sub>2</sub> content were then prepared with the doping elements indicated in Figure 27 to observe how these dopants work in this system. With the assistance of commercial thin film seeds, single domain, bulk SmBCO samples of dimensions of 20 mm and 16 mm in diameter and correspondingly 10 mm and 7 mm in thickness with different dopants have been fabricated successfully in air by a TSMG process using a conventional chamber furnace. Detailed studies were performed on  $T_c$  and  $J_c$  along the  $a/b$ - and  $c$ - axes of the single grains containing 1 mol. % ZrO<sub>2</sub>, BaZrO<sub>3</sub>, TiO<sub>2</sub> and ‘Sm-2411’, respectively. In conclusion,  $J_c$  of a sample containing 1 mol. % BaZrO<sub>3</sub>-doped SmBCO show a value as high as  $1.20 \times 10^5$  A cm<sup>-2</sup> at 77 K when the applied field was 1.722 T.

Constituent elements in SmBa<sub>2</sub>Cu<sub>3</sub>O<sub>7-δ</sub>  
 Doping elements into SmBa<sub>2</sub>Cu<sub>3</sub>O<sub>7-δ</sub>

1																	18
1 <b>H</b> 1.008																	2 <b>He</b> 4.0026
3 <b>Li</b> 6.94	4 <b>Be</b> 9.0122											5 <b>B</b> 10.81	6 <b>C</b> 12.011	7 <b>N</b> 14.007	8 <b>O</b> 15.999	9 <b>F</b> 18.998	10 <b>Ne</b> 20.180
11 <b>Na</b> 22.990	12 <b>Mg</b> 24.305	3	4	5	6	7	8	9	10	11	12	13 <b>Al</b> 26.982	14 <b>Si</b> 28.085	15 <b>P</b> 30.974	16 <b>S</b> 32.06	17 <b>Cl</b> 35.45	18 <b>Ar</b> 39.948
19 <b>K</b> 39.098	20 <b>Ca</b> 40.078	21 <b>Sc</b> 44.956	22 <b>Ti</b> 47.867	23 <b>V</b> 50.942	24 <b>Cr</b> 51.996	25 <b>Mn</b> 54.938	26 <b>Fe</b> 55.845	27 <b>Co</b> 58.933	28 <b>Ni</b> 58.693	29 <b>Cu</b> 63.546	30 <b>Zn</b> 65.38	31 <b>Ga</b> 69.723	32 <b>Ge</b> 72.630	33 <b>As</b> 74.922	34 <b>Se</b> 78.97	35 <b>Br</b> 79.904	36 <b>Kr</b> 83.798
37 <b>Rb</b> 85.468	38 <b>Sr</b> 87.62	39 <b>Y</b> 88.906	40 <b>Zr</b> 91.224	41 <b>Nb</b> 92.906	42 <b>Mo</b> 95.95	43 <b>Tc</b> (98)	44 <b>Ru</b> 101.07	45 <b>Rh</b> 102.91	46 <b>Pd</b> 106.42	47 <b>Ag</b> 107.87	48 <b>Cd</b> 112.41	49 <b>In</b> 114.82	50 <b>Sn</b> 118.71	51 <b>Sb</b> 121.76	52 <b>Te</b> 127.60	53 <b>I</b> 126.90	54 <b>Xe</b> 131.29
55 <b>Cs</b> 132.91	56 <b>Ba</b> 137.33	57-71 *	72 <b>Hf</b> 178.49	73 <b>Ta</b> 180.95	74 <b>W</b> 183.84	75 <b>Re</b> 186.21	76 <b>Os</b> 190.23	77 <b>Ir</b> 192.22	78 <b>Pt</b> 195.08	79 <b>Au</b> 196.97	80 <b>Hg</b> 200.59	81 <b>Tl</b> 204.38	82 <b>Pb</b> 207.2	83 <b>Bi</b> 208.98	84 <b>Po</b> (209)	85 <b>At</b> (210)	86 <b>Rn</b> (222)
87 <b>Fr</b> (223)	88 <b>Ra</b> (226)	89-103 #	104 <b>Rf</b> (265)	105 <b>Db</b> (268)	106 <b>Sg</b> (271)	107 <b>Bh</b> (270)	108 <b>Hs</b> (277)	109 <b>Mt</b> (276)	110 <b>Ds</b> (281)	111 <b>Rg</b> (280)	112 <b>Cn</b> (285)	113 <b>Nh</b> (286)	114 <b>Fl</b> (289)	115 <b>Mc</b> (289)	116 <b>Lv</b> (293)	117 <b>Ts</b> (294)	118 <b>Og</b> (294)
* Lanthanide series		57 <b>La</b> 138.91	58 <b>Ce</b> 140.12	59 <b>Pr</b> 140.91	60 <b>Nd</b> 144.24	61 <b>Pm</b> (145)	62 <b>Sm</b> 150.36	63 <b>Eu</b> 151.96	64 <b>Gd</b> 157.25	65 <b>Tb</b> 158.93	66 <b>Dy</b> 162.50	67 <b>Ho</b> 164.93	68 <b>Er</b> 167.26	69 <b>Tm</b> 168.93	70 <b>Yb</b> 173.05	71 <b>Lu</b> 174.97	
# Actinide series		89 <b>Ac</b> (227)	90 <b>Th</b> 232.04	91 <b>Pa</b> 231.04	92 <b>U</b> 238.03	93 <b>Np</b> (237)	94 <b>Pu</b> (244)	95 <b>Am</b> (243)	96 <b>Cm</b> (247)	97 <b>Bk</b> (247)	98 <b>Cf</b> (251)	99 <b>Es</b> (252)	100 <b>Fm</b> (257)	101 <b>Md</b> (258)	102 <b>No</b> (259)	103 <b>Lr</b> (262)	

**Figure 27** Periodic Table of Elements marked with the constituent elements in SmBCO and the elements doped into the SmBCO precursor powder.

**Table 4** Summary of the elements and corresponding compounds doped into the SmBCO precursor powder.

Elements doped into SmBCO	Corresponding compounds doped in SmBCO
Na	Na <sub>2</sub> CO <sub>3</sub>
Rb	RbCl
Ca	CaMoO <sub>4</sub> , CaCO <sub>3</sub>
Sr	SrCO <sub>3</sub>
Sc	Sc <sub>2</sub> O <sub>3</sub>
Ti	TiO <sub>2</sub>
Zr	ZrO <sub>2</sub> , BaZrO <sub>3</sub> , nano-ZrO <sub>2</sub>
Nb	NbO <sub>2</sub>
Ta	Ta <sub>2</sub> O <sub>3</sub>
Mo	CaMoO <sub>4</sub>
Fe	Fe <sub>2</sub> O <sub>3</sub> , FeB
Pt	Pt
Zn	ZnO
Ga	Ga <sub>2</sub> O <sub>3</sub>
B	FeB
Sn	SnO
Bi	Bi <sub>2</sub> O <sub>3</sub>
Ce	CeO <sub>2</sub>

---

Gd	Gd <sub>2</sub> O <sub>3</sub>
Tb	Tb <sub>4</sub> O <sub>7</sub>
Hf	HfO <sub>2</sub>
Sm, Ba, Cu	Fine Sm-211

---

## **5.2. Comparison of the Effects of Platinum and CeO<sub>2</sub> on the Properties of Single-grain, SmBCO Bulk Superconductors**

### **5.2.1. Experimental Details**

Commercially available precursor powders were used to fabricate SmBCO bulk single grains. Both SmBCO + CeO<sub>2</sub> and SmBCO + Pt precursors contained 75 wt. % Sm-123 (Toshiba, average particle size: 2-3  $\mu\text{m}$ ), 25 wt. % Sm-211 (Toshiba, average particle size: 1-2  $\mu\text{m}$ ) and 2 wt. % BaO<sub>2</sub> (Sigma-Aldrich, purity 95 %; to suppress Sm/Ba substitution [70]). 1 wt. % CeO<sub>2</sub> (Sigma-Aldrich, purity 99.9 %) and 0.1 wt. % Pt (Alfa Aesar, purity 99.98 %, 350 mesh) were added subsequently to each precursor powders, corresponding to the optimised amount [117]. The mixed powders were then pressed uniaxially under a load of 1.5 tons in a cylindrical die of diameter 20 mm. Pellet pre-forms of thickness 9 mm were obtained for each composition (each pellet shrinks to about 80 % of its original size after TSMG, corresponding approximately to as-processed dimensions of 16 mm diameter and 7 mm thickness). Pure SmBCO containing only Sm-123 and Sm-211 was also prepared for the purpose of comparison using the same TSMG procedure of comparable overall volume and weight.

A thin film seed [118] consisting of NdBCO of thickness 700 nm deposited on a single crystal MgO-substrate provided by Ceraco was placed at the centre of the top surface of the

as-prepared pre-forms to control single grain nucleation and growth in the required orientation, as illustrated schematically in Figure 28.

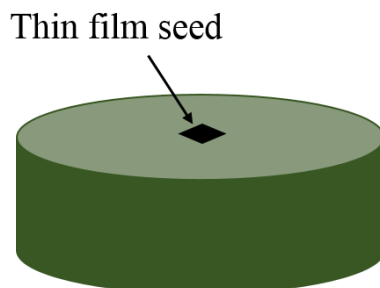


**Figure 28** Schematic illustration of the bulk pre-form with a thin film seed.

The TSMG method based on the heating profile shown in Figure 29 was used to fabricate bulk single grains of SmBCO + CeO<sub>2</sub> and SmBCO + Pt in air. Initially, the temperature was raised slowly to 400 °C at a rate of 50 °C h<sup>-1</sup> to stabilise the thin film seed, followed by a more rapid increase to 900 °C. The temperature was then increased further to 1087 °C ( $T_{\max}$ ) and held at this level for 0.5 h to allow the precursor pellet to decompose. The sample was then cooled in three stages. Firstly, the furnace temperature was decreased to 1075 °C ( $T_s$ ) at a rate of 75 °C h<sup>-1</sup> and then to 1067 °C ( $T_{g1}$ ) at a rate of 1 °C h<sup>-1</sup>. The solidification procedure was completed by reducing the temperature to 1041 °C ( $T_{g2}$ ) at a rate of 0.8 °C h<sup>-1</sup>. Finally, the samples were furnace cooled to room temperature at a rate of 150 °C h<sup>-1</sup>.

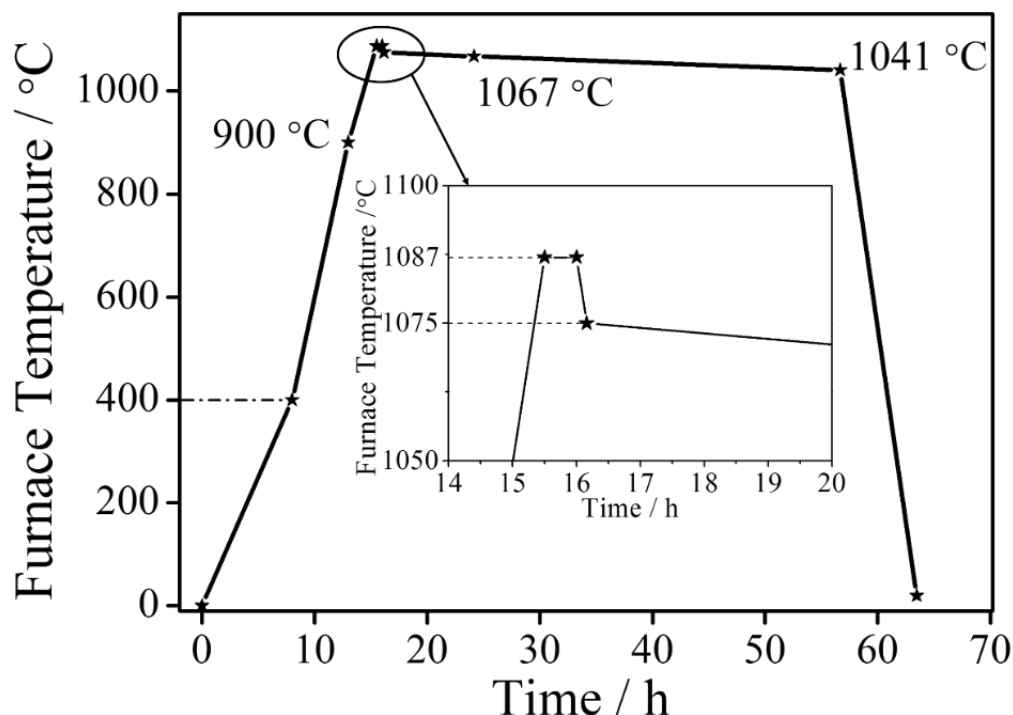


**Figure 29** Heating profile used to produce SmBCO + CeO<sub>2</sub> and SmBCO + Pt single grains.

The as-grown samples were oxygenated at 360 °C for fourteen days to drive the non-superconducting, tetragonal phase to the desired orthorhombic superconducting phase.

Differential thermal analysis (DTA) was performed on the SmBCO + CeO<sub>2</sub> and SmBCO + Pt precursor powders to enable the various growth-related temperatures in the melt process to be determined. The details of DTA measurements were described in Section 3.3.3.

Each sample was cut in half using a diamond saw, as illustrated schematically in Figure 30. One half of each bulk SmBCO cross-section was polished for microstructural observation as summarised in Section 3.3.1.1, and the other half was prepared for measurement of the magnetic moment for calculating  $J_c$  and measuring  $T_c$  as described in Section 3.3.2.1.

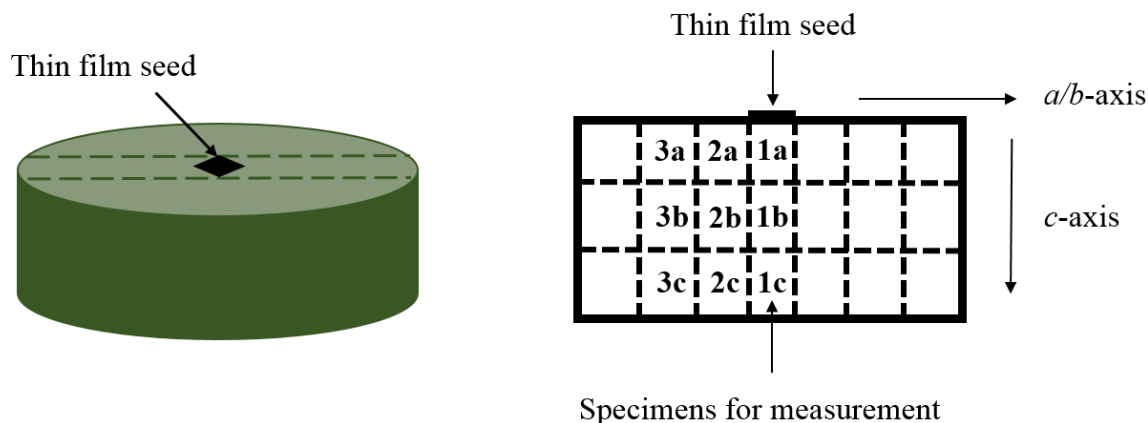


**Figure 30** Schematic illustration of the positions of the bulk specimens within the single grain.

Scanning electron microscopy (SEM) was used to investigate the microstructure of each specimen, with chemical analysis being performed simultaneously by energy dispersive x-ray spectrometry (EDX).

## 5.2.2. Results and Discussion

DTA was performed in order to estimate the peritectic reaction temperatures of the SmBCO precursor powders containing  $\text{CeO}_2$  and Pt to simulate the TSMG process at elevated temperatures. The peak DTA values identified subsequently in Figure 31 were then used as the corresponding peritectic reaction temperatures. It is clear from this figure that both compositions exhibit similar values ( $1071.5\text{ }^\circ\text{C}$ ) of this key process parameter at which each precursor powder decomposes and this allows the same heating profile to be used to grow these two samples. This, in turn, makes subsequent comparison of the properties of the single grains more meaningful. As a result, combining further knowledge of the growth kinetics and fabrication of SmBCO,  $T_{\text{max}}$  in the heating profile was set to  $1087\text{ }^\circ\text{C}$  rather than the peritectic reaction temperature,  $1071\text{ }^\circ\text{C}$ , to ensure complete decomposition of the precursor powders. In addition, a growth temperature  $T_{g2}$  of  $1041\text{ }^\circ\text{C}$  was established, which is lower than the peritectic temperature, but sufficient to guarantee enough undercooling and a wide growth window, which is beneficial to successful SmBCO growth.

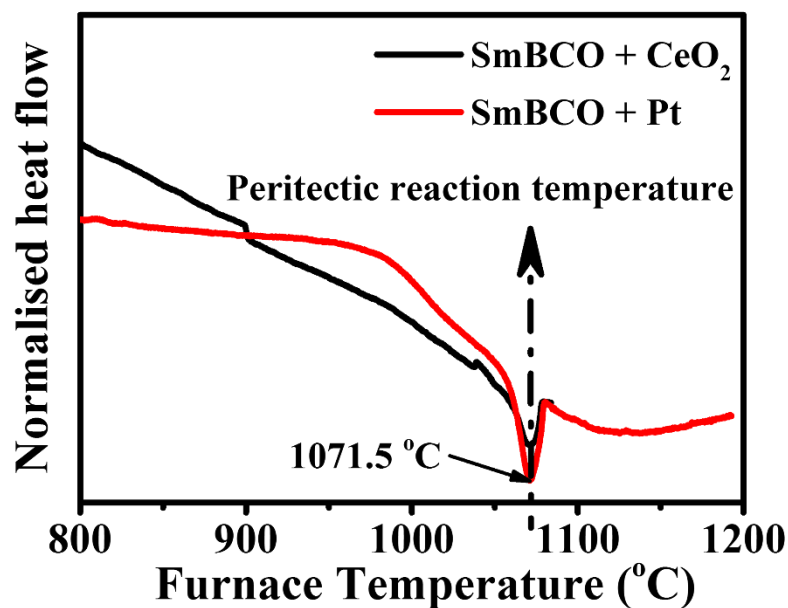


**Figure 31** Differential thermal analysis traces of SmBCO + CeO<sub>2</sub> and SmBCO + Pt precursor powders.

Photographs of successfully grown single grains of diameter 16 mm for SmBCO containing CeO<sub>2</sub> and Pt are shown in Figure 32. Both samples were synthesised in the same batch, prepared using the same furnace and heating profile and oxygenated under the same conditions. It can be seen that four clear growth facet lines extend from the seed to the edges of each sample, indicating that each is grown fully by TSMG in air in the form of a large single grain.

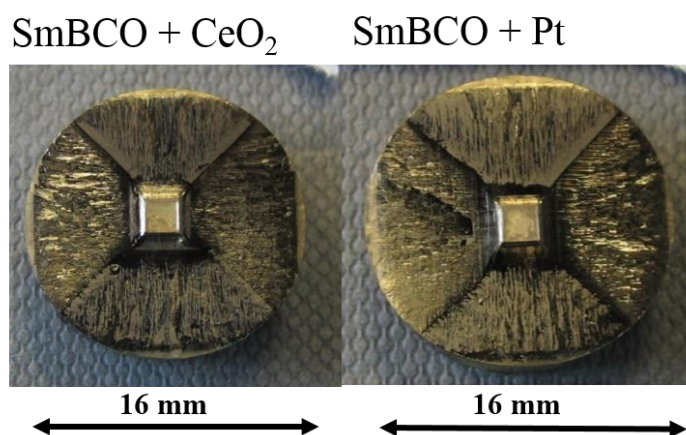


**Figure 32** Photographs of the top surfaces of SmBCO + CeO<sub>2</sub> and SmBCO + Pt single grains.

The variation of  $T_c$  along both crystallographic axes and at different locations within the bulk single grain are compared for the different sample compositions in Figure 33. By considering  $T_c$  and the observed transition width,  $\Delta T_c$ , it can be concluded that the variation in superconducting properties is greater for both sets of specimens along the  $a/b$ -axis than along the  $c$ -axis, independently of whether the sample is composed of SmBCO + CeO<sub>2</sub> or SmBCO + Pt.

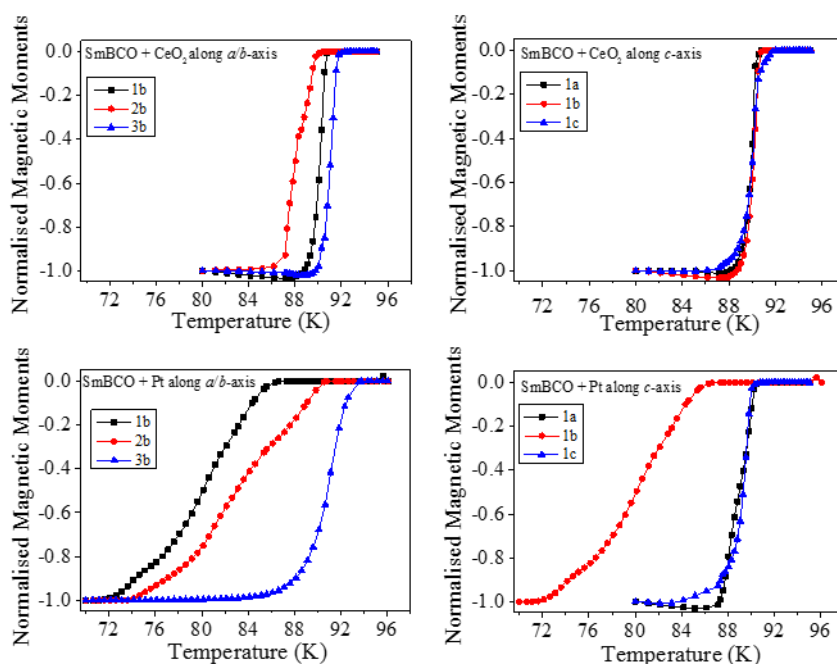


**Figure 33** Comparison of  $T_c$  for the sub-specimens along the  $a/b$ -axis and  $c$ -axis of the SmBCO + CeO<sub>2</sub> and SmBCO + Pt single grains.

The  $T_c$  of SmBCO is affected significantly by substitution of Ba by Sm in the Sm-123 phase matrix [74]. This effect can vary with sample positions, assuming that the concentration of Sm in the melt increases with the distance from the seed, which may lead to more severe substitution of Ba by Sm. The melt composition in SmBCO + CeO<sub>2</sub> and SmBCO + Pt will be different because the reaction of CeO<sub>2</sub> with the Sm-123 phase generates an excess of CuO in the melt, which will therefore increase with distance from the seed and potentially influence the extent of Sm/Ba substitution [119].

Comparison of the  $T_c$  of the specimens at equivalent positions in the two single grain samples at the five positions measured along the  $a/b$ -axis and  $c$ -axis in this study indicates clearly that the sample fabricated from SmBCO + Pt is not as good as that containing CeO<sub>2</sub> in Figure 34. The data indicate a lower  $T_c$  and a broader  $\Delta T_c$  in the former, with only one exception at

position 3b, where a higher  $T_c$  was observed in the SmBCO + Pt single grain. However, it should be noted that  $\Delta T_c$  at this position in the SmBCO + Pt sample is also much broader than that in SmBCO + CeO<sub>2</sub>. As a result, such a high local  $T_c$  does not contradict the general conclusion that the effect of the addition of Pt to SmBCO is not as beneficial to its superconducting properties as the addition of CeO<sub>2</sub>.

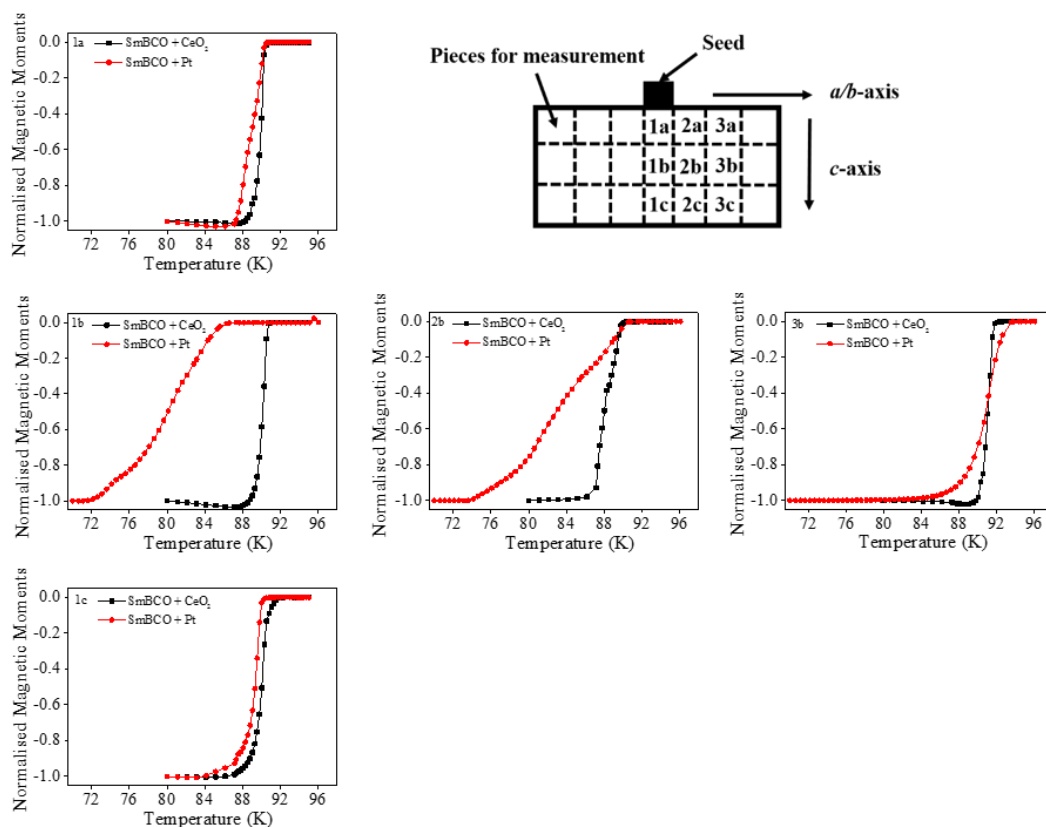


**Figure 34** Comparison of  $T_c$  for specimens at the same position in the parent single grain for SmBCO + CeO<sub>2</sub> and SmBCO + Pt compositions.

$J_c$  at 77 K calculated using the extended Bean critical state model [62] for the specimens along the  $a/b$ - and  $c$ - axes of each sample are shown in Figure 35. Although there is a significant variation with position,  $J_c$  is consistently higher in the single grain sample containing CeO<sub>2</sub>. In addition, no regular trends are apparent in these data, and the specimens exhibit different  $J_c$  values in both samples along the  $a/b$ - and  $c$ - axes as shown in Figure 30, with different associated peak effects and irreversibility fields.

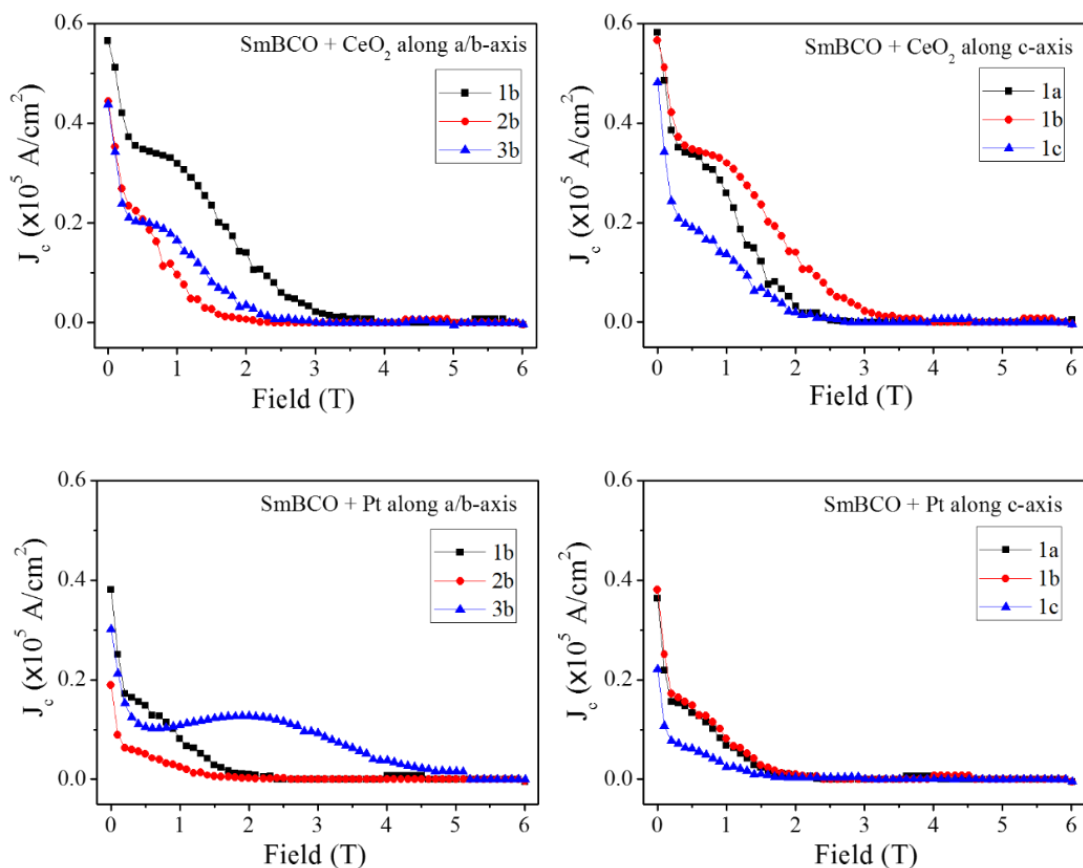


**Figure 35** Comparison of  $J_c$  for specimens at the same position in the parent single grain for SmBCO + CeO<sub>2</sub> and SmBCO + Pt compositions.

Figure 36 shows a comparison of  $J_c$  for the specimens at the same locations in the parent single grain for the two sample compositions. Although the values of  $J_c$  vary from position to position, generally speaking, the sample containing CeO<sub>2</sub> exhibits a more pronounced peak effect and higher irreversibility field than the sample containing Pt across the entire cross-section of the single grain.

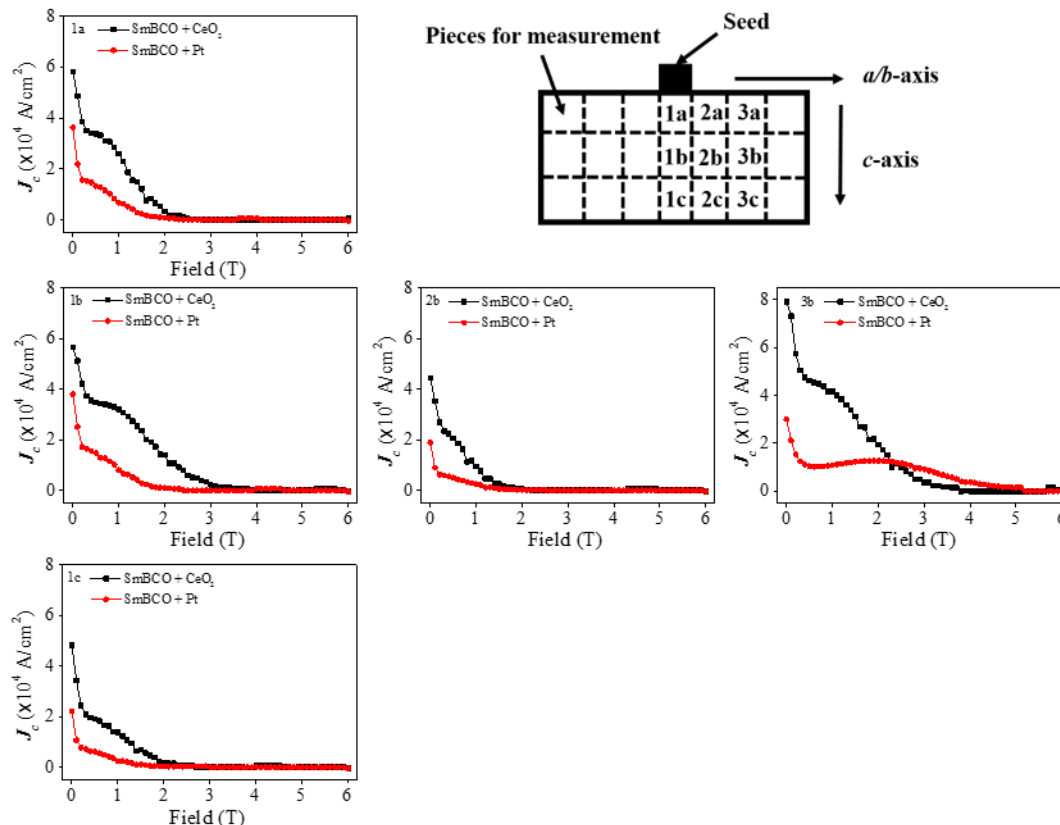


**Figure 36** Comparison of  $J_c$  for sub-specimens at the same position in sample-compositions of SmBCO + CeO<sub>2</sub> and SmBCO + Pt.

Further microscopic studies were performed on the single grain samples in an attempt to explain the differences in  $J_c$  between these samples given that  $J_c$  is related closely to the ability of the single grain to pin magnetic flux lines, and therefore to generate higher trapped field, which, in turn, is determined variously by inhomogeneities in the sample microstructure, such as micro-cracks, RE-211 particle inclusions and twin planes, *etc* [5].

Kim *et al.* reported that both Pt and CeO<sub>2</sub> are capable of refining the size of the RE-211 particles in the (RE)BCO single grain microstructure [104], which is further confirmed in this study. Micrographs (1a), (2a) and (3) in Figure 37 exhibit different Sm-211 particle sizes in the three compositions investigated [(SmBCO + CeO<sub>2</sub>, SmBCO + Pt and the undoped SmBCO (pure SmBCO)]. The largest Sm-211 particle size observed in single grain samples fabricated without the addition of either CeO<sub>2</sub> or Pt can be as large as 10  $\mu\text{m}$ , which is more than 5 times the size of those observed in the samples containing CeO<sub>2</sub> or Pt.

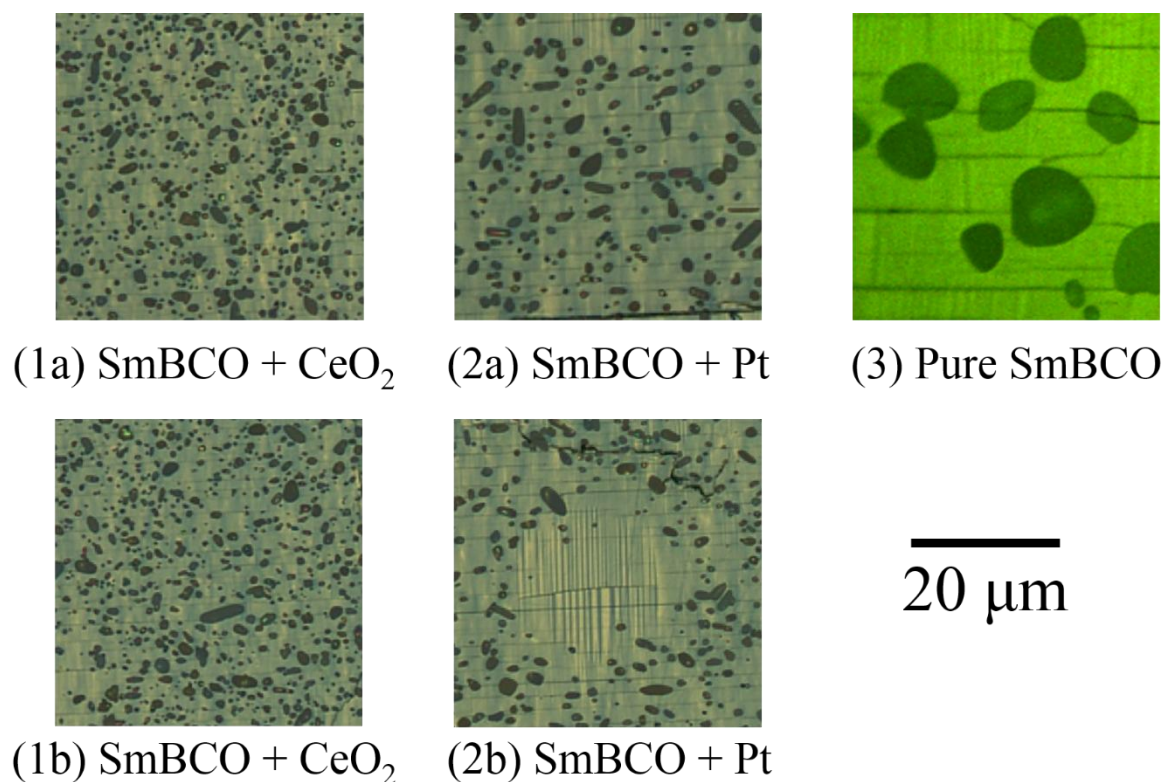


**Figure 37** Micrographs at a magnification of  $500\times$  for the SmBCO + CeO<sub>2</sub> [(1a) and (1b)] and SmBCO + Pt samples [(2a) and (2b)] observed at equivalent positions in the parent single grain (position 1b in Figure 30). Micrograph (3) is for the undoped single grain SmBCO sample (pure SmBCO).

Micrographs (1a), (1b), (2a) and (2b) in Figure 37 reveal that the presence of CeO<sub>2</sub> refines the Sm-211 particles further, so that a smaller average Sm-211 particle size is observed in this material. The Sm-211 particles are also much better distributed across the entire cross-section of the single grain in SmBCO + CeO<sub>2</sub> compared to SmBCO + Pt. The inferior superconducting properties in SmBCO + Pt may be attributed, in part, to the presence of a relatively large number of Sm-211 free regions, as shown in Figure 37 (2b), which is not observed in the SmBCO + CeO<sub>2</sub> samples.

The results of the energy dispersive x-ray spectrometry (EDX) analysis are summarised in Figures 38 and 39, and Tables 5 and 6. These indicate that CeO<sub>2</sub> exists mainly in the single grain bulk in the form of BaCeO<sub>3</sub> (the trace amount of Sm and Cu is due to the background signal from the bulk matrix), which is consistent with the findings of a previous study of YBCO [113]. The rectangular BaCeO<sub>3</sub> particles are distributed homogeneously in the bulk and their size is comparable with the size of Sm-211 particles, so they can contribute effectively

to flux pinning. The images also give information on the distribution of  $\text{BaCeO}_3$  in the single grain. The particles tend to form agglomerates generally in pores or in the vicinity of macro-cracks, which limits the propagation of the latter under an applied stress (their stoichiometry can be estimated by EDX more closely to  $\text{BaCeO}_3$ ). This, in turn, leads to the formation of fewer macro-cracks, which prohibit the flow of the supercurrents through the bulk single grain. Such a distribution, on the other hand, cannot be found in the SmBCO samples containing Pt. This could account further for the superior superconducting properties observed for the SmBCO sample containing  $\text{CeO}_2$ .

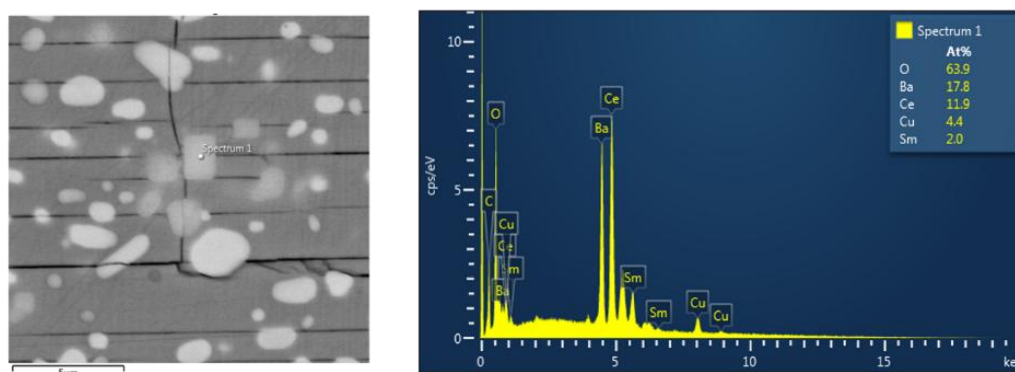


**Figure 38** EDX analysis of the Ce-containing second phase located on macro-cracks formed orthogonally to the  $c$ -axis in the single grain sample of composition SmBCO +  $\text{CeO}_2$ .

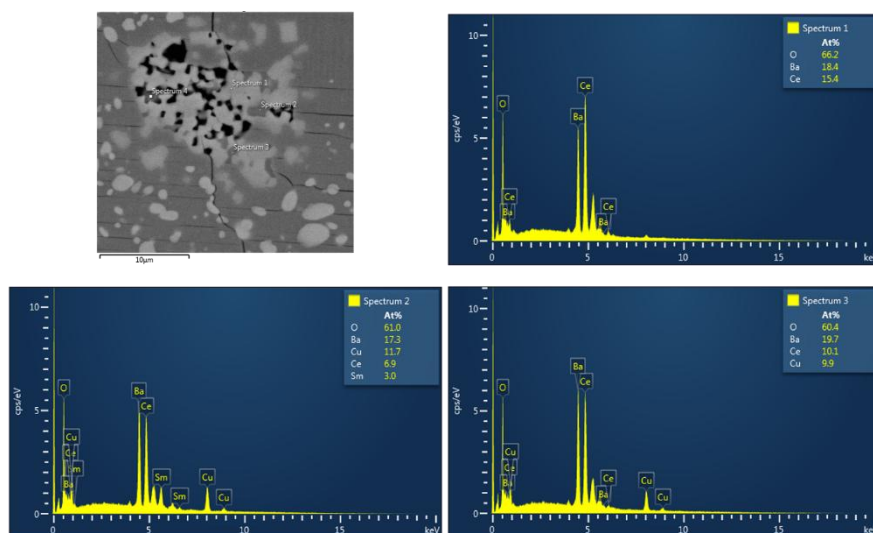


**Figure 39** EDX analysis of the Ce-containing second phase formed in pores in the single grain sample of composition SmBCO +  $\text{CeO}_2$ .

**Table 5** Summary of the EDX analysis for the Ce-containing second phase located on macro-cracks formed orthogonally to the *c*-axis in the single grain sample of composition SmBCO + CeO<sub>2</sub>.

Spectrum No.	Element amount detected / At. %				
	Ba	Ce	O	Sm	Cu
Spectrum 1	17.8	11.9	63.9	2.0	4.4

**Table 6** Summary of the EDX analysis for the Ce-containing second phase formed in pores in the single grain sample of composition SmBCO + CeO<sub>2</sub>.

Spectrum No.	Element amount detected / At. %				
	Ba	Ce	O	Sm	Cu
Spectrum 1	18.4	15.4	66.2	-	-
Spectrum 2	17.3	6.9	61.0	3.0	11.7
Spectrum 3	19.7	10.1	60.4	-	9.9

The cost of the addition of Pt and CeO<sub>2</sub> to SmBCO should be compared to establish the economic viability of the single grain fabrication process. The price of the commercially available CeO<sub>2</sub> (Sigma-Aldrich, purity 99.9 %, 100 g) and Pt (Alfa Aesar, purity 99.98 %, 350 mesh, 5 g) chemicals used in this study was £ 37.20 and £ 767.00, respectively. As a result, 1 wt. % of CeO<sub>2</sub> (£0.372 g<sup>-1</sup>) costs less than one 40<sup>th</sup> of 0.1 wt. % of Pt (£ 153.4 g<sup>-1</sup>). Hence, the SmBCO + CeO<sub>2</sub> single grain exhibits superior superconducting properties at significantly lower cost, which demonstrates clearly that CeO<sub>2</sub> is not only a better candidate as an inclusion refiner than Pt, but is also a more economic option for production of single grain SmBCO samples for commercially viable applications.

### 5.2.3. Summary

Bulk single grain SmBCO samples melt processed in air with Pt and CeO<sub>2</sub> additions have been fabricated successfully by TSMG. Comparisons of the measured superconducting properties of both single grains have shown clearly that CeO<sub>2</sub> is more effective at refining the Sm-211 inclusions in the bulk microstructure than Pt. Microstructural analysis of the two single grains has indicated further that the SmBCO + CeO<sub>2</sub> sample contains fewer macro cracks, finer Sm-211 particles and a more homogeneous Sm-211 distribution within the parent single grain, which, collectively, contribute to enhanced bulk superconducting performance for this composition. Finally, the addition of CeO<sub>2</sub> is significantly more cost effective than the addition of Pt, which is important for the development of a commercially viable single grain fabrication process. Therefore, CeO<sub>2</sub> offers superior performance and commercial benefits over Pt to improve the superconducting and mechanical properties and cost efficiency of large, single grain SmBCO for practical applications. As a result, CeO<sub>2</sub> is employed as a standard dopant in the samples fabricated and repeated in the remainder of this thesis.

## 5.3. Growth and Superconducting Properties of SmBCO Single Grains fabricated with Different Dopants

### 5.3.1. Experimental Details

(RE)<sub>2</sub>Ba<sub>4</sub>Cu<sub>1</sub>(M)<sub>1</sub>O [RE-2411(M)] has been reported by the Bulk Superconductivity Group in Cambridge to be an effective pinning dopant [120] [121] and has been studied thoroughly in the YBCO system [122] [123]. In these studies, Y-2411(Zr) phase has been discovered to form particularly effective flux pinning centres in bulk YBCO due primarily to its ability to exist as stable, nano-size inclusions in the superconducting phase matrix. An attempt has been made, therefore, to introduce Sm<sub>2</sub>Ba<sub>4</sub>CuZrO<sub>10</sub> [Sm-2411(Zr)] into bulk SmBCO as part

of this research. Commercial powders of  $\text{Sm}_2\text{O}_3$  (Alfa Aesar, purity 99.9 %),  $\text{BaCO}_3$  (ALDRICH, purity 99.999 %),  $\text{CuO}$  (Alfa Aesar, purity 99.7 %, metals basis) and  $\text{ZrO}_2$  (Alfa Aesar, purity 99 %, metals basis excluding Hf) were employed to synthesize Sm-2411 (Zr) single phase dopant. The mixed powders with an appropriate ratio were mixed thoroughly and calcined at different temperatures for different lengths of time in air followed by intermediate, repeated mechanical grinding. In total, the powder mixture underwent the following calcinations: (1) 800 °C for 20 h; (2) 850 °C for 20 h; (3) 850 °C for 20 h; (4) 870 °C for 40 h; (5) 870 °C for 40 h; (6) 890 °C for 50 h; (7) 895 °C for 40 h; (8) 910 °C for 50 h; (9) 950 °C for 10 h; (10) 990 °C for 10 h; (11) 990 °C for 30 h; (12) 1020 °C for 30 h; (13) 1030 °C for 30 h; (14) 1040 °C for 20 h; (15) 1040 °C for 30 h and (16) 1040 °C for 30 h.

To prepare SmBCO bulk pre-forms, mixed precursor powders, including dopants, were prepared using commercially available Sm-123 (TOSHIMA, average particle size: 2-3  $\mu\text{m}$ ), Sm-211 (TOSHIMA, average particle size: 1-2  $\mu\text{m}$ ),  $\text{BaO}_2$  (ALDRICH, purity 95 %; to suppress Sm/Ba substitution [70]) and  $\text{CeO}_2$  (Alfa Aesar, purity 99.9 %; to refine the Sm-211 particles [104]) powders. A motorized pestle and mortar was used to mix thoroughly powders of composition [(75 wt. % Sm-123 + 25 wt. % Sm-211) + 2 wt. %  $\text{BaO}_2$  + 1 wt. %  $\text{CeO}_2$ ] + x mol. % dopant (with different x values serving different purposes discussed later in this chapter), prior to being pressed uniaxially under a load of 1.5 tons into a green pre-form (pellet-like) with sizes of 25 mm and 20 mm in diameter and 13 mm and 9 mm in thickness (each pellet shrinks to about 80% of its original size after TSMG, corresponding to 20 mm and 16 mm in diameter and 10 mm and 7 mm as-processed dimensions). Doped, green pellets were prepared by adding different dopants (source and purity information is listed in Table 7) in different amount summarised in Table 8, into the precursor powders. The powder mixing procedure was largely similar to that of the undoped SmBCO precursor pellets, except for the presence of dopants in the starting powders. Therefore, the doped samples had the same overall volume and weight as the undoped SmBCO green bodies.

**Table 7** A list of commercial source and purity information on dopants added into SmBCO in this research.

No.	Dopants	Company	Purity	No.	Dopants	Company	Purity
1	$\text{ZrO}_2$	Alfa Aesar	99 % <sup>1</sup>	12	$\text{Ta}_2\text{O}_5$	Alfa Aesar	99 %
2	$\text{Ga}_2\text{O}_3$	Alfa Aesar	99 + % <sup>2</sup>	13	SnO	JOHNSON <sup>5</sup>	99 %

3	Gd <sub>2</sub> O <sub>3</sub>	Alfa Aesar	99 + % <sup>2</sup>	14	RbCl	Alfa Aesar	99 %
4	Na <sub>2</sub> CO <sub>3</sub>	ALDRICH	99.995 %	15	Tb <sub>4</sub> O <sub>7</sub>	ALDRICH	99.9 %
5	NbO <sub>2</sub>	Alfa Aesar	99 + % <sup>2</sup>	16	ZnO	ALDRICH	99.99 %
6	Nano-ZrO <sub>2</sub>	HOSOKAWA <sup>3</sup>	-	17	CaCO <sub>3</sub>	Alfa Aesar	99.95 % <sup>2</sup>
7	CaMoO <sub>4</sub>	Alfa Aesar	99 %	18	Sc <sub>2</sub> O <sub>3</sub>	ALDRICH	99.99 %
8	Fe <sub>2</sub> O <sub>3</sub>	Alfa Aesar	99 %	19	Bi <sub>2</sub> O <sub>3</sub>	JOHNSON <sup>5</sup>	99.95 %
9	FeB	Alfa Aesar	99 %	20	SrCO <sub>3</sub>	JOHNSON <sup>5</sup>	99 %
10	HfO <sub>2</sub>	Alfa Aesar	99 % <sup>4</sup>	21	TiO <sub>2</sub>	ALDRICH	99.9 %
11	BaZrO <sub>3</sub>	Alfa Aesar	99.999 % <sup>2</sup>				

<sup>1</sup>: (metals basis excluding Hf)

<sup>2</sup>: (metals basis)

<sup>3</sup>: HOSAKAWA Powder Technology Research Institute

<sup>4</sup>: (metals basis excluding Zr)

<sup>5</sup>: JOHNSON MATTHEY

**Table 8** A list of dopants added into SmBCO and the corresponding amount used in this research.

No.	Dopants	Amount	No.	Dopants	Amount	No.	Dopants	Amount
1	ZrO <sub>2</sub>	1 mol. %	16	TiO <sub>2</sub>	4 mol. %	31	SnO	1 mol. %
2	ZrO <sub>2</sub>	2 mol. %	17	TiO <sub>2</sub>	1 wt. %	32	RbCl	1 mol. %
3	ZrO <sub>2</sub>	4 mol. %	18	TiO <sub>2</sub>	2 wt. %	33	Tb <sub>4</sub> O <sub>7</sub>	1 mol. %
4	ZrO <sub>2</sub>	1 wt. %	19	Bi <sub>2</sub> O <sub>3</sub>	1 mol. %	34	ZnO	1 mol. %
5	ZrO <sub>2</sub>	2 wt. %	20	SrCO <sub>3</sub>	1 mol. %	35	CaCO <sub>3</sub>	1 mol. %
6	Nano-ZrO <sub>2</sub>	1 mol. %	21	Sc <sub>2</sub> O <sub>3</sub>	1 mol. %	A mixture of x mol. % ZrO <sub>2</sub> + y mol. % BaZrO <sub>3</sub>		
7	'Sm-2411'	1 mol. %	22	Ta <sub>2</sub> O <sub>5</sub>	1 mol. %			
8	'Sm-2411'	4 mol. %	23	HfO <sub>2</sub>	1 mol. %			
9	'Sm-2411'	1 wt. %	24	CaMoO <sub>4</sub>	1 mol. %			
10	'Sm-2411'	2 wt. %	25	Fe <sub>2</sub> O <sub>3</sub>	1 mol. %			

11	BaZrO <sub>3</sub>	1 mol. %	26	FeB	1 mol. %	x	y
12	BaZrO <sub>3</sub>	4 mol. %	27	Ga <sub>2</sub> O <sub>3</sub>	1 mol. %	36	1.0
13	BaZrO <sub>3</sub>	1 wt. %	28	Gd <sub>2</sub> O <sub>3</sub>	1 mol. %	37	0.75
14	BaZrO <sub>3</sub>	2 wt. %	29	Na <sub>2</sub> CO <sub>3</sub>	1 mol. %	38	0.5
15	TiO <sub>2</sub>	1 mol. %	30	NbO <sub>2</sub>	1 mol. %	39	0.25

Most samples in this section were grown using thin film seeds consisting of NdBCO of thickness 700 nm deposited on a single crystal MgO-substrate provided by Ceraco [118] to save time. Several of the samples were also fabricated using generic seeds on buffers to reduce the cost of production. Buffers were prepared using commercially available Sm-123 (TOSHIMA, average particle size: 2-3  $\mu\text{m}$ ) and Sm-211(TOSHIMA, average particle size: 1-2  $\mu\text{m}$ ) powders. A motorized pestle and mortar was again used to mix the powders thoroughly, prior to being pressed uniaxially under a load of 0.5 tons into a green pre-form with dimensions of 3 mm in both diameter and thickness.

The TSMG process was used to fabricate large, single grain SmBCO superconductors. For samples grown without buffers, such as that illustrated schematically in Figure 40 (a), a thin film seed was placed at the centre of the upper surface of the sample with its  $a/b$ -plane in direct contact with the sample in order to yield the required grain orientation, while, for samples grown with buffers, a MgO-NdBCO generic seed was placed with its  $a/b$ -plane in direct contact with the top of the as-prepared buffer and the buffer-seed arrangement placed at the centre of the upper surface of the pre-form, as shown in Figure 40 (b).

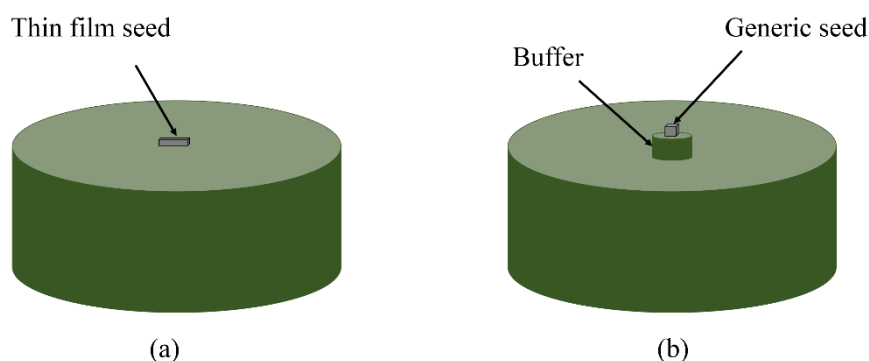


**Figure 40** Schematic illustration of the bulk pre-form with: (a) a thin film seed; and (b) a MgO-NdBCO generic seed on a buffer.

The heating profile used is illustrated in Figure 41. The appropriate values of the melting temperature of the precursor powders, grain nucleation temperature, crystallization temperature and the optimum final growth temperatures,  $T_m$ ,  $T_s$ ,  $T_{g1}$  and  $T_{g2}$ , were determined using differential thermal analysis (DTA). Adjustments to these temperatures were made according to different sample compositions. In general, the pellet was initially heated slowly at  $50\text{ }^\circ\text{C h}^{-1}$  to  $200\text{ }^\circ\text{C}$  to stabilize the furnace temperature and the thin film seed, then more rapidly at a rate of  $200\text{ }^\circ\text{C h}^{-1}$  to  $900\text{ }^\circ\text{C}$ . The temperature was then raised slowly to  $T_{max}$  and held for 0.5 hour to ensure complete decomposition of the precursor pellet. The partially molten sample was then cooled at  $B\text{ }^\circ\text{C h}^{-1}$  to its seeding temperature,  $T_s$ , followed by further cooling to its crystallization temperature  $T_{g1}$  at a rate of  $C\text{ }^\circ\text{C h}^{-1}$ , followed by another slower cooling stage to  $T_{g2}$  at the rate of  $D\text{ }^\circ\text{C h}^{-1}$ . Finally, the sample was furnace cooled to room temperature at  $150\text{ }^\circ\text{C h}^{-1}$ . The specific values in the heating profile will be discussed further with the DTA results for samples with different compositions.

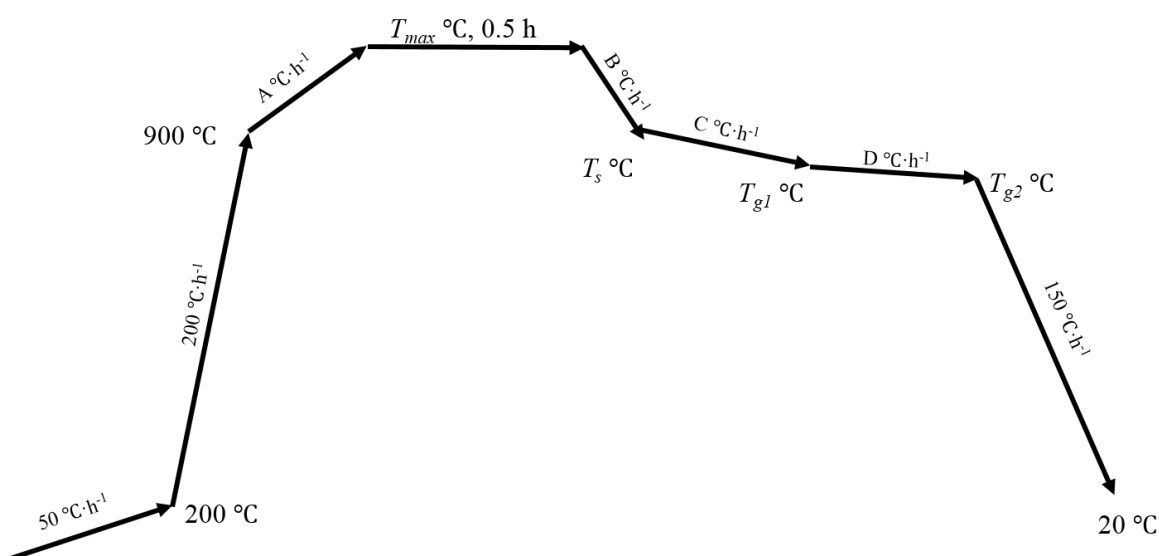


**Figure 41** Schematic illustration of the TSMG process for the growth of bulk SmBCO.

The as-grown samples were oxygenated at  $360\text{ }^\circ\text{C}$  for fourteen days to drive the non-superconducting, tetragonal phase to the desired orthorhombic superconducting phase.

After each calcination at a different temperature, x-ray powder diffraction (XRD) was performed by SIEMENS Diffractometer D500 and used to confirm when a Sm-2411(Zr) single phase had formed. The International Centre for Diffraction Data Database was employed to determine the phase after each calcination. The particle size of this phase was not measured in this study, however, an earlier study on the  $\text{Y}_2\text{Ba}_4\text{CuNbO}_y$  phase synthesized

under similar conditions revealed the presence of nano-scale (20-100 nm) particles [123], indicating that the calcination process refines the size of the particles.

In order to decide the melting ( $T_m$ ), seeding ( $T_s$ ), crystallization ( $T_{g1}$ ) and final growth ( $T_{g2}$ ) temperatures in the heating profile used in TSMG, differential thermal analysis (DTA) was performed for most of the precursor powders. Pellets of the same diameter and thickness of 3 mm with the composition as listed in Table 4 were prepared for DTA measurements. In each case, a small generic seed was placed at the centre of the top surface of the pellet to simulate the TSMG process at elevated temperatures.

Optical microscopy was carried out as described in Section 3.3.1.1 to examine the size and distribution of Sm-211 particles in the as-grown SmBCO single grains, along both the  $a/b$ - and  $c$ - axes.

The samples were cut into slices across their centre, with each slice being cut into smaller specimens, as shown schematically in Figure 42. The spatial changes in  $T_c$  and  $J_c$  of the specimens with proximity to the seed were measured as described in Section 3.3.2.1.

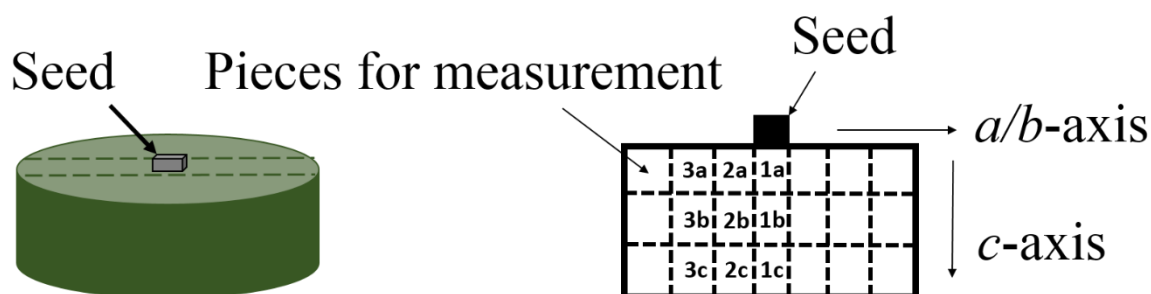


**Figure 42** How each single grain was cut following melt processing and illustration of the position of the sub-specimens within the parent bulk used for measuring  $T_c$  and  $J_c$ .

## 5.3.2. Results and Discussion

### 5.3.2.1. The Formation of Sm-2411 (Zr)

X-ray diffraction patterns of the powders calcined at different temperatures in order to fabricate Sm-2411(Zr), as shown in Figures 43 (1)-(11), reveal changes to crystalline content

after each heat treatment. A peak corresponding to a new phase starts to appear after calcining at 870 °C for 80 h, while, at the same time, the characteristic peaks of the constituent precursor oxides gradually weaken. Additional peaks corresponding to the new phase emerge and become more intense as further calcination is performed. Most of the precursor oxide peaks disappear and the new phase becomes dominant as the calcination temperature is increased to 990 °C for 40 h. The mixture was finally sintered at 1040 °C for 50 h, when the XRD pattern displayed the peaks of the new phase, as illustrated in Figure 43 (11).

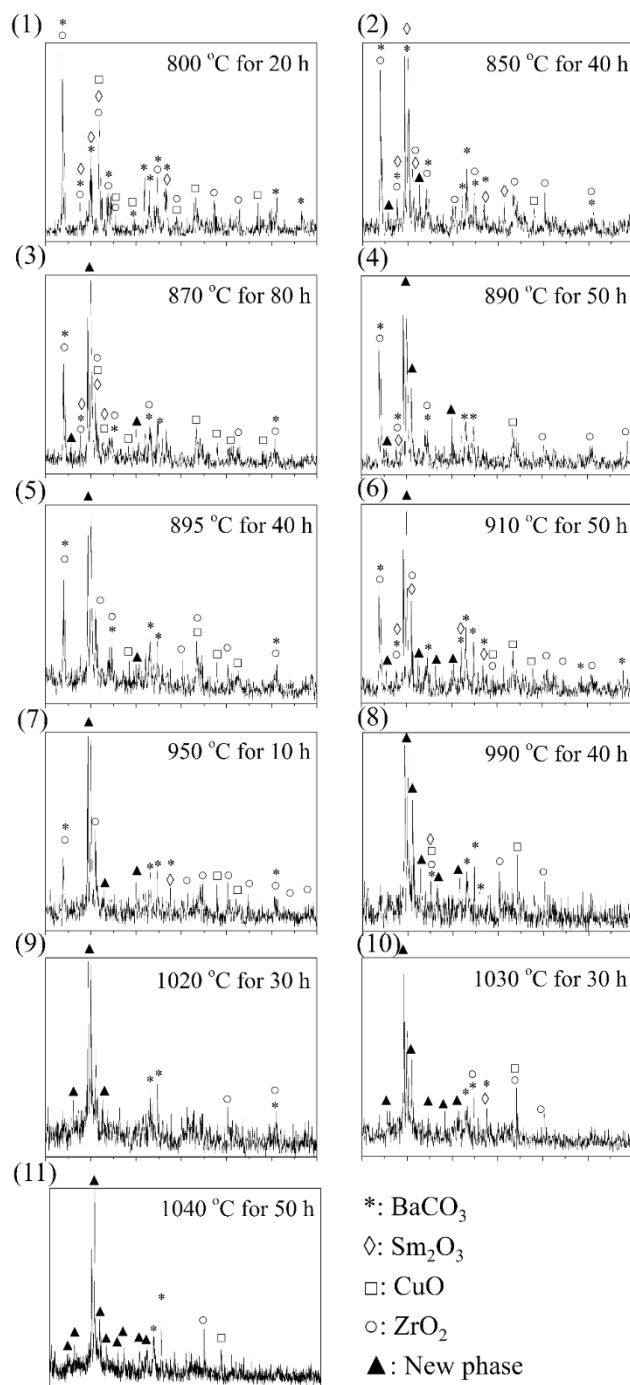


**Figure 43** X-ray diffraction patterns for solid-state reacted powders with starting compositions of Sm<sub>2</sub>O<sub>3</sub>, BaCO<sub>3</sub>, CuO and ZrO<sub>2</sub> after each calcination with the standard oxides as references for the temperatures and times shown. All peaks are indexed with different symbols to attribute the peaks to different standard oxides.

The new phase was identified as ‘00-046-0142: Ba(Sm<sub>1.8</sub>Y<sub>0.2</sub>)CuO<sub>5</sub>’ using the International Centre for Diffraction Data Database, as shown in Figure 44 (a). The yttrium in

$\text{Ba}(\text{Sm}_{1.8}\text{Y}_{0.2})\text{CuO}_5$  should correspond, in this case, to samarium since there is no yttrium in the precursor powders. Indeed, after repeated calcination at elevated temperatures, the new phase obtained was mainly  $\text{Sm}_2\text{BaCuO}_5$  (Sm-211) rather than Sm-2411 (Zr). The comparison of the XRD patterns between the new phase and the standard Sm-211 further confirms this observation. Although the attempt to synthesize Sm-2411 (Zr) failed, Sm-211 obtained after repeated calcination and grinding should have smaller particle sizes and, therefore, still serves as an effective dopant. This new phase is referred to as ‘fine Sm-211’ in the remainder of this thesis.

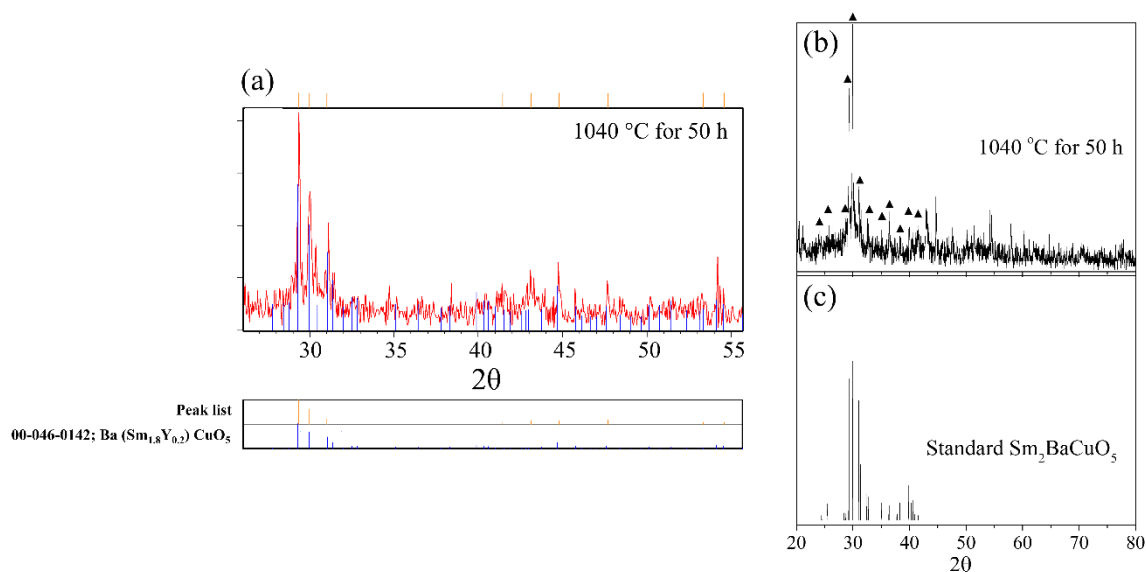


**Figure 44** (a) Analysis using International Centre for Diffraction Data Database; X-ray diffraction patterns for (b) powders after final calcination at 1040 °C for 50 h and (c) standard Sm-211.

### 5.3.2.2. The Effects of Doping on the Growth of SmBCO Single Grains

The melting ( $T_m$ ), seeding ( $T_s$ ), crystallization ( $T_{g1}$ ) and final growth ( $T_{g2}$ ) temperatures in Figure 41 were measured using differential thermal analysis (DTA), with the DTA traces shown in Figure 45. The measurement of all the different precursor powders can provide information on how these temperatures are influenced by the various dopants. For DTA measurements, pellets with a small, generic seed placed at the centre of the top surface were

prepared to simulate the TSMG process at elevated temperatures. With all these different dopants, the decomposition (melting) temperatures in Figure 45, determined from the peak DTA value, vary only from 1066 °C to 1072 °C, as shown by the dotted lines. Only the 1 wt. % and 2 wt. % TiO<sub>2</sub>-doped SmBCO indicated by the arrows exhibit peaks outside the range. Therefore, it is possible to grow these samples with a heating profile that is largely the same with only minor adjustments in specific cases. According to the DTA traces, at an interval of 1 °C,  $T_{max}$  was set generally within the range between 1060 °C and 1087 °C,  $T_s$  between 1046 °C and 1078 °C,  $T_{g1}$  between 1046 °C and 1064 °C and  $T_{g2}$  between 1041 °C and 1058 °C.

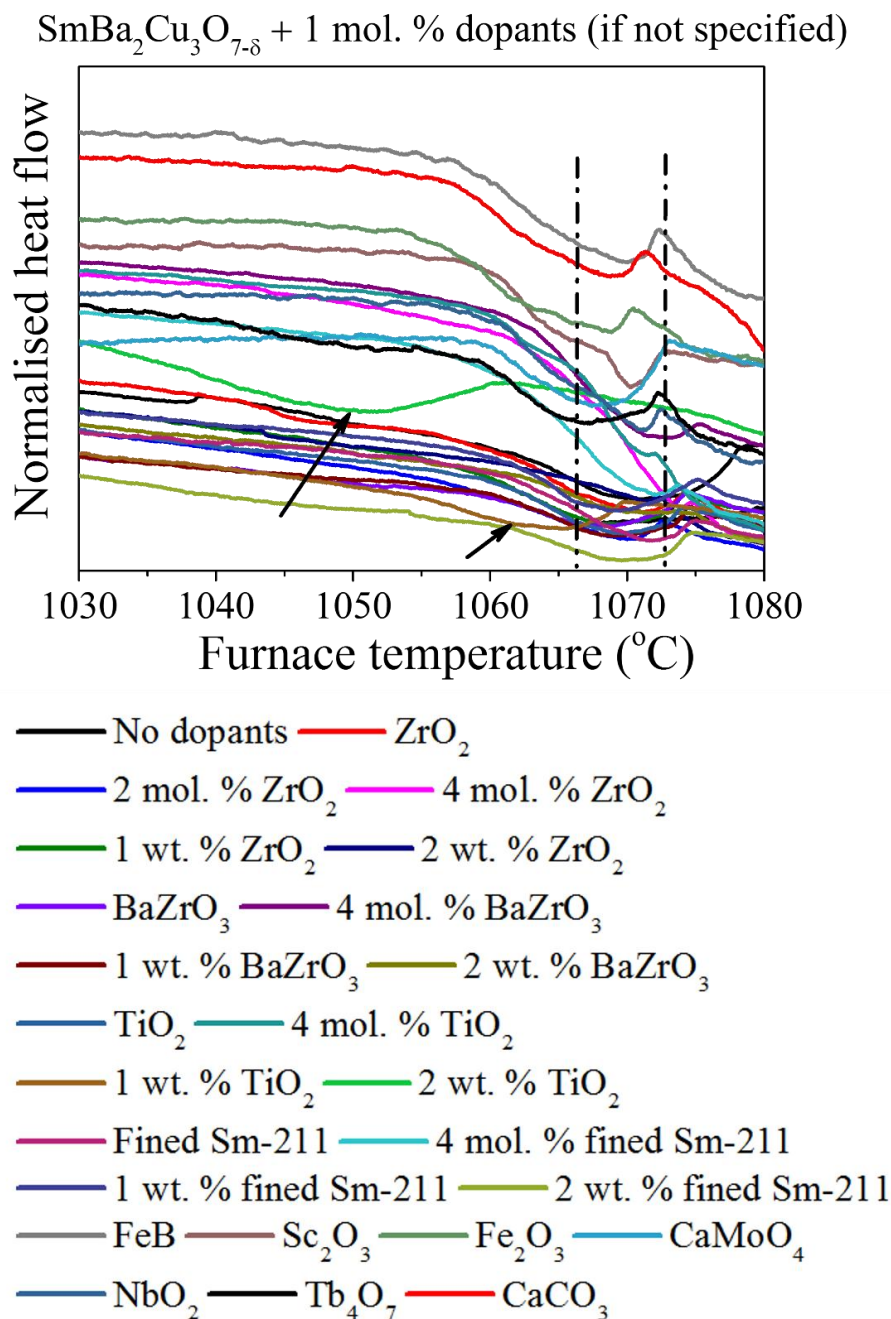


**Figure 45** DTA traces of doped and undoped SmBCO with MgO-NdBCO generic seeds indicating the decomposition (melting) temperatures.

The heating profile shown in Figure 46 was used to melt process standard SmBCO samples. SmBCO samples containing 1 mol. % dopants were fabricated by lowering the growth-related temperatures by 2  $^{\circ}\text{C}$ , and an even lower temperature was used if the amount of dopants was increased to 2 mol. %, or even larger. Additionally, for dopants such as  $\text{Sc}_2\text{O}_3$  and  $\text{Bi}_2\text{O}_3$ , which did not fit the general heating profile, these temperatures were further

adjusted empirically to achieve fully grown single grains. There are four important ramping rates in the heating profile, A, B, C and D, respectively (Figure 41). For A and B, the main purpose is to ensure a comparatively stable furnace temperature increase and cool-down to a target temperature so that the precursors powders were decomposed stably. The ramp rate A was set at four different values,  $50\text{ }^{\circ}\text{C h}^{-1}$ ,  $60\text{ }^{\circ}\text{C h}^{-1}$ ,  $75\text{ }^{\circ}\text{C h}^{-1}$  and  $100\text{ }^{\circ}\text{C h}^{-1}$ , and B at three,  $60\text{ }^{\circ}\text{C h}^{-1}$ ,  $75\text{ }^{\circ}\text{C h}^{-1}$  and  $100\text{ }^{\circ}\text{C h}^{-1}$  during the heating profile adjustments. For the current heating profile, both A and B were set empirically at  $75\text{ }^{\circ}\text{C h}^{-1}$  based on an extensive set of experimental trials. C and D, which are more crucial for single grain growth, determine the melting and growing time. In the current heating profile, appropriate values of C ( $1\text{ }^{\circ}\text{C h}^{-1}$ ) and D ( $0.8\text{ }^{\circ}\text{C h}^{-1}$ ) were selected to reduce liquid loss whilst ensuring sufficient growth time for the single grain. In previous experiments, C and D had been set as  $3\text{ }^{\circ}\text{C h}^{-1}$  and  $0.2\text{ }^{\circ}\text{C h}^{-1}$ , although these relatively extreme values did not produce positive results. A fast ramping rate C leads to the growth of sub-grains, whereas a slow ramping rate D increases the difficulty in retaining sufficient liquid for growth. Furthermore, these temperatures should be adjusted according to individual furnace conditions, while at the same time taking the properties of different dopants and their amounts into account.

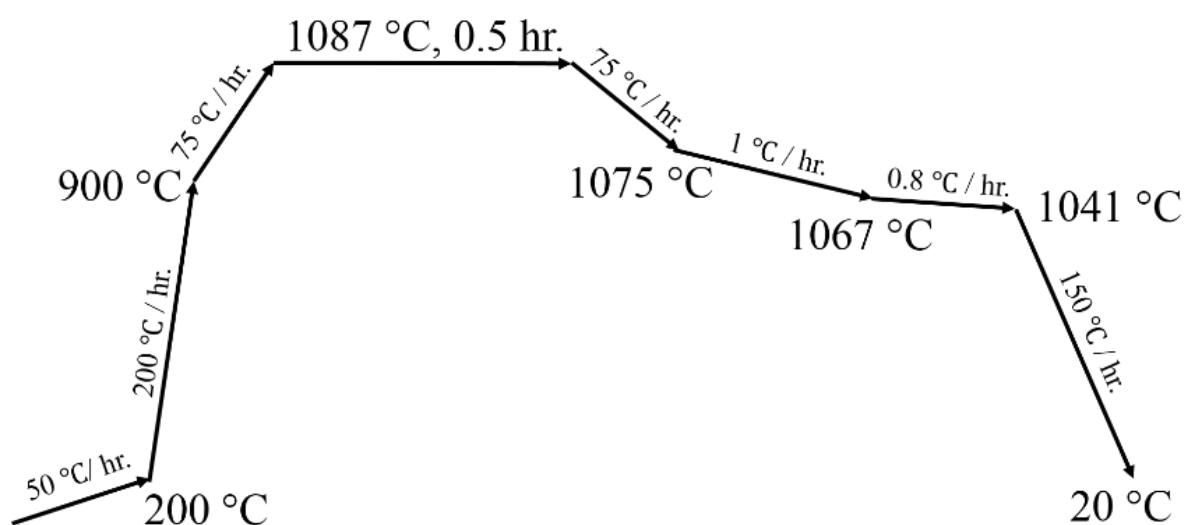


**Figure 46** Schematic illustration of the TSMG process for standard SmBCO growth.

Figure 47 shows photographs of the top surfaces of 21 standard SmBCO and SmBCO samples containing 1 mol. % dopants (10 g, 16 mm in diameter) grown successfully using the heating profile illustrated in Figure 46. The presence of the four orthogonal growth sector boundaries indicates successful single grain growth. Dopants added in this research are chosen from a wide range of chemicals as summarised in Table 4, including oxides,

carbonates, nano materials, cuprates, borides and chlorides. However, the attempt to grow these samples did not generally succeed in the first trial. Photographs of a selection of failed samples are shown in Figure 48 (the reasons for failure in each case are generally different). For example, seed melting during TSMG leads to the formation of random sub-grains for  $ZrO_2$ ,  $BaZrO_3$ , fine Sm-211,  $Tb_4O_7$ , ZnO and  $Na_2CO_3$ . The seeds tend to melt on one of their four corners, resulting in the growth of the single grain from three quarters instead of four. The reasons for this phenomenon may be attributed to the imperfection of the seed itself or to details of the heat distribution inside the furnace. It is not necessary to adjust the heating profile if the sample does not grow for this reason. Instead, better choice of seed or adding a partition inside the furnace to balance the heat distribution would create better conditions for growing a single grain, as shown on the right-hand side in each group of photographs. The failed sample in the case of  $Sc_2O_3$  did grow in the form of a small single grain at the centre of the bulk but is surrounded by numerous sub-grains, indicating that the growth-related temperatures in the heating profile are generally too high for 1 mol. %  $Sc_2O_3$ -doped SmBCO. The single grain grown successfully on the right-hand side of the figure was obtained by further lowering the growth-related temperatures in the heating profile by 2 °C.

**SmBa<sub>2</sub>Cu<sub>3</sub>O<sub>7-δ</sub> + 1 mol. % dopant**

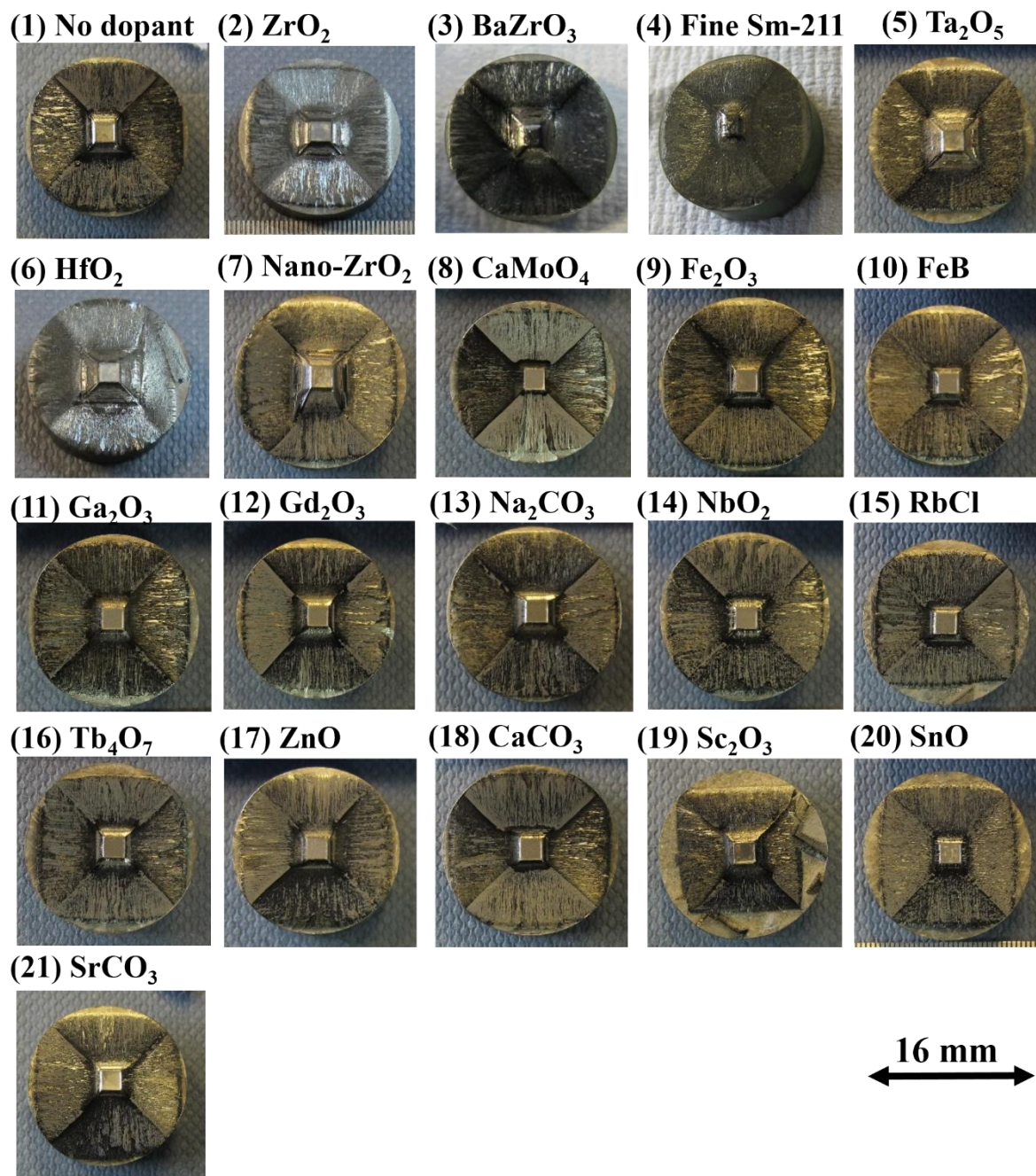


**Figure 47** SmBCO single grains grown successfully with 1 mol. % different dopants (16 mm in diameter).

Failed  $\text{SmBa}_2\text{Cu}_3\text{O}_{7-\delta}$  + 1 mol. % dopant and well-grown samples with the same compositions

(1)  $\text{ZrO}_2$



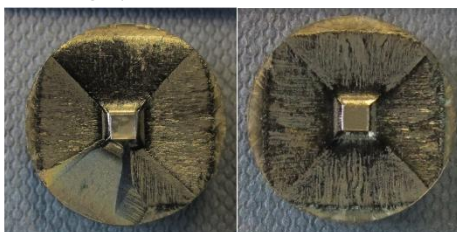
(2)  $\text{BaZrO}_3$



(3) Fine Sm-211



(4)  $\text{Tb}_4\text{O}_7$



(5)  $\text{Na}_2\text{CO}_3$



(6)  $\text{Sc}_2\text{O}_3$



(7)  $\text{ZnO}$



16 mm



**Figure 48** Failed SmBCO single grain samples in the first batch and grown subsequently into single grains after minor adjustments in a following batch.

The difficulties of successful growth increase with the increase of doping level in SmBCO. As shown in Figure 49, samples with different dopants in larger amounts fail to grow into single grains either due to the failure of seeds, as in the cases of 1 mol. %, 4 mol. % 1 wt. % and 2 wt. %  $\text{TiO}_2$ , 2 mol. % and 4 mol. %  $\text{ZrO}_2$ , 1 mol. %  $\text{Bi}_2\text{O}_3$ , 4 mol. % fine Sm-211 and 1 wt. %  $\text{BaZrO}_3$  dopants, or due to inappropriate temperatures in the heating profiles, as in the cases of 4 mol. % and 2 wt. %  $\text{BaZrO}_3$ , 1 wt. % and 2 wt. % fine Sm-211 and 1 wt. %  $\text{ZrO}_2$  dopants. Since the uniformity of the precursor powders is critical to obtaining a single grain, achieving a homogeneity of a dopant in the precursor powders is more difficult for higher amounts of dopant and contamination of the seed by the bulk leads further to unsuccessful

seeding, and the success rate is lowered significantly, even with a perfect seed and an appropriate heating profile.

**Failed SmBa<sub>2</sub>Cu<sub>3</sub>O<sub>7-δ</sub> + dopant**

(1) 1 mol. % TiO<sub>2</sub> (2) 4 mol. % ZrO<sub>2</sub> (3) 4 mol. % BaZrO<sub>3</sub> (4) 4 mol. % Fine Sm-211



(5) 4 mol % TiO<sub>2</sub> (6) 1 mol. % Bi<sub>2</sub>O<sub>3</sub> (7) 1 wt. % ZrO<sub>2</sub> (8) 1 wt. % Fine Sm-211



(9) 1 wt. % TiO<sub>2</sub> (10) 1 wt. % BaZrO<sub>3</sub> (11) 2 wt. % ZrO<sub>2</sub> (12) 2 wt. % Fine Sm-211



(13) 2 wt. % TiO<sub>2</sub> (14) 2 wt. % BaZrO<sub>3</sub> (15) 2 mol. % ZrO<sub>2</sub>



16 mm

**Figure 49** Failed SmBCO with different dopants in different amounts.

### 5.3.2.3. Doping Effects to Superconducting Properties and Microstructure of SmBCO Single Grains

Samples containing 1 mol. %  $\text{ZrO}_2$ ,  $\text{BaZrO}_3$ ,  $\text{TiO}_2$ , and fine Sm-211 were prepared for SQUID magnetometry measurement and microstructural analysis to further investigate the effects of the dopants on superconducting properties. A SmBCO sample without any dopant was analysed as a benchmark to enable meaningful comparison of the properties of the doped samples. The top views of all the five samples are displayed in Figure 50. It can be seen that, except for SmBCO + 1 mol. %  $\text{TiO}_2$ , which has grown into only three quarters of a single grain, the remaining four samples are fully grown single grains with four clear facet lines, extending to the edges of the samples.

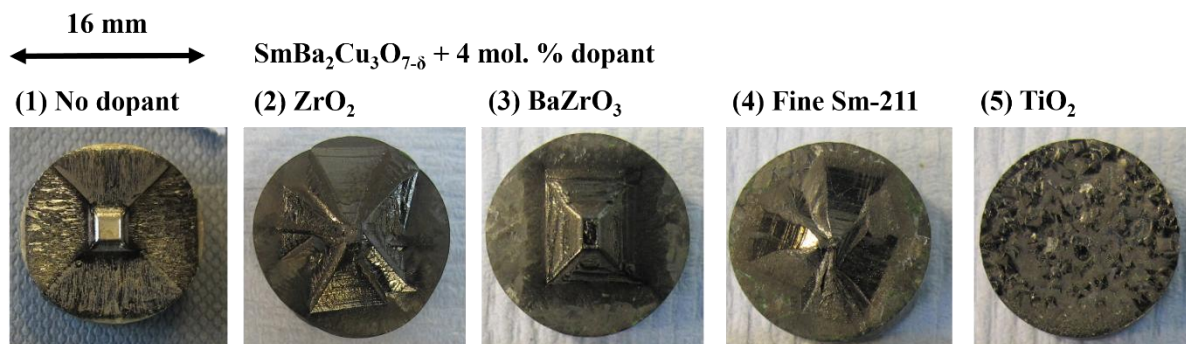


**Figure 50** Successfully grown (1) SmBCO and SmBCO doped with 1 mol. %: (2)  $\text{ZrO}_2$ ; (3)  $\text{BaZrO}_3$ ; (4) Fine Sm-211; and (5)  $\text{TiO}_2$  (three quarter of a single grain).

Figures 51 (a)-(e) show the results of the measurement of  $T_c$  ( $B = 0.002$  T,  $B \parallel c$ -axis) of standard SmBCO, 1 mol. %  $\text{ZrO}_2$ -doped SmBCO, 1 mol. %  $\text{BaZrO}_3$ -doped SmBCO, 1 mol. %  $\text{TiO}_2$ -doped SmBCO and 1 mol. % fine Sm-211-doped SmBCO at positions shown in Figure 51 (h).

Figure 51 (a) shows the onset  $T_c$  of standard SmBCO. The onset  $T_c$  at positions of 1a, 1b and 1c are the highest, while position 3c is the lowest, with the remaining positions exhibiting similar values. Also,  $\Delta T_c$  does not vary significantly for the remaining nine samples.

Figures 51 (b) and (d) show the onset  $T_c$  of 1 mol. %  $\text{ZrO}_2$ -doped and 1 mol. %  $\text{BaZrO}_3$ -doped SmBCO. These dopants yield no obvious distribution in the onset  $T_c$  and  $\Delta T_c$ .  $\Delta T_c$  in 1 mol. %  $\text{BaZrO}_3$ -doped SmBCO at position 1c exhibits the narrowest transition width.

The onset  $T_c$  of 1 mol. %  $\text{TiO}_2$ -doped SmBCO is shown in Figure 51 (c) and can be seen to be lower than the values observed for the other samples.

Figure 51 (e) shows the onset  $T_c$  of the sample containing 1 mol. % fine Sm-211-doped SmBCO. As in the case of 1 mol. %  $\text{ZrO}_2$ -doped and 1 mol. %  $\text{BaZrO}_3$ -doped SmBCO, there is no obvious variation in the onset  $T_c$  and  $\Delta T_c$  of this sample.

Specimens from the sample set with the highest onset  $T_c$  are summarised in Figure 51 (f). It can be seen that, 1 mol. % fine Sm-211 does not change significantly the onset  $T_c$  of SmBCO, since the doped sample has the same onset  $T_c$  of 93.30 K as the standard sample. A possible reason for this is that repeated calcination of the chemically stable Sm-211 merely refines the dopant powder. In addition, the net difference in composition between standard SmBCO and that containing 1 mol. % fine Sm-211 is too small to influence the onset  $T_c$ . On the other hand,  $\text{ZrO}_2$ ,  $\text{BaZrO}_3$  and  $\text{TiO}_2$  have a significant effect on onset  $T_c$ ; positively for  $\text{ZrO}_2$  and  $\text{BaZrO}_3$ , but negatively for  $\text{TiO}_2$ . The onset  $T_c$  of the bulk increases from 93.30 K to 93.55 K for 1 mol. %  $\text{ZrO}_2$  and  $\text{BaZrO}_3$  and  $\Delta T_c$  becomes narrower. An obvious decrease in the onset  $T_c$  from 93.30 K to 92 K is observed for the sample containing 1 mol. %  $\text{TiO}_2$ , which is accompanied by a broadening of  $\Delta T_c$  compared to the standard sample, indicating that the addition of  $\text{TiO}_2$  does not improve the superconducting properties of SmBCO.

The five samples are compared in Figure 51 (g) by averaging the magnetic moment at each temperature to find an overall onset  $T_c$  over the measured specimens in a given single grain. These average data show that the addition of  $\text{ZrO}_2$  and  $\text{BaZrO}_3$  has a favourable effect on sample properties, but that  $\text{TiO}_2$  does not. Fine Sm-211 has little impact on the SmBCO system. The ideal sample should be a homogenous single grain with similar superconducting properties across the whole bulk matrix, although, in practice, a distribution of the onset  $T_c$  is always observed in large grain samples. Therefore, when averaging onset  $T_c$ ,  $\text{ZrO}_2$  performs better than  $\text{BaZrO}_3$  in terms of  $\Delta T_c$ . Furthermore, adding 1 mol. % fine Sm-211 into SmBCO should not affect significantly the superconducting properties of SmBCO, since Sm-211 is present in the precursor composition. The wider average  $\Delta T_c$  with the addition of 1 mol. % fine Sm-211, compared to the standard sample indicates that the extra 1 mol. % fine Sm-211 may react with Zr-containing residue in the system, suggesting indirectly the assumption that the failure of the sample growth could be attributed to the insufficient mixing of the dopants into the precursor powders or the presences of Zr-containing impurities.

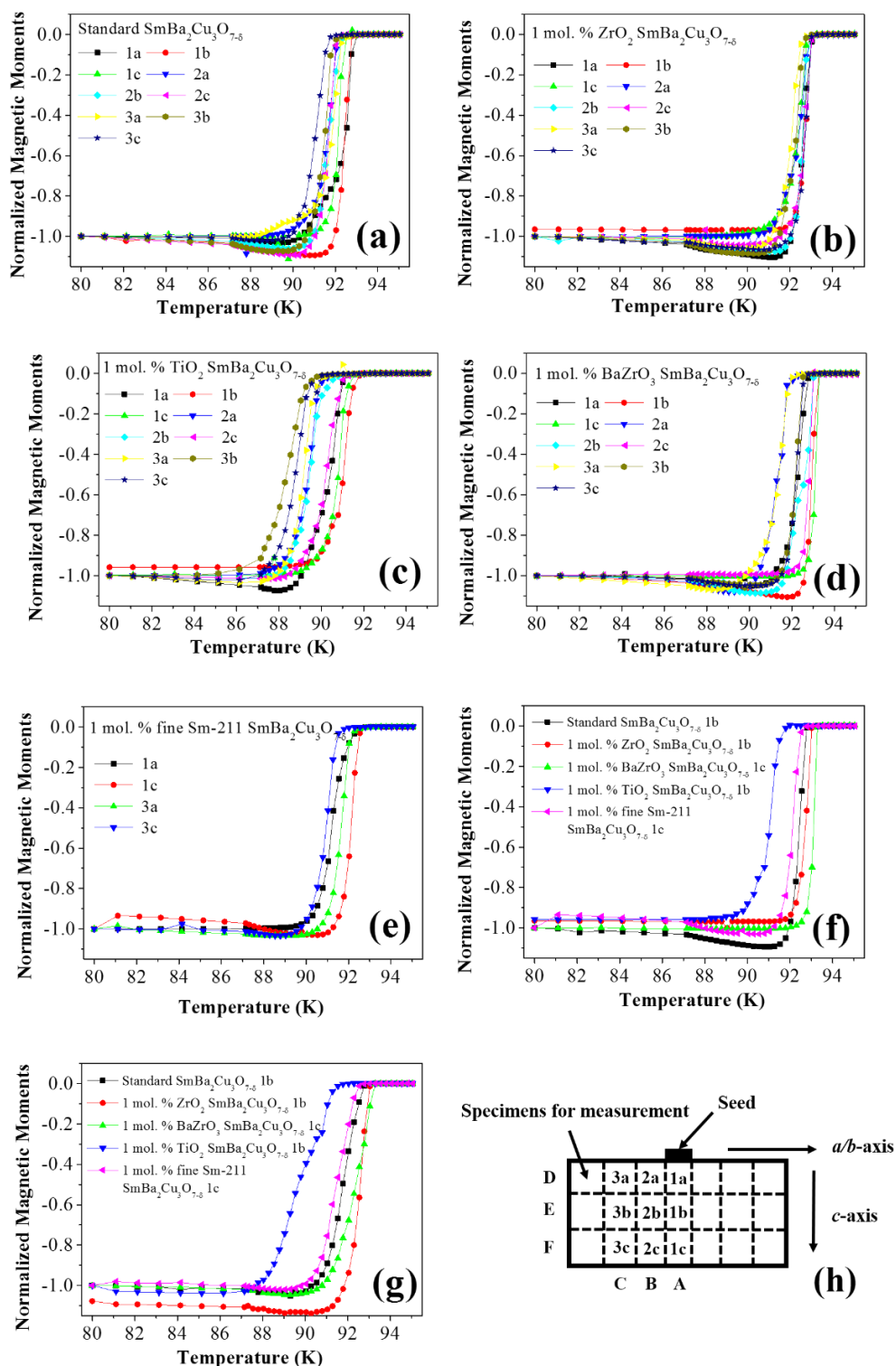


**Figure 51** Comparison of  $T_c$  for the specimens measured along the a/b-axis and the c-axis of (a) SmBCO; (b) SmBCO + 1 mol. %  $\text{ZrO}_2$ ; (c) SmBCO + 1 mol. %  $\text{TiO}_2$ ; (d) SmBCO + 1 mol. %  $\text{BaZrO}_3$ ; (e) SmBCO + 1 mol. % fine Sm-211; (f) the specimens yielding the highest  $T_c$  in each sample and (g) the average  $T_c$  in each sample and (h) schematic illustration of the positions of the specimens within the parent bulk used for measuring  $T_c$ .

Figures 52 (a)-(g) compare the  $J_c$ - $H$  ( $B \parallel c$ -axis) curves at 77 K at different positions in layers D, E and F for all five samples (standard SmBCO, 1 mol. %  $ZrO_2$ -doped SmBCO, 1 mol. %  $BaZrO_3$ -doped SmBCO, 1 mol. %  $TiO_2$ -doped SmBCO and 1 mol. % fine Sm-211-doped SmBCO). The field trapping ability of SmBCO,  $B=J_c \cdot R$ , is an important parameter for applications, and, therefore, it is important to understand the distribution of  $J_c$  at different positions in the sample. It is well known that  $J_c$  varies with position within each specimen as a result of the effects of grain misorientation and the presence of defects, such as cracks, pores, variation in Sm-211 concentration and impurities. In addition, each specimen measured was relatively small (approximate dimensions: 1.5 mm  $\times$  2.0 mm  $\times$  1.2 mm), so these data are representative only of a relatively small volume within the parent bulk single grain. As a result, specimens were selected for comparison at different positions in each single grain [illustrated schematically in Figures 52 (h)].

Figures 52 (a) shows the variation of  $J_c$  with field and position for standard SmBCO. The differences in  $J_c$  between layers A, B and C are quite pronounced, with specimens from the A layer giving more pronounced peak effects and higher irreversibility fields, whereas,  $J_c$ s in layers B and C are slightly lower than those in layer A. Therefore, it can be concluded that  $J_c$  decreases from the position of the seed in the standard samples. Additionally, specimens in layer E (1b, 2b, 3b) exhibit generally the best  $J_c$  characters. Possible explanations would be: (1) layer E is not directly under the seed, and so avoids contamination from the seeding material; (2) the distribution of Sm-211 particles in this layer is more homogenous compared to that in layers D or F, because the reaction with Sm-211 is less extensive (compared to that in layer D) and the aggregation of Sm-211 is not sufficiently severe to cause uneven pinning (compared to that in layer F), both of which would correspond to higher  $J_c$ .

The situation in 1 mol. %  $ZrO_2$ -doped SmBCO samples [Figures 52 (b)] is largely similar, with  $J_c$ s in layer A also giving the best peak effects and highest irreversibility fields, followed by those in layer B and then those in layer C. However, the fluctuation in properties between these specimens is larger than that in the standard sample. In addition, with the increasing viscosity due to the introduction of  $ZrO_2$  to the precursor powder, the reaction of Sm-211 in the vicinity of the seed is not as fast as in the standard sample, so, generally speaking, specimens in the top layer tend to exhibit better  $J_c$  [124]. Overall, with a considerably pronounced peak effect, the sample containing 1 mol. %  $ZrO_2$ -doped displays the most promising superconducting properties.

Samples containing BaZrO<sub>3</sub>, TiO<sub>2</sub> and fine Sm-211, in layer A generally yielded higher  $J_c$ s, further indicating that these dopants can improve the performance of the specimens under the seed relative to those at positions 3a, 3b or 3c at the extrema of the single grain, as shown in Figures 52 (c), (d) and (e).

The best performing specimens in each sample are compared in Figures 52 (f) to further clarify the effects of different dopants on the properties of bulk SmBCO. Peak effect and the irreversibility field are shown for the five specimens. The peak effect for the sample containing 1 mol. % ZrO<sub>2</sub> at position 1a has the highest value, followed by that containing 1 mol. % BaZrO<sub>3</sub> at position 1b, then standard SmBCO at position 1a. The samples containing 1 mol. % fine Sm-211 and 1 mol. % TiO<sub>2</sub> exhibit a much less pronounced peak effect. Regarding the irreversibility field, the sample containing 1 mol. % BaZrO<sub>3</sub> displays the highest field value, with 1 mol. % ZrO<sub>2</sub> and standard SmBCO showing slightly smaller values. Finally, the samples containing 1 mol. % fine Sm-211 and 1 mol. % TiO<sub>2</sub> do not exhibit particularly high values of irreversibility field.

The average  $J_c$  of all the specimens with different dopants measured by SQUID are shown in Figures 52 (g). Sm-211 is already a component of the precursor powders, there is no obvious change in  $J_c$  for the sample containing this dopant compared to the standard sample. The ZrO<sub>2</sub> and BaZrO<sub>3</sub> containing samples perform slightly better, and are both dopants capable of enhancing  $J_c$  in SmBCO, and generating a higher peak effect in higher field and higher irreversibility field. The sample containing TiO<sub>2</sub> exhibits the highest  $J_c$  of the five samples between an applied field of 0.3 T and 0.7 T, although it will not be considered further as a favourable dopant for bulk SmBCO since, on average, its performance is the lowest of the five bulk single grains investigated.

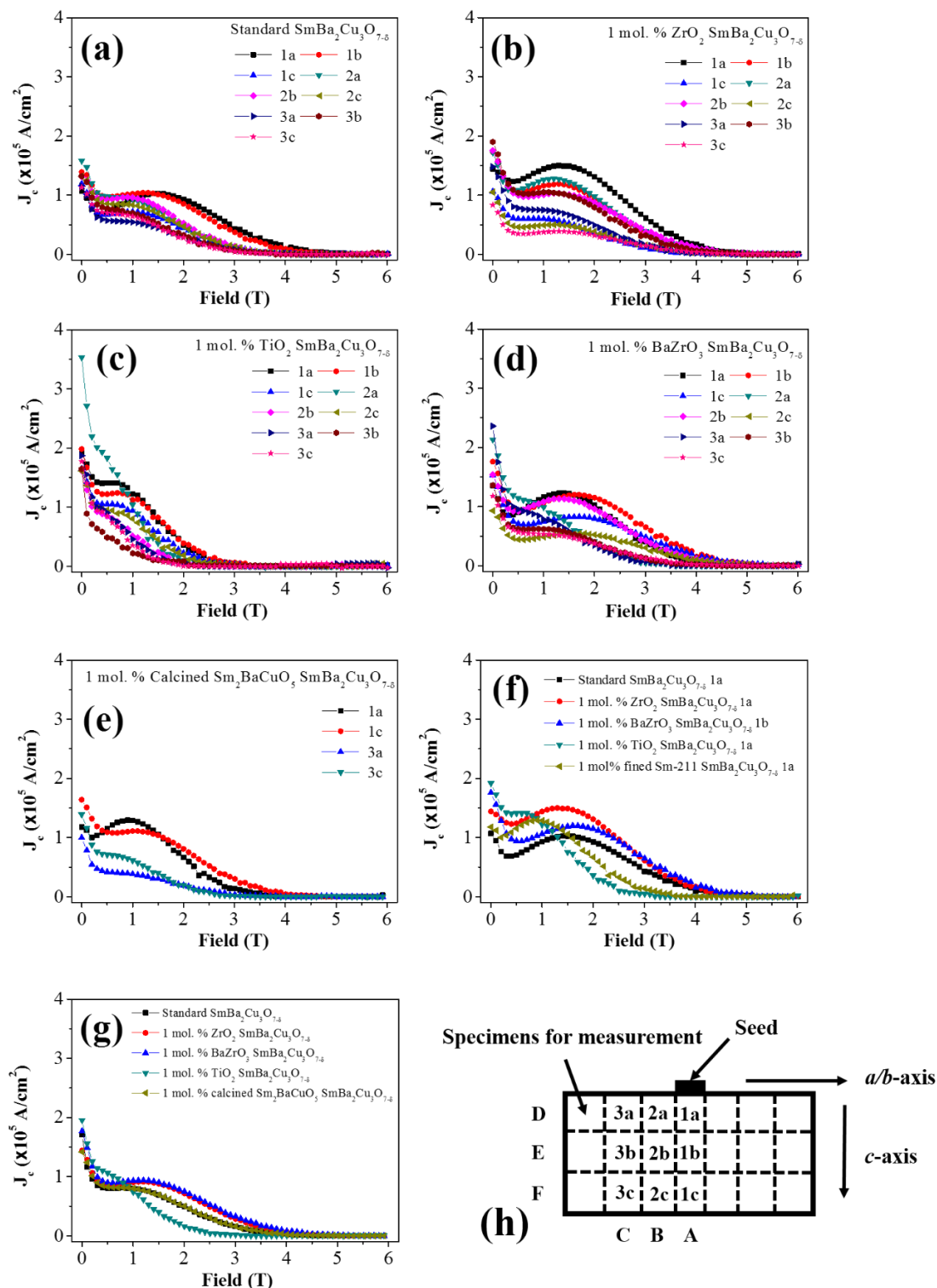


**Figure 52** (a) Comparison of  $J_c$  for specimens along the a/b-axis and the c-axis of (a) SmBCO; (b) SmBCO + 1 mol. % ZrO<sub>2</sub>; (c) SmBCO + 1 mol. % TiO<sub>2</sub>; (d) SmBCO + 1 mol. % BaZrO<sub>3</sub>; (e) SmBCO + 1 mol. % fine Sm-211; (f) the specimens giving the highest  $J_c$  in each sample; (g) the average  $J_c$  in each sample and (h) illustration of the position of the specimens within the parent bulk used for measuring  $J_c$ .

The analysis of  $T_c$  and  $J_c$  of the 1 mol. %  $ZrO_2$ - and  $BaZrO_3$ - doped samples indicates clearly that these two dopants are the most promising of those studied. Therefore, in an attempt to investigate these two dopants further, samples of mixed composition of  $x$  mol. %  $ZrO_2$  and  $y$  mol. %  $BaZrO_3$  [( $x, y$ )=(1, 0.5), (0.75, 0.25), (0.5, 0.5) and (0.25, 0.75)] were fabricated, as shown in Figure 53. The four characteristic facet lines that appear on the top surface and extend down the side of the single grains toward the base are immediate visual indications of the successful formation of single grains in these samples.

$SmBa_2Cu_3O_{7-\delta}$  + A mixture of  $x$  mol. %  $ZrO_2$  +  $y$  mol. %  $BaZrO_3$  ( $x, y$ )

(1) (1, 0.5)

(2) (1, 0)

(3) (0.75, 0.25)



(4) (0.5, 0.5)

(5) (0.25, 0.75)

(6) (0, 1)



16 mm



**Figure 53** Successfully grown SmBCO samples containing (1) 1 mol. %  $ZrO_2$  + 0.5 mol. %  $BaZrO_3$ ; (2) 1 mol. %  $ZrO_2$ ; (3) 0.75 mol. %  $ZrO_2$  + 0.25 mol. %  $BaZrO_3$ ; (4) 0.5 mol. %  $ZrO_2$  + 0.5 mol. %  $BaZrO_3$ ; (5) 0.25 mol. %  $ZrO_2$  + 0.75 mol. %  $BaZrO_3$  and (6) 1 mol. %  $BaZrO_3$ .

The comparison of the standard sample and those containing 1 mol. %  $ZrO_2$  and 1 mol. %  $BaZrO_3$  was discussed in the previous section. Here, the samples with a mixture of dopants

are considered in a similar way. The  $T_c$  and  $J_c$  of the specimens of four samples at positions 1a, 1b and 1c indicated in Figure 42 are shown in Figure 54. These samples include: standard SmBCO, 1 mol. %  $ZrO_2$ -SmBCO, 1 mol. %  $ZrO_2$  + 0.5 mol. %  $BaZrO_3$ -SmBCO and 0.5 mol. %  $ZrO_2$  + 0.5 mol. %  $BaZrO_3$ -SmBCO. The onset  $T_c$  of standard SmBCO, 1 mol. %  $ZrO_2$ -SmBCO, 1 mol. %  $ZrO_2$  + 0.5 mol. %  $BaZrO_3$ -SmBCO and 0.5 mol. %  $ZrO_2$  + 0.5 mol. %  $BaZrO_3$ -SmBCO are 91.06 K, 93.56 K, 93.01 K and 92.60 K, respectively.  $\Delta T_c$  for these specimens is largely the same. The sample containing 1 mol. %  $ZrO_2$  exhibits a more pronounced peak effect and a higher irreversibility field. Although samples processed with a mixture of dopants tend to perform better than the standard sample, in terms of peak effect and the irreversibility field, their overall properties remain inferior to those of the sample containing  $ZrO_2$  as a single dopant. This could be attributed to some extent to the homogeneity of the precursor powders. Although the dopants can clearly improve the superconducting properties of SmBCO single grains by generating extra pinning centres, two different dopants are more difficult to mix uniformly than a single dopant, leading to a potentially variable and less reliable precursor powder composition and further deterioration of the superconducting properties of SmBCO. Therefore, a combination of various dopants is not considered to be an effective way to further improve superconducting properties as in the case of a single dopant.

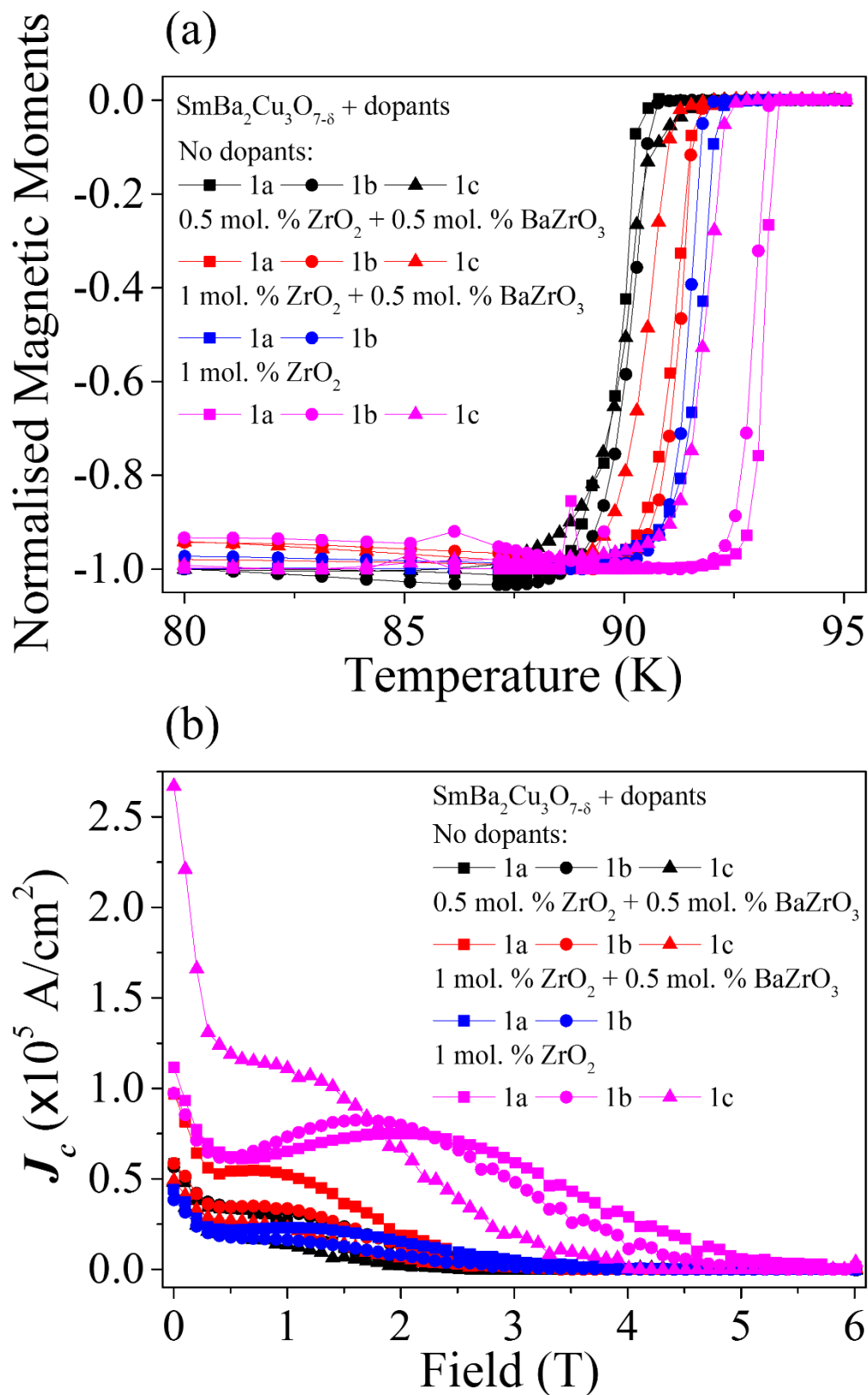


**Figure 54** Comparison of  $T_c$  (a) and  $J_c$  (b) for the specimens at 1a, 1b and 1c positions in Figure 42 of standard SmBCO, 1 mol. %  $\text{ZrO}_2$ -SmBCO, 1 mol. %  $\text{ZrO}_2$  + 0.5 mol. %  $\text{BaZrO}_3$ -SmBCO and 0.5 mol. %  $\text{ZrO}_2$  + 0.5 mol. %  $\text{BaZrO}_3$ -SmBCO.

ZrO<sub>2</sub> and BaZrO<sub>3</sub> have been identified as effective dopants for SmBCO bulk superconductors from the results of SQUID measurements of  $T_c$  and  $J_c$ . In order to explore how ZrO<sub>2</sub> and BaZrO<sub>3</sub> dopants improve the superconducting properties of SmBCO, their microstructures were observed optically to examine the size and distribution of Sm-211, which is considered usually to be the key variable determining  $J_c$ . Therefore, microstructural observation was performed on 1 mol. % ZrO<sub>2</sub>-doped SmBCO and 1 mol. % BaZrO<sub>3</sub>-doped SmBCO with standard SmBCO as a reference.

Figures 55 (a)-(f) show the microstructures of SmBCO single grains processed without any dopants, and with 1 mol. % ZrO<sub>2</sub> and 1 mol. % BaZrO<sub>3</sub> addition observed using an optical microscope at different positions within the bulk single grain. Previous research has indicated that Y-211 particles tend to distribute throughout an as-grown single grain bulk sample [105], and similar trends are observed in the SmBCO sub-specimens prepared here, regardless of the presence of dopants. There are fewer Sm-211 particles in the vicinity of the seed and towards the edge of the sample due to the better diffusion of Sm-211 in the Ba-rich liquid phase for forming Sm-123 near the seed at elevated temperatures. On the other hand, there is an obvious aggregation of Sm-211 particles within these samples.

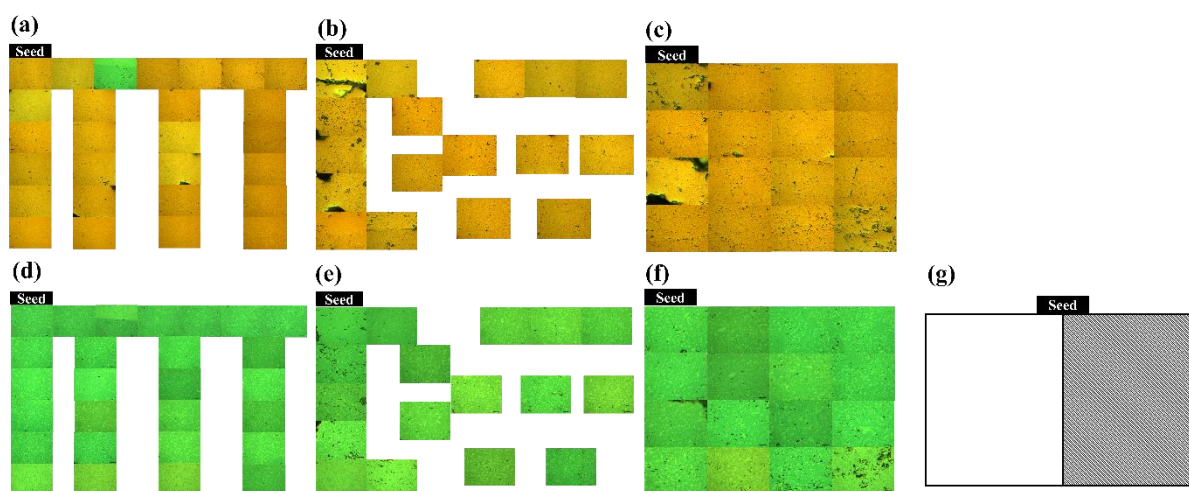


**Figure 55** Micrographs showing the Sm-211 distribution and particle size in SmBCO, 1 mol. % ZrO<sub>2</sub>-doped SmBCO and 1 mol. % BaZrO<sub>3</sub>-doped SmBCO: with a magnification of 500 times: (a) SmBCO; (b) 1 mol. % ZrO<sub>2</sub>-doped SmBCO; (c) 1 mol. % BaZrO<sub>3</sub>-doped SmBCO; with a magnification of 1000 times: (d) SmBCO; (e) 1 mol. % ZrO<sub>2</sub>-doped SmBCO; (f) 1 mol. % BaZrO<sub>3</sub>-doped SmBCO and (g) an illustration of the positions where the micrographs were taken (the shaded area).

Figures 57 to 60, which are derived from Figure 55, show the Sm-211 size (with a magnification of 1000 times) and distribution (with a magnification of 500 times) of standard SmBCO, 1 mol. %  $\text{ZrO}_2$ -doped SmBCO and 1 mol. %  $\text{BaZrO}_3$ -doped SmBCO, respectively, in the region labelled A, B, C and D in Figure 56. In section A in Figure 57, in the vicinity of the seed, there are more Sm-211 particles with smaller size in the sample containing 1 mol. %  $\text{ZrO}_2$  and 1 mol. %  $\text{BaZrO}_3$ , which explains the high  $J_c$  in this region. Further comparison of the samples containing 1 mol. %  $\text{ZrO}_2$  and 1 mol. %  $\text{BaZrO}_3$ , although the number of Sm-211 particles did not vary significantly, suggests that both are capable of improving the local  $J_c$ , at positions near the seed. This is consistent with the observation that  $\text{ZrO}_2$  performs better as a dopant, since the size of the particles is observed to be smaller in 1 mol. %  $\text{ZrO}_2$ -doped SmBCO.

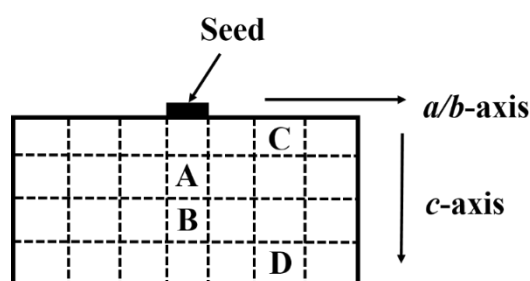


**Figure 56** Illustration of the positions of the regions where the microstructures were taken and compared in Figures 57 to 60.

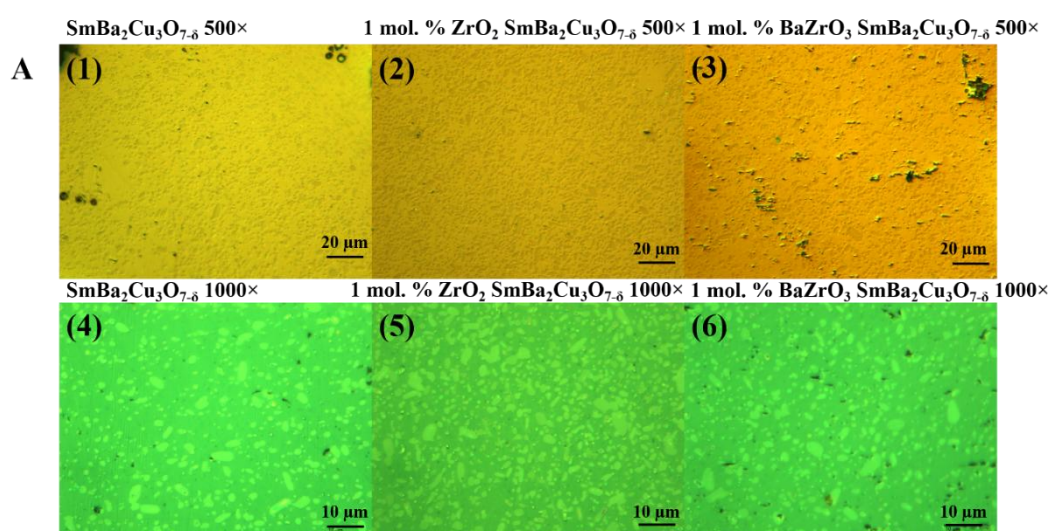


**Figure 57** Micrographs showing the Sm-211 distribution and particle size in SmBCO, 1 mol. %  $\text{ZrO}_2$ -doped SmBCO and 1 mol. %  $\text{BaZrO}_3$ -doped SmBCO at section A in Figure 56 with a magnification of 500 times: (1) SmBCO; (2) 1 mol. %  $\text{ZrO}_2$ -doped SmBCO; (3) 1 mol. %

BaZrO<sub>3</sub>-doped SmBCO with a magnification of 1000 times: (4) SmBCO; (5) 1 mol. % ZrO<sub>2</sub>-doped SmBCO and (6) 1 mol. % BaZrO<sub>3</sub>-doped SmBCO.

Comparing the properties of the Sm-211 inclusions at positions A and B (shown in Figure 58) reveals that the aggregation of Sm-211 particles is more visible in 1 mol. % ZrO<sub>2</sub>-doped and standard SmBCO samples, whereas in the 1 mol. % BaZrO<sub>3</sub>-doped SmBCO, there are still many Sm-211 particles of relatively small size. So, in the vicinity of region B, the peak effect and the irreversibility field derived from the  $J_c$  curves are most prominent in 1 mol. % BaZrO<sub>3</sub>-doped SmBCO, which is opposite to the case for 1 mol. % ZrO<sub>2</sub>-doped and standard SmBCO samples, which exhibit an obvious decrease in  $J_c$ .

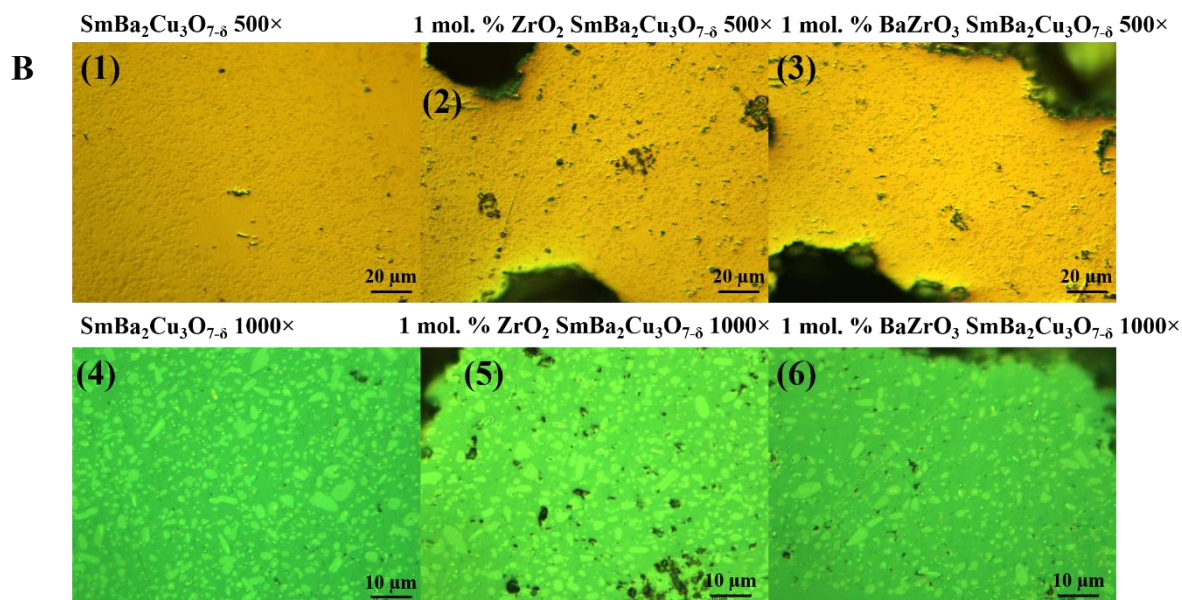


**Figure 58** Micrographs showing the Sm-211 distribution and particle size in SmBCO, 1 mol. % ZrO<sub>2</sub>-doped SmBCO and 1 mol. % BaZrO<sub>3</sub>-doped SmBCO at section B in Figure 56 with a magnification of 500 times: (1) SmBCO; (2) 1 mol. % ZrO<sub>2</sub>-doped SmBCO; (3) 1 mol. % BaZrO<sub>3</sub>-doped SmBCO with a magnification of 1000 times: (4) SmBCO; (5) 1 mol. % ZrO<sub>2</sub>-doped SmBCO and (6) 1 mol. % BaZrO<sub>3</sub>-doped SmBCO.

The accumulation of Sm-211 particles is generally severe along both  $a/b$ - and  $c$ - axes as shown in Figures 59 and 60, which correlates directly with a significant decrease in  $J_c$ . The observed size of the Sm-211 particles increases from a few micrometres to nearly 10  $\mu\text{m}$ . In particular, for region D in 1 mol. % BaZrO<sub>3</sub>-doped SmBCO, the largest Sm-211 particle has a

diameter of approximately  $15\ \mu\text{m}$ , which is significantly greater than the average Sm-211 particle size.

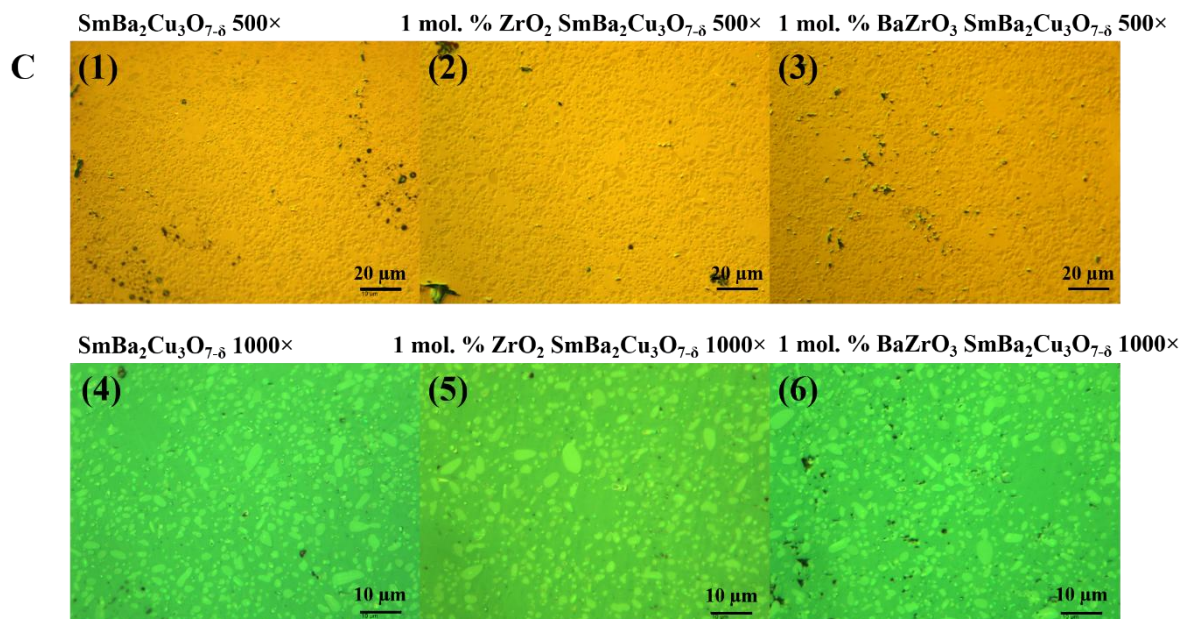


**Figure 59** Micrographs showing the Sm-211 distribution and particle size in SmBCO, 1 mol. % ZrO<sub>2</sub>-doped SmBCO and 1 mol. % BaZrO<sub>3</sub>-doped SmBCO at section C in Figure 56 with a magnification of 500 times: (1) SmBCO; (2) 1 mol. % ZrO<sub>2</sub>-doped SmBCO; (3) 1 mol. % BaZrO<sub>3</sub>-doped SmBCO with a magnification of 1000 times: (4) SmBCO; (5) 1 mol. % ZrO<sub>2</sub>-doped SmBCO and (6) 1 mol. % BaZrO<sub>3</sub>-doped SmBCO.

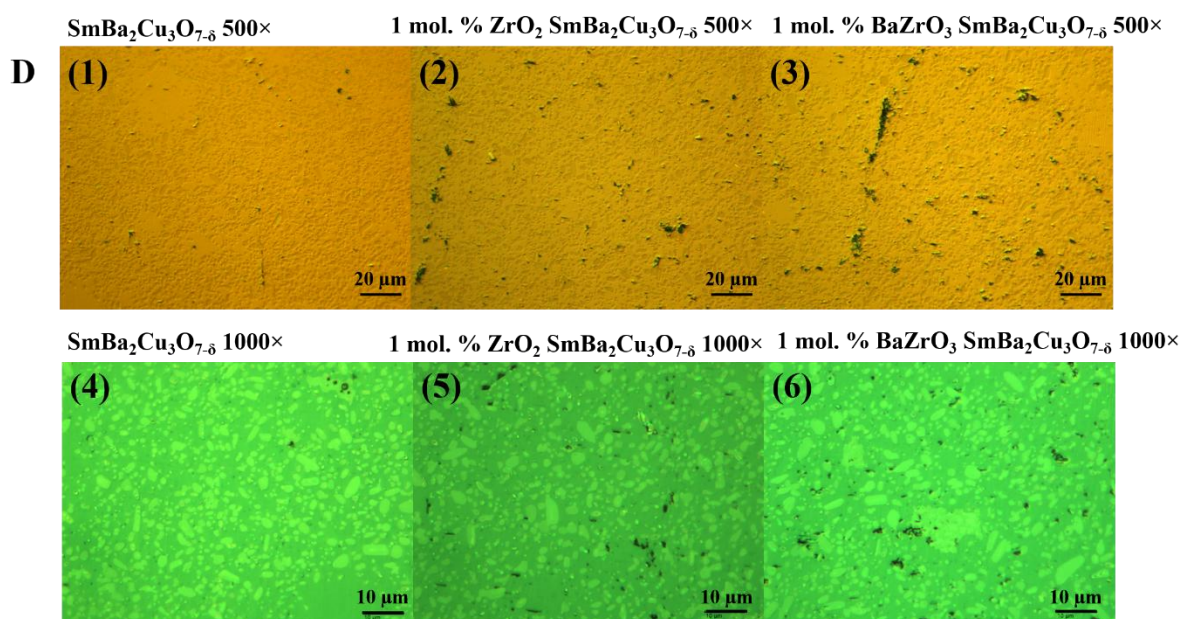


**Figure 60** Micrographs showing the Sm-211 distribution and particle size in SmBCO, 1 mol. % ZrO<sub>2</sub>-doped SmBCO and 1 mol. % BaZrO<sub>3</sub>-doped SmBCO at section D in Figure 56 with a

magnification of 500 times: (1) SmBCO; (2) 1 mol. % ZrO<sub>2</sub>-doped SmBCO; (3) 1 mol. % BaZrO<sub>3</sub>-doped SmBCO with a magnification of 1000 times: (4) SmBCO; (5) 1 mol. % ZrO<sub>2</sub>-doped SmBCO and (6) 1 mol. % BaZrO<sub>3</sub>-doped SmBCO.

### 5.3.3. Summary

SmBCO single grains melt processed with dopants selected from a wide range of chemicals and added in different concentrations have been fabricated successfully. However, several difficulties occurred during the synthesis of doped SmBCO, such as an uneven mixing of precursor powders, poor seed-choice and the impurity intolerance of the seeds. In order to grow SmBCO single grains reliably and to conserve precursor materials, the growth-related temperatures in the heating profile were adjusted by 1 °C at a time over 30 trials based on the results of DTA measurements using very small quantities of precursor powders (50 mg). Even though the growth window is comparatively smaller for the SmBCO system compared to the rest of the (RE)BCO family, the successful fabrication of single grains doped and undoped SmBCO has been achieved by TSMG in air in a conventional chamber furnace. In this research, the dopants investigated include oxides (ZrO<sub>2</sub>, BaZrO<sub>3</sub>, HfO<sub>2</sub>, CaMoO<sub>4</sub>, Fe<sub>2</sub>O<sub>3</sub>, Ga<sub>2</sub>O<sub>3</sub>, Gd<sub>2</sub>O<sub>3</sub>, NbO<sub>2</sub>, Tb<sub>4</sub>O<sub>7</sub>, ZnO, Sc<sub>2</sub>O<sub>3</sub>, SnO, Ta<sub>2</sub>O<sub>3</sub>), carbonates (Na<sub>2</sub>CO<sub>3</sub>, CaCO<sub>3</sub>, SrCO<sub>3</sub>), nano materials (nano-ZrO<sub>2</sub>), cuprates (fined Sm-211), borides (FeB) and chlorides (RbCl) in various concentrations. This study has shown that doping levels of 1 mol. % do not affect greatly the growth of SmBCO single grains, and that the growth of these samples is tolerant to oxide dopant at a doping level of 1 mol. %.

SQUID measurements of  $T_c$  and  $J_c$  confirmed the physical effects of the dopants on the bulk samples studied in this research. Some dopants, such as TiO<sub>2</sub>, reduce  $T_c$  and exhibit reduced  $J_c$  with weaker peak effects and lower irreversibility fields, while some dopants, such as ZrO<sub>2</sub> and BaZrO<sub>3</sub>, appear to be favourable in improving the superconducting properties of the bulk SmBCO samples. The highest superconducting  $T_c$  of the specimens measured was 93.6 K in 1 mol. % BaZrO<sub>3</sub>-doped SmBCO.  $J_c$  of the same specimen also exhibited a more pronounced peak effect and a higher irreversibility field. In general, 1 mol. % ZrO<sub>2</sub>-doped SmBCO shows the most superior overall superconducting properties. Furthermore, the attempt to combine individual dopants failed to replicate the superconducting properties of SmBCO processed

with an individual dopant, although positive effects of the dopants on the single grain properties were observed compared to standard SmBCO samples. A plausible explanation of this observation is that the non-uniform mixture of the precursor powders results in a deterioration in the superconducting properties of the large, single grain.

The microstructures of SmBCO single grains fabricated with and without dopants have been studied by extensive analysis of a large number of optical micrographs. This study has shown that Sm-211 inclusions in the Sm-123 matrix tend to distribute non-uniformly with the distance from the seed, with more Sm-211 particles accumulating towards the bottom of the bulk single grains. The Sm-211 particle size within the SmBCO matrix processed with and without dopants is observed to increase from the position of the seed. An even distribution and optimum Sm-211 particle size are advantageous for the industrial applications of bulk superconductors, based primarily on their superior superconducting properties.

## 5.4. Summary and Conclusions

The focus of this chapter has been on enhancing the superconducting properties of SmBCO by introducing a range of chemical dopants into the Sm-123 phase matrix, to act either as inclusion refiners, such as Pt and CeO<sub>2</sub> or as dopants, such as ZrO<sub>2</sub>, BaZrO<sub>3</sub> and TiO<sub>2</sub>. The successful growth of SmBCO single grains containing different dopants has been achieved by adjusting growth-related temperatures in the heating profiles by 1 °C at a time based on the results of DTA necessitated by the comparatively small growth window for the SmBCO system. Comparisons of the measured superconducting properties have shown clearly that CeO<sub>2</sub> is more effective at refining Sm-211 inclusions in the bulk microstructure than Pt. Furthermore, dopants such as ZrO<sub>2</sub> and BaZrO<sub>3</sub> appear to be effective in improving the superconducting properties of single grain SmBCO bulk superconductors. The highest  $T_c$  of the specimens studied was 93.6 K in 1 mol. % BaZrO<sub>3</sub>-doped SmBCO.  $J_c$  of this specimen also produced a more prominent peak effect, with a higher irreversibility field. Finally, doping SmBCO with 1 mol. % ZrO<sub>2</sub> yields the best overall superconducting properties of the single grains fabricated in this study.

# CHAPTER 6

## SMBCO BULK SINGLE GRAIN SCALE-UP THROUGH SILVER ADDITION

### 6.1. Introduction and Motivation

In terms of growth, poor mechanical properties will lead to crack formation during fabrication, leading, in turn, to the failure to obtain a bulk single grain. Although such problems are minimal for the small-scale processing of bulk single grains, it is necessary to synthesize samples with larger diameters to generate large trapped magnetic fields. As a result, it is crucial to improve the mechanical properties of (RE)BCO bulk single grains if they are to be used in practical applications. There are two, commonly exploited, approaches to enhance the mechanical properties of (RE)BCO bulk single grains: one is resin impregnation, which involves immersing a (RE)BCO bulk single grain in molten resin under a partial vacuum, resulting in back-filling into the bulk interior through the surface cracks and connected open pores [55]. A second, and more common approach employed to improving the mechanical properties of bulk superconductors is the addition of silver (Ag) to the bulk microstructure. Ag particles dispersed in the RE-123 matrix can improve mechanical properties significantly without reducing the superconducting properties of (RE)BCO bulk single grains, which can be achieved by adding  $\text{Ag}_2\text{O}$  powder to the nominal precursor powder composition. Moreover, it has also been established that SmBCO is more susceptible to cracking than YBCO, which is evidenced by the fact that it is more difficult to grow large single-grain SmBCO without the addition of Ag [93]. Furthermore, in order to increase the field trapping capability of SmBCO bulk single grains, it is also important to improve the uniformity of the mechanical properties in the bulk samples. However, the amount of added silver required to achieve the improved mechanical properties is at least 10-15 wt. % of the precursor powder content [93] and, in turn, such large amount of addition will hinder the

growth of the bulk single grains. Additionally, the processing temperatures employed during the TSMG process of SmBCO single grains with silver are significantly higher than the melting point of Ag, which may pose a problem of retaining Ag within the composite, and, consequently, lower the success rate of reliable single grain growth [125]. Hence, although Ag addition has been found to be effective in improving the mechanical properties of large single-grain SmBCO superconductors on the whole without any deterioration in their field-trapping capability or critical current densities, the reliable growth of SmBCO single grains with Ag addition has not yet generally been achieved.

Lo *et al.* investigated the influence of the physical and chemical properties of precursor green pre-forms on the properties of fully melt-processed YBCO [126]. A study of the loss of liquid from YBCO during partial melting has revealed that the total percentage weight loss is sensitive to both the heating rate and proportion of excess Y-211 phase and is maximum at a temperature corresponding to the peak of the differential thermal analysis partial melting endotherm. Generally speaking, in the peritectic reaction employed to grow (RE)BCO, the RE-211 phase and the liquid phase can be produced by rapidly heating a (RE)BCO pre-form of the desired composition to a temperature well above the peritectic temperature,  $T_p$ . Formation of the required RE-123 phase is then achieved by cooling the partially molten (RE)BCO material slowly through  $T_p$ . It is desirable to add up to 30 mol. % of the RE-211 phase to the RE-123 phase prior to melt processing, both to generate more flux pinning centres and to reduce loss of liquid during melting. Such peritectic solidification processes place certain requirements on the (RE)BCO pre-form if melt processing is to be performed effectively. Lo *et al.* discovered that, firstly, the RE-211 phase particles in RE-211-enriched RE-123 phase matrix should be fine in the bulk pre-form if they are to form a fine dispersion in the fully melt-processed material. Secondly, the material must be able to retain the liquid phase resulting from the peritectic reaction within its bulk composition at temperatures significantly above  $T_p$  to enable formation of the RE-123 phase on cooling. This depends on the homogeneity and density of the precursor green body and on the size distribution of the RE-211 phase particles it contains. Finally, the (RE)BCO pre-form should be free from compositional and surface contaminants that form heterogeneous grain nucleation sites and hence limit the grain size that can be achieved during the melt growth process. The processes responsible for a change in geometry and density of the specimens during partial melting have also been identified, including the densification process and expansion of the bulk material. The densification process, which tends to eliminate porosity, results from surface

tension of the liquid and a capillary effect between the liquid and the RE-211 phase particles. Expansion of the sample, on the other hand, which takes place close to the onset of partial melting and tends to cause non-uniformity in the specimens, is dominated by the rate of oxygen desorption during melt processing. The expansion process terminates on completion of partial melting whereas the densification process, which is dominated by the volume proportion of liquid, continues but at a reduced rate in the partially molten state. Oxygen desorption from the sample leads to the formation of pores, corresponding to a relative expansion of the specimen. At higher temperature, however, the surface tension associated with the molten state and the reduced oxygen desorption rate are responsible for densification of the sample. Porosity in bulk samples cannot be eliminated completely by control of the heating rate alone due to increased liquid loss, and other processing parameters need to be considered if a fully dense material is to be obtained. In the same research, Lo *et al.* also reported that cold isostatic pressing (CIP) allows better control of the size and distribution of Y-211 phase inclusions in the melt-processed ceramic than a combination of die pressing and sintering. The formation of green bodies has been studied with respect to die pressing, CIP and sintering. Although sintering of the die-pressed specimen yielded the highest density, this process produces significant particulate coarsening that inhibits control of the size and distribution of Y-211 phase inclusions in the melt-processed sample, which, in turn, limits  $J_c$  and trapped field. Cold isostatic pressing does not yield the highest green body density but it does preserve the particle size and hence enables better control of the final Y-211 phase distribution with a reasonably high density. Therefore, CIP is considered to be an effective pre-treatment for the (RE)BCO bulk pre-forms.

Given that avoiding the loss of liquid during TSMG process is difficult, Zhou *et al.* developed a modified TSMG process by inserting a Y-123 layer beneath the GdBCO bulk pre-form [127]. As a result, a homogeneous dispersion of Gd-211 particles is expected to maintain a mass balance to minimize the residue of unreacted liquid phase and to avoid the accumulation of Gd-211 particles due to particle pushing effects. By employing Y-123 powder as liquid source, the leakage of liquid phase becomes negligible even up to 1090 °C. More importantly, a more uniform distribution of Gd-211 particles, rather than an accumulation of Gd-211 particles at the growth sector boundaries (GSBs), is often observed in the single grain microstructure. By providing a liquid rich environment, the formation of high density sub-grain boundaries is largely inhibited. As a result, the field trapping ability of

textured GdBCO bulk single grains grown by the use of a Y-123 layer has been almost doubled, with the resulting samples showing a perfect conical trapped field distribution.

This chapter reports an attempt to scale-up the SmBCO system to fabricate samples for quasi-magnet industrial applications by adding silver to the SmBCO system and by incorporating a Y-123 layer beneath the SmBCO bulk pre-form. As a result, reliable growth of a SmBCO single grain with silver addition has been achieved through various approaches, including precursor-powder sintering, doping with 1 mol. %  $\text{ZrO}_2$ , CIP of the bulk pre-form and, finally, the addition of the Y-123 layer. Secondly, to compare the impact of the process modifications on SmBCO with silver addition, the measurement of the trapped field of the successfully grown single grains have been carried out, correlated and analysed. The role of the Y-123 layer and its impact on the appearance, superconducting properties ( $T_c$  and  $J_c$ ), microstructure, chemical compositions and field-trapping ability of the bulk single grains is discussed in detail. In consequence, a SmBCO bulk single grain with silver addition of diameter as large as 41 mm was obtained and a trapped field of + 1.033 T was measured on the top surface of a 31 mm SmBCO single grain with silver addition, which is the largest magnetic field trapped reported in the SmBCO system to date for samples in a similar size grown in air.

## **6.2. Experimental**

### **6.2.1. Production of SmBCO Single Grains with Silver Additions in Air by Cold Seeding with and without a Y-123 Layer**

Commercial Sm-123 (TOSHIMA, average particle size: 2-3  $\mu\text{m}$ ) and Sm-211 (TOSHIMA, average particle size: 1-2  $\mu\text{m}$ ) precursor powders in a weight ratio of 3:1 with 2 wt. %  $\text{BaO}_2$  (ALDRICH, purity 95 %) or 2 wt. %  $\text{BaO}$  (ALDRICH, purity 97 %) (to suppress Sm/Ba substitution [70]), 1 wt. %  $\text{CeO}_2$  (Alfa Aesar, purity 99.9%) (to reduce the coarsening of Sm-211 second phase particles [128]), and 10 wt. % of  $\text{Ag}_2\text{O}$  (Alfa Aesar, purity 99+ %, metal basis) (to improve the mechanical strength and cracking resistance [125]) were mixed thoroughly using a mortar and pestle to yield a net composition of (75 wt. % Sm-123 +

25 wt. % Sm-211) + 2 wt. % BaO<sub>2</sub> (or 2 wt. % BaO)+ 1 wt. % CeO<sub>2</sub> + 10 wt. % Ag<sub>2</sub>O (abbreviated to Ag-SmBCO). The resulting powder was pressed uniaxially into a dark green pellet of the sizes shown in Table 9 with the corresponding as-processed dimensions of each sample, since each pellet shrinks to about 80 % of its original size after TSMG. The effect of buffer layers on the success rate of the seeding procedure has also been investigated. Both thin film seeds and MgO-NdBCO generic seeds [100] have been used in this research (specifically, a thin film seed [118] consisting of NdBCO of thickness 700 nm deposited on a single crystal MgO-substrate provided by Ceraco was used). Buffers were prepared using commercially available 75 wt. % Sm-123 (TOSHIMA, average particle size: 2-3 μm) and 25 wt. % Sm-211 (TOSHIMA, average particle size: 1-2 μm). A motorized pestle and mortar was again used to mix thoroughly the buffer precursor powders, prior to being pressed uniaxially under a load of 0.5 tons into small green pre-forms with the dimensions of the same diameter and thickness of 3 mm. 1 mol. % ZrO<sub>2</sub> was added to the precursor powders following the same mixing and pressing procedure as the Ag-SmBCO pre-forms. Similarly, commercially available Y-123 (TOSHIMA, average particle size: 2-3 μm) and Yb<sub>2</sub>O<sub>3</sub> (American Elements, purity 99%, inert supporting layer) were pressed as a combined supporting pellet using the same size mould as the bulk pre-forms with the different weights listed in Table 10 to replace the yttrium-stabilised ZrO<sub>2</sub> rods. The seed, the buffer layer and the Ag-SmBCO preform (with or without the Y-123 and Yb<sub>2</sub>O<sub>3</sub> layer) were aligned to yield the required grain orientation, as shown in Figure 61. Subsequently, the arrangement was placed on an alumina plate in a box furnace prior to TSMG using the heating profile shown schematically in Figure 62. To grow a Ag-SmBCO single grain, the temperature was ramped initially to  $T_{max}$  °C, held at this temperature for 20 min to allow a thorough decomposition of the precursor powders, then the furnace is cooled to  $T_s$  °C at a rate of B °C h<sup>-1</sup>, during which the growth of the bulk single grain begins. The duration of the subsequent stages in growth depends on the sizes of the target sample; the larger the sample, the longer the growth stage.  $T_{g1}$  °C is reached at a rate of C °C h<sup>-1</sup>, followed by a change of the cooling rate to D °C h<sup>-1</sup> to  $T_{g2}$  °C and then slow cooling to  $T_{g3}$  °C at E °C h<sup>-1</sup>. Another growth stage is added to  $T_{g4}$  °C at the rate of F °C h<sup>-1</sup> if the size of the sample further increases. Finally, the sample is furnace-cooled to room temperature.

**Table 9** The dimension of each Ag-SmBCO pellet as a bulk pre-form and as a processed bulk single grain.

No.	Diameter (mm)	
	Pre-form	Post-size
1	16	13
2	20	16
3	25	20
4	32	25
5	38	31
6	50	41

**Table 10** The weight of Y-123 and Yb<sub>2</sub>O<sub>3</sub> pressed as a combined supporting pellet under the Ag-SmBCO bulk pre-form.

No.	Liquid-rich layer (g)	
	Y-123	Yb <sub>2</sub> O <sub>3</sub>
1	12	8
2	6	2
3	4	2
4	4 × 1	2
5	9.5	4
6	16.5	6

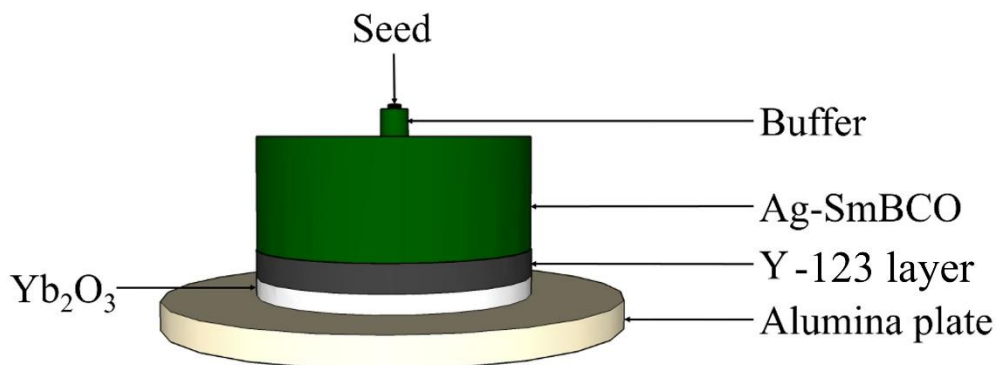


**Figure 61** Schematic diagram of an Ag-SmBCO bulk pre-form with a Y-123 layer prior to TSMG.

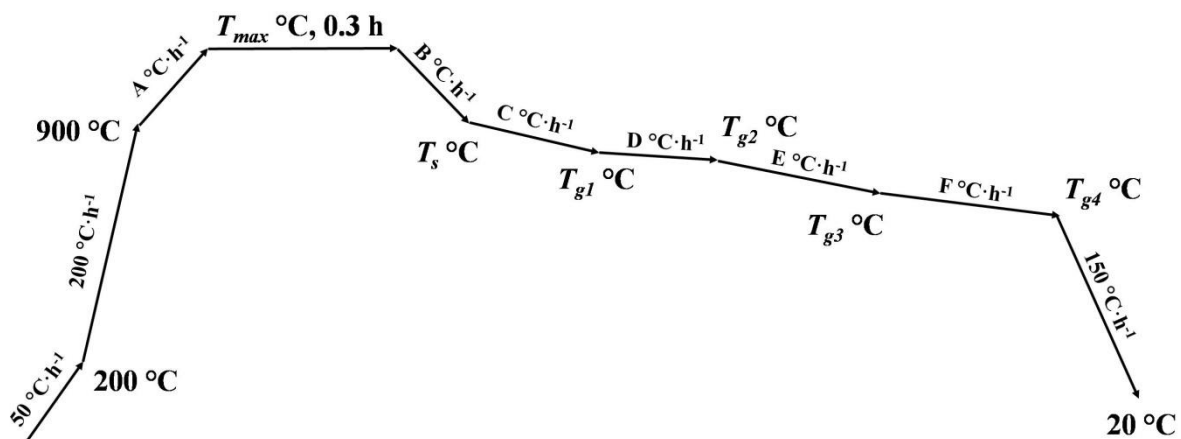


**Figure 62** Schematic illustration of the heating profile used in the TSMG process for the assorted Ag-SmBCO single grains.

The as-grown samples were oxygenated subsequently at 360 °C for fourteen days to drive the non-superconducting, tetragonal Sm-123 phase to the desired orthorhombic, superconducting phase.

## 6.2.2. Characterisation

### 6.2.2.1. Differential Thermal Analysis (DTA)

Differential thermal analysis (DTA) was performed on the 10 wt. % Ag-SmBCO precursor powders to determine their melting temperatures. The growth-related temperatures in the heating profile used in the TSMG process were adjusted accordingly by comparing the SmBCO systems with and without silver addition. The details of DTA measurements were summarised in Section 3.3.3.

### 6.2.2.2. Microstructure and Superconducting Properties, $T_c$ and $J_c$ , of the Ag-SmBCO Single Grains

Optical microscopy was carried out as described in Section 3.3.1.1 to examine the size and distribution of Sm-211 particles in the as-grown SmBCO single grains, along both the  $a/b$ - and  $c$ - axes.

The samples were cut into slices across their centre, with each slice being cut into smaller specimens of size approximately  $1.5 \text{ mm} \times 2.0 \text{ mm} \times 1.2 \text{ mm}$  at different positions, as shown schematically in Figure 63. The spatial changes in  $T_c$  and  $J_c$  of the specimens with proximity to the seed were measured as described in Section 3.3.2.1.

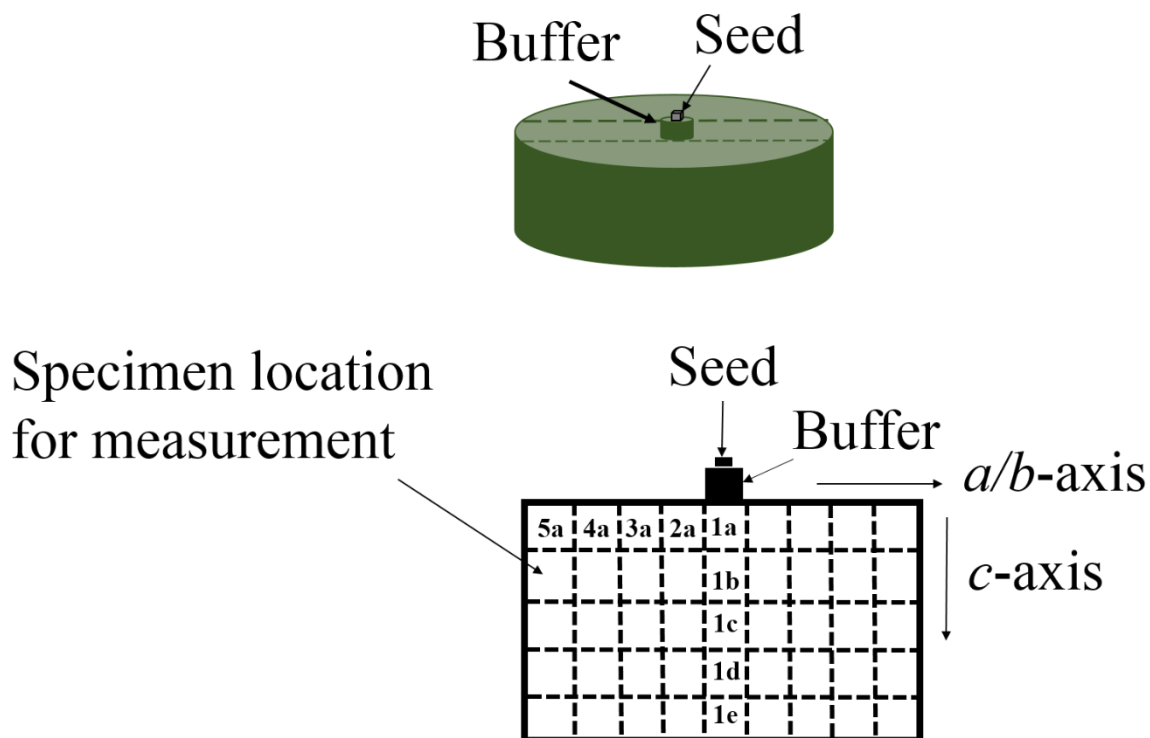


**Figure 63** Schematic illustration of the cutting scheme for the preparation of the SQUID specimens.

### 6.2.2.3. Chemical Composition Analysis of the Ag-SmBCO Bulk Single Grains with and without a Y-123 Layer

Detailed analysis of the chemical composition of the  $\text{Sm}_{1+x}\text{Ba}_{2-x}\text{Cu}_y\text{O}_z$  matrix of the Ag-SmBCO single grains prepared with and without Y-123 layers with increasing position from the seed along the  $c$ -axis was carried out using an electron probe micro-analyser (EPMA, CAMECA SX 100) to understand the role of the Y-123 layer in modifying the chemical composition of the superconducting matrix. An electron beam of a size of  $1 \mu\text{m}$  was focused on the Sm-211 free regions away from the seed along the  $c$ -axis at all positions to the bottom of the bulk single grain. Cu,  $\text{BaTiSi}_3\text{O}_9$  and  $\text{SmF}_3$  were used as standard compositions for the Sm, Ba and Cu elements included in the matrix in the EPMA analysis in order to minimize errors in determination of the  $\text{Sm}_{1+x}\text{Ba}_{2-x}\text{Cu}_y\text{O}_z$  composition.

#### **6.2.2.4. Trapped Field Measurements of the Ag-SmBCO Bulk Single Grains**

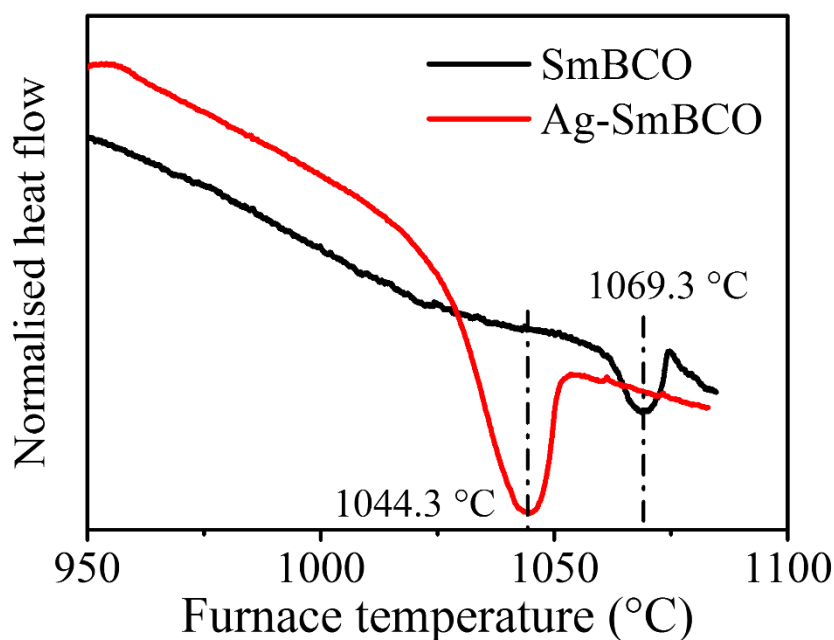
Measurements of the trapped magnetic fields were carried out by magnetizing the bulk samples with an electromagnet as described in Section 3.3.2.2.

### **6.3. Results and Discussion**

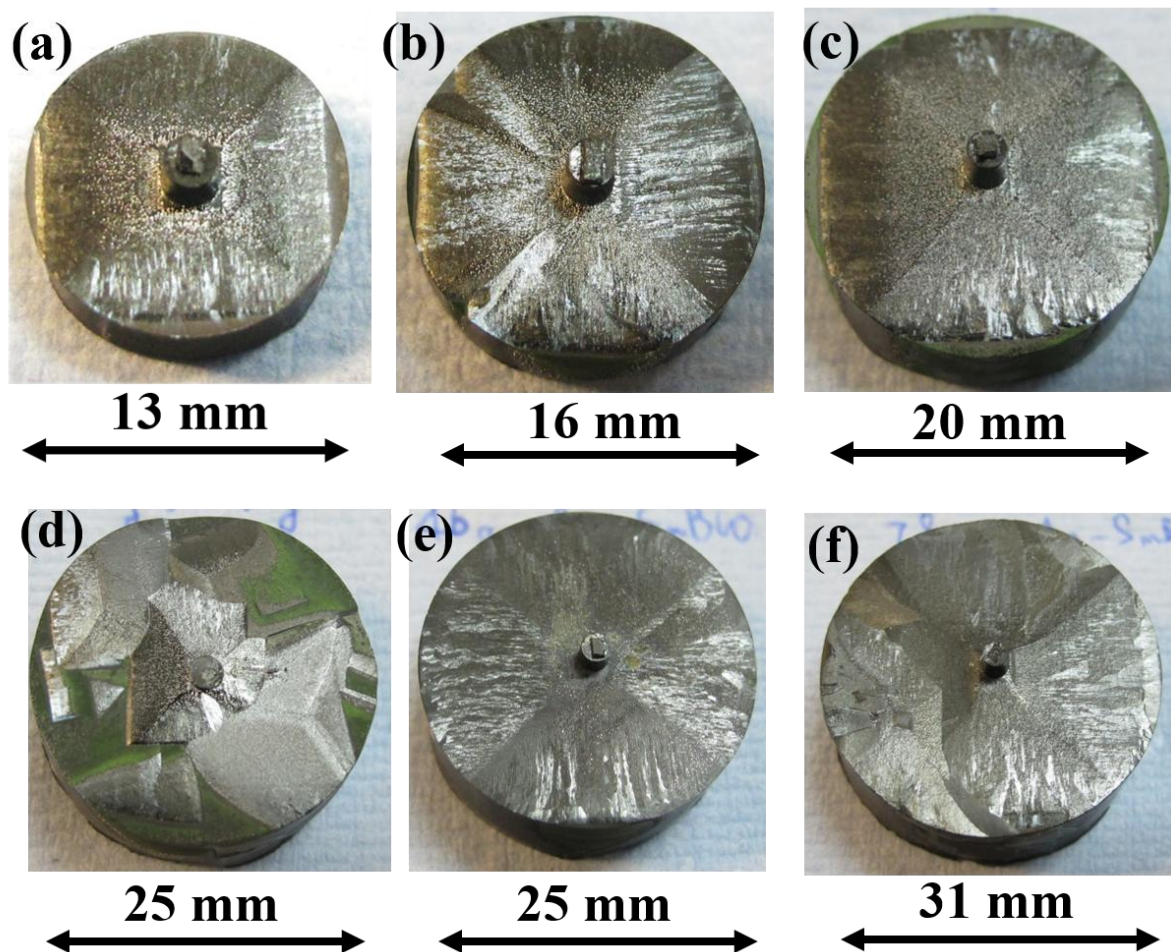
#### **6.3.1. Reliable Growth of the Ag-SmBCO System (Scale-up from 10 mm to 41 mm in Diameter)**

Figure 64 shows the differential thermal analysis (DTA) traces of SmBCO and Ag-SmBCO for comparison. The addition of 10 wt. % Ag to the SmBCO precursor powders results in lowering of the decomposition temperature from 1069.3 °C to 1044.3 °C. Therefore, in order to successfully grow Ag-SmBCO, it is necessary to adjust the heating profile accordingly. In addition, the extra Ag not only affects the decomposition temperature, but also the viscosity of the precursor powders. As a result, it is also necessary to modify the ramping rates in the heating profile. The heating profile used generally to synthesize Ag-SmBCO is shown in Figure 62. The critical growth-related parameters in Figure 62 were modified according to different sizes of the Ag-SmBCO bulk single grains. Photographs of the first batch of Ag-SmBCO single grains grown from a heating profile adjusted based on the DTA results are shown in Figure 65. The sizes and weights of these samples are listed in Table 11. Table 12 shows information on the growth parameters used to fabricate these samples. It can be seen from Figure 65 that the bigger the sample, the more difficult it is to grow. Smaller, successfully-grown Ag-SmBCO single grains of diameters 13 mm [(Figure 65 (a))], 16 mm [(Figure 65 (b))] and 20 mm [(Figure 65 (c))] were obtained in the first trial. In an attempt to grow a 25 mm-in-diameter sample, smaller ramping rates were used and  $T_s$  was raised from 1035 °C to 1037 °C to extend the growth stage. However, of the two attempts to grow

25 mm-in-diameter samples, only one produced a bulk single grain [Figure 65 (e)], with the failed sample shown in Figure 65 (d), which indicates the low success rate of Ag-SmBCO single-grain fabrication. Increasing the growth stage further failed to yield a 31 mm-in-diameter sample with a mass of 78 g in the form of a single grain, as shown in Figure 65 (f). The failure to optimise the single grain fabrication process meant it was necessary to combine other approaches with the adjustment of the heating profile to achieve larger Ag-SmBCO bulk single grain samples. Optimization of the ramping rates in the heating profile, calcination of the precursor powders, CIP preparation of the bulk pre-forms and the addition of a Y-123 layer under the bulk pre-form were performed subsequently, as presented in the following section.



**Figure 64** Differential thermal analysis traces of SmBCO and Ag-SmBCO.



**Figure 65** Ag-SmBCO samples grown successfully: (a) 13 mm in diameter; (b) 16 mm in diameter; (c) 20 mm in diameter and (e) 25 mm in diameter; the samples of diameter 25 mm (d) and 31 mm (f) failed to grow in the form of a single grain.

**Table 11** The size and weight of each Ag-SmBCO sample displayed in Figure 65.

Sample No.	Sample photographs	Size / mm	Weight / g
1	Figure 65 (a)	13	5
2	Figure 65 (b)	16	10
3	Figure 65 (c)	20	20
4	Figure 65 (d)	25	46
5	Figure 65 (e)	25	46
6	Figure 65 (f)	31	78

**Table 12** The growth-related parameters of the corresponding heating profile for the Ag-SmBCO samples listed in Figure 65 (the changes are highlighted in red).

Sample No.	Heating profile parameters ( $T_{max} = 1070 \text{ }^\circ\text{C}$ ; $A = 50 \text{ }^\circ\text{C h}^{-1}$ ; $B = 50 \text{ }^\circ\text{C h}^{-1}$ ; $C = 1 \text{ }^\circ\text{C h}^{-1}$ )							
	$T / \text{ }^\circ\text{C}$					Growth rate / $^\circ\text{C h}^{-1}$		
	$T_s$	$T_{g1}$	$T_{g2}$	$T_{g3}$	$T_{g4}$	D	E	F
1 Figure 65 (a)	1035	1024	1004	-	-	0.4	-	-
2 Figure 65 (b)	1035	1024	1004	-	-	0.4	-	-
3 Figure 65 (c)	1035	1024	1004	-	-	0.4	-	-
4 Figure 65 (d)	1037 ↑	1024	1010	1004	-	0.3 ↓	0.2	-
5 Figure 65 (e)	1037 ↑	1024	1010	1004	-	0.3 ↓	0.2	-
6 Figure 65 (f)	1037 ↑	1030 ↑	1022 ↑	1004	992	0.3 ↓	0.2	1

It can be seen from the failed, 31 mm-in-diameter Ag-SmBCO sample shown in Figure 65 (f) that a second nucleation centre is observed at the top surface of the sample. Given that the SmBCO system has a higher growth rate than YBCO [129], an effective way to avoid growth from multiple nucleation centres is to set faster ramping rates to allow the sample grow into a single grain before secondary nucleation can occur. Based on the heating profile used to successfully fabricate the 16 mm-in-diameter Ag-SmBCO single grain (No. 2 in Table 12), a further six samples (details summarised in Table 13) with the adjusted growth parameters summarised in Table 14 were grown and are shown in Figure 66. The isothermal growth conditions of the samples in Figures 66 (c) and (d) indicate that insufficient undercooling is not advantageous for the growth of Ag-SmBCO bulk single grains. Although, theoretically, a higher growth rate should be able to prevent the sub-grains from forming, at the same time, this requires the temperature distribution in the furnace to be relatively even and stable. In other words, if such balance cannot be maintained during the synthesis procedure, instead of assisting the growth of Ag-SmBCO bulk single grains, a faster growth rate lowers the single grain grown success rate. As a result, attempts to grow 25 mm-in-diameter samples also failed [Figures 66 (d) and (e)].

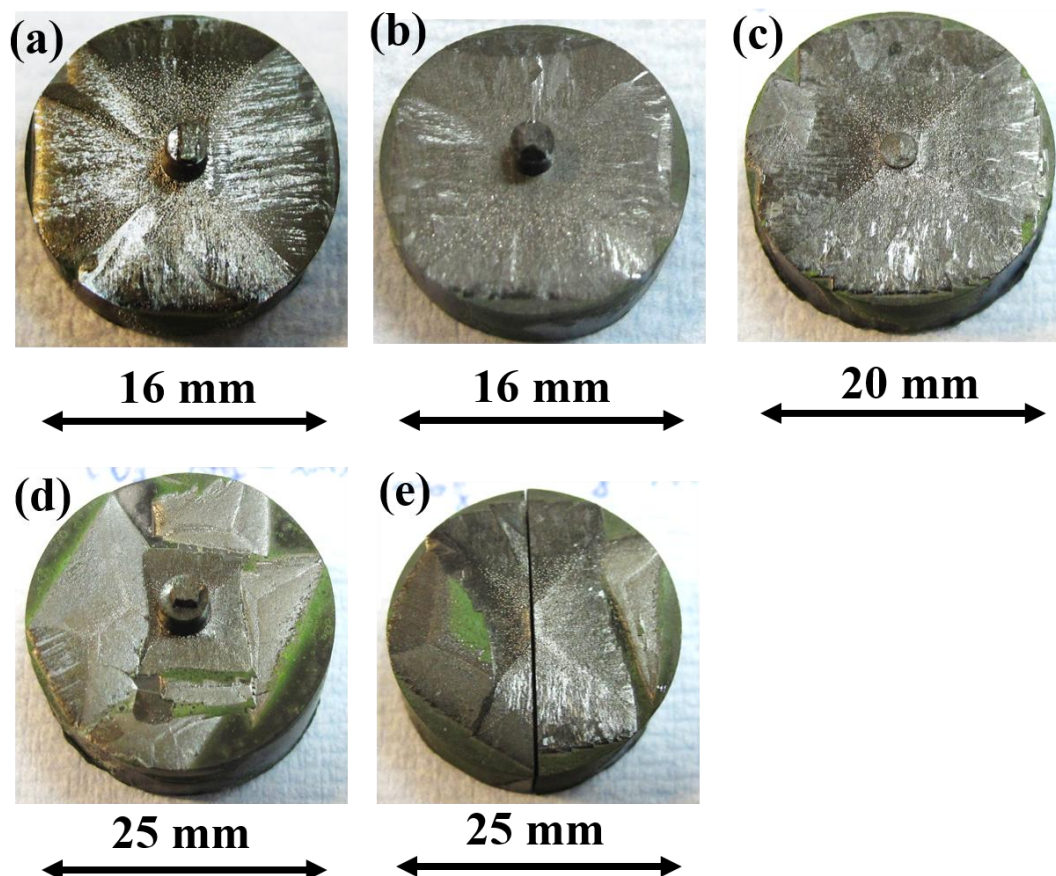


**Figure 66** Ag-SmBCO samples with adjusted growth parameters in the heating profile: (a) 16 mm in diameter (as a benchmark); (b) 16 mm in diameter; (c) 20 mm in diameter were grown successfully; (d) and (e) 25 mm in diameter samples failed to grown in the form of a single grain.

**Table 13** The size and weight of each Ag-SmBCO sample displayed in Figure 66.

Sample No.	Sample photographs	Post size / mm	Weight / g
1	Figure 66 (a)	16	10
2	Figure 66 (b)	16	10
3	-	20	20
4	Figure 66 (c)	20	20
5	Figure 66 (d)	25	46
6	Figure 66 (e)	25	46

**Table 14** The growth-related parameters of the corresponding heating profile for the Ag-SmBCO samples listed in Figure 66 (the changes are highlighted in red).

Sample No.	Heating profile parameters ( $T_{max} = 1070 \text{ }^\circ\text{C}$ ; $C = 1 \text{ }^\circ\text{C h}^{-1}$ )							
	$T / \text{ }^\circ\text{C}$				Growth rate / $^\circ\text{C h}^{-1}$			
	$T_s$	$T_{g1}$	$T_{g2}$	$T_{g3}$	A	B	D	E
1 Figure 66 (a)	1035	1024	1004	-	50	50	0.4	-
2 Figure 66 (b)	1031 ↓	1023 ↓	997 ↓	-	75 ↑	75 ↑	0.8 ↑	-
3 -	1031 ↓	1023 ↓	997 ↓	-	75 ↑	75 ↑	0.8 ↑	-
4 Figure 66 (c)	1031 ↓	1023 ↓	1004 10 h	-	75 ↑	75 ↑	0.8 ↑	-
5 Figure 66 (d)	1031 ↓	1023 ↓	1004 10 h	-	75 ↑	75 ↑	0.8 ↑	-
6 Figure 66 (e)	1037 ↑	1024	1010 ↑	1004	50	50	0.5 ↑	0.3

Calcination of the precursor powders at  $550 \text{ }^\circ\text{C}$  for 6 h was carried out before pressing the powders into the pellet pre-form in order to improve their uniformity. The heating profile to grow the Ag-SmBCO single grains summarised in Figure 68 is shown in Figure 67. The sample in Figure 68 (a) is a failed Ag-SmBCO sample 25 mm in diameter without any precursor-powder calcination. Precursor powders for the remaining Ag-SmBCO samples in Figures 68 (b)-(h) were all calcined at  $550 \text{ }^\circ\text{C}$  for 6 h, whereas for the sample in Figure 68 (i) an additional sintering of the bulk pre-form was carried out at  $900 \text{ }^\circ\text{C}$  for 6 h. A thin film seed was used, instead of an MgO-NdBCO generic seed, for the sample in Figure 68 (h). The results show that, even with the same treatment of the precursor powders, such as the samples in Figures 68 (b)-(g), the growth of a single grain is not guaranteed, even though most Ag-SmBCO single grain [samples in Figures 68 (c)-(f)] were grown largely into single grains, on the other hand, Figures 68 (b) and (g) show two failed samples. However, the success rate of the sample fabrication is improved significantly when compared to the earlier batches in this chapter. In addition, this set of experiments illustrates that the calcination of the bulk pre-form with the objective of densifying the sample and the use of a thin film seed is not necessarily favourable to synthesize Ag-SmBCO. However, although the success rate clearly is improved by calcination, it is not a beneficial treatment because Sm-211 particles in the

precursor powders tend to aggregate when heat treatment is applied. This coarsens the fine Sm-211 particles in the melt-processed superconducting Sm-123 matrix to produce a Ag-SmBCO single grain with inferior superconducting properties [126]. Therefore, although calcination is effective in increasing the growth success rate of Ag-SmBCO single grains, it is not employed in the Ag-SmBCO system since it compromises the superconducting properties.

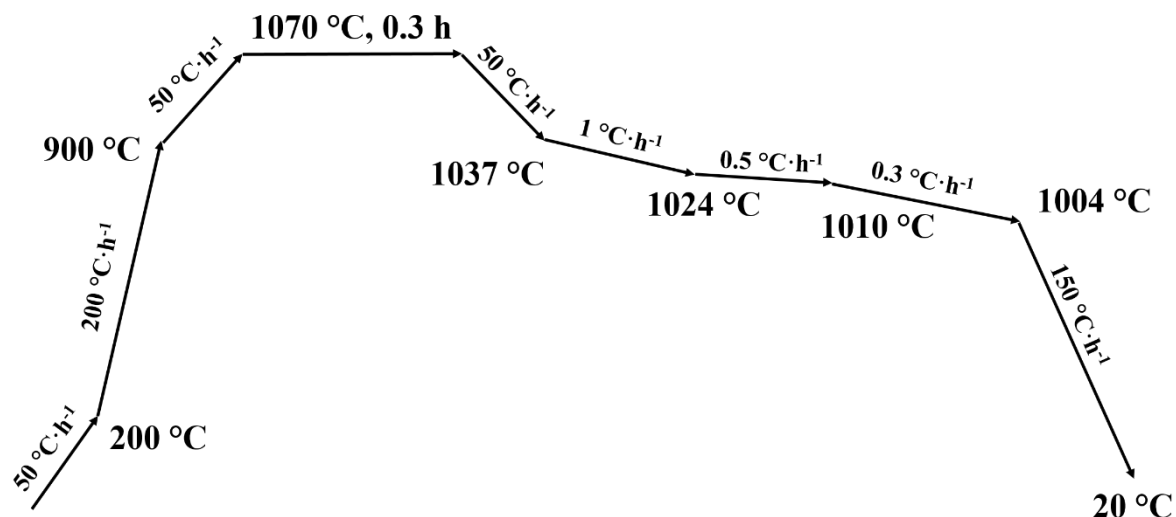


**Figure 67** Schematic illustration of the heating profile used in the TSMG process for the Ag-SmBCO single grains with calcined precursor powders.

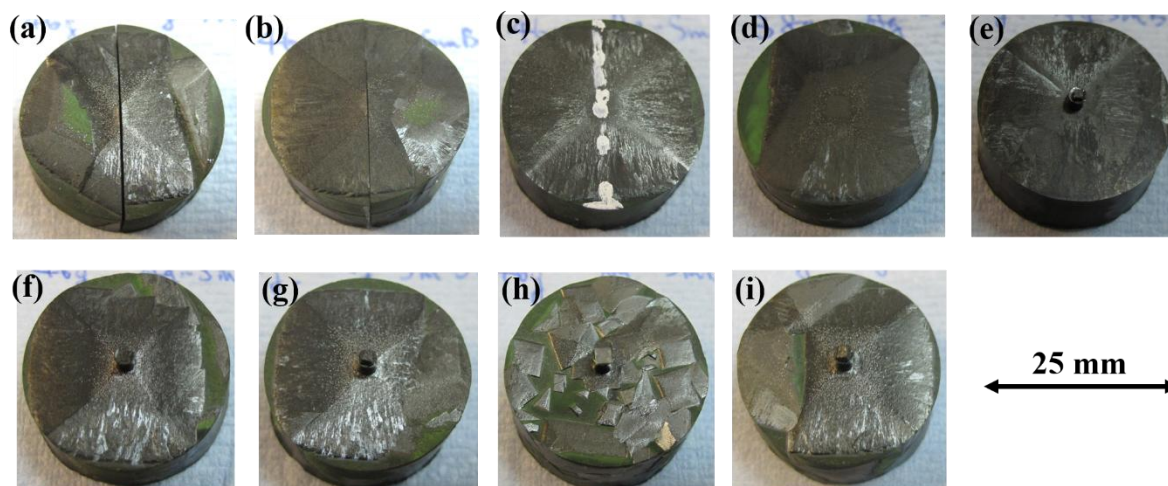


**Figure 68** Ag-SmBCO samples fabricated from calcined precursor powders: (a) without any treatment (as a benchmark); (b)-(g) precursor powders calcined at 550 °C for 6 h with MgO-NdBCO generic seeds; (h) precursor powders calcined at 550 °C for 6 h with a film seed and (i) precursor powders calcined at 550 °C for 6 h and bulk pre-form at 900 °C for 6 h and then melt-processed with an MgO-NdBCO generic seed.

So far, several approaches have been applied to the processing of the Ag-SmBCO system, including the adjustment of the heating profile and the calcination of the precursor powders. However, the problem of random growth of an Ag-SmBCO bulk single grain remains unsolved. Given that extra liquid phase added to other (RE)BCO systems has assisted the growth of (RE)BCO [127], therefore, an attempt to add an extra Y-123 layer to Ag-SmBCO system was performed with the heating profile shown in Figure 69. Photographs of the resulting samples are shown in Table 15, with the details of the treatments on each sample summarised in Table 16. The sample in Table 15 (a) is used as a bench mark for discussing the effects of the Y-123 layer. The samples processed with a 12 g Y-123 layer at the bottom of the Ag-SmBCO pre-form and with thin film seeds are displayed in Table 15 (b) - (g). Of these seven samples, only one failed to grow into a single grain [Table 15 (c)], indicating a significantly improved success rate for the Ag-SmBCO system when a Y-123 layer is used. An otherwise similar sample processed without a Y-123 layer failed to grow in the form of a single grain, as shown in Table 15 (h). Previous research in other (RE)BCO systems has demonstrated that CIP can produce a sample with a reasonable density and a controlled RE-211 phase distribution [126]. As a result, CIP treatment was carried out on an Ag-SmBCO sample with 12 g Y-123 liquid phase using an MgO-NdBCO generic seed and the as-prepared sample was grown into a single grain [Table 15 (i)], illustrating the effectiveness of the CIP process. In addition, the amount of the Y-123 layer was reduced to 6 g in an attempt to determine the optimised weight for Ag-SmBCO single-grain growth. From the samples shown in Table 15 (j) - (n), the reduced amount of Y-123 did not affect the successful growth of the Ag-SmBCO single grains significantly, since grown successfully using both seed options, with or without CIP, as shown in Table 15 (j), (m) and (n) whereas the samples shown in Table 15 (k) and (l) failed. Until this point, Ag-SmBCO single grains 25 mm in diameter had only been synthesised reliably with the assistance of a Y-123 layer.

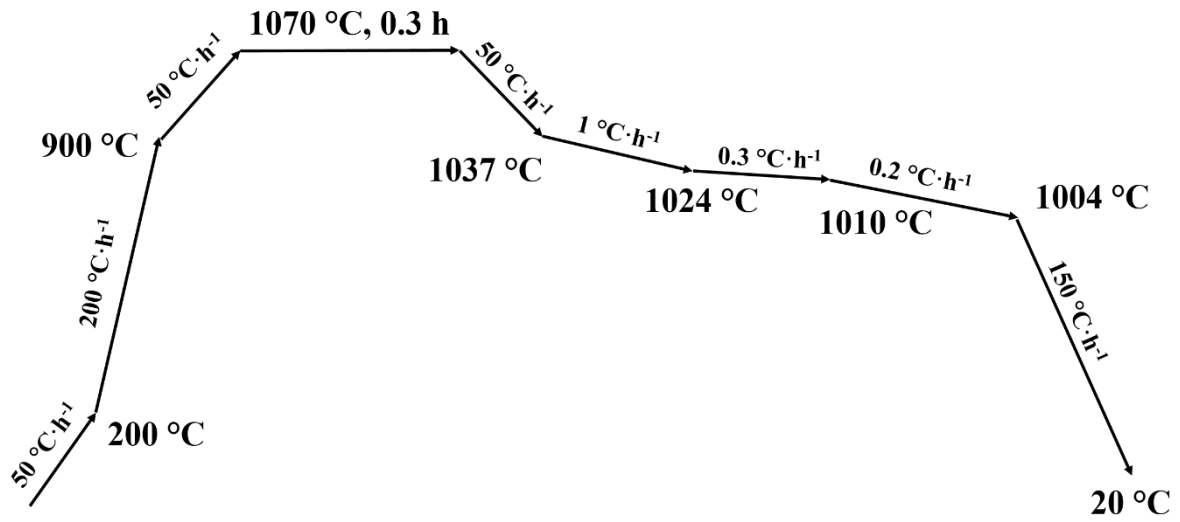


**Figure 69** Schematic illustration of the heating profile used in the TSMG process for Ag-SmBCO with a Y-123 layer.

**Table 15** Ag-SmBCO samples 25 mm in diameter with different amounts of Y-123 layers and pre-treatment with fabrication details summarised in Table 16.

Sample No.	Sample photographs	Sample status	Sample No.	Sample photographs	Sample status
(a)		Failed	(h)		Failed
(b)		Successfully grown	(i)		Successfully grown
(c)		Failed	(j)		Successfully grown
(d)		Successfully grown	(k)		Failed
(e)		Successfully grown	(l)		Failed
(f)		Successfully grown	(m)		Successfully grown
(g)		Successfully grown	(n)		Successfully grown

**Table 16** Details of Ag-SmBCO samples shown in Table 15 with different amounts of the Y-123 layers and pre-treatments.

Sample No.	Liquid phase		CIP	Sample photographs	Seed
	Y-123 / g	Yb <sub>2</sub> O <sub>3</sub> / g			
1	-	-	-	Table 15 (a)	Buffer + generic seed
2-7	12	8	-	Table 15 (b), (c), (d), (e), (f) and (g)	Film seed
8	-	-	-	Table 15 (h)	
9	12	8	-	-	
10	12	8	√	Table 15 (i)	Buffer + generic seed
11-12	6 ↓	2 ↓	√	Table 15 (j)	
				Table 15 (k)	
13-14	6 ↓	2 ↓	-	Table 15 (l)	
				Table 15 (m)	
15	6 ↓	2 ↓	√	Table 15 (n)	Film seed

It was reported in Chapter 5 that the use of ZrO<sub>2</sub> as a dopant has positive effects on improving the superconducting properties of SmBCO and therefore it is recognised as a practical dopant to the SmBCO system. As a result, ZrO<sub>2</sub> was also added to the Ag-SmBCO system to explore its effects on the growth of Ag-SmBCO single grains while, in turn, investigating the influence of the Y-123 layer on ZrO<sub>2</sub>-doped Ag-SmBCO. 1 mol. % ZrO<sub>2</sub>-doped Ag-SmBCO bulk single grains were fabricated and, due to the low doping level, the heating profile used to grow 25 mm Ag-SmBCO shown in Figure 69 was also employed to grow 1 mol. % ZrO<sub>2</sub>-doped Ag-SmBCO. The details of the as-prepared samples are listed in Table 18 with the corresponding photographs of the samples shown in Table 17.

For this batch, MgO-NdBCO generic seeds were used predominantly due to their enhanced stability and lower costs compared with thin film seeds, except for the sample shown in

Table 17 (b). A further reduction in the amount of the Y-123 layer was attempted for this batch of doped Ag-SmBCO samples in two ways: firstly, the 6 g Y-123 pellet was replaced by a 4 g Y-123 pellet [Table 17 (c)]; secondly, four smaller 1 g pellets were employed [Table 17 (d)] instead of one 6 g Y-123 pellet. Both attempts resulted in the successful growth of bulk single grains (the superconducting properties of these samples will be discussed in the following section). 6 g of Y-123 was then used in subsequent attempts to grow 1 mol. % ZrO<sub>2</sub>-doped Ag-SmBCO. Pre-forms of the samples listed in Table 18 (5) - (12) were all CIP-ed with 6 g Y-123 and 2 g Yb<sub>2</sub>O<sub>3</sub> layers. Table 17 (e) - (h) show 1 mol. % ZrO<sub>2</sub>-doped Ag-SmBCO samples with BaO<sub>2</sub> in the precursor powder, while Table 17 (i) - (l) show 1 mol. % ZrO<sub>2</sub>-doped Ag-SmBCO sample with BaO in the precursor powders. The latter samples were prepared in an attempt to reduce the porosity in the bulk single grains because there is less oxygen in BaO than in BaO<sub>2</sub> (oxygen atoms entering and leaving the bulk composition leaves pores in the matrix of the single grain [126]). 1 mol. % ZrO<sub>2</sub>-doped Ag-SmBCO bulk single grains containing BaO and BaO<sub>2</sub> have been fabricated successfully [Table 17 (a), (e), (f) and (k)], albeit with a slightly lower success rate than observed for the growth of Ag-SmBCO bulk single grains.

**Table 17** CIP-ed 1 mol. % ZrO<sub>2</sub>-doped Ag-SmBCO samples 25 mm in diameter with different starting compositions of the precursor powders with BaO<sub>2</sub> or BaO and different amounts and arrangements of Y-123 layers with fabrication details summarised in Table 18.

Sample No.	Sample photographs	Sample status	Sample No.	Sample photographs	Sample status
(a)		Successfully grown	(g)		Failed
(b)		Failed	(h)		Failed
(c)		Successfully grown	(i)		Failed
(d)		Successfully grown	(j)		Failed
(e)		Successfully grown	(k)		Successfully grown
(f)		Successfully grown	(l)		Failed

**Table 18** Details of CIP-ed 1 mol. % ZrO<sub>2</sub>-doped Ag-SmBCO samples shown in Table 17 with different starting compositions of the precursor powders with BaO<sub>2</sub> or BaO and different amounts and arrangements of the Y-123 layers (the changes are highlighted in red).

Sample No.	Liquid phase		Precursor powder composition		Sample photographs	Seed (Buffer + generic seed: √; Thin film seed: x)
	Y-123 / g	Yb <sub>2</sub> O <sub>3</sub> / g	BaO <sub>2</sub>	BaO		
	1	6	2	√		
2	6	2	√		Table 17 (b)	x
3	4 ↓	2	√		Table 17 (c)	√
4	4 × 1 ↓	2	√		Table 17 (d)	√
5-8	6	2	√		Table 17 (e), (f), (g) and (h)	√
9-12	6	2		√	Table 17 (i), (j), (k) and (l)	√

Since the field-trapping capability of SmBCO single grains with similar critical current density  $J_c$  is proportional to the gradient of the field profile and the current loop (size of the single grain), theoretically, the larger the sample the higher field it can trap. Therefore, for reliable growth of 25 mm-in-diameter Ag-SmBCO with the assistance of a Y-123 layer, it is necessary to further scale-up the size of the Ag-SmBCO single grains to trap higher magnetic fields for quasi-magnet engineering applications.

Figure 70 shows a schematic illustration of the heating profile used to grow larger Ag-SmBCO samples. For Ag-SmBCO with as-processed sizes of 31 mm and 41 mm in diameter, the heating profile remains largely the same, except for  $T_{max}$  for the growth of a 41 mm Ag-

SmBCO single grain, which was set to be 10 °C higher than that of 1070 °C used for the growth of a 31 mm Ag-SmBCO single grain to ensure thorough decomposition of the precursor powders. Thin film seeds were used instead of the MgO-NdBCO generic seeds to ensure the integrity of the seeding material, in the case of the 41 mm Ag-SmBCO single grain.

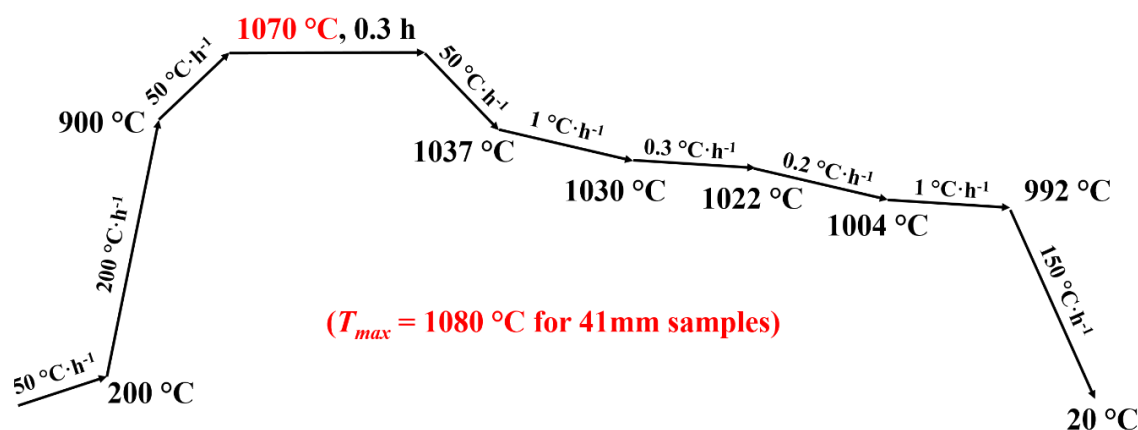


**Figure 70** Schematic illustration of the TSMG process heating profile for fabricating Ag-SmBCO bulk single grains of diameter 31 mm and 41 mm.

The sample details are summarised in Table 20 with the corresponding sample photographs shown in Table 19. The weight of the Y-123 layer was calculated from the ratio to the area of the grown single grain samples. 6 g Y-123 was used to grow a 25 mm-in-diameter bulk single grain, so proportionally, 9.5 g and 16.5 g Y-123 were used to grow 31 mm- and 41 mm-in-diameter bulk single grains, respectively, with an adjusted amount of  $\text{Yb}_2\text{O}_3$ . As a result, although only one out of the four samples of diameter 31 mm grew into a bulk single grain [Table 19 (b)], the remaining attempts in Table 19 (a), (c) and (d) all failed. However, reliable growth of Ag-SmBCO 41 mm in diameter was realized in all three trials [Table 19 (e), (f) and (g)], indicating that the Y-123 layer is capable of assisting the growth of the Ag-SmBCO bulk single grains very effectively.

**Table 19** Ag-SmBCO in the sizes of 31 mm and 41 mm with fabrication details summarised in Table 20.

Sample No.	Sample photographs	Sample status	Sample No.	Sample photographs	Sample status
(a)		Successfully grown	(e)		Successfully grown
(b)		Failed	(f)		Successfully grown
(c)		Successfully grown	(g)		Failed
(d)		Successfully grown			

**Table 20** Details of the Ag-SmBCO single grains grown into 31 mm and 41 mm in Table 19.

Sample No.	Liquid phase		Sample photographs	Size / mm	Weight / g	Seed: Buffer + generic seed: $\checkmark$ (thin film seed: x)
	Y-123 / g	Yb <sub>2</sub> O <sub>3</sub> / g				
1-4	9.5	4	Table 19 (a), (b), (c) and (d)	31	78	$\checkmark$
5-7	16.5	6	Table 19 (e), (f) and (g)	41	130	x

In conclusion, with the aid of a Y-123 layer, combined with CIP treatment of the Ag-SmBCO pre-forms using a carefully adjusted heating profile, 41 mm-in-diameter Ag-SmBCO bulk single grains can be synthesised in a reliable manner with an improved success rate.

### 6.3.2. Trapped Field Analysis of the Optimised Ag-SmBCO Bulk Single Grains

The maximum value and shape of the trapped field indicates the superconducting quality and uniformity of a bulk, single grain material. Therefore, measurement of the trapped field profiles at the top and bottom surfaces of the sample can be used to establish whether a bulk sample constitutes a single-grain, as well as indicating the quality of the single grain. At the same time, comparison of the maximum trapped field between bulk Ag-SmBCO single grains processed under different conditions can also illustrate the effects of the process variables on the Ag-SmBCO system. All the figures in this section show the trapped field profiles of Ag-SmBCO single-grain samples measured at 77 K. The maximum observed value of trapped field at both the top and bottom surfaces of each sample is indicated in each figure, along with photographs of the polished top surface of the single grain.

### **6.3.2.1. 2D-contour Maps of the Trapped Magnetic Fields of 1 mol. % ZrO<sub>2</sub>-doped Ag-SmBCO**

Doping in the SmBCO system was shown to be an effective approach for improving the superconducting properties of SmBCO in Chapter 5. When adding Ag into the SmBCO system, therefore, the initial challenge is to dope Ag-SmBCO with 1 mol. % ZrO<sub>2</sub> (one of the most advantageous dopants in the SmBCO system). 2D-contour maps of both surfaces of the Ag-SmBCO single grains with and without 1 mol. % ZrO<sub>2</sub> are shown in Figure 71 with corresponding photographs of the top surface of each sample shown in Figures 71 (a) and (d), respectively. It can be concluded that the additional 1 mol. % ZrO<sub>2</sub> is capable of improving the field-trapping ability of Ag-SmBCO single grains, since the magnetic field trapped at the top surface of 1 mol. % ZrO<sub>2</sub>-doped Ag-SmBCO is + 0.93 T [Figure 71 (e)], which is an improvement of 0.1 T compared to that of the control Ag-SmBCO single grain [+ 0.83 T shown in Figure 71 (b)]. Significantly, the magnetic field trapped at the bottom surface of 1 mol. % ZrO<sub>2</sub>-doped Ag-SmBCO is – 0.60 T [Figure 71 (f)], which is also higher than that of the Ag-SmBCO control sample [– 0.46 T in Figure 71 (c)]. Such an increase could be attributed to the extra pinning centres introduced into the system by the 1 mol. % ZrO<sub>2</sub> dopant. Additionally, from the shapes of the 2D-contour maps of both samples, the ZrO<sub>2</sub> dopant can also help the Ag-SmBCO sample to grow into a more homogenous bulk single grain with a trapped field contour geometry that consists approximately of concentric circles, which is important for industrial applications of Ag-SmBCO bulk single grains.

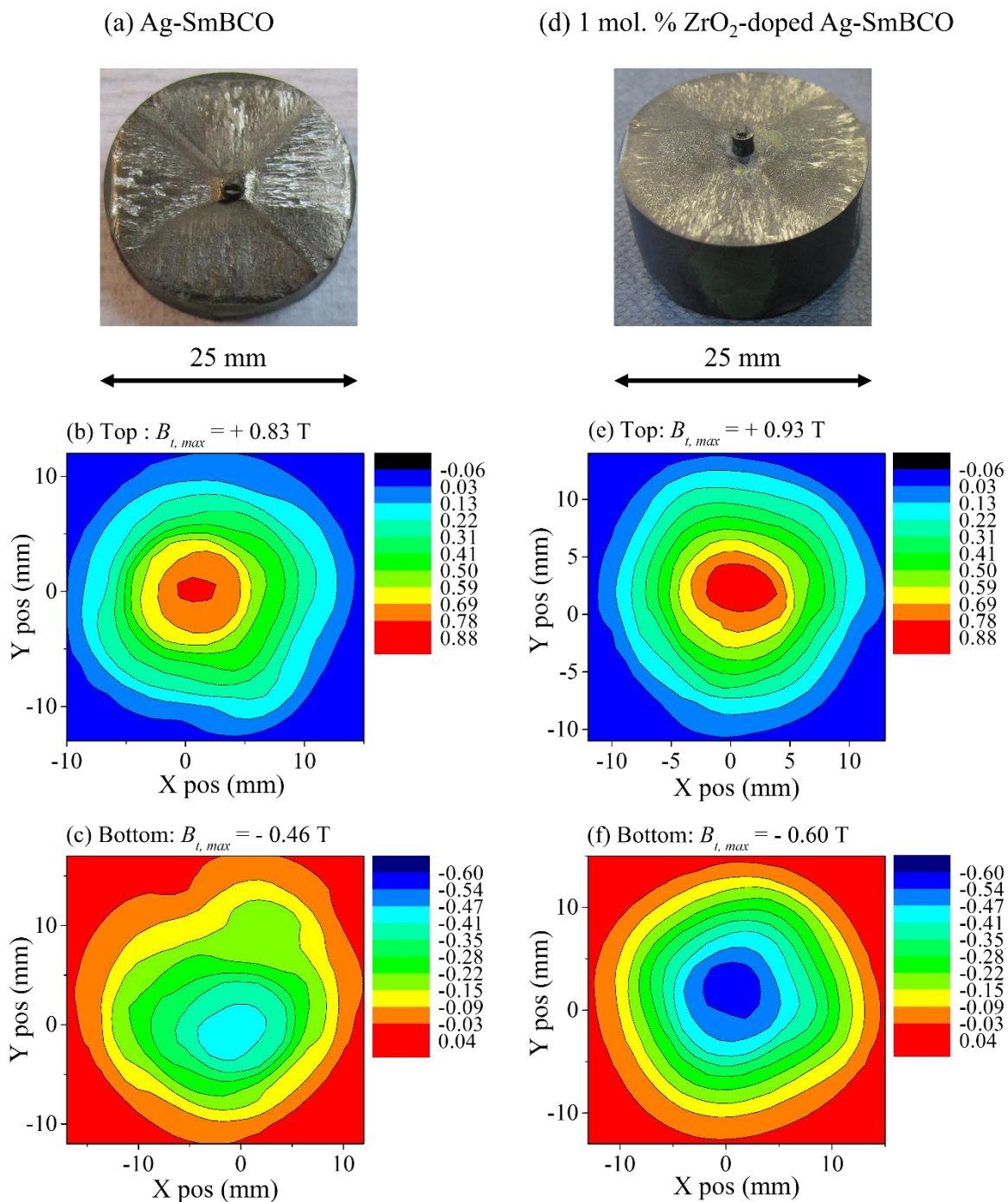


**Figure 71** Photographs of the polished top surfaces of (a) Ag-SmBCO and (d) 1 mol. %  $\text{ZrO}_2$ -doped Ag-SmBCO and their trapped field profiles at both the top: (b) Ag-SmBCO and (e) 1 mol. %  $\text{ZrO}_2$ -doped Ag-SmBCO and bottom: (c) Ag-SmBCO and (f) 1 mol. %  $\text{ZrO}_2$ -doped Ag-SmBCO surfaces measured at a distance of 0.5 mm above the sample surface. The maximum trapped field values at the top and bottom surfaces are indicated in the figure.

### 6.3.2.2. 2D-contour Maps of the Magnetic Trapped Fields of the Ag-SmBCO Single Grains with Y-123 Layers

Zhou *et al.* [127] have performed extensive research on the function of the Y-123 layer on the growth and superconducting properties of GdBCO bulk single grains. Considering the similarities between the GdBCO and SmBCO systems, therefore, it is entirely reasonable to introduce a Y-123 layer to the bottom surface of the SmBCO bulk pre-form. This is particularly significant for the Ag-SmBCO system and helps explore the effects of the liquid-rich layer on the growth and superconducting properties of large Ag-SmBCO single grains.

Figure 72 summarises the field-trapping properties of the Ag-SmBCO single grains processed with and without 12 g Y-123 layers. The samples in Figures 72 (d), (g) and (j) show Ag-SmBCO bulk single grains of the same size and weight processed with 12 g Y-123 layers, while the Ag-SmBCO single grain in Figure 72 (a) processed without a Y-123 layer was used as a benchmark. The success rate of the growth of Ag-SmBCO single grains is increased significantly with the extra Y-123 layer. Secondly, the variation in measured trapped field between the three samples fabricated using an Y-123 layer is relatively large at the top surface, varying from + 0.588 T [Figure 72 (e)], to + 0.625 T [Figure 72 (h)] and to + 0.693 T [Figure 72 (k)], and from - 0.650 T [Figure 72 (i)], to - 0.669 T [Figure 72 (l)] and to - 0.798 T [Figure 72 (f)] at the bottom surface. The top surface in the samples fabricated with the Y-123 layers trapped a smaller magnetic field than the samples without a Y-123 layer [+ 0.83 T in Figure 72 (b)], although the field trapped at the bottom of the samples with a Y-123 layer is largely improved from - 0.46 T [Figure 72 (c)], albeit even with a relatively large fluctuation, indicating the potential of using a Y-123 liquid-rich source to process the Ag-SmBCO system.

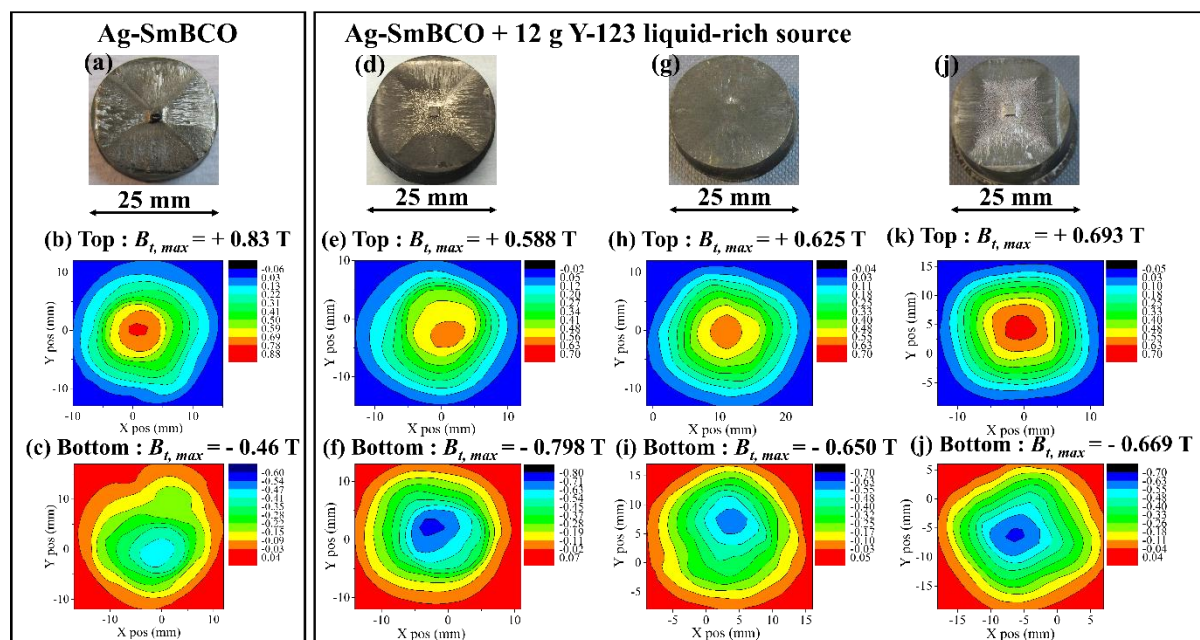


**Figure 72** Photographs of the polished top surfaces of: (a) Ag-SmBCO without a Y-123 layer; (d), (g) and (j) Ag-SmBCO with Y-123 layers (repeated experiments) and their trapped field profiles at both the top: (b) Ag-SmBCO without a Y-123 layer; (e), (h) and (k) Ag-SmBCO with Y-123 layers and bottom: (c) Ag-SmBCO without a Y-123 layer; (f), (i) and (l) Ag-SmBCO with Y-123 layers surfaces measured at a distance of 0.5 mm above the sample surface. The maximum trapped field values at the top surfaces and bottom surfaces are indicated in the figure.

It is of considerable importance to further investigate the Ag-SmBCO system with a Y-123 layer, given that the Y-123 layer is beneficial for the growth and the superconducting properties of Ag-SmBCO single grains. As a preliminary attempt, the amount of the Y-123 layer was reduced to half of its weight used in the initial trials, i.e. from 12 g to 6 g. Figure 73 (a) and (d) show the measured trapped fields of samples fabricated from 12 g and 6 g Y-123 layers. The field trapped at the top surface of the sample with a 6 g Y-123 layer is +0.883 T in Figure 73 (e), which is a significant improvement from +0.693 T in Figure 73 (b) for the sample with a 12 g Y-123 layer. Similarly, at the bottom surface, an improved trapped field of  $-0.873$  T in Figure 73 (f) is observed for the sample with the 6 g Y-123 layer, compared to a trapped field of  $-0.831$  T in Figure 73 (c) for the 12 g Y-123 layer. The shapes of the 2D contour maps for the Ag-SmBCO single grain grown with a 6 g Y-123 layer appear to be more ring-like than the less regular shapes of the sample prepared using the 12 g Y-123 layer.

In conclusion, a Y-123 layer of mass 6 g is preferable for the growth of Ag-SmBCO bulk single grains with improved field-trapping abilities.

Ag-SmBCO + 12 g Y-123 liquid-rich source    Ag-SmBCO + 6 g Y-123 liquid-rich source

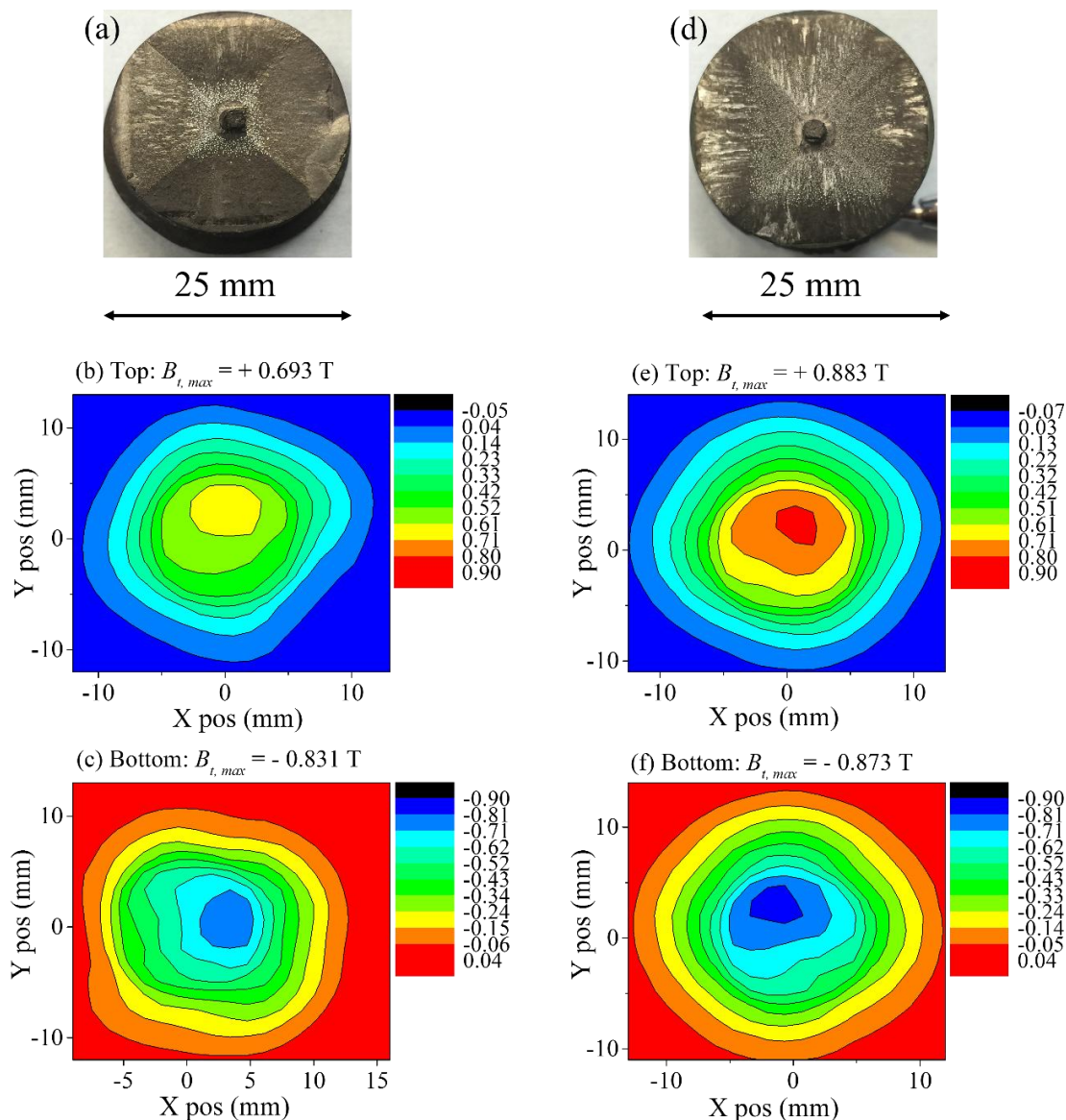


**Figure 73** Photographs of the polished top surfaces of: (a) Ag-SmBCO with a 12 g Y-123 layer and (d) Ag-SmBCO with a 6 g Y-123 layer and their trapped field profiles at both the top: (b) Ag-SmBCO with a 12 g Y-123 layer and (e) Ag-SmBCO with a 6 g Y-123 layer and bottom: (c) Ag-SmBCO with a 12 g Y-123 layer and (f) Ag-SmBCO with a 6 g Y-123 layer surfaces measured at a distance of 0.5 mm above the sample surface. The maximum trapped field values at the top surfaces and bottom surfaces are indicated in the figure.

1 mol. %  $\text{ZrO}_2$  was added to the system in an attempt to further improve the field-trapping ability of Ag-SmBCO with a Y-123 layer, and 2D contour maps of the trapped field of these samples are shown in Figure 74. The samples shown in Figures 74 (d), (g) and (j) are Ag-SmBCO bulk single grains synthesized under the same processing conditions with 1 mol. %  $\text{ZrO}_2$ . Comparison with Figure 74 (a) indicates that the field trapping ability of the liquid-enriched Ag-SmBCO did not increase further as was the case for the 1mol. %  $\text{ZrO}_2$ -doped Ag-SmBCO samples fabricated without a Y-123 liquid-rich source. A further increase in trapped field from + 0.883 T at the top surface of the sample in Figure 74 (b) and - 0.873 T at the bottom surface in Figure 74 (c) was not observed as expected with the addition of extra  $\text{ZrO}_2$ . Instead, the trapped field measured at the top surfaces of the 1mol. %  $\text{ZrO}_2$ -doped liquid-enriched Ag-SmBCO single grains are: + 0.861 T [Figure 74 (e)], + 0.787 T [Figure 74 (h)] and + 0.705 T [Figure 74 (k)], with corresponding values at the bottom surfaces of - 0.703 T [Figure 74 (f)], - 0.746 T [Figure 74 (i)] and - 0.585 T [Figure 74 (l)]. In addition, the differences in the trapped fields between these samples are obvious at both the top and bottom surfaces of the samples, which indicates that further attempts are necessary to stabilise the Ag-SmBCO system.

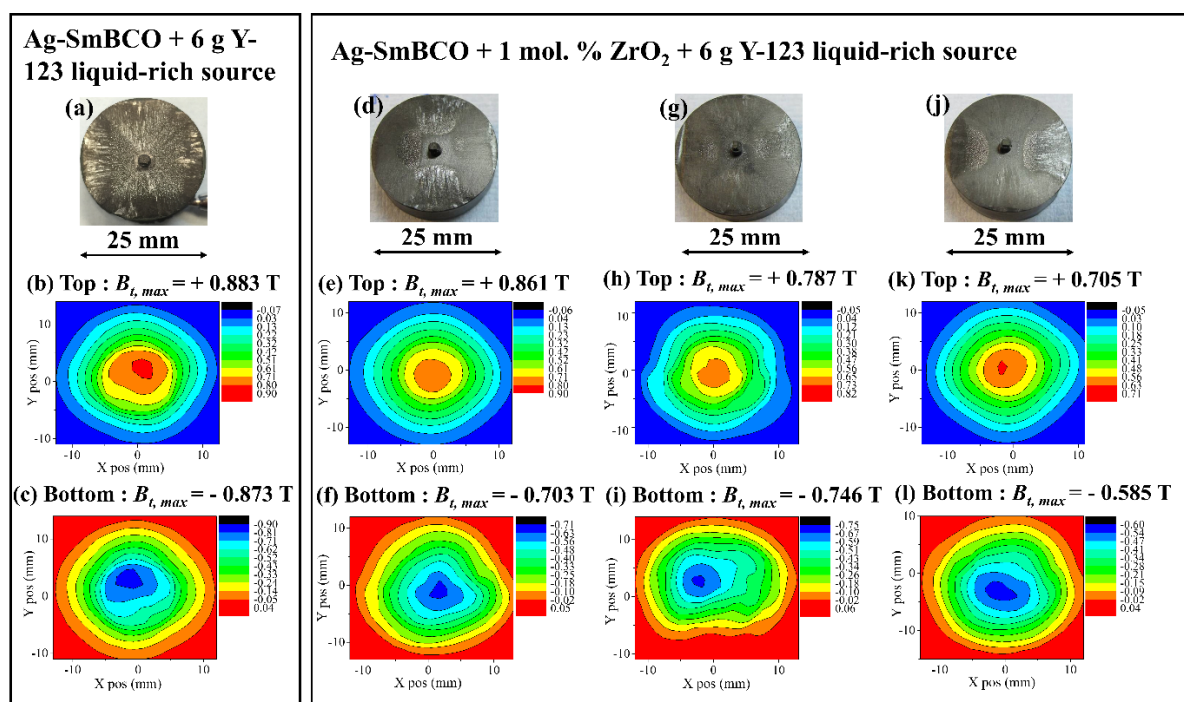


**Figure 74** Photographs of the polished top surfaces of: (a) Ag-SmBCO with a 6 g Y-123 layer; (d), (g) and (j) 1 mol. %  $ZrO_2$ -doped Ag-SmBCO with a 6 g Y-123 layer (repeated experiments) and their trapped field profiles at both the top: (b) Ag-SmBCO with a 6 g Y-123 layer; (e), (h) and (k) 1 mol. %  $ZrO_2$ -doped Ag-SmBCO with a 6 g Y-123 layer; (c) Ag-SmBCO with a 6 g Y-123 layer; (f), (i) and (l) 1 mol. %  $ZrO_2$ -doped Ag-SmBCO with a 6 g Y-123 layer surfaces measured at a distance of 0.5 mm above the sample surface. The maximum trapped field values at the top surfaces and bottom surfaces are indicated in the figure.

Further reduction of the mass of the Y-123 layer was applied in a sample fabricated from 1 mol. %  $ZrO_2$ -doped Ag-SmBCO with a 4 g Y-123 liquid-rich source in two different arrangements, as shown in Figure 75. One method involved preparing the Y-123 layer as a 4 g pellet of the same diameter as the bulk pre-form. The second involved introducing the Y-123 liquid-rich source in the form of four 1 g pellets to support the bulk pre-form, as shown in Figure 75 (h). Difficulties were encountered during the preparation of both sets of Y-123 pellets. The 4 g pellet was too thin to press into a stable bulk form, and pressing of the four individual pellets prolongs significantly the fabrication procedure. Compared with the sample containing 1 mol. %  $ZrO_2$ -doped Ag-SmBCO prepared with a 6 g Y-123 layer in Figure 75 (a), which can trap +0.861 T at its top surface [(Figure 75 (b))] and  $-0.703$  T at its bottom surface [Figure 75 (c)], however, the trapped fields suggest that such further reduction in

mass and the new arrangement of the Y-123 liquid-rich source does not improve the field-trapping ability of the 1 mol. %  $\text{ZrO}_2$ -doped Ag-SmBCO sample. In this case, the single grain prepared with a 4 g Y-123 layer in Figure 75 (d) can trap +0.636 T [Figure 75 (e)] and  $-0.605$  T [Figure 75 (f)] at its bottom surface, whereas the single grain prepared with four, 1 g Y-123 pellets in Figure 75 (g) can trap +0.548 T at its top surface [Figure 75 (i)] and  $-0.302$  T [Figure 75 (j)] at its bottom surface. This is due possibly to the deformation of the Y-123 layer during TSMG. As a result, a 6 g Y-123 layer was used as the optimized liquid-rich source in subsequent experiments.

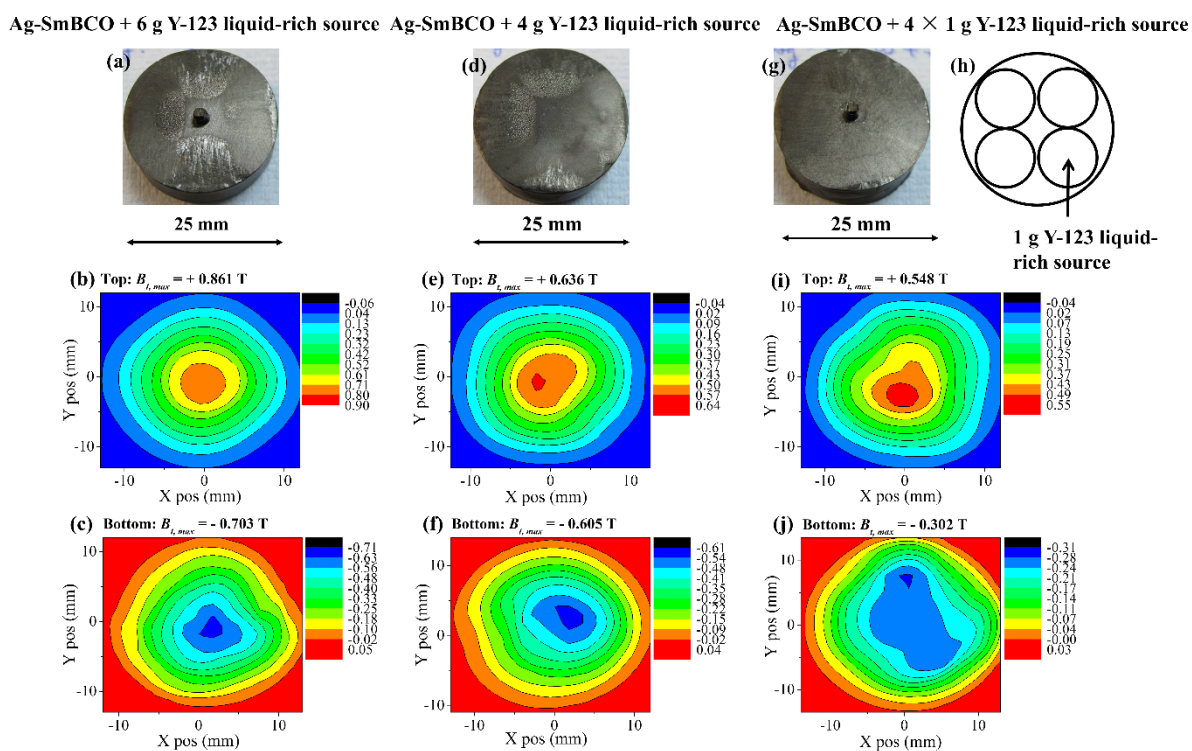


**Figure 75** Photographs of the polished top surfaces of: (a) Ag-SmBCO with a 6 g Y-123 layer; (d) Ag-SmBCO with a 4 g Y-123 layer and (g) Ag-SmBCO with four 1 g Y-123 pellets (arrangement shown in (h)) and their trapped field profiles at both the top: (b) Ag-SmBCO with a 6 g Y-123 layer; (e) Ag-SmBCO with a 4 g Y-123 layer and (i) Ag-SmBCO with four 1 g Y-123 pellets and bottom: (c) Ag-SmBCO with a 6 g Y-123 layer; (f) Ag-SmBCO with a 4 g Y-123 layer and (j) Ag-SmBCO with four 1 g Y-123 pellets surfaces measured at a distance of 0.5 mm above the sample surface. The maximum trapped field values at the top surfaces and bottom surfaces are indicated in the figure.

Cold isostatic pressing (CIP) was applied to densify the Ag-SmBCO pre-form and reduce the porosity of the sample, leading to further improvement of the superconducting properties of

the Ag-SmBCO bulk single grains. The trapped field measurements for the CIP-ed Ag-SmBCO single grains are shown in Figure 76. It can be seen that the field-trapping ability for both top and bottom surfaces of the CIP-ed sample is enhanced, increasing to + 0.883 T [Figure 76 (e)] from + 0.799 T for the un-CIP-ed sample in Figure 76 (a) on the top surface [Figure 76 (b)] and to - 0.873 T [Figure 76 (f)] from - 0.82 T for the un-CIP-ed on the bottom surface [Figure 76 (c)]. Subsequently, the samples were cut in half for observation of their cross-sections to confirm whether the CIP treatment had been effective in reducing the porosity of the Ag-SmBCO single grains. The images of the cross-sections of these two samples are shown in Figure 77 [Ag-SmBCO without CIP in Figure 77 (a) and Ag-SmBCO with CIP in Figure 77 (b)]. From these, it can be concluded that the enhancement of the superconducting properties of the CIP-ed sample are due largely to the reduced porosity in the sample, indicating that a more compact sample containing fewer pores can trap higher magnetic field.

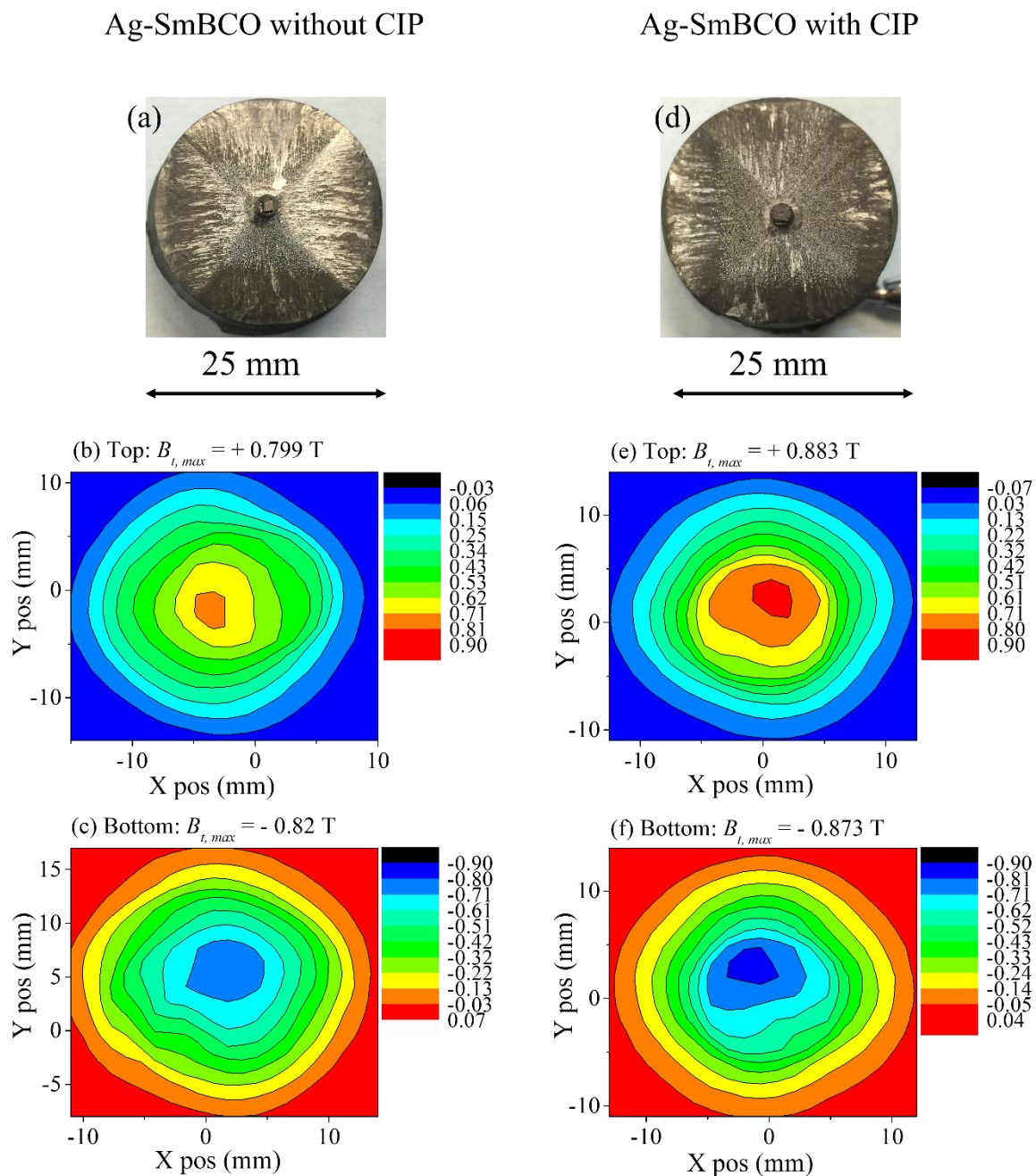


**Figure 76** Photographs of the polished top surfaces of: (a) Ag-SmBCO without CIP and (d) Ag-SmBCO with CIP and their trapped field profiles at both the top: (b) Ag-SmBCO without CIP and (e) Ag-SmBCO with CIP and bottom: (c) Ag-SmBCO without CIP and (f) Ag-SmBCO with CIP surfaces measured at a distance of 0.5 mm above the sample surface. The maximum trapped field values at the top surfaces and bottom surfaces are indicated in the figure.

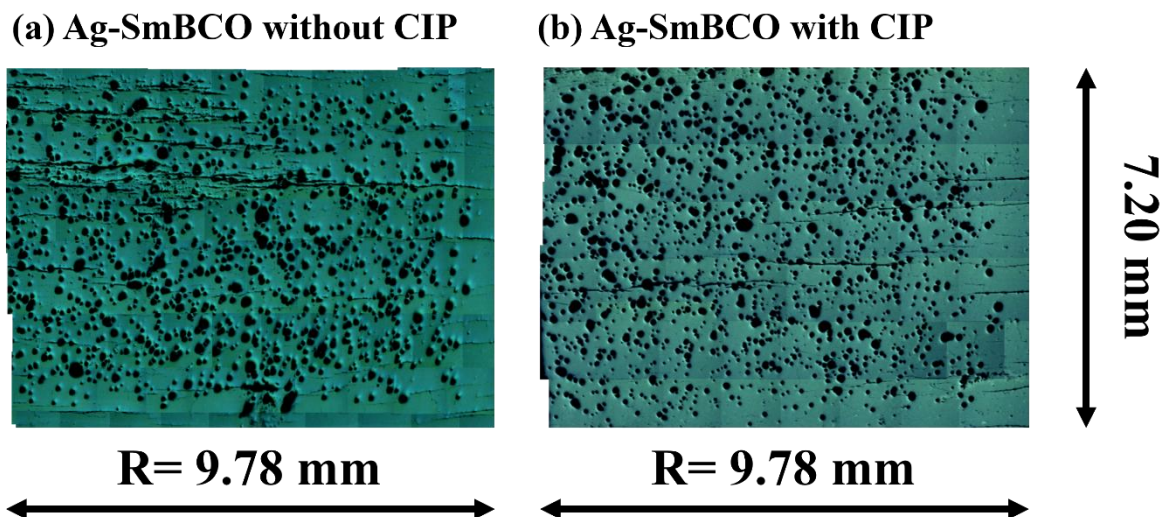


**Figure 77** Optical photographs of the cross sections of (a) Ag-SmBCO without CIP; (b) Ag-SmBCO with CIP.

Two further Ag-SmBCO samples were fabricated using thin film and MgO-NdBCO generic seeds, respectively, with the assistance of a Y-123 layer to establish whether the liquid-rich source has an impact on seeding material. The 2D trapped field contour maps of these samples, which are shown in Figure 78, exhibit similar values for both samples [Figure 78 (a) and (d)] on both surfaces summarised in Table 21 (sample grown with a thin film seed: top: + 0.883 T [Figure 78 (b)] and bottom: - 0.882 T [Figure 78 (c)]; sample grown with an MgO-NdBCO generic seed: top: + 0.883 T [Figure 78 (e)] and bottom: - 0.873 T [Figure 78 (f)]). It can be concluded that the growth of single grain Ag-SmBCO with a Y-123 layer can be achieved for thin film and MgO-NdBCO generic seeds with reasonable superconducting properties without being affected by the presence of the additional Y-123 liquid-rich source.

Ag-SmBCO with a film seed

Ag-SmBCO with a MgO-NdBCO generic seed

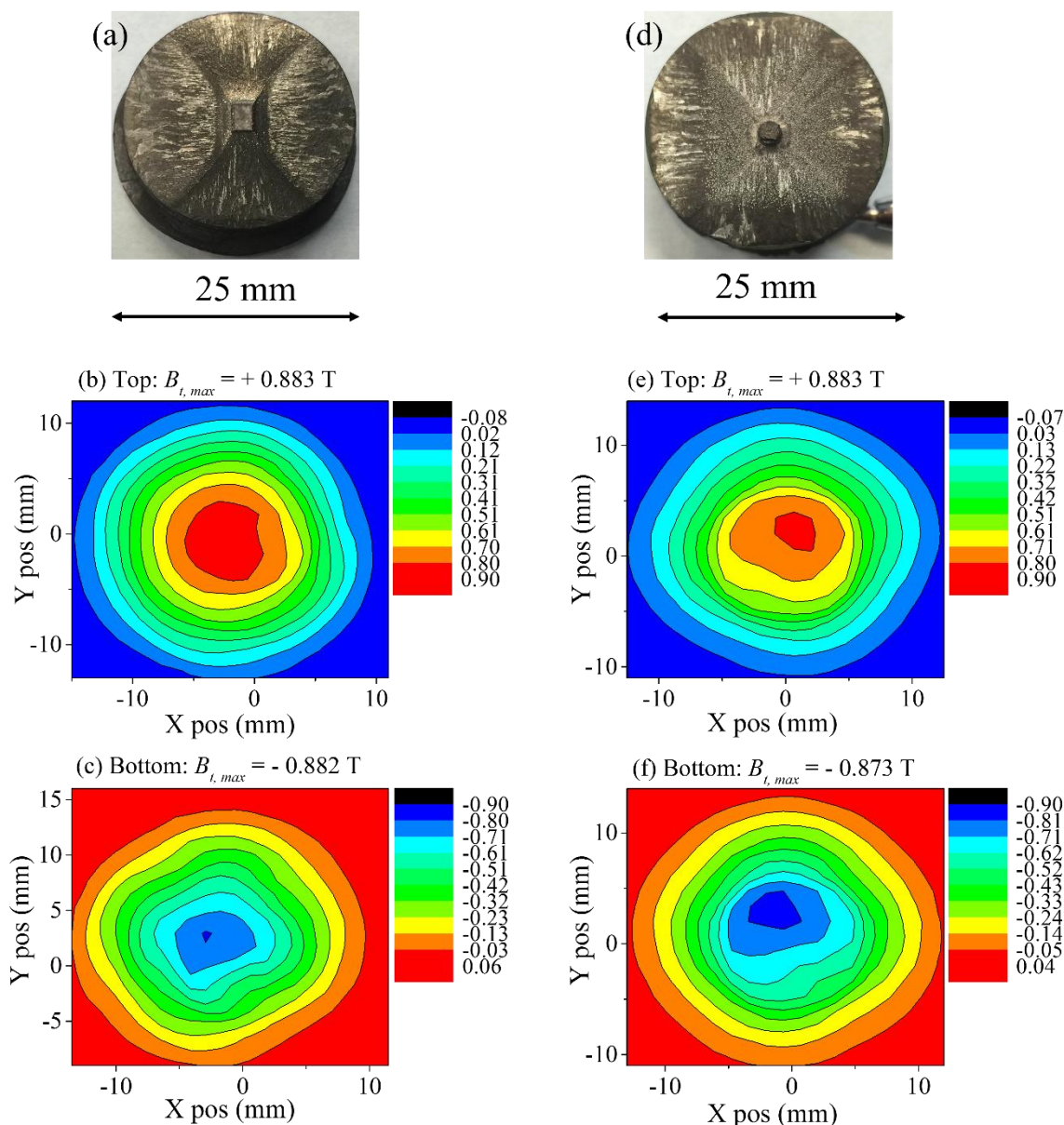


**Figure 78** Photographs of the polished top surfaces of: (a) Ag-SmBCO a film seed and (d) Ag-SmBCO with an MgO-NdBCO generic seed and their trapped field profiles at both the top: (b) Ag-SmBCO a film seed and (e) Ag-SmBCO with an MgO-NdBCO generic seed and bottom: (c) Ag-SmBCO a film seed and (f) Ag-SmBCO with an MgO-NdBCO generic seed surfaces measured at a distance of 0.5 mm above the sample surface. The maximum trapped field values at the top surfaces and bottom surfaces are indicated in the figure.

**Table 21** The maximum trapped field values measured at a distance of 0.5 mm above the sample surface at the top and bottom surfaces of Ag-SmBCO with thin film and MgO-NdBCO generic seeds (samples 25 mm in diameter).

Sample	Seeding material		Trapped field (T)		Size (mm)
	Thin film	MgO-NdBCO	Top	Bottom	
Figure 78 (a)	√		+ 0.883	- 0.882	25
Figure 78 (d)		√	+ 0.883	- 0.873	25

Single grain Ag-SmBCO samples with diameters of 25 mm were fabricated reliably with the assistance of the Y-123 layer introduced to the process. The extra Ba-source ( $\text{BaO}_2$ ) introduced in the precursor powders to suppress the substitution of Sm/Ba was then replaced with BaO in an attempt to reduce the amount of oxygen released on peritectic decomposition, so that the cracks caused by the oxygen entering and leaving the bulk can be reduced. Table 22 summarises the trapped fields of the Ag-SmBCO bulk single grains prepared with BaO (samples b and c) using an Ag-SmBCO bulk single grain with  $\text{BaO}_2$  as a reference (sample a). It can be seen that although the field trapped by the bulk single grains fluctuates significantly when  $\text{BaO}_2$  is replaced by BaO in the precursor powders, the magnetic field trapped by the samples are still improved, and especially at the top surface of the sample. As a result, sample b can trap + 0.881 T and - 0.808 T at its top and bottom surfaces and sample c can trap + 0.954 T and - 0.770 T. Therefore, samples with diameters larger than 25 mm can be grown by using BaO instead of  $\text{BaO}_2$  in the precursor powders.

**Table 22** The maximum trapped field values measured at a distance of 0.5 mm above the sample surface at the top surfaces and bottom surfaces of Ag-SmBCO with BaO<sub>2</sub> and BaO in the precursor powders (samples 25 mm in diameter).

Sample No.	Precursor powder composition		Trapped field (T)		Size (mm)
	BaO <sub>2</sub>	BaO	Top	Bottom	
a	√		+ 0.787	− 0.746	25
b		√	+ 0.881	− 0.808	25
c		√	+ 0.954	− 0.770	25

The 2D trapped-field contour maps of larger single grains, of diameter 31 mm and 41 mm respectively, are shown in Figure 79. As discussed in Section 6.1, in theory, the larger the bulk single grain, the higher its field trapping ability. This is consistent with the observation that the Ag-SmBCO single grain sample of diameter 31 mm [Figure 79 (a)] can trap + 1.033 T at its top surface in Figure 79 (b) and − 0.917 T at its bottom surface as shown in Figure 79 (c), which is the highest field trapped to date in the SmBCO system for a sample in a similar size grown in air. However, for the 41 mm diameter sample shown in Figure 79 (d), instead of trapping an even higher field, trapped fields of only + 0.996 T in Figure 79 (e) and − 0.792 T in Figure 79 (f) are observed at the top and bottom surfaces, respectively. This could be attributed to the fact that samples with larger diameters tend to form more defects during the fabrication process, which, in turn, will affect the superconducting properties of the Ag-SmBCO single grains. In general, larger samples are more difficult to grow due to the criticality of every step of the synthesis procedure, such as the mixing of the precursor powders and the temperature distribution of the furnace. Therefore, in practice, additional processing challenges always appear when a (RE)BCO melt process is scaled-up and the growth of larger samples is always accompanied with new problems that are detrimental to the field-trapping ability of a bulk single grain.

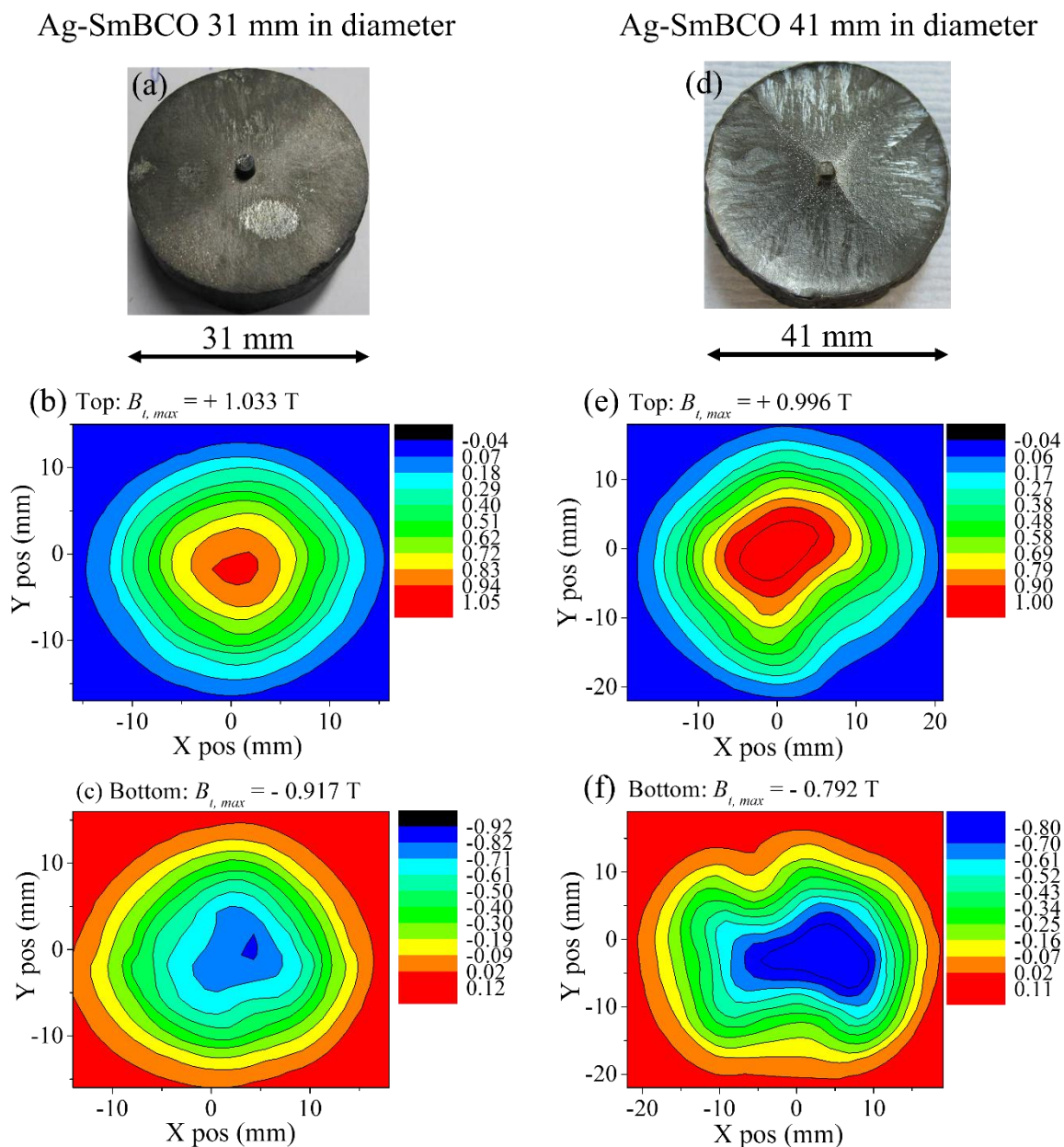


**Figure 79** Photographs of the polished top surfaces of: (1) Ag-SmBCO 31 mm in diameter and (4) Ag-SmBCO 41 mm in diameter and their trapped field profiles at both the top: (2) Ag-SmBCO 31 mm in diameter and (5) Ag-SmBCO 41 mm in diameter and bottom: (3) Ag-SmBCO 31 mm in diameter and (6) Ag-SmBCO 41 mm in diameter surfaces measured at a distance of 0.5 mm above the sample surface. The maximum trapped field values at the top surfaces and bottom surfaces are indicated in the figure.

In summary, Ag-SmBCO bulk single grains can be fabricated in a reliable manner up to a diameter of 41 mm with the aid of a Y-123 liquid-rich layer. In addition, by using cold isostatic pressing (CIP) to compact the bulk pre-form combined with the replacement of

BaO<sub>2</sub> by BaO in the precursor powders, a Ag-SmBCO single grain sample with diameter 31 mm can trap a magnetic field as high as + 1.033 T at its top surface, which is the highest magnetic field reported to date for the SmBCO system for a sample in a similar size grown in air.

### **6.3.3. Discussion of the Effects of a Y-123 Layer on Ag-SmBCO System**

A Y-123 liquid-rich layer has been shown to be beneficial to the synthesis and the superconducting properties of Ag-SmBCO bulk single grains. The effects of this Y-123 layer will be discussed further in this section.

#### **6.3.3.1. Reliable Growth of Ag-SmBCO Single Grains**

Samples grown with and without a Y-123 layer exhibited typical fourfold growth sector boundaries on their top surfaces [Figures 80 (a) and (b)], indicating that single grains may be fabricated regardless of the presence of a Y-123 layer. Although the morphology of the top surfaces of these samples are similar, the bulk single grains display different macrostructures when viewed from the side of the sample. With the assistance of a Y-123 layer, a shorter *c*-axis direction growth was observed in the as-prepared sample when compared to the sample grown by regular TSMG due to the increased growth rate along the *c*-axis induced by the presence of the Y-123 liquid-rich phase [53] [Figures 80 (c), (d), (g) and (h)]. Krauns *et al.* reported that the growth rate is limited by the low solubility of the RE ions [130] and, due to the anisotropic growth rate along *a/b*- and *c*-axis, a super-saturation of RE ions is established quickly along the *c*-axis, which, in due course, inhibits growth along the *a/b*-axis. As a result, the Y-123 layer provides a supplementary liquid phase to dissolve more RE ions in the matrix to address these limitations of the growth process, and, as a result, is beneficial for bulk single grain growth along both growth directions. A limited growth along the *c*-axis can be attributed to a higher *c*-axis direction growth rate. Additionally, from the bottom views of the samples shown in Figures 80 (e) and (f), it can be inferred that the contact between the

bottom of the bulk sample and the Y-123 layer leads to a lower melting temperature in the vicinity of the interface, since the melting temperature of Ag-SmBCO is 1044.3 °C in Figure 64, whereas that of Y-123 is much lower (1005 °C) [130]. This results in the formation of fewer sub-grains and misorientations, which form weak links in bulk single grains, which are unsuitable for engineering applications [131]. A Y-123 layer can also serve as a supporting and partition layer between the Ag-SmBCO pre-form and the yttrium-stabilised ZrO<sub>2</sub> rods used previously to hold the bulk pre-form during TSMG, which inhibits further sub-grain growth (the yttrium-stabilised ZrO<sub>2</sub> rods can induce nucleation during TSMG). In addition, the liquid phase in the pre-form is consumed due to the porous nature of the alumina plate, when both the Ag-SmBCO pre-form and the yttrium-stabilised ZrO<sub>2</sub> rods are placed on the alumina plate.

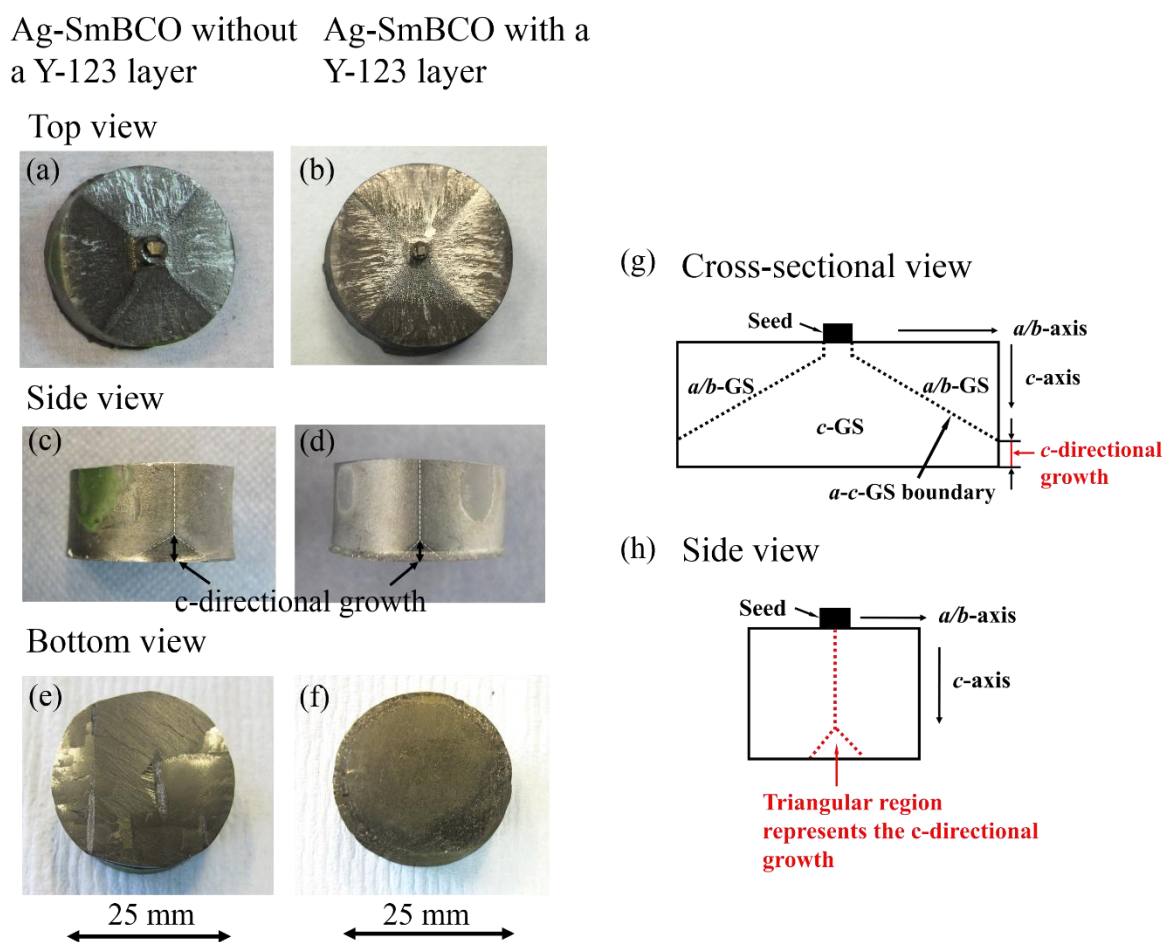


**Figure 80** Photographs of the Ag-SmBCO single grain samples without a Y-123 layer: (a) top view, (c) side view and (e) bottom view and Ag-SmBCO with a Y-123 layer: (b) top view, (d) side view and (f) bottom view. Illustrations of the cross-sectional view (g) and side view (h) of the growth along the *c*-axis.

### 6.3.3.2. Superconducting Properties: $T_c$ and $J_c$

The superconducting properties,  $T_c$  and  $J_c$ , of the samples fabricated with the Y-123 layer along the  $c$ -axis are summarised in Figures 81 and 82, respectively. The same scales are used in the figures to enable meaningful comparison.

It can be concluded from  $T_c$  and the transition width,  $\Delta T_c$  in Figure 81 that the variation in superconducting properties is greater for Ag-SmBCO fabricated without a Y-123 layer than Ag-SmBCO with a Y-123 layer. By adding a Y-123 layer to assist bulk growth, at positions near the top surface under the position of the seed, such as 1b and 1c, higher  $T_c$  (93 K) is observed in the Ag-SmBCO sample fabricated without a Y-123 layer and this sample exhibits a narrower  $\Delta T_c$ . For specimens further away from the seed, at positions 1d and 1e, Ag-SmBCO processed with a Y-123 layer exhibits a similar  $T_c$  (92.7 K) and  $\Delta T_c$ . However, for the Ag-SmBCO fabricated without a Y-123 layer,  $T_c$  at position 1d decreases to 92.5 K and even further to 92.0 K at position 1e with wider  $\Delta T_c$  at both positions.

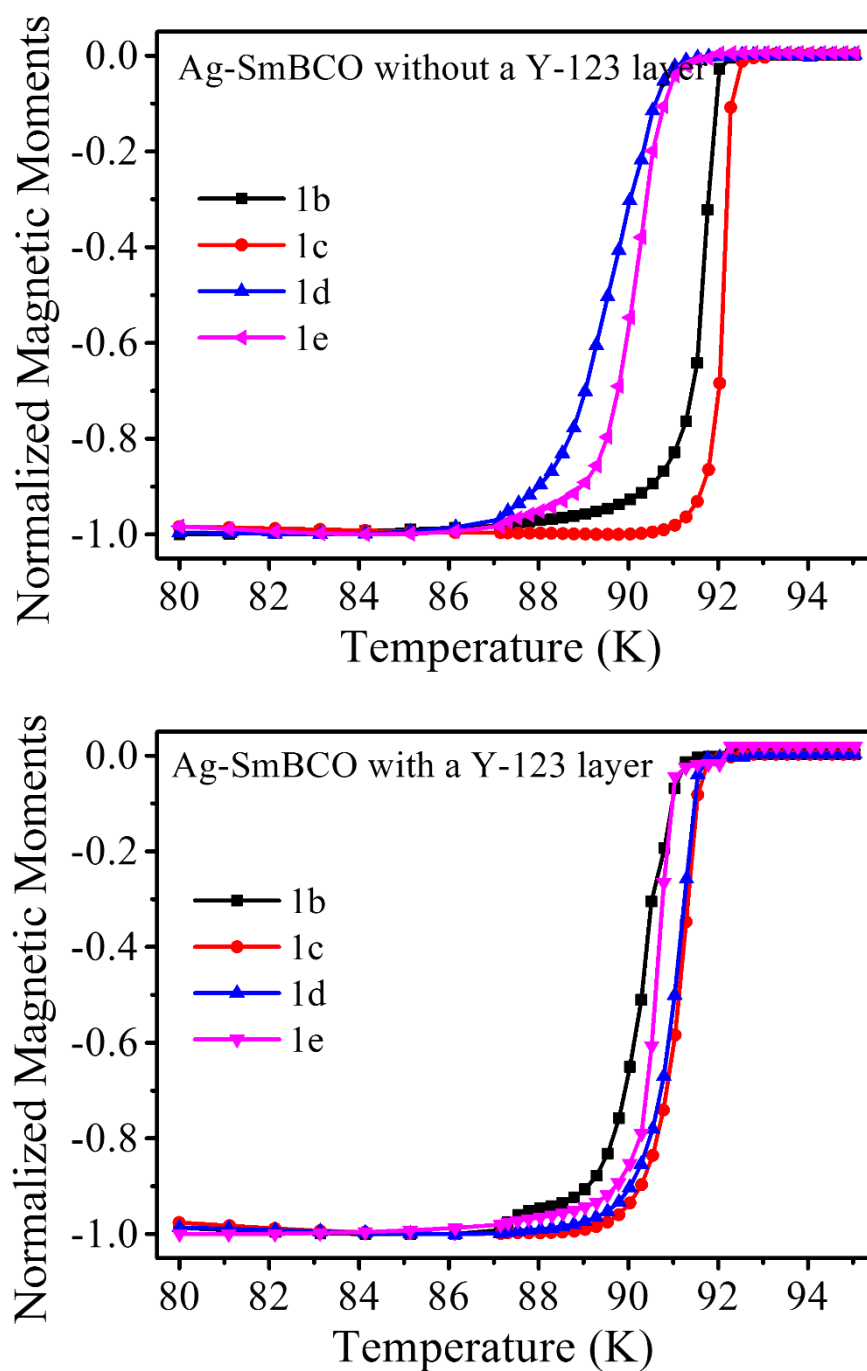


**Figure 81** Normalised magnetic moment as a function of temperature for Ag-SmBCO with and without a Y-123 layer with specimens corresponding to positions shown in Figure 63.

$J_c$  calculated using the extended Bean's critical state model [62] for these samples exhibits a similar trend as  $T_c$  as shown in Figure 82.  $J_c$  for the sample fabricated with a Y-123 layer is distributed more homogeneously throughout the parent single grain, which is more favourable for trapping magnetic field [55]. In general, the Ag-SmBCO specimens at

positions 1b and 1c exhibit a more pronounced peak effect and higher irreversibility field than at positions 1d and 1e. Adding a Y-123 layer tends to help the sample maintain similar  $J_c$ s at all positions in the single grain. In summary,  $J_c$  of Ag-SmBCO fabricated with a Y-123 layer exhibits a smaller irreversibility field and an inferior second peak effect with a significantly lower  $J_{c0}$  than Ag-SmBCO fabricated without a Y-123 layer. A more homogeneous distribution of  $J_c$ , which is beneficial to field trapping, is observed in Ag-SmBCO fabricated with a Y-123 layer.

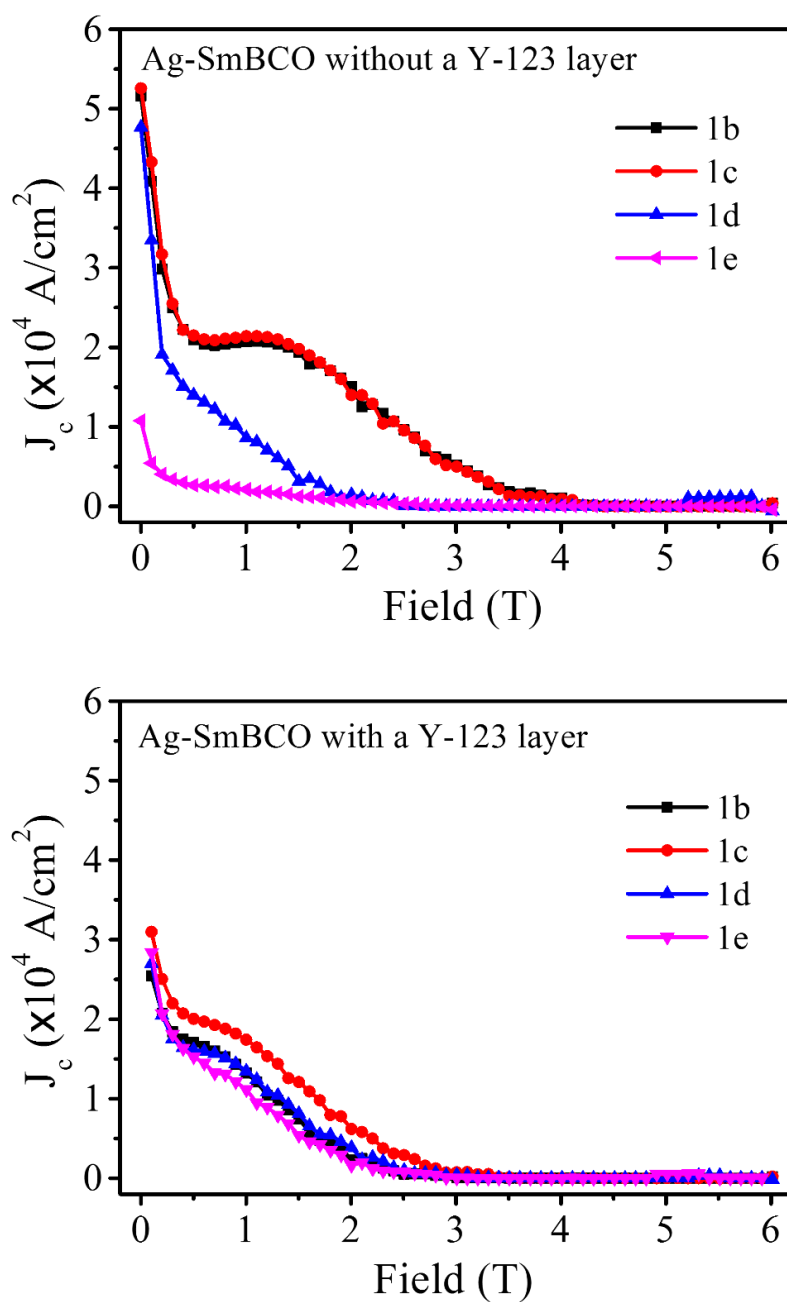


**Figure 82** Critical current density,  $J_c$ , as a function of magnetic field for Ag-SmBCO with and without a Y-123 layer with specimens corresponding to positions shown in Figure 63.

EMPA further confirmed the SQUID magnetometer results on the composition distribution along the  $c$ -axis, as seen in Figure 83. The green solid lines in Figure 83 are drawn to highlight the trend of the data. The amount of Sm decreases away from the seed for the sample fabricated without a Y-123 layer and as the amount of Ba increases, indicating more severe Sm/Ba substitution effects in the vicinity of the bottom of the bulk single grain, which

is consistent with  $T_c$  and  $J_c$  results. However, such a trend is not seen in the Y-123 liquid-enriched sample. Additional horizontal, solid green lines have been included in order to compare and indicate the relative stability of the values of  $x$  and  $y$  in the chemical formula  $\text{Ag-Sm}_x\text{Ba}_y\text{Cu}_3\text{O}_{7-\delta}$  of the superconducting bulk matrix.

In summary, the sample fabricated with a Y-123 layer exhibits a more homogeneous distribution of  $T_c$  and  $J_c$  along the  $c$ -axis with increasing distance from the seed, which is confirmed by EPMA compositional analysis.

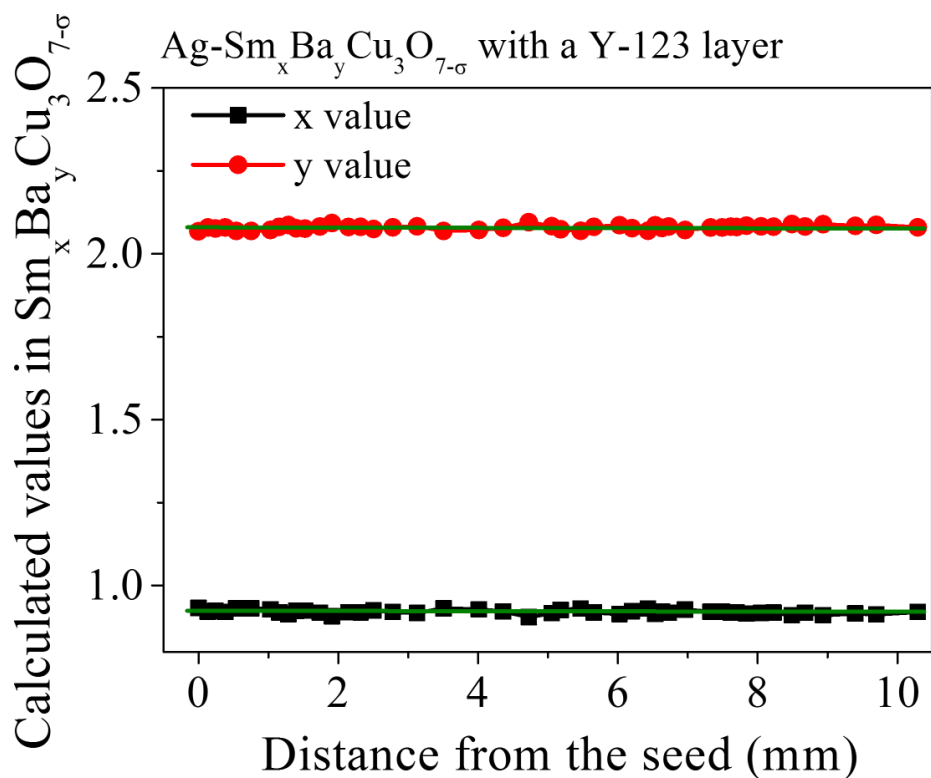
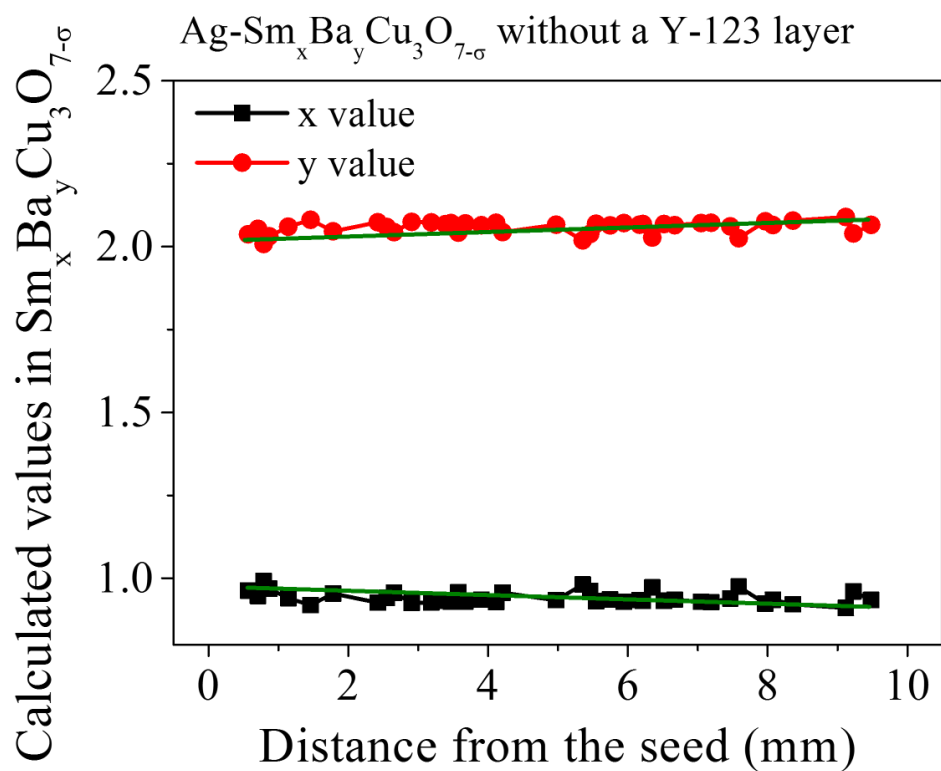


**Figure 83** Calculated values of x and y in Ag-SmBCO with and without a Y-123 layer from the seed along *c*-axis.

### 6.3.3.3. Microstructural Analysis of the Distribution of Sm-211 Particles

Further microstructural studies have been performed on Ag-SmBCO single grains fabricated with and without a Y-123 layer in an attempt to observe the distribution of Sm-211 inclusions within the cross section of the Sm-123 matrix. Previous research concluded that  $J_c$  is determined by inhomogeneities in the sample microstructure, such as micro-cracks, RE-211 particle inclusions and twin planes [5]. To obtain complete information on the Sm-211 distribution, the present research examined the sample microstructure at intervals of 1 mm from the seed along the primary axes across the whole cross section. The selection of micrographs shown in Figure 84 form the basis of discussion of the effects of the Y-123 layer on the particle Sm-211 dispersion within the superconducting phase matrix. Figures 84 (a) and (b) show magnification at  $\times 500$  at a position under the seed and near the bottom of the Ag-SmBCO sample fabricated without a Y-123 layer. Figures 84 (c) and (d) show corresponding images for the Ag-SmBCO sample with a Y-123 layer. In the micrographs, the darker regions represent the Sm-211 particles in the Sm-123 matrix, whereas the larger bright spots indicate the presence of silver. The black regions are pores in the matrix. It can be seen that more Sm-211 particles accumulate towards the bottom of the Ag-SmBCO fabricated without a Y-123 layer, whereas the degree of aggregation of Sm-211 particles in Ag-SmBCO fabricated with a Y-123 layer is much less severe. The more uniform distribution of Sm-211 particles is consistent with the observed homogeneous superconducting properties along the  $c$ -axis with increasing distance from the seed in Ag-SmBCO fabricated with a Y-123 layer.

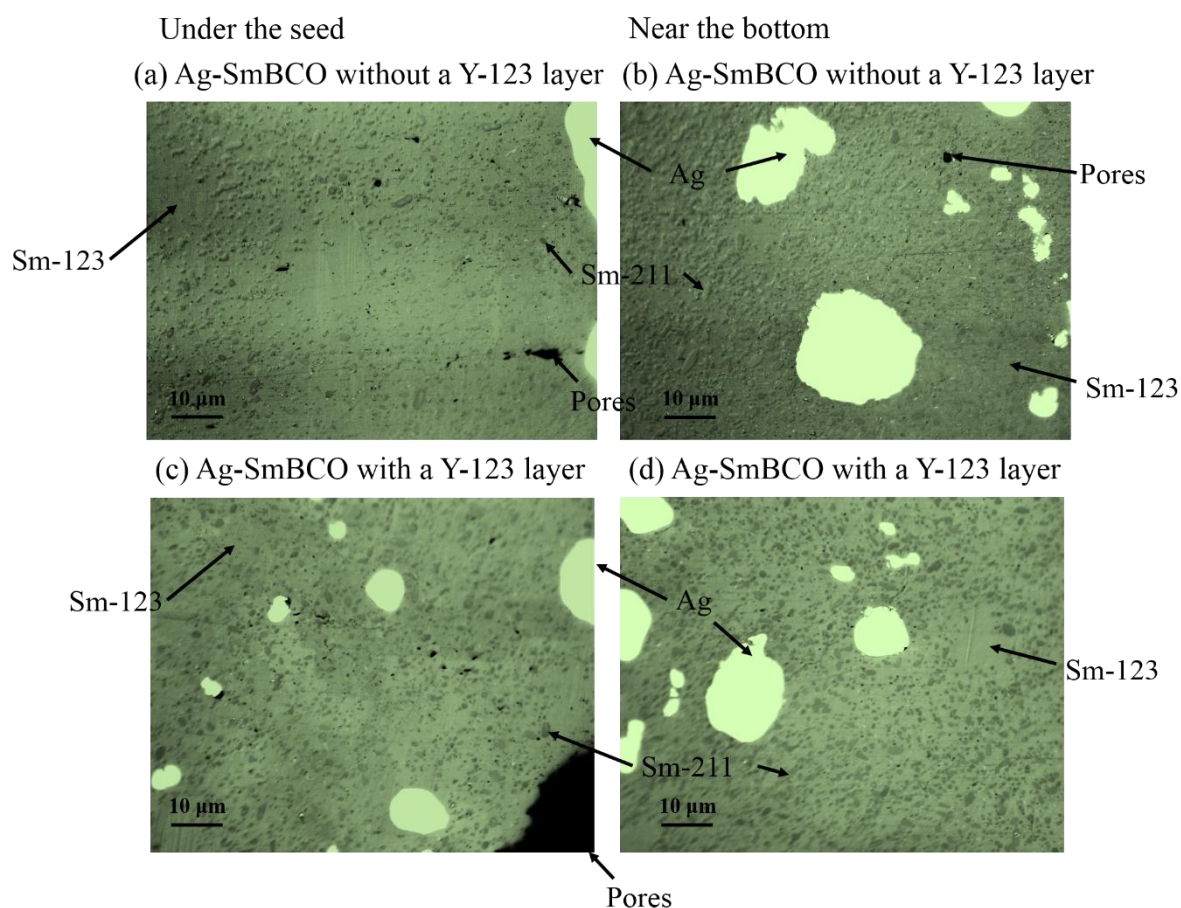


**Figure 84** Micrographs at a magnification of  $500\times$  for Ag-SmBCO fabricated without a Y-123 layer: (a) under the seed, (b) near the bottom of the sample; and Ag-SmBCO with a Y-123 layer: (c) under the seed, (d) near the bottom of the sample.

#### 6.3.3.4. Chemical Composition of the $\text{Sm}_{1+x}\text{Ba}_{2-x}\text{Cu}_y\text{O}_z$ Matrix in Ag-SmBCO Processed with and without a Y-123 Layer

EPMA measurements were used to further estimate the extent of Sm/Ba substitution within the SmBCO bulk single grains. Instead of measuring directly the atomic ratio of oxygen in  $\text{Sm}_{1+x}\text{Ba}_{2-x}\text{Cu}_y\text{O}_z$ , the amount of oxygen in the ceramic was estimated by data processing software on data acquired for Sm, Ba and Cu based on the stoichiometric composition of the SmBCO single grain. Figure 85 shows the atomic ratios of Sm, Ba and Cu along the  $c$ -axis

with increasing distance from the seed. Both figures show that the content of Cu is consistent along the  $c$ -axis. Therefore, when calculating  $x$  in the  $\text{Sm}_{1+x}\text{Ba}_{2-x}\text{Cu}_y\text{O}_z$  superconducting phase formula, only Sm and Ba need specific consideration, whereas the amounts of Cu and O are recognised to be constant.

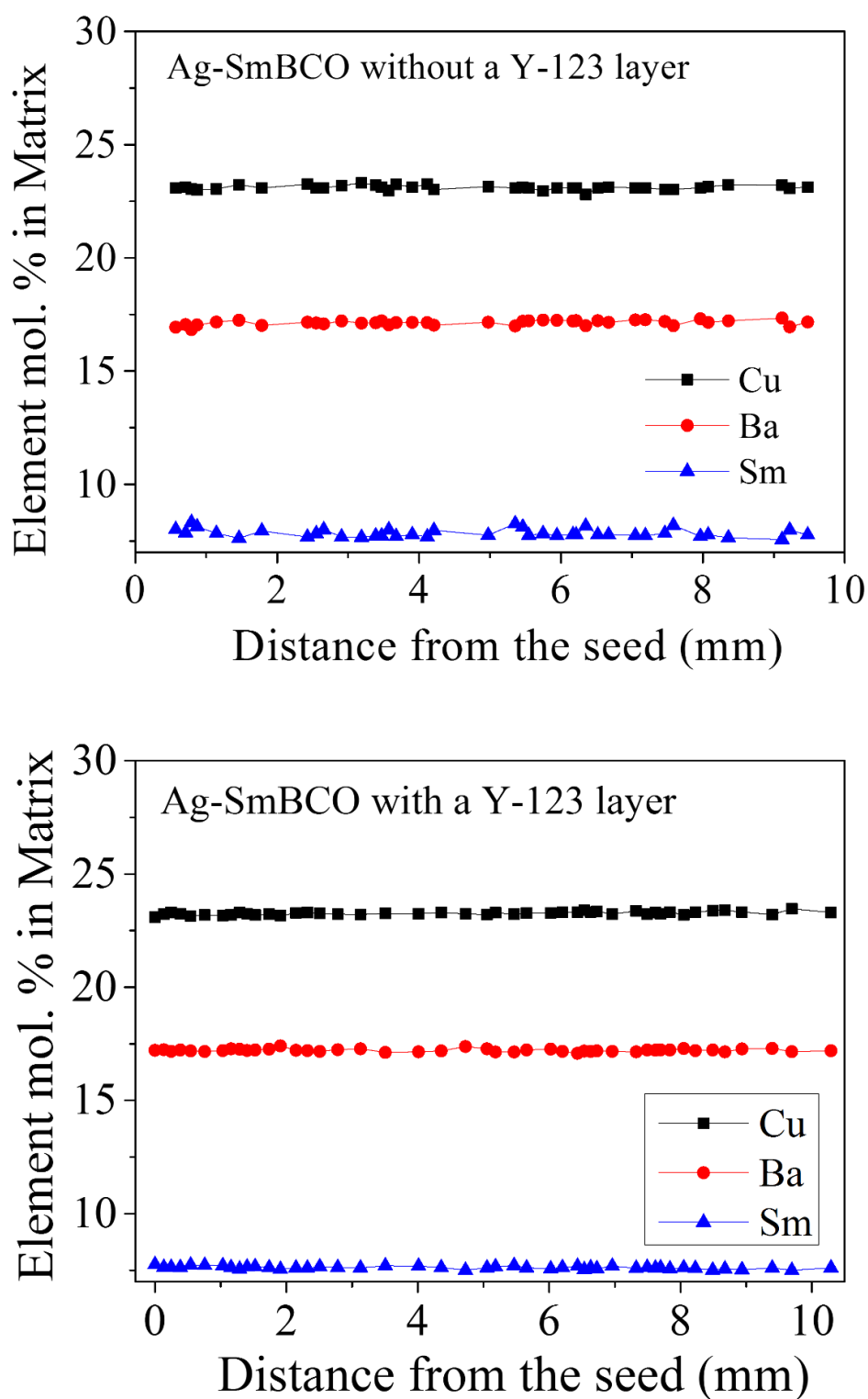


**Figure 85** Molar ratios of the elements in the matrix of Ag-SmBCO fabricated with and without a Y-123 layer with increasing distance from the seed along  $c$ -axis.

The average value of  $x$  in  $\text{Sm}_{1+x}\text{Ba}_{2-x}\text{Cu}_y\text{O}_z$  was estimated from the data shown in Figure 86. Greater dispersion is observed in Ag-SmBCO fabricated without a Y-123 layer, whereas the value of  $x$  varies more gently with a Y-123 layer, further confirming that the presence of a Y-123 layer is beneficial to processing a more uniform Ag-SmBCO bulk single grain. The value of  $x$  in  $\text{Sm}_{1+x}\text{Ba}_{2-x}\text{Cu}_3\text{O}_{7-\delta}$  can be determined reliably since the collected data are reasonably constant and their variations are within 1 mol. %, which is within the error of EPMA. The calculated average values of  $x$  for both samples are negative,  $-0.080$  and  $-0.058$  for samples grown with and without a Y-123 layer, respectively. This indicates that the substitution of Sm on the Ba site is enhanced by adding a Y-123 layer, which increases the concentration of Sm ions in the liquid. In addition, the data provide further explanation of the inferior superconducting properties,  $T_c$  and  $J_c$ , in the sample grown with a Y-123 layer due to the more severe Sm/Ba substitution effects, since it is reasonable to assume a close-to-zero value of  $x$  for the standard sample, which exhibits a high  $T_c$  of around 94 K [132] and a sharp  $\Delta T_c$  of less than 1 K [133].

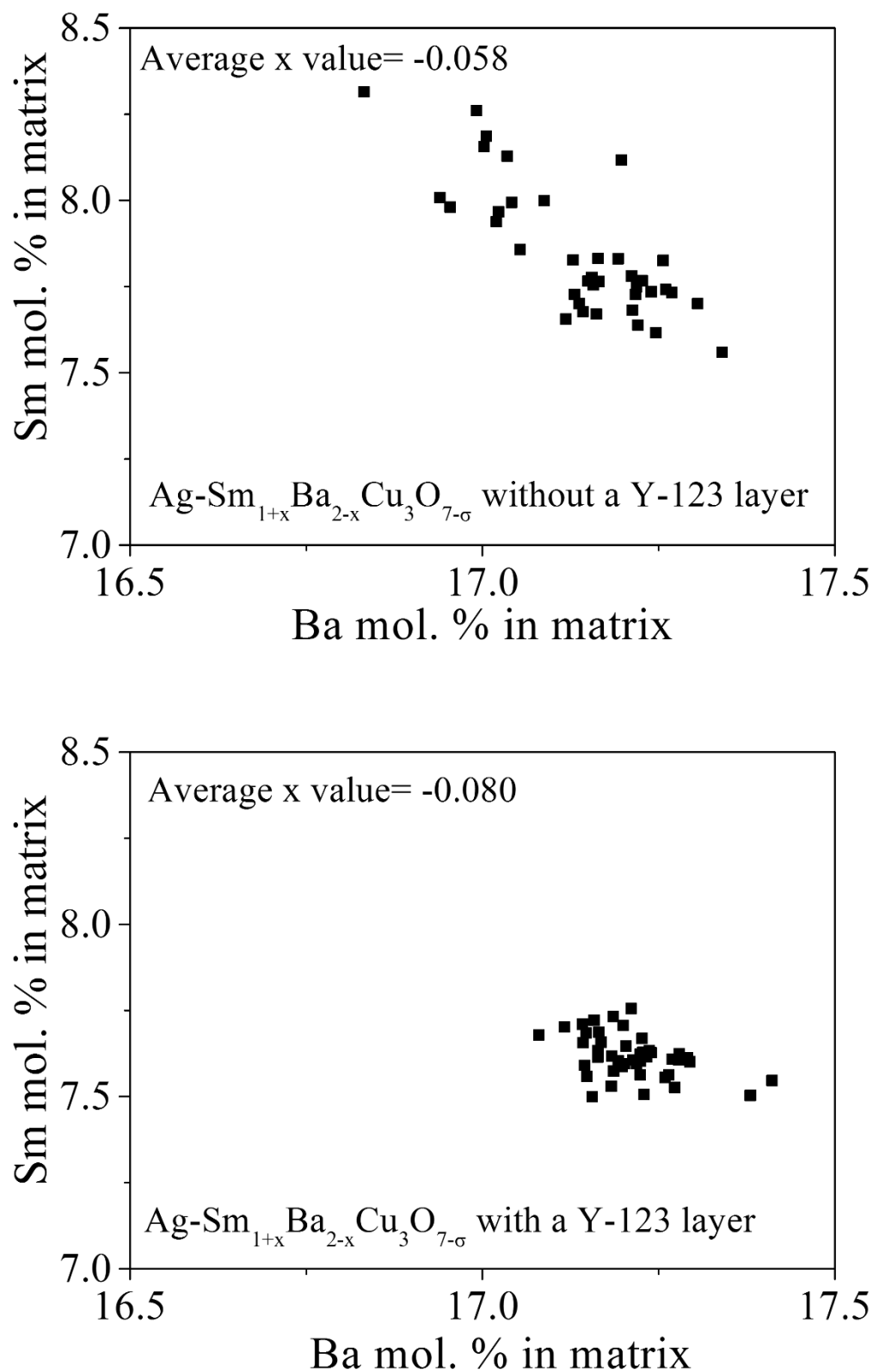


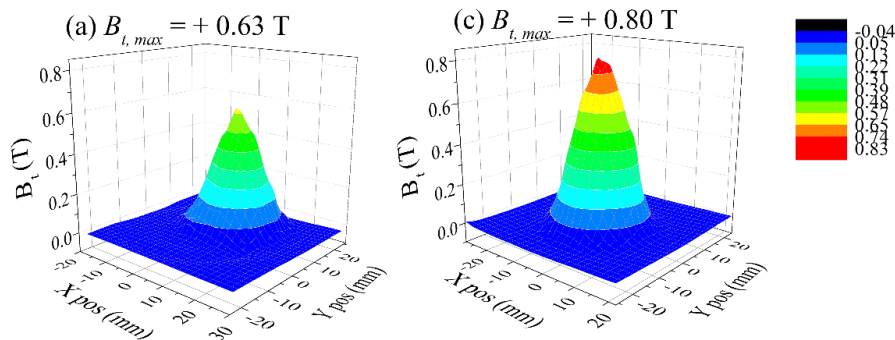
**Figure 86** The concentration distribution of Sm and Ba in Ag-SmBCO fabricated with and without a Y-123 layer.

### 6.3.3.5. Trapped Field Profiles

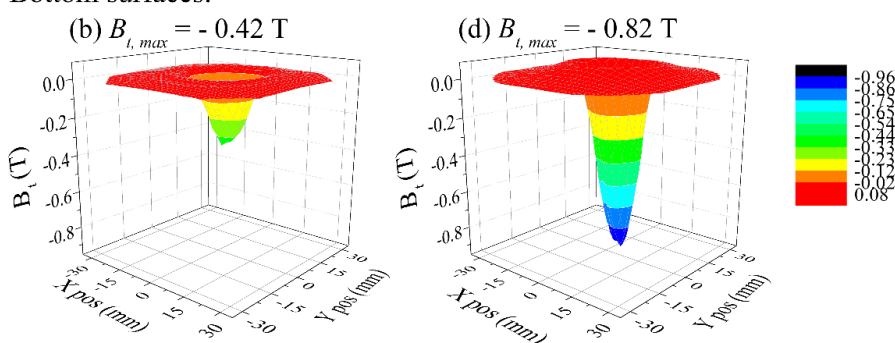
A maximum field of + 0.80 T is trapped at the top surface of the sample with a Y-123 layer for an applied magnetic field of 1.3 T [Figures 87 (c) and (g)] while a – 0.82 T is detected at the bottom surface [Figures 87 (d) and (h)], which represents a significant improvement compared to the sample grown without a Y-123 layer [Top: + 0.63 T (Figures 87 (a) and (e)); Bottom: – 0.42 T [Figures 87 (b) and (f)]. Such improvement can be attributed to the uniform distribution of  $J_c$  in Ag-SmBCO fabricated with a Y-123 layer as indicated by SQUID magnetometer and the observed improved magnetic flux pinning. It is reasonable to attribute the observed field induced flux pinning to the effects of substitution [127] since the characteristic length of the disorder caused by substitution is approximate to the coherent length ( $\xi$ ). Adding a Y-123 layer increased the effects of Sm/Ba substitution, which can act as extra pinning centres in bulk single grains, leading to improved field trapping ability. Moreover, compared with Ag-SmBCO fabricated without a Y-123 layer, Ag-SmBCO with a Y-123 layer can trap almost twice the field at its bottom surface mainly because sufficient liquid phase provided by a Y-123 layer, which aids significantly the growth of more superconducting phase close to the bottom of the sample. Such an improvement in the field-trapping capability is promising for the development of further practical applications of Ag-SmBCO bulk, single grains.

Ag-SmBCO without a Y-123 layer    Ag-SmBCO with a Y-123 layer

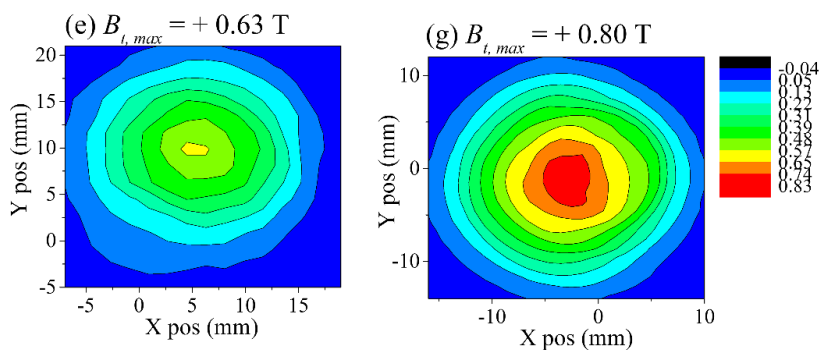
3D maps: top surfaces:



Bottom surfaces:



2D contour maps: top surfaces:



Bottom surfaces:

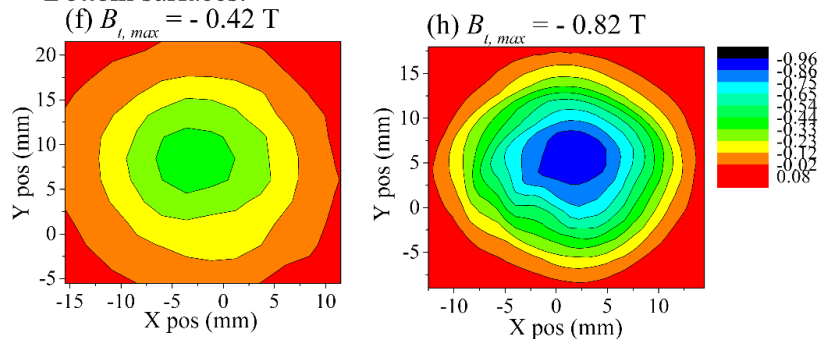


**Figure 87** 3D and 2D contour maps of the trapped field distribution at the top surfaces: (a), (c), (e) and (g) and at the bottom surfaces: (b), (d), (f) and (h) of Ag-SmBCO single grains fabricated with and without a Y-123 layer.

## 6.4. Summary

In this chapter, the scale-up of the SmBCO bulk single grains was achieved for the purpose of quasi-magnet engineering applications by the addition of silver to the SmBCO system to form large, Ag-SmBCO single grains. Initially, a reliable growth of Ag-SmBCO single grains was achieved by various approaches including the adjustment of the composition of the precursor powders (replacement of BaO<sub>2</sub> with BaO), cold isostatic pressing (CIP) of the Ag-SmBCO pre-forms and the addition of a Y-123 liquid-rich layer beneath the bulk pre-form prior to melt processing. Secondly, comparison of the measured trapped fields of the successfully grown Ag-SmBCO samples was performed. The various roles of the Y-123 liquid-rich layer and its impact on the appearance, superconducting properties ( $T_c$  and  $J_c$ ), microstructure, chemical compositions and field-trapping ability of the Ag-SmBCO bulk single grains were examined in detail. Ag-SmBCO bulk single grains were fabricated subsequently by a reliable technique up to a diameter of 41 mm with the aid of a Y-123 liquid-rich layer. In addition, by using CIP to prepare the bulk pre-form, with the replacement of BaO<sub>2</sub> with BaO in the precursor powders, a Ag-SmBCO single grain of diameter 31 mm was obtained to trap a magnetic field as high as + 1.033 T at its top surface, which is the highest magnetic field trapped reported to date for the SmBCO system for a sample in a similar size grown in air. Subsequently, the effects of a Y-123 layer were investigated further, along with the benefits and effects of introducing a Y-123 layer beneath the Ag-SmBCO pre-form to provide a reliable route to improve the success rate of fabricating Ag-SmBCO bulk single grains by inhibiting the growth of sub-grains from the bottom of the sample. By adding a Y-123 layer, the interface between the very bottom of the bulk and the Y-123 layer tends to have a lower melting temperature than the temperatures used typically in the growth window of Ag-SmBCO, which, in turn, reduces the probability of the nucleation and growth of sub-grains at this position. More importantly, a Y-123 layer has a positive influence on the field-trapping ability of the Ag-SmBCO bulk single grains, especially at the bottom surface, yielding nearly twice as much trapped magnetic flux compared to the sample grown without a Y-123 layer. Such enhancement is attributed mainly to a more homogenous sample and a more uniform distribution of superconducting properties,  $T_c$  and  $J_c$  measured by SQUID magnetometer, a more consistent chemical composition from the seed along the  $c$ -axis analysed by EMPA and more evenly-dispersed Sm-211 particles within the sample cross

section. These improvements can all be attributed to the addition of a Y-123 layer beneath the Ag-SmBCO pre-form prior to melt processing, thereby increasing the likelihood for further engineering applications of this material in the long term.

# CHAPTER 7

## CONCLUSIONS AND FUTURE WORK

### 7.1. Conclusions

The majority of the primary challenges in processing large, single SmBCO grains for potential applications have been addressed and overcome in this study based on the fabrication, measurement and analysis of over 300 SmBCO bulk single grains. Several approaches for optimizing the growth of top-seeded-melt growth (TSMG) for the reliable processing of SmBCO bulk single grains with enhanced superconducting properties have been presented.

The principal contribution of this research to the development of these technologically important materials includes the realisation of a reliable SmBCO-single-grain growth process to yield a more uniform microstructure with significantly improved superconducting properties. The approaches investigated in this thesis include: first, the insertion of a buffer layer between the seed and the SmBCO bulk pre-form to inhibit the diffusion of elements from the seed into bulk samples, and vice versa, and to accommodate lattice mismatch between the seed and the precursor pellet; second, improvement of the superconducting properties,  $T_c$  and  $J_c$ , by controlled doping of the SmBCO bulk single grains to reduce the size of Sm-211 particles and to increase the pinning centres in the superconducting Sm-123 phase matrix; third, a combination of the introduction of silver into the precursor powders, cold isostatic pressing of the bulk pre-form and the addition of a Y-123 layer under the bulk pre-form was applied in SmBCO system to enable reliable growth of SmBCO bulk single grains in large diameters. As a result, SmBCO bulk single grains containing silver of diameters as large as 41 mm have been obtained and a trapped field of + 1.033 T has been measured at the top surface of a 31 mm diameter Ag-SmBCO single grain, which is the largest magnetic field trapped in the SmBCO system for samples grown in air to date.

The success rate of the growth of SmBCO single grains is improved significantly via the buffer technique. In order to improve the reliability of seeding, buffers of different compositions were used and their geometric configurations investigated in detail. As a result, SmBCO bulk single grains of various dimensions were fabricated successfully using the optimised buffer layer technique. Furthermore, the superconducting properties,  $T_c$  and  $J_c$ , of specimens cut from the parent bulk single grain, and particularly directly beneath the buffer layer, were investigated in detail. The trapped fields of SmBCO single grains synthesized with and without a buffer layer were measured and compared in order to establish the advantages of this technique. As a result, SmBCO single grains up to 20 mm in diameter and 10 mm in thickness with starting compositions of (75 wt. % Sm-123 + 25 wt. % Sm-211) + 2 wt. % BaO<sub>2</sub> + 1 wt. % CeO<sub>2</sub> have been fabricated successfully by TSMG in air using an MgO-NdBCO generic seed with a Sm-123 + Sm-211 mixed-powder buffer in a conventional chamber furnace. Buffer layers with an aspect ratio of 1, where the diameter is equal to the thickness, represent an optimum geometry for the growth of SmBCO single grains. Furthermore, it has been established that the use of a buffer layer simplifies the choice of a seed crystal, leads to a more uniform distribution of Sm-211 particles throughout the single grain sample, overcomes the lattice mismatch between an MgO-NdBCO generic seed and the SmBCO bulk single grain, and is relatively more tolerant to the presence of impurities in the precursor pellets compared to the use of an MgO-NdBCO generic seed. Consequently, the superconducting properties,  $T_c$  and  $J_c$ , in the buffered SmBCO single grain samples have been improved significantly.  $T_c$  for samples fabricated with and without a buffer layer are similar, while  $\Delta T_c$  in the buffered SmBCO is narrower. The irreversibility fields are similar in both samples, and the buffered SmBCO exhibits a more pronounced peak effect. The peak values of the trapped fields remain largely unchanged between the SmBCO bulk single grains fabricated with and without a Sm-123 + Sm-211 mixed-powder buffer layer.

Two different kinds of doping of the SmBCO system have been investigated for different purposes: firstly, the addition of platinum and CeO<sub>2</sub> was discussed in terms of their impact on refining the size of Sm-211 particles trapped in the superconducting Sm-123 phase matrix, which act as effective flux pinning centres. The microstructures of SmBCO bulk single grains with platinum and CeO<sub>2</sub> show clearly that CeO<sub>2</sub> is more effective at refining Sm-211 inclusions in the bulk microstructure than Pt, while, at the same time, comparison of the measured superconducting properties indicate that the addition of CeO<sub>2</sub> results in broadly improved superconducting performance of the fully grown bulk single grain. Furthermore, 1

wt. % CeO<sub>2</sub> is significantly cheaper than 0.1 wt. % Pt, which has clear economic benefits for use in medium to large scale production processes for these technologically important materials. The use of CeO<sub>2</sub> results generally in the generation of fewer macro-cracks and Sm-211 free regions in the sample microstructure; secondly, with the optimized precursor-powder composition of CeO<sub>2</sub>, compounds with different elements were then added to the SmBCO bulk single grains to observe how these dopants affect the SmBCO system. Single domain, bulk SmBCO samples with different dopants have been fabricated successfully in air using commercial thin film seeds by an established TSMG process using a conventional chamber furnace with dimensions of 20 mm and 16 mm diameter and 10 mm and 7 mm thickness. Detailed studies were performed on  $T_c$  and  $J_c$  along the  $a/b$ - and  $c$ -axes of the single grains fabricated with 1 mol. % ZrO<sub>2</sub>, BaZrO<sub>3</sub>, TiO<sub>2</sub> and fine Sm-211, respectively. In conclusion, the effects of dopants such as ZrO<sub>2</sub> and BaZrO<sub>3</sub> appear to be favourable in improving the superconducting properties of SmBCO single grains. The highest  $T_c$  of all the tested specimens was 93.6 K in 1 mol. % BaZrO<sub>3</sub>-doped SmBCO with  $J_c$  of the same specimen exhibiting a more predominant peak effect and a higher irreversibility field, of  $1.20 \times 10^5$  A cm<sup>-2</sup> at 77 K for an applied field of 1.722 T. Furthermore, the single grain sample containing 1 mol. % ZrO<sub>2</sub>-doped SmBCO exhibits superior overall superconducting properties of all the samples investigated.

In general, SmBCO superconducting bulk single grains have significant potential for engineering applications due to their superior electromagnetic properties (magnetic trapped field  $B_t$  and critical current density  $J_c$ ). The maximum magnetic trapped field  $B_{t, max}$  of a SmBCO bulk single grain depends not only on the gradient of the field but also on the radius of the current loop that flow within the bulk sample, which, for a bulk single grain, equate approximately to its diameter. Therefore it is necessary to synthesize uniform bulk single grains with larger diameters to achieve a higher  $B_{t, max}$ . However, one of the largest obstacles in processing bulk single grains to being applied to quasi-magnet industrial applications is their poor mechanical properties, due primarily to their ceramic nature. Pores and cracks formed in the superconducting matrix during the TSMG process, which can lead to fracture under large electromagnetic forces when it traps a large magnetic field. In order to solve these potential problems and to scale-up the SmBCO system for applications, silver was added to the SmBCO system and a Y-123 layer was employed under the SmBCO bulk pre-form, which was cold isostatic pressed (CIP-ed) before undergoing TSMG. As a result, reliable growth of the Ag-SmBCO single grains has been accomplished through various approaches,

including adjustment of the precursor powder composition, replacing BaO<sub>2</sub> with BaO, CIP compaction of the Ag-SmBCO pre-forms and the addition of a Y-123 liquid-rich layer under the bulk pre-form. Subsequently, comparison of the measured trapped fields of the successfully grown Ag-SmBCO samples was performed to establish the influence of the various aspects of the processing. The roles of the Y-123 liquid-rich layer and its impact on the appearance, superconducting properties ( $T_c$  and  $J_c$ ), microstructure, chemical compositions and field-trapping ability of the Ag-SmBCO bulk single grains have been examined and discussed in detail. With the aid of a Y-123 liquid-rich layer, Ag-SmBCO bulk single grains can be fabricated in a reliable manner up to a size of 41 mm in diameter. Additionally, by compacting the bulk pre-form with CIP, and combined with the replacement of BaO<sub>2</sub> with BaO in the precursor powders, a Ag-SmBCO single grain of 31 mm in diameter was produced with a trapped magnetic field as high as + 1.033 T at its top surface for an applied field of 1.3 T, which is highest magnetic field trapped to date in the SmBCO system for samples grown in air. The effects of a Y-123 layer were investigated further and the introduction of a Y-123 layer beneath the Ag-SmBCO pre-form demonstrated to form a reliable route to improve the success rate of fabricating Ag-SmBCO bulk single grains by preventing the formation of sub-grains from growing from the bottom of the sample. By adding a Y-123 layer, the interface between the very bottom of the bulk sample and the Y-123 layer tends to lower the melting temperature in the growth window of Ag-SmBCO and that, in turn, reduces the probability of nucleating a sub-grain at this position. More importantly, a Y-123 layer has a positive influence on the field-trapping ability of Ag-SmBCO bulk single grains, especially at the bottom surface, yielding nearly twice as much trapped magnetic flux compared to a control sample grown without a Y-123 layer. Such enhancement is attributed mainly to a more homogeneously grown sample, which, in turn, exhibits a more uniform distribution of superconducting properties,  $T_c$  and  $J_c$ , a more consistent chemical composition with increasing distance from the seed along the  $c$ -axis as analysed by EMPA and a more even dispersion of Sm-211 particles throughout the sample cross section. As a result, the addition of a Y-123 layer directly beneath the Ag-SmBCO pre-form increases the potential of these technologically important materials for practical applications.

## 7.2. Future Work

One of the most important superconducting properties of bulk SmBCO superconductors is their field-trapping ability, which enables the material to act as a permanent magnet in practical applications. The main purpose of this study was to scale-up processing of the SmBCO system to obtain bulk single grains with superior field-trapping abilities since the field-trapping ability of a bulk SmBCO superconductor is known to increase with the increase of the size of the sample. In this thesis, through a combination of the addition of a buffer layer, doping the bulk material with different chemicals and the addition of silver and with a Y-123 layer under the bulk pre-form, a 31 mm-in-diameter Ag-SmBCO single grain was produced to trap a magnetic field as high as + 1.033 T at its top surface when a field of 1.3 T is applied, which is highest magnetic field trapped reported to date in the SmBCO system for samples grown in air. However, this value remains below the full field-trapping potential of SmBCO bulk single grains. Therefore, based on the results reported in this thesis, further research is suggested in the following areas:

The reasons for the improvement of the superconducting properties with  $ZrO_2$  and  $BaZrO_3$  in the SmBCO bulk single grains are still unclear following investigation of the doping effects discussed in Chapter 5. As a result, it is necessary to carry out further characterisation at higher precision to detect such low amount of dopants on a small scale in the superconducting Sm-123 matrix to understand fully the fundamentals of the doping effects on the SmBCO system. Similarly, the research on the effects of nano-scale dopants presented in Chapter 5 is incomplete. In particular, a larger variety of nanoscale chemicals should be investigated, given that these dopants generally behave differently compared to larger scale materials. Secondly, the synthesis of the Sm-2411 (Zr) dopant, which is on a nano scale, failed in this investigation. Therefore, the fabrication of Sm-2411 (Zr) and other Sm-2411 (M) dopants is of significant relevance to the SmBCO system, since Sm-2411 inclusions are known to form effective nano, non-superconducting flux pinning centres that can potentially improve the superconducting properties of SmBCO bulk superconductors.

Although, to date, a Ag-SmBCO single grain of 31 mm-in-diameter can trap a magnetic field as high as + 1.033 T at its top surface, results have shown that the severe substitution effects between samarium and barium in the superconducting Sm-123 matrix are not suppressed

completely by the techniques developed in this study. It is of great importance, therefore, to suppress this effect by other methods since it represents one of the most serious challenges in the processing of the SmBCO system for the development of industrial applications. One of the most promising approaches is to determine the kinetics of Sm and Ba and their relation with one and the other phases during the TSMG and the oxygenation processes by developing a more detailed phase diagram in the region of the relevant processing temperatures.

A variety of techniques and approaches has been developed in this study and demonstrated to improve the growth and the superconducting properties of SmBCO bulk single grains, including the addition of the Sm-123 + Sm-211 mixed-powder buffers, doping, silver addition, cold isostatic pressing (CIP) of the bulk pre-form, replacement of BaO<sub>2</sub> with BaO in the precursor powders and the addition of a Y-123 layer beneath the bulk pre-form. Although the optimisation of each approach was performed independently and presented in different chapters, the optimisation of the combination of these approaches has not yet been attempted systematically. It is therefore necessary to consider the integrated impact of these different approaches on the SmBCO system given that the optimization of each may differ and be influenced by any other (for example, the amount of the optimal silver addition may change due to the existence of a Y-123 layer). Additionally, the conditions for CIP in pressing SmBCO pre-form were not explained in this study, including the pressure used during the treatment and the holding time and frequency of CIP. Furthermore, the amount of the BaO as a replacement for BaO<sub>2</sub> in the precursor powders needs to be studied more thoroughly. Therefore, it will be important to include these additional means of optimization in future research.

In conclusion, this study has presented and evolved several processing methods that are beneficial to the growth and the superconducting properties of SmBCO bulk single grains based on large quantity of experimental data. These include the introduction of Sm-123 + Sm-211 mixed-powder buffers, doping, silver addition, CIP of the bulk pre-form and the addition of a Y-123 layer beneath the bulk pre-form. These attempts have increased to varying degrees the success rate of the growth of SmBCO bulk single grains, and at the same time have yielded enhanced superconducting properties in the field-trapping ability,  $T_c$  and  $J_c$  of the product large single grains. The scale-up of the system enabling the successful fabrication of Ag-SmBCO samples of diameter 41 mm has been achieved. Finally, by compacting the bulk pre-form with CIP, combined with the replacement of BaO<sub>2</sub> with BaO in the precursor powders, a Ag-SmBCO single grain of 31 mm-in-diameter can trap a magnetic

field as high as + 1.033 T at its top surface with an applied magnetic field of 1.3 T, which is highest magnetic field trapped reported to date for the SmBCO system for samples in a similar size grown in air.

# REFERENCES

- [1] J. G. Bednorz and K. A. Muller, "Possible High  $T_c$  Superconductivity in the Ba-La-Cu-O System," *Zeitschrift für Phys. B Condens. Matter*, vol. 64, pp. 189-193, 1986.
- [2] M. K. Wu, J. R. Ashburn, C. J. Torng, P. H. Hor, R. L. Meng, L. Gao, Z. J. Huang, Y. Q. Wang, and C. W. Chu, "Superconductivity at 93 K in a new mixed-phase Yb-Ba-Cu-O compound system at ambient pressure," *Phys. Rev. Lett.*, vol. 58, no. 9, pp. 908-910, 1987.
- [3] R. Takahata, H. Ueyama, and A. Kubo, "Characterization of Superconducting Magnetic Bearings (Runnout Performance at High Speed Rotation)," in *Advances in Superconductivity V: Proceedings of the 5th International Symposium on Superconductivity (ISS '92), November 16-19, 1992, Kobe*, Y. Bando and H. Yamauchi, Eds. Tokyo: Springer Japan, 1993, pp. 1309-1312.
- [4] Y. Miyagawa, H. Kamenno, R. Takahata, and H. Ueyama, "A 0.5 kWh Flywheel Energy Storage System using A High- $T_c$  Superconducting Magnetic Bearing," *IEEE Trans. Appl. Supercond.*, vol. 9, no. 2, pp. 996-999, 1999.
- [5] D. A. Cardwell, "Processing and properties of large grain (RE)BCO," *Mater. Sci. Eng.*, vol. B53, pp. 1-10, 1998.
- [6] H. S. Chauhan and M. Murakami, "Hot seeding for the growth of  $c$ -axis-oriented Nd-Ba-Cu-O," *Supercond. Sci. Technol.*, vol. 13, pp. 672-675, 2000.
- [7] D. van Delft and P. Kes, "The discovery of superconductivity," *Phys. Today*, vol. 63, no. 9, pp. 38-43, 2010.
- [8] B. W. Roberts, "Survey of superconductive materials and critical evaluation of selected properties," *J. Phys. Chem. Ref. Data*, vol. 5, pp. 581-821, 1976.
- [9] B. T. Matthias, T. H. Geballe, S. Geller, and E. Corenzwit, "Superconductivity of  $Nb_3Sn$ ," *Phys. Rev.*, vol. 95, no. 6, pp. 1435, 1954.
- [10] H. Takagi, H. Eisaki, S. Uchida, A. Maeda, S. Tajima, K. Uchinokura, and S. Tanaka, "Transport and optical studies of single crystals of the 80 K Bi-Sr-Ca-Cu-O superconductor," *Nature*, vol. 332, pp. 236-238, 1988.
- [11] R. M. Hazen, L. W. Finger, R. J. Angel, C. T. Prewitt, N. L. Ross, C. G. Hadidiacos, P.

- J. Heaney, D. R. Veblen, Z. Z. Sheng, A. El Ali, and A. M. Hermann, "100 K superconducting phases in the Tl-Ca-Ba-Cu-O system," *Phys. Rev. Lett.*, vol. 60, no. 16, pp. 1657-1660, 1988.
- [12] C. W. Chu, L. Gao, F. Chen, Z. J. Huang, R. L. Meng, and Y. Y. Xue, "Superconductivity above 150 K in  $\text{HgBa}_2\text{Ca}_2\text{Cu}_3\text{O}_{8+\delta}$  at high pressures," *Nature*, vol. 365, pp. 323-325, 1993.
- [13] C. Buzea and T. Yamashita, "Review of the superconducting properties of  $\text{MgB}_2$ ," *Supercond. Sci. Technol.*, vol. 14, pp. R115-R146, 2001.
- [14] J. Ge, Z. L. Liu, C. Liu, C. Gao, D. Qian, Q. Xue, Y. Liu, and J. F. Jia, "Superconductivity above 100 K in single-layer FeSe films on doped  $\text{SrTiO}_3$ ," *Nat. Mater.*, vol. 14, pp. 285-289, 2014.
- [15] A. P. Drozdov, M. I. Erements, I. A. Troyan, V. Ksenofontov, and S. I. Shylin, "Conventional superconductivity at 203 Kelvin at high pressures in sulfur hydride system," *Nature*, vol. 525, pp. 73-76, 2015.
- [16] K. Takada, H. Sakurai, E. Takayama-Muromachi, F. Izumi, R. A. Dilanian, and T. Sasak, "Superconductivity in two-dimensional  $\text{CoO}_2$  layers," *Nature*, vol. 422, pp. 53-55, 2003.
- [17] G. Horn and E. Saur, "Praparation und Supraleitungseigenschaften von Niobnitrid sowie Niobnitrid mit Titan-, Zirkon- und Tantalzusatz," *Zeitschrift fur Phys.*, vol. 210, pp. 70-79, 1968.
- [18] G. F. Hardy and J. K. Hulm, "The Superconductivity of Some Transition Metal Compounds," *Phys. Rev.*, vol. 93, no. 5, pp. 1004-1016, 1954.
- [19] J. R. Gavaler, "Superconductivity in Nb-Ge films above 22 K," *Appl. Phys. Lett.*, vol. 23, pp. 480-482, 1973.
- [20] L. F. Mattheiss, E. M. Gyorgy, and D. W. Johnson, "Superconductivity above 20 K in the Ba-K-Bi-O system," *Phys. Rev. B*, vol. 37, no. 7, pp. 3745-3746, 1988.
- [21] H. Fujii, S. Ikeda, T. Kimura, S. Arisawa, K. Hirata, H. Kumakura, K. Kadowaki, and K. Togano, "Structure and Superconducting Properties of Y-Pd-B-C System," *Jpn. J. Appl. Phys.*, vol. 33, pp. L590-L593, 1994.
- [22] K. Shimizu, H. Ishikawa, D. Takao, T. Yagi, and K. Amaya, "Superconductivity in

- compressed lithium at 20 K,” *Nature*, vol. 419, pp. 597-599, 2002.
- [23] T. T. M. Palstra, O. Zhou, Y. Iwasa, P. E. Sulewski, R. M. Fleming, and B. R. Zegarski, “Superconductivity at 40 K in cesium doped  $C_{60}$ ,” *Solid State Commun.*, vol. 93, no. 4, pp. 327-330, 1995.
- [24] P. W. Stephens, L. Mihaly, P. L. Lee, R. L. Whetten, S. M. Huang, R. Kaner, F. Deiderich, and K. Holczer, “Structure of single-phase superconducting  $K_3C_{60}$ ,” *Nature*, vol. 351, pp. 632-634, 1991.
- [25] K. Tanigaki, T. W. Ebbesen, S. Saito, J. Mizuki, J. S. Tsai, Y. Kubo, and S. Kuroshima, “Superconductivity at 33 K in  $Cs_xRb_yC_{60}$ ,” *Nature*, vol. 352, pp. 222-223, 1991.
- [26] D. Jérôme, A. Mazaud, M. Ribault, and K. Bechgaard, “Superconductivity in a synthetic organic conductor:  $(TMTSF)_2PF_6$ ,” *J. Phys. Lett.*, vol. 41, no. 4, pp. 95-98, 1980.
- [27] Z. K. Tang, L. Zhang, N. Wang, X. X. Zhang, G. H. Wen, G. D. Li, J. N. Wang, C. T. Chan, and P. Sheng, “Superconductivity in 4 Angstrom Single-Walled Carbon Nanotubes,” *Science*, vol. 292, pp. 2462-2465, 2001.
- [28] I. Takesue, J. Haruyama, N. Kobayashi, S. Chiashi, S. Maruyama, T. Sugai, and H. Shinohara, “Superconductivity in Entirely End-Bonded Multiwalled Carbon Nanotubes,” *Phys. Rev. Lett.*, vol. 96, pp. 57001-1-4, 2006.
- [29] E. A. Ekimov, V. A. Sidorov, E. D. Bauer, N. N. Mel’nik, N. J. Curro, J. D. Thompson, and S. M. Stishov, “Superconductivity in diamond,” *Nature*, vol. 428, pp. 542-545, 2004.
- [30] T. E. Weller, M. Ellerby, S. S. Saxena, R. P. Smith, and N. T. Skipper, “Superconductivity in the intercalated graphite compounds  $C_6Yb$  and  $C_6Ca$ ,” *Nat. Phys.*, vol. 1, pp. 39-41, 2005.
- [31] F. Steglich, J. Aarts, C. D. Bredl, W. Lieke, D. Meschede, W. Franz, and H. Schäfer, “Superconductivity in the presence of strong pauli paramagnetism:  $CeCu_2Si_2$ ,” *Phys. Rev. Lett.*, vol. 43, no. 25, pp. 1892-1896, 1979.
- [32] J. L. Sarrao, L. A. Morales, J. D. Thompson, B. L. Scott, G. R. Stewart, F. Wastin, J. Rebizant, P. Boulet, E. Colineau, and G. H. Lander, “Plutonium-based superconductivity with a transition temperature above 18 K,” *Nature*, vol. 420, pp. 297-299, 2002.

- [33] H. R. Ott, H. Rudigier, Z. Fisk, and J. L. Smith, "UBe<sub>13</sub>: An unconventional actinide superconductor," *Phys. Rev. Lett.*, vol. 50, no. 20, pp. 1595-1598, 1983.
- [34] G. R. Stewart, Z. Fisk, J. O. Willis, and J. L. Smith, "Possibility of coexistence of bulk superconductivity and spin fluctuations in UPt<sub>3</sub>," *Phys. Rev. Lett.*, vol. 52, no. 8, pp. 679-682, 1984.
- [35] C. Geibel, U. Ahlheim, C. D. Bredl, J. Diehl, A. Grauel, R. Helfrich, H. Kitazawa, R. Kohler, R. Modler, M. Lang, C. Schank, S. Thies, F. Steglich, N. Sato, and T. Komatsubara, "UPd<sub>2</sub>Al<sub>3</sub>-a new heavy-fermion superconductor with  $T_c=2$  K," *Phys. C*, vol. 185-189, pp. 2651-2652, 1991.
- [36] C. Petrovic, P. G. Pagliuso, M. F. Hundley, R. Movshovich, J. L. Sarrao, J. D. Thompson, Z. Fisk, and P. Monthoux, "Heavy-fermion superconductivity in CeCoIn<sub>5</sub> at 2.3 K," *J. Phys. Condens. Matter*, vol. 13, pp. L337-L342, 2001.
- [37] F. Wastin, P. Boulet, J. Rebizant, E. Colineau, and G. H. Lander, "Advances in the preparation and characterization of transuranium systems," *J. Phys. Condens. Matter*, vol. 15, pp. S2279-S2285, 2003.
- [38] A. Schilling, M. Cantoni, J. D. Guo, and H. R. Ott, "Superconductivity above 130 K in the Hg-Ba-Ca-Cu-O system," *Nature*, vol. 363, pp. 56-58, 1993.
- [39] G. F. Sun, K. W. Wong, B. R. Xu, Y. Xin, and D. F. Lu, " $T_c$  enhancement of HgBa<sub>2</sub>Ca<sub>2</sub>Cu<sub>3</sub>O<sub>8</sub> by Tl substitution," *Phys. Lett. A*, vol. 192, pp. 122-124, 1994.
- [40] Y. Kamihara, H. Hiramatsu, M. Hirano, R. Kawamura, H. Yanagi, T. Kamiya, and H. Hosono, "Iron-based layered superconductor: LaOF<sub>2</sub>P," *J. Am. Chem. Soc.*, vol. 128, pp. 10012-10013, 2006.
- [41] Y. Kamihara, T. Watanabe, M. Hirano, and H. Hosono, "Iron-based layered superconductor La[O<sub>1-x</sub>F<sub>x</sub>]FeAs (x= 0.05-0.12) with  $T_c=26$  K," *J. Am. Chem. Soc.*, vol. 130, pp. 3296-3297, 2008.
- [42] T. Watanabe, H. Yanagi, T. Kamiya, Y. Kamihara, H. Hiramatsu, M. Hirano, and H. Hosono, "Nickel-based oxyphosphide superconductor with a layered crystal structure, LaNiOP," *Inorg. Chem.*, vol. 46, pp. 7719-7721, 2007.
- [43] Bruker Energy and Supercon Technologies, "Low- $T_c$  Superconductor Wires Low Temperature Superconductors ( LTS )," 2012. [Online]. Available: [https://www.bruker.com/fileadmin/user\\_upload/1-Products/SuperconductingWireDevices/PDF/Low-](https://www.bruker.com/fileadmin/user_upload/1-Products/SuperconductingWireDevices/PDF/Low-)

- Tec\_Superconductor\_wires.pdf.
- [44] S. E. Ltd., “Bismuth-based superconducting wire.” [Online]. Available: [http://global-sei.com/super/hts\\_e/index.html](http://global-sei.com/super/hts_e/index.html).
- [45] SuperPower, “Configuration of SuperPower® 2G HTS Wire.” [Online]. Available: <http://www.superpower-inc.com/content/2g-hts-wire>.
- [46] S. Nariki, H. Teshima, and M. Morita, “Performance and applications of quench melt-growth bulk magnets,” *Supercond. Sci. Technol.*, vol. 29, pp. 034002 (9pp), 2016.
- [47] L. Ye, M. Majoros, A. M. Campbell, T. Coombs, D. Astill, S. Harrison, M. Husband, M. Rindfleisch, and M. Tomsic, “Experimental studies of the quench behaviour of MgB<sub>2</sub> superconducting wires for fault current limiter applications,” *Supercond. Sci. Technol.*, vol. 20, pp. 621-628, 2007.
- [48] W. Meissner and R. Ochsenfeld, “Ein neuer Effekt bei Eintritt der Supraleitfähigkeit,” *Naturwissenschaften*, vol. 21, pp. 787-788, 1933.
- [49] A. C. Rose-innes and E. H. Rhoderick, *Introduction to superconductivity Second Edition*. Peramon Press plc, 1978.
- [50] A. A. Abrikosov, “Nobel Lecture: Type-II superconductors and the vortex lattice,” *Rev. Mod. Phys.*, vol. 76, pp. 975-979, 2004.
- [51] T. Takizawa and M. Murakami, *Critical Currents in Superconductors*. Japan: Fuzambo International, 2005.
- [52] V. L. Ginzburg and L. D. Landau, “On the theory of superconductivity,” *J. Exp. Theor. Phys.*, vol. 20, pp. 1064-1082, 1950.
- [53] Y. Shiohara and A. Endo, “Crystal growth of bulk high- $T_c$  superconducting oxide materials,” *Mater. Sci. Eng. R Reports*, vol. R19, pp. 1-86, 1997.
- [54] G. Krabbes, G. Fuchs, W. R. Canders, H. May, and R. Palka, *High Temperature Superconductor Bulk Materials*. 2006.
- [55] D. A. Cardwell and D. S. Ginley, *Handbook of Superconducting Materials, Volume 1*, vol. I. 2003.
- [56] E. W. Collings, *Applied Superconductivity*. New York and London: Plenum, 1986.
- [57] A. M. Campbell and J. E. Evetts, “Flux vortices and transport currents in type II

- superconductors,” *Adv. Phys.*, vol. 21, no. 90, pp. 199-428, 1972.
- [58] Y. B. Kim, C. F. Hempstead, and A. R. Strnad, “Critical persistent currents in hard superconductors,” *Phys. Rev. Lett.*, vol. 9, no. 7, pp. 306-309, 1962.
- [59] A. Umezawa, G. W. Crabtree, J. Z. Liu, H. W. Weber, W. K. Kwok, L. H. Nunez, T. J. Moran, C. H. Sowers, and H. Claus, “Enhanced critical magnetization currents due to fast neutron irradiation in single-crystal  $\text{YBa}_2\text{Cu}_3\text{O}_{7-\delta}$ ,” *Phys. Rev. B*, vol. 36, no. 13, pp. 7151-7154, 1987.
- [60] J. W. Ekin, A. J. Panson, and B. A. Blankenship, “Method for making low-resistivity contacts to high  $T_c$  superconductors,” *Appl. Phys. Lett.*, vol. 52, no. 4, pp. 331-333, 1988.
- [61] C. P. Bean, “Magnetization of high-field superconductors,” *Rev. Mod. Phys.*, vol. 36, no. 1, pp. 31-39, 1964.
- [62] D. X. Chen and R. B. Goldfarb, “Kim model for magnetization of type-II superconductors,” *J. Appl. Phys.*, vol. 66, no. 6, pp. 2489-2500, 1989.
- [63] A. M. Campbell, “The response of pinned flux vortices to low frequency fields,” *J. Phys. C*, vol. 2, pp. 1492-1501, 1962.
- [64] Y. Itoh and U. Mizutani, “Pulsed Field Magnetization of Melt-Processed Y-Ba-Cu-O Superconducting Bulk Magnet,” *Japanese J. Appl. Phys. Part 1-Regular Pap. Short Notes Rev. Pap.*, vol. 35, pp. 2114-2125, 1996.
- [65] M. Murakami, “Progress in applications of bulk high temperature superconductors,” *Supercond. Sci. Technol.*, vol. 13, pp. 448-450, 2000.
- [66] S. I. Yoo, T. Higuchi, N. Sakai, H. Fujimoto, and M. Murakami, “RE-Ba-Cu-O for high functional superconducting magnet,” *Mater. Sci. Eng. B*, vol. 53, pp. 203-210, 1998.
- [67] T. Otani and M. Murakami, “Performance of Sm-Ba-Cu-O bulk superconductors for a magnetic,” *Supercond. Sci. Technol.*, vol. 13, pp. 866-869, 2000.
- [68] A. C. Day, M. Strasik, K. E. McCrary, P. E. Johnson, J. W. Gabrys, J. R. Schindler, R. A. Hawkins, D. L. Carlson, M. D. Higgins, and J. R. Hull, “Design and testing of the HTS bearing for a 10 kWh flywheel system,” *Supercond. Sci. Technol.*, vol. 15, pp. 838-841, 2002.

- [69] J. H. Durrell, A. R. Dennis, J. Jaroszynski, M. D. Ainslie, K. G. B. Palmer, Y. H. Shi, A. M. Campbell, J. Hull, M. Strasik, E. E. Hellstrom, and D. A. Cardwell, "A trapped field of 17.6 T in melt-processed, bulk Gd-Ba-Cu-O reinforced with shrink-fit steel," *Supercond. Sci. Technol.*, vol. 27, no. 8, pp. 82001 (5 pp), 2014.
- [70] N. H. Babu, Y. Shi, K. Iida, and D. A. Cardwell, "A practical route for the fabrication of large single-crystal (RE)-Ba-Cu-O superconductors," *Nat. Mater.*, vol. 4, pp. 476-480, 2005.
- [71] Y. H. Shi, M. Desmedt, J. H. Durrell, A. R. Dennis, and D. A. Cardwell, "Improving the superconducting properties of single grain Sm-Ba-Cu-O bulk superconductors fabricated in air by increased control of Sm/Ba substitution effects," *Supercond. Sci. Technol.*, vol. 26, no. 9, pp. 95012 (7 pp), 2013.
- [72] N. Hari Babu, K. Iida, Y. Shi, and D. A. Cardwell, "Processing of bulk Sm-Ba-Cu-O nano-composite superconductors," *Phys. C*, vol. 468, pp. 1340-1344, 2008.
- [73] M. Scavini, M. Coduri, M. Allieta, L. Mollica, M. Brunelli, L. Malavasi, A. Lascialfari, and C. Ferrero, "Effect of Local Disorder on the Transport Properties of Al-Doped  $\text{SmBa}_2\text{Cu}_3\text{O}_{6+\delta}$  Superconductors," *J. Phys. Chem. C*, vol. 114, no. 45, pp. 19509-19520, 2010.
- [74] L. Sun, W. Li, S. Liu, T. Mertelj, and X. Yao, "Growth of a high performance SmBCO bulk superconductor with the addition of a  $\text{Sm}_2\text{Ba}_4\text{Cu}_2\text{O}_9$  phase," *Supercond. Sci. Technol.*, vol. 22, no. 12, pp. 125008 (6 pp), 2009.
- [75] B. Peng, L. Cheng, Y. Zhuang, H. Xu, and X. Yao, "Trapping Mode Controlled Continuous Growth of SmBCO Bulk Superconductors," *Cryst. Growth Des.*, vol. 13, no. 8, pp. 3734-3738, 2013.
- [76] J. V. J. Congreve, Y. H. Shi, A. R. Dennis, J. H. Durrell, and D. A. Cardwell, "Microstructure and Composition of Primary and Recycled Single Grains of YBCO, GdBCO-Ag, and SmBCO-Ag Bulk Superconductors," *J. Am. Ceram. Soc.*, vol. 3119, pp. 3111-3119, 2016.
- [77] Q. Li and W. M. Yang, "Preparation of high quality single domain SmBCO bulks by modified TSIG method in air with new solid phase of  $\text{Sm}_2\text{O}_3 + x\text{BaCuO}_2$ ," *J. Alloys Compd.*, vol. 650, pp. 610-615, 2015.
- [78] N. Sakai, A. Mase, H. Ikuta, S. Seo, U. Mizutani, and M. Murakami, "Mechanical

- properties of Sm-Ba-Cu-O/Ag bulk superconductors,” *Supercond. Sci. Technol.*, vol. 13, pp. 770-773, 2000.
- [79] H. Ikuta, S. Ikeda, A. Mase, M. Yoshikawa, Y. Yanagi, Y. Itoh, T. Oka, and U. Mizutani, “Melt-processing of Ag-added LRE-Ba-Cu-O (LRE=Nd, Sm),” *Appl. Supercond.*, vol. 6, no. 2-5, pp. 109-117, 1998.
- [80] X. Wu, K. X. Xu, and P. Pan, “Growth and investigation of SmBCO/Ag single grain bulk for batch production of Sm123 seed crystals,” *Phys. C Supercond.*, vol. 469, no. 21, pp. 1906-1909, 2009.
- [81] A. V. Narlikar, *High Temperature Superconductivity 1: Materials*. Springer Science & Business Media, 2004.
- [82] M. Murakami, S. Yoo, T. Higuchi, N. Sakai, J. Wertz, N. Koshizuka, and S. Tanaka, “Flux Pinning in Melt-Grown NdBa<sub>2</sub>Cu<sub>3</sub>O<sub>y</sub> and SmBa<sub>2</sub>Cu<sub>3</sub>O<sub>y</sub> Superconductors,” *Jpn. J. Appl. Phys.*, vol. 715, no. 5B, pp. L715-L717, 1994.
- [83] W. Lo, D. A. Cardwell, C. D. Dewhurst, and S. L. Dung, “Fabrication of large grain YBCO by seeded peritectic solidification,” *J. Mater. Res.*, vol. 11, no. 4, pp. 786-794, 1996.
- [84] T. Izumi, Y. Nakamura, and Y. Shiohara, “Crystal growth mechanism of YBa<sub>2</sub>Cu<sub>3</sub>O<sub>y</sub> superconductors with peritectic reaction,” *J. Cryst. Growth*, vol. 128, no. 1-4 PART 2, pp. 757-761, 1993.
- [85] D. A. Cardwell and D. S. Ginley, Eds., *Handbook of Superconducting Materials*, Illustrate. CRC Press, 2003.
- [86] A. Endo, H. S. Chauhan, and Y. Shiohara, “Entrapment of Y<sub>2</sub>BaCuO<sub>5</sub> particles in melt-textured YBa<sub>2</sub>Cu<sub>3</sub>O<sub>7-δ</sub> crystals and its effect on  $J_c$  properties,” *Phys. C Supercond.*, vol. 273, no. 1-2, pp. 107-119, 1996.
- [87] J. C. L. Chow, W. Lo, H. T. Leung, C. D. Dewhurst, and D. A. Cardwell, “Processing, Y<sub>2</sub>BaCuO<sub>5</sub> distribution and critical current density in large grain Pt-doped YBCO,” *Mater. Sci. Eng. B*, vol. 53, no. 1-2, pp. 79-85, 1998.
- [88] M. P. Delamare, H. Walter, B. Bringmann, A. Leenders, and H. C. Freyhardt, “Macrosegregation of Y<sub>2</sub>BaCuO<sub>5</sub> particles in top-seeded melt textured monoliths,” *Phys. C Supercond. its Appl.*, vol. 323, no. 3, pp. 107-114, 1999.

- [89] N. Chikumoto, S. Ozawa, S. I. Yoo, N. Hayashi, and M. Murakami, "Effects of oxygen content on the superconducting properties of melt-textured LRE123 superconductors," *Phys. C Supercond.*, vol. 278, no. 97, pp. 187-191, 1997.
- [90] F. Sandiumenge, S. Piñol, X. Obradors, E. Snoeck, and C. Roucau, "Microstructure of directionally solidified high-critical-current  $\text{YBa}_2\text{Cu}_3\text{O}_{7-y}$ - $\text{Y}_2\text{BaCuO}_5$  composites," *Phys. Rev. B. Condens. Matter*, vol. 50, no. 10, pp. 7032-7045, 1994.
- [91] X. Obradors, B. Martinez, and F. Sandiumenge, "Directional solidification of  $\text{YBa}_2\text{Cu}_3\text{O}_7$ : defects and pinning mechanisms," *4th Euro-Ceram*, vol. 6, pp. 173-184, 1995.
- [92] M. Daumling, A. Erb, E. Walker, J. Y. Genoud, and R. Flukiger, "Monotonic dependence of  $J_c$  on magnetic field in twinned crystals of  $\text{YBa}_2\text{Cu}_3\text{O}_{7-\delta}$  and  $\text{ErBa}_2\text{Cu}_3\text{O}_{7-\delta}$ ," *Phys. C*, vol. 257, pp. 371-374, 1996.
- [93] T. Miyamoto, J. Katagiri, K. Nagashima, and M. Murakami, "Effect of Ag addition on the mechanical properties of bulk superconductors," *IEEE Trans. Appl. Supercond.*, vol. 9, no. 2, pp. 2066-2069, 1999.
- [94] M. Tomita and M. Murakami, "Improvement of the mechanical properties of bulk superconductors with resin impregnation," *Supercond. Sci. Technol.*, vol. 13, pp. 722-724, 2000.
- [95] S. I. Yoo, N. Sakai, H. Takaichi, T. Higuchi, and M. Murakami, "Melt processing for obtaining  $\text{NdBa}_2\text{Cu}_3\text{O}_y$  superconductors with high  $T_c$  and large  $J_c$ ," *Appl. Phys. Lett.*, vol. 65, no. 5, pp. 633-635, 1994.
- [96] D. A. Cardwell and D. Ginley, *Handbook of Superconducting Materials Volume I: Superconductivity, Materials and Processes*. CRC Press, 2002.
- [97] A. J. Young, G. W. Hong, C. J. Kim and T. H. Sung, "Deposition of  $\text{SmBa}_2\text{Cu}_3\text{O}_{7-y}$  seed crystal during top-seeded melt growth of  $\text{YBa}_2\text{Cu}_3\text{O}_{7-y}$ ," *Supercond. Sci. Technol.*, vol. 11, pp. 650-658, 1998.
- [98] W. Lo, D. A. Cardwell, and P. D. Hunneyball, "Growth morphology of large YBCO grains fabricated by seeded peritectic solidification □ : ( I ) The seeding process," *J. Mater. Res.*, vol. 13, pp. 2048-2056, 1998.
- [99] M. Oda, X. Yao, Y. Yoshida, and H. Ikuta, "Melt-textured growth of (LRE)-Ba-Cu-O by a cold-seeding method using  $\text{SmBa}_2\text{Cu}_3\text{O}_y$  thin film as a seed," *Supercond. Sci.*

- Technol.*, vol. 22, pp. 075012 (6 pp), 2009.
- [100] Y. H. Shi, N. Hari Babu, and D. A. Cardwell, "Development of a generic seed crystal for the fabrication of large grain (RE)-Ba-Cu-O bulk superconductors," *Supercond. Sci. Technol.*, vol. 18, pp. L13-L16, 2005.
- [101] H. H. Xu, Y. Y. Chen, L. Cheng, S. B. Yan, D. J. Yu, L. S. Guo, and X. Yao, "YBCO-buffered NdBCO film with higher thermal stability in seeding REBCO growth and recycling failed bulk YBCO superconductors," *Supercond. Sci. Technol.*, vol. 25, pp. 035014 (4 pp), 2012.
- [102] C. J. Kim, J. H. Lee, S. D. Park, B. H. Jun, S. C. Han, and Y. H. Han, "Y<sub>2</sub>BaCuO<sub>5</sub> buffer block as a diffusion barrier for samarium in top seeded melt growth processed YBa<sub>2</sub>Cu<sub>3</sub>O<sub>7-y</sub> superconductors using a SmBa<sub>2</sub>Cu<sub>3</sub>O<sub>7-d</sub>," *Supercond. Sci. Technol.*, vol. 24, pp. 15008 (7 pp), 2011.
- [103] D. Zhou, K. Xu, S. Hara, B. Li, Z. Deng, K. Tsuzuki, and M. Izumi, "MgO buffer-layer-induced texture growth of RE-Ba-Cu-O bulk," *Supercond. Sci. Technol.*, vol. 25, pp. 025022 (7 pp), 2012.
- [104] C. Kim, K. Kim, and G. Hong, "Y<sub>2</sub>BaCuO<sub>5</sub> morphology in melt-textured Y-Ba-Cu-O oxides with PtO<sub>2</sub> H<sub>2</sub>O/CeO<sub>2</sub> additions," *Phys. C*, vol. 232, pp. 163-173, 1994.
- [105] W. Zhai, Y. H. Shi, J. H. Durrell, A. R. Dennis, N. A. Rutter, S. C. Troughton, S. C. Speller, and D. A. Cardwell, "The processing and properties of single grain Y-Ba-Cu-O fabricated from graded precursor powders," *Supercond. Sci. Technol.*, vol. 26, pp. 125021 (11 pp), 2013.
- [106] Y. H. Shi, A. R. Dennis, and D. A. Cardwell, "A new seeding technique for the reliable fabrication of large, SmBCO single grains containing silver using top seeded melt growth," *Supercond. Sci. Technol.*, vol. 28, pp. 035014 (7 pp), 2015.
- [107] Y. Shi, D. Kumar Namburi, W. Zhao, J. H. Durrell, A. R. Dennis, and D. A. Cardwell, "The use of buffer pellets to pseudo hot seed (RE)-Ba-Cu-O-(Ag) single grain bulk superconductors," *Supercond. Sci. Technol.*, vol. 29, pp. 015010 (8 pp), 2016.
- [108] W. Zhai, Y. Shi, J. H. Durrell, A. R. Dennis, and D. A. Cardwell, "The influence of Y-211 content on the growth rate and Y-211 distribution in Y-Ba-Cu-O single grains fabricated by top seeded melt growth," *Cryst. Growth Des.*, vol. 14, pp. 6367-6375, 2014.

- [109] W. Zhai, Y. Shi, J. H. Durrell, A. R. Dennis, Z. Zhang, and D. A. Cardwell, "Processing and Properties of Bulk Y-Ba-Cu-O Superconductors Fabricated by Top Seeded Melt Growth from Precursor Pellets Containing a Graded CeO<sub>2</sub> Composition," *Cryst. Growth Des.*, vol. 15, no. 2, pp. 907-914, 2015.
- [110] J. M. S. Skakle, "Crystal chemical substitutions and doping of YBa<sub>2</sub>Cu<sub>3</sub>O<sub>x</sub> and related superconductors," *Mater. Sci. Eng. R Reports*, vol. 23, pp. 1-40, 1998.
- [111] T. Izumi, Y. Nakamura, T. H. Sung, and Y. Shiohara, "Reaction mechanism of Y-system superconductors in the MPMG method," *J. Mater. Res.*, vol. 7, no. 4, pp. 801-807, 1992.
- [112] C. Kim, K. Kim, I. Kuk, and G. Hong, "Role of PtO<sub>2</sub> on the refinement of Y<sub>2</sub>BaCuO<sub>5</sub> second phase particles in melt-textured Y-Ba-Cu-O oxides," *Phys. C*, vol. 281, pp. 244-252, 1997.
- [113] P. Diko, M. Šeřčíková, M. Kaňuchová, and K. Zmorayová, "Microstructure of YBCO bulk superconductors with CeO<sub>2</sub> addition," *Mater. Sci. Eng. B*, vol. 151, pp. 7-10, 2008.
- [114] P. Diko, C. Wende, D. Litzkendorf, T. Klupsch, and W. Gawalek, "The influence of starting YBa<sub>2</sub>Cu<sub>3</sub>O<sub>7-x</sub> particle size and Pt/Ce addition on the microstructure of YBa<sub>2</sub>Cu<sub>3</sub>O<sub>7-x</sub>-Y<sub>2</sub>BaCuO<sub>5</sub> melt processed bulks," *Supercond. Sci. Technol.*, vol. 11, pp. 49-53, 1998.
- [115] M. Muralidhar, M. Jirsa, S. Nariki, and M. Murakami, "Influence of combined Pt and CeO<sub>2</sub> additions on microstructure and magnetic properties in (Nd, Eu, Gd)-Ba-Cu-O," *Supercond. Sci. Technol.*, vol. 14, pp. 832-838, 2001.
- [116] M. Muralidhar, M. R. Koblishka, and M. Murakami, "(Nd, Eu, Gd)-Ba-Cu-O superconductors with combined addition of CeO<sub>2</sub> and Pt," *Supercond. Sci. Technol.*, vol. 13, pp. 693-697, 2000.
- [117] C. E. Mancini, "The development of high quality, cost-effective bulk superconductors for production processes," Mphil thesis, University of Cambridge, 2012.
- [118] Y. Chen, X. Cui, and X. Yao, "Peritectic melting of thin films, superheating and applications in growth of REBCO superconductors," *J. Prog. Mater. Sci.*, vol. 68, pp. 97-159, 2015.
- [119] D. Volochova, P. Diko, V. Antal, M. Radusovska, and S. Piovarci, "Influence of Y<sub>2</sub>O<sub>3</sub>

- and CeO<sub>2</sub> additions on growth of YBCO bulk superconductors,” *J. Cryst. Growth*, vol. 356, pp. 75-80, 2012.
- [120] N. H. Babu, E. S. Reddy, Y. Shi, K. Iida, T. D. Withnell and D. A. Cardwell, “Large Single Grain (RE) -Ba-Cu-O Superconductors With Nano-Phase Inclusions,” vol. 15, no. 2, pp. 3090-3093, 2005.
- [121] Y. Shi, N. H. Babu, K. Iida, W. K. Yeoh, A. R. Dennis, and D. A. Cardwell, “The influence of Gd-2411(Nb) on the superconducting properties of GdBCO/Ag single grains,” *Supercond. Sci. Technol.*, vol. 22, no. 7, pp. 075025 (5 pp), 2009.
- [122] Y. H. Shi, W. Yoeh, A. R. Dennis, N. H. Babu, S. Pathak, Z. Xu, and D. A. Cardwell, “Growth rate of YBCO single grains containing Y-2411(M),” *J. Phys. Conf. Ser.*, vol. 234, no. 1, pp. 12039, 2010.
- [123] N. H. Babu, K. Iida, Y. Shi, T. D. Withnell, and D. A. Cardwell, “YBa<sub>2</sub>Cu<sub>3</sub>O<sub>7-δ</sub>/Y<sub>2</sub>Ba<sub>4</sub>CuMO<sub>y</sub> single grain nanocomposite superconductors with high critical current densities,” *Supercond. Sci. Technol.*, vol. 19, no. 7, pp. S461-S465, 2006.
- [124] D. Zhou, B. Li, S. Hara, K. Xu, K. Tsuzuki, M. Miki, B. Felder, and M. Izumi, “Process technology and superconducting properties of bulk HTS with multi-RE elements,” *IEEE Trans. Appl. Supercond.*, vol. 23, no. 3, pp. 31-34, 2013.
- [125] A. Goyal, P. D. Funkenbusch, D. M. Kroeger, and S. J. Burns, “Fabrication of highly aligned YBa<sub>2</sub>Cu<sub>3</sub>O<sub>7-δ</sub>-Ag melt-textured composites,” *Phys. C*, vol. 182, pp. 203-218, 1991.
- [126] W. Lo, D. A. Cardwell, S. L. Dung, and R. G. Barter, “Processing of bulk YBa<sub>2</sub>Cu<sub>3</sub>O<sub>7-δ</sub> ceramics prior to peritectic solidification,” *J. Mater. Sci.*, vol. 30, no. 16, pp. 3995-4002, 1995.
- [127] D. Zhou, S. Hara, B. Li, J. Noudem, and M. Izumi, “Flux pinning properties of Gd-Ba-Cu-O trapped field magnets grown by a modified top-seeded melt growth,” *Supercond. Sci. Technol.*, vol. 27, no. 4, pp. 44015 (7 pp), 2014.
- [128] S. Pinol, F. Sandiumenge, B. Martinez, V. Gomis, J. Fontcuberta, X. Obradors, E. Snoeck, and C. Roucau, “Enhanced critical currents by CeO<sub>2</sub> additions in directionally solidified YBa<sub>2</sub>Cu<sub>3</sub>O<sub>7</sub>,” *Appl. Phys. Lett.*, vol. 65, no. 11, pp. 1448-1450, 1994.
- [129] C. Krauns, M. Tagami, M. Nakamura, Y. Yamada, and Y. Shiohara, *Advances in Superconductivity VII*. Tokyo: Springer, 1995.

- [130] C. Krauns, M. Sumida, M. Tagami, Y. Yamada, and Y. Shiohara, "Solubility of RE elements into Ba-Cu-O melts and the enthalpy of dissolution," *Zeitschrift fur Phys. B Condens. Matter*, vol. 96, no. 2, pp. 207-212, 1994.
- [131] K. Ogasawara, N. Sakai, M. R. Koblishka, A. Koblishka-Veneva, and M. Murakami, "Effects of subgrains on critical current properties in melt-processed RE-Ba-Cu-O bulk superconductors," *Supercond. Sci. Technol.*, vol. 17, no. 2, pp. S61-S65, 2004.
- [132] P. H. Hor, R. L. Meng, Y. Q. Wang, L. Gao, Z. J. Huang, J. Bechtold, K. Forster, and C. W. Chu, "Superconductivity above 90 K in the square-planar compound system  $ABa_2Cu_3O_{6+x}$  with A=Y, La, Nd, Sm, Eu, Gd, Ho, Er and Lu," *Phys. Rev. Lett.*, vol. 58, no. 18, pp. 1891-1894, 1987.
- [133] M. Nakamura, C. Krauns, Y. Yamada, and Y. Shiohara, "Crystal growth of  $SmBa_2Cu_3O_{7-x}$  under low oxygen partial pressure," *J. Cryst. Growth*, vol. 166, pp. 859-862, 1996.